The role of X-linked cell adhesion molecule Protocadherin 19 in neurogenesis and synapse formation

A thesis submitted to Cardiff University in accordance with the requirements for the degree of Doctor of Philosophy in the discipline of Neuroscience

Jessica Griffiths

May 2019

In memory of my Gramps, Gerald Griffiths.

Declaration

This work has not been submitted in substance for any other degree or award at this or any other university or place of learning, nor is being submitted concurrently in candidature for any degree or other award.

Signed ……Date……..……

STATEMENT 1

This thesis is being submitted in partial fulfilment of the requirements for the degree of Ph.D.

Signed ……Date……..……

STATEMENT 2

This thesis is the result of my own independent work/investigation, except where otherwise stated, and the thesis has not been edited by a third party beyond what is permitted by Cardiff University's Policy on the Use of Third Party Editors by Research Degree Students. Other sources are acknowledged by explicit references. The views expressed are my own.

Signed ……Date……..……

STATEMENT 3

I hereby give consent for my thesis, if accepted, to be available online in the University's Open Access repository and for inter-library loan, and for the title and summary to be made available to outside organisations.

Signed ……Date……..……

STATEMENT 4: PREVIOUSLY APPROVED BAR ON ACCESS

I hereby give consent for my thesis, if accepted, to be available online in the University's Open Access repository and for inter-library loans **after expiry of a bar on access previously approved by the Academic Standards & Quality Committee.**

Signed ……Date……..……

Acknowledgments

Firstly, I would like to thank my supervisor, Dr. Isabel Martinez Garay. Words cannot describe how grateful I am for your support, guidance, and the wonderful opportunities you have given me. Your knowledge and passion have truly inspired me every day and you have made me grow as a scientist and as a person. Thank you for everything.

I would like to express my deepest appreciation to my second supervisor, Prof. Yves-Alain Barde. I feel so fortunate to have worked in the lab with you these past few years. Your wise words and encouragement have greatly helped me throughout.

Thanks also go to Dr. Stéphane Baudouin. Even though you were not my supervisor I always felt like I could ask for your advice whenever I needed it.

This project was funded by the Wellcome Trust and the Welsh Government's Sêr Cymru program. I would like to thank you for your support.

Thanks also go to Bridget Allen and the Wales Gene Park for supporting me with the ESC harvest process and to Prof. Paul Kemp for introducing me to the world of electrophysiology and allowing me to use all the equipment. I would also like to thank Prof. Ros John's research group for providing the D4/XEGFP mouse line and Prof. Wieland Hüttner for providing the Tis21GFP mouse line.

To my brilliant summer project students, Rosie and David, thank you for your help in conducting the RGC experiments and analysis.

I am immensely grateful to have shared this experience with my past and present lab family who have taught me so much and have made this whole experience so enjoyable. Special thanks go to Shireene, Ellen, Natalia, and Laura. You have been there for me since the beginning and I am lucky enough to be finishing this marathon with you all and as friends for life. I would also like to extend my thanks to my buddy Sylvia for providing daily bouts of hysterical laughter and a "posi" friendship. Sincere thanks go to Hayley, Xinsheng, and Katharina for your generous sharing of knowledge and fruitful support throughout. Thanks also go to my good friend Oli, for assisting me with the MEA analysis and for helping me believe in myself. You are all amazing!

To my housemates and incredible friends; Ellie, Millie and Emily. Thank you for always brightening my days even after a long and hard day in the lab. Also, to my rays of sunshine and day ones; Tasha, Aimee, Jess and Ellie. Thank you for keeping me sane by making sure I took breaks while writing this thesis.

From the bottom of my heart, I would like to thank my family. Mum and Dad, thank you for your unconditional love and endless support, it has allowed me to put my heart and soul into this Ph.D. and everything that has come before it. Amy, thank you for being the best running and travel companion, you always know how to give me a boost just at the right time. To my grandparents, thank you for being my number one fans. I love you all.

Last but certainly not least, I would like to thank my partner Alex. You have been my rock throughout this journey and have made me smile even during the hardest of times. I wouldn't have been able to do this without you and all your love.

…my heart is full.

Abstract

Mutations in X-linked protocadherin 19 (PCDH19) lead to EIEE9 (Early Infantile Epileptic Encephalopathy 9), a syndrome characterised by early-onset epilepsy and cognitive impairment. PCDH19 tissue mosaicism is thought to be a critical driver of the disorder as the coexistence of PCDH19-expressing and non-expressing cells is believed to disrupt cell-cell communication, leading to hyperexcitability of neurons and the epileptic phenotype. The early-onset of the disorder and the spatiotemporal expression of *Pcdh19* in the developing cortex suggests a role for PCDH19 in cortical neurogenesis and synapse formation. Those two processes were therefore investigated in this thesis.

Firstly, during corticogenesis, *Pcdh19* expression was found to be complementary to the neurogenic gradient. Expression was high in RGC progenitors and declined in IPCs. Remarkably, PCDH19-expressing and non-expressing progenitors segregated in the cortex of *Pcdh19* HET mice, leading to an unusual phenomenon. Although cell cycle parameters, progenitor cell numbers, and neuronal output did not differ between PCDH19-expressing and non-expressing progenitors in WT and KO cortices, **within** the HET cortex, these progenitors had opposing neurogenic properties, producing significantly less and more neurons, respectively. Interestingly, these opposed behaviours resulted in a lack of differences overall between genotypes, suggesting a potential regulatory mechanism.

PCDH19's role in synaptogenesis was assessed in ESC-derived "cortical-like" neurons. A co-culture system of WT and KO neurons was generated to study PCDH19 mosaicism *in vitro*. No overall differences were found in the number of synapses formed; however, a preliminary assessment of spontaneous neuronal activity and calcium handling indicated that KO and co-cultured neurons had altered excitability and KCl-evoked calcium responses.

Together, this study shows that the co-existence of PCDH19-expressing and non-expressing cells affects cortical development. The *in vivo* and *in vitro* approaches developed in this thesis will help decipher the cellular and molecular mechanisms that govern these behaviours, to help understand the pathophysiology of EIEE9.

List of Abbreviations

+	Plus
%	Minus
-	Percentage
°C	Degrees Celsius
±	Plus or minus
≤	Less than or equal to
≥	Greater than or equal to
A	Alpha
B	Beta
Δ	Delta
E	Epsilon
Γ	Gamma
Mg	Microgram
Ml	Microliter
Mm	Micrometer
µM	Micromolar
5-FdU	5-fluoro2'-deoxyuridine
ASD	Autism spectrum disorder
Abi-1	Ab1 interactor 1
AMPA	α-amino-3-hydroxy-5-methyl-4-isoxazolepropionic acid
ANOVA	Analysis of variance
AS	Antisense
AU	Arbitrary units
BCA	Bicinchoninic acid
BDNF	Brain derived neutrophic factor
Bp	Base pair
BrdU	5-bromo-2'-deoxyuridine
bRGC	Basal radial glial cell
CA	Cellular aggregates
$CaCl_2$	Calcium chloride
CAM	Cell adhesion molecule

CDK	Cyclin-dependent kinase
cDNA	Cyclic DNA
CR	Cajal Retzuis
CRISPR	Clustered regularly interspaced short palindromic repeats
CM	Cytoplasmic domain
CNS	Central nervous system
CP	Cortical plate
Ct	Cycle threshold
Ctip2	chicken ovalbumin upstream promoter transcription factor interacting protein 2
Cux1	Cut-like homeobox protein 1
Cux2	Cut-like homeobox protein 2
CYFIP	Cytoplasmic FMR1-interacting protein
DAPI	4',6-diamidino-2-phenylindol dihydrochloride
ddH_20	Distilled water
DIG	Digoxigenin
DIV	Day *in vitro*
DG	Dentate gyrus
DII1	Delta-like 1
DMEM	Dulbecco's Modified Eagle Medium
DMSO	Dimethyl sulfoxide
DNA	Deoxyribonucleic acid
dNTP	Deoxynucleotide
DTT	Dithiothreitol
E	Embryonic day
EC	Extracellular domain
ECS	Embryonic stem cells
EDTA	Ethylenediaminetetraacetic acid
EdU	Ethynyl-2′-deoxyuridine
EIEE9	Early Infantile Epileptic Encephalopathy 9
EtOH	Ethanol
FBS	Fetal bovine serum
FGF	Fibroblast growth factor
FMRP	Fragile X mental retardation protein

GABA	Gamma-aminobutyric acid A
$GABA_A$	Gamma-aminobutyric acid A receptor, subunit gamma 1
GLAST	Glutamate aspartate transporter
gDNA	Genomic DNA
GFP	Green fluorescent protein
HA	Hemagglutinin
HET	Heterozygous
HRP	Horseradish peroxidase
Hrs	Hours
IPC	Intermediate progenitor cell
iPSC	Induced pluripotent stem cell
IZ	Intermediate zone
Kb	Kilobase
KCl	Potassium chloride
KO	Knockout
ICC	Immunocytochemistry
IHC	Immunohistochemistry
ISH	*In situ* hybridisation
KA	Kainate
LB	Lysogeny broth
LIF	Leukaemia inhibitory factor
M	Molar
MAP2	Microtubule-associated protein 2
MADM	Mosaic Analysis with Double Markers
MAPK	Mitogen-activated protein kinase
MAZ	Multipolar accumulation zone
MEA	Multi-electrode array
MEF	Mouse embryonic fibroblasts
MEF2	Myocyte enhancer factor-2
Min	Minute/s
$MgCl_2$	Magnesium chloride
mM	Millimolar
mRNA	Messenger RNA

Ms	Millisecond/s
MZ	Marginal zone
NaCl	Sodium chloride
NAP	Nucleosome assembly protein
NE	Neuroepithelial cell
NEAA	Non-essential amino acids
Ncad	N-cadherin
Ng	Nanograms
Nm	Nanometer
nM	Nanomolar
NMDA	N-methyl-D-aspartic acid
NP	Neural progenitor
NSPC	Neural stem progenitor cell
NONO	Non-POU-domain-containing, octamer binding protein
OCT	Optimal cutting medium
Pax6	Paired box protein 6
PAZ	Pre-synaptic active zone
PBS	Phosphate buffered saline
PCDH	Protocadherin
PCR	Polymerase chain reaction
pHH3	Phosphohistone H3
PP	Preplate
PSD	Post-synaptic density
PTV	Piccolo transport vesicle
RGC	Radial glial cell
RNA	Ribonucleic acid
Rpm	Revolutions per minute
RT	Room temperature
S	Sense
SATB2	Special AT-rich sequence-binding protein 2
SEM	Standard error of the mean
shRNA	Short hairpin RNA
SP	Subplate

SSC	Saline-sodium citrate
SVT	Synaptic transport vesicle
SVZ	Subventricular zone
Tbr1	T-box brain gene 1
TBS	Tris buffered saline
TSP	Thrombospondins
TUJ1	Class III beta-tubulin
VASP	Vasodilator-stimulated phosphoprotein
VGCC	Voltage gated calcium channel
vGLUT1	Vesicular glutamate transporter 1
vGLUT2	Vesicular glutamate transporter 2
vs.	Versus
WASP	Wiskott-Aldrich syndrome protein
WAVE	WASP family verprolin-homologous protein
WIRS	WAVE interacting regulatory sequence
WRC	WAVE regulatory sequence
WT	Wild-type
XCI	X-chromosome inactivation

Table of Contents

List of Figures

List of Tables

Chapter 1: Introduction

1.1 Cadherins

The cadherin superfamily contains over 110 transmembrane glycoproteins that are involved in mediating cell-cell interactions and intracellular signalling that are essential in animal morphogenesis (Takeichi 2007). They are calcium-dependent cell adhesion molecules that are mainly composed of a cytoplasmic domain, a transmembrane domain, and a calcium-binding extracellular domain. The extracellular domain is subdivided into repetitive extracellular cadherin (EC) repeats that are approximately 110 amino acids in length and are linked via Ca^{2+} binding motifs (Hirano and Takeichi 2012). The conserved extracellular domain mediates homophilic and heterophilic cell-cell interactions, while the cytoplasmic domain has a range of roles in signal transduction (Shapiro and Weis 2009). Although the classification of the superfamily can vary in different publications due to functional diversity, the cadherins can be phylogenetically divided into three groups: the classical cadherins, protocadherins, and desmosomal cadherins (Hulpiau and van Roy 2009). The architectural structures of the main cadherin subfamilies are highlighted in **Figure 1.1** (adapted from (Hayashi and Takeichi 2015)).

All cadherin groups are highly expressed within the nervous system, with different distinctive spatiotemporal patterns of expression throughout the developing and adult brain, suggesting a role in neural development and function (Sano *et al.* 1993; Vanhalst *et al.* 2005; Gaitan and Bouchard 2006; Kim *et al.* 2007; Zou *et al.* 2007; Kim *et al.* 2010). Interestingly, cadherins have been shown to have numerous roles in brain development; including neurogenesis, migration, axon pathfinding, synaptogenesis, connectivity and signal transduction (reviewed by (Takeichi 2007; Gärtner *et al.* 2014; Yamagata *et al.* 2018). In the developing mammalian cortex, several cadherins and protocadherins are expressed in specific subsets of cells as part of a combinational code that contributes to the complexity of the developing cortex (Krishna-K *et al.* 2011).

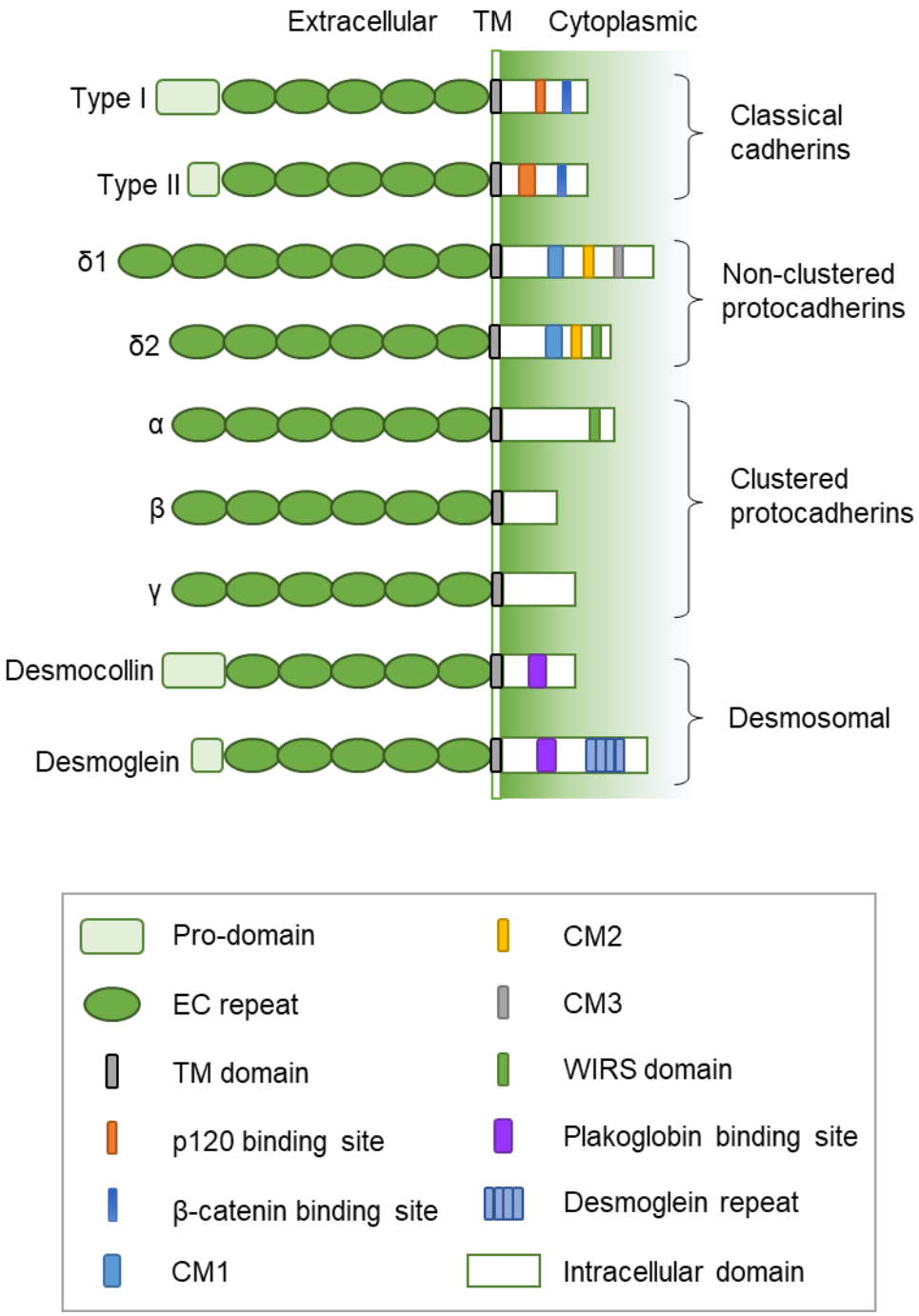

Figure 1.1: Architectural structures of the main cadherin subfamilies (adapted from (Hayashi and Takeichi 2015)). Structural features of the three main cadherin sub-families: classical cadherins, protocadherins (clustered and non-clustered) and desmosomal cadherins. Representation of the structural diversity with each domain and structure labelled (grey box). TM, transmembrane; EC, extracellular domain; CM, cytoplasmic domain; WIRS, WAVE interacting regulatory sequence.

1.1.1 Protocadherins

Protocadherins (PCDH) are the largest group within the cadherin superfamily and can be segregated into two main categories: (1) clustered protocadherins organised into three tandem arrays on chromosome 5q31 in human and chromosome 18 in mouse (Wu *et al.* 2001), and (2) non-clustered protocadherins that are scattered around the genome. Additionally, based on structural differences, the family also includes groups such as the seven-pass transmembrane cadherins which include the Flamingo/CELRS protocadherins, Fat-like protocadherins and other protocadherins. They all have more than five EC repeats, and unlike classical cadherins do not contain catenin binding sites (Hayashi and Takeichi 2015). Importantly, protocadherins are only capable of weak homophilic interactions, but have been shown to function by mediating cell-cell adhesion through the regulation of other adhesion molecules and by forming multi-cadherin complexes on the cell surface (Kim *et al.* 2011; Rubinstein *et al.* 2017).

1.1.1.1 Clustered Protocadherins

Clustered protocadherins comprise the α, β, and γ sub-groups. Recent work has shown that clustered protocadherins are important in neuronal survival and promote repulsive mechanisms that control dendritic self-avoidance, regulating neural connectivity and circuit formation (Lefebvre *et al.* 2012; Hasegawa *et al.* 2017; Ing-Esteves *et al.* 2018). Interactions between different gene clusters can also act synergistically to mediate these processes (Ing-Esteves *et al.* 2018). Clustered protocadherins are known to interact in cis forming dimeric recognition units. These cis-dimeric units can further interact in trans to form a zipper-like assembly (Rubinstein *et al.* 2017). It has been shown that the EC6 domain is required to form cis dimers, and isoform-specific binding between a subset of trans-interface residues causes head-to-tail interactions between EC1:EC4 and EC2:EC3 domains (Rubinstein *et al.* 2015; Goodman *et al.* 2016). These large zipper-like assemblies of complementary clustered PCDH's form between neurites from the same neuron when they come into contact, and they are assumed to produce a signal that triggers repulsion of neurites. When neurites from two different neurons come into contact, the likelihood of mismatched isoforms is high, limiting the size of the zipper assembly formed and are thought to prevent any repulsion signals from being produced (Rubinstein *et al.* 2017). This highlights a

mechanism where protocadherins contribute to the specificity and diversity required for correct neuronal circuitry.

1.1.1.2 Non-clustered Protocadherins

Non-clustered protocadherins can be sub-grouped into δ1, δ2 and ε (Kim *et al.* 2011). δ1 protocadherins have seven EC repeats and three conserved cytoplasmic motifs, and this subfamily is comprised of protocadherins 1, 7, 9, and 11. δ2 protocadherins contain six EC repeats and two conserved cytoplasmic motifs and include protocadherins 8, 10, 17, 18 and 19. Finally, ε protocadherins have variable numbers of EC repeats and include protocadherins 15, 16, 21, and -MUDCHL. Many non-clustered protocadherins have weak homophilic adhesive properties as shown by cell-cell interaction studies (Biswas *et al.* 2010; Tai *et al.* 2010; Emond *et al.* 2011).

These PCDHs are highly expressed in the central nervous system (CNS) and have been shown to play multiple roles in neuronal migration, cell segregation and synaptic plasticity (Kim *et al.* 2011). In Xenopus gastrulation, δ2 protocadherins play a key role in cell sorting and convergent extension, and in zebrafish they are involved in cell movement in neurulation, motor axon arborisation, soma topography and axonal growth (Chen and Gumbiner 2006; Emond *et al.* 2009; Biswas *et al.* 2014; Asakawa and Kawakami 2018). In mammals, PCDH10 and PCDH17 are detected in axonal fibers and are important in the extension and formation of axonal tracts in the amygdala and ventral telencephalon (Uemura *et al.* 2007; Hayashi *et al.* 2014). Furthermore, PCDH17 is involved in neuromuscular connectivity, through cell repulsion mechanisms that regulate soma topography and axonal growth in the abducens motor neurons (Asakawa and Kawakami 2018).

All the δ2 protocadherins also have a WAVE interacting regulatory sequence (WIRS) that interacts with the WAVE complex to regulate actin cytoskeleton dynamics (Chen *et al.* 2014a). PCDH17 bound-WAVE binds to lamellipodin and Ena/VASP and has been shown to be expressed in excitatory and inhibitory synapses of the basal ganglia (Hayashi *et al.* 2014; Hayashi and Takeichi 2015). Finally, non-clustered protocadherins are also thought to enhance spine dynamics as PCDH8 has been found to regulate endocytosis of the classical cadherin, N-

cadherin via an activity-dependent process, through its binding to TAO2β kinase in hippocampal neurons (Takeichi and Abe 2005; Yasuda *et al.* 2007).

In addition, combinatorial expression of δ-protocadherins has recently been shown to provide another level of complexity to this relatively small subfamily. Olfactory sensory neurons express different numbers of δ-protocadherins per cell, and each δ-protocadherin had a different adhesive affinities (Bisogni *et al.* 2018). Remarkably, δ-protocadherins were found to modulate their adhesive behaviour depending on their relative surface expression and could also control the adhesive behaviour of other non-clustered and clustered protocadherin family members (Bisogni *et al.* 2018). Combining their combinational expression and self-modulatory behaviour, protocadherins could provide cell surface diversity that is required for circuit assembly during brain development.

1.1.2 Protocadherins in Pathology

Several protocadherins have been previously associated with carcinogenesis and neurological and neurodevelopmental disorders.

Homozygous deletions of protocadherins on chromosome 13q21 have been associated with several cancers. Non-clustered protocadherins 8, 9, 10, 17 and 20 have been reported as tumour suppressor genes (Kim *et al.* 2011). Mutations in *PCDH8,* for example, have been found to promote oncogenesis in human epithelial cancers such as breast cancer (Yu *et al.* 2008; Kim *et al.* 2011).

Regarding neurodevelopmental disorders, PCDH10 has been associated with autism spectrum disorder (ASD) through myocyte enhancer factor (MEF2) and fragile X mental retardation protein (FMRP) - mediated synapse elimination. Mechanistically, PSD-95, a post-synaptic scaffolding protein, is ubiquitinated and subsequently binds to PCDH10, leading to its proteasome degradation (Morrow *et al.* 2008; Tsai *et al.* 2012). Single-nucleotide polymorphisms (SNPs) spanning *PCDH15* and *PCDH17* have been shown to have an involvement in major mood disorders, including psychotic bipolar disorder and schizophrenia (Dean *et al.* 2007; Narayanan *et al.* 2015; Chang *et al.* 2017). Also, *PCDH17* polymorphisms were found to decrease amygdala volume, amygdala function, and reduce dendritic spine density in primary cortical neurons and post-mortem brains (Chang

et al. 2017). Furthermore, mutations in *PCDH19* lead to early-onset epilepsy and cognitive impairment, a syndrome designated as EIEE9 (Early Infantile Epileptic Encephalopathy 9) (Dibbens *et al.* 2008).

1.2 Early Infantile Epileptic Encephalopathy 9 (EIEE9)

EIEE9 is a disorder with variable degrees of epilepsy and intellectual disability, with seizure onset in infancy between 6-36 months. These seizures usually occur in clusters and are exacerbated by fever. Alongside the epileptic phenotype, hyperactivity, autistic and obsessive-compulsive features are among those neuropsychiatric symptoms most commonly seen in individuals with EIEE9 (Kolc *et al.* 2018). Additionally, early seizure onset (≤12 months) has been associated with more severe intellectual disability than late seizure onset (≥12 months) (Kolc *et al.* 2018).

The disorder was initially discovered in 1971 and was designated as Juberg-Hellman syndrome (Juberg and Hellman 1971). It was only in 2008 that mutations in *PCDH19* were determined as the genetic cause for this disorder (Dibbens *et al.* 2008) when seven families were identified to have a mutated *PCDH19* via systematic re-sequencing of X-chromosome genes (Dibbens *et al.* 2008).

EIEE9 has now become the second most common cause of monogenic epilepsy, after *SCN1A* in Dravet syndrome (Depienne and LeGuern 2012). Approximately 150 mutations have been identified in *PCDH19*, including whole gene deletions, partial gene deletions and point mutations, of which 50% are missense (Kolc *et al.* 2018). Most of the reported mutations, including all missense mutations, have been found in exon 1 of the gene, which encodes the extracellular and transmembrane domains of the protein. Moreover, few mutations have been found in the cytoplasmic domain (van Harssel *et al.* 2013; Duszyc *et al.* 2015; Kolc *et al.* 2018).

As with most X-linked genes, *PCDH19* is subjected to X-chromosome inactivation (XCI). XCI is a dosage compensation mechanism by which genes undergo epigenetic silencing in either the maternal or paternal X chromosome to normalise gene expression levels in cells that have two X chromosomes (Lyon 1961). XCI is implicated in several neurological disorders, and variable phenotypes can usually be found in females due to XCI mosaicism (Gribnau and Barakat 2017). In a

classical model of X-linked inheritance, males are usually more severely affected than females, independent of whether there is an X-linked dominant or X-linked recessive environment (Scheffer *et al.* 2008). In the case of EIEE9, mutations can be familial or sporadic and have an unusual inheritance pattern. Although the mutated gene was initially thought to be sex-limited (Juberg and Hellman 1971), X-chromosome linkage was later determined, and the disorder was described as "X-linked dominant with male sparing" (Ryan *et al.* 1997). The epileptic and intellectual disability phenotype was only seen in the heterozygous females, and hemizygous males were spared of the symptoms. Some hemizygous males were, however, also reported to have some autistic-like traits but with no cases of epilepsy or other phenotypic features (Scheffer *et al.* 2008). Interestingly, a number of male patients have since been diagnosed with EIEE9 that present with somatic mutations in *PCDH19* (Depienne *et al.* 2009; Terracciano *et al.* 2012; Terracciano *et al.* 2016; Thiffault *et al.* 2016; de Lange *et al.* 2017; Perez *et al.* 2017).

Several theories have been suggested to explain the pathological mechanism of EIEE9. The unusual mode of inheritance was initially proposed to be caused by a dominant negative effect in heterozygous females, a compensatory gene on the Y chromosome in males, or a male rescue factor (Ryan *et al.* 1997). However, with further research these theories were discarded. Dibbens *et al.* found that mutated *PCDH19* mRNA in primary skin fibroblasts introduced premature STOP codons that were recognised and degraded by nonsense-mediated decay surveillance systems, indicating that complete loss of *PCDH19* was not pathogenic and that the truncated protein was not likely to lead to the disorder. Furthermore, as mentioned above, there are cases of males with somatic mutations that present with the disorder. Additionally, a recent study documented a male with Klinefelter syndrome (KS) presenting with EIEE9 (Romasko *et al.* 2018). Klinefelter syndrome is a disorder where an individual has a sex-chromosome abnormality (XXY, 47 chromosomes). In this particular case, a male with KS presented with a mutant copy of *PCDH19* of one X-chromosome and a normal copy of *PCDH19* on the other X-chromosome. There are now two hypotheses that surround the pathological mechanism of the disorder; the cellular interference hypothesis and the neurosteroid hypothesis.

1.2.1 Cellular interference hypothesis

In light of the studies described above, it has been hypothesised that EIEE9 arises because of a phenomenon called “cellular interference” (**Figure 1.2**; adapted from (Depienne *et al.* 2009)). Originally termed metabolic interference, this theory explains how mosaic expression of certain proteins within the same individual or organism can cause disruption in the interactions between mutated and wild-type cells (Johnson 1980)**.** In EIEE9, heterozygous females and mosaic males have a mixture of PCDH19-expressing (WT) and non-expressing cells (KO). In contrast, hemizygous males and unaffected males and females have homogenous populations of PCDH19 KO cells, and PCDH19 WT cells, respectively. The fact that only heterozygous females and males with a somatic mutation are symptomatic suggests that tissue mosaicism is an underlying factor for EIEE9. In fact, it has been hypothesised that the mixture of KO and WT cells in the heterozygous brains disrupts cell-cell communication and synapse formation leading to hyperexcitability of neurons (Dibbens *et al.* 2008; Depienne *et al.* 2009). Although the inheritance pattern supports this hypothesis, no direct proof has been obtained so far. To further support this hypothesis, it should be confirmed that females with homozygous mutations of PCDH19 are also unaffected. In addition, although *in vitro* systems have been designed to create mosaic cultures that may mimic the mosaicism found in EIEE9 (Homan *et al.* 2018), it has not yet been determined whether these cultures are a suitable model for the disorder and if they have phenotypic features that deviate from a PCDH19 WT or KO culture. Finally, it is still to be proven whether synapse formation or function is altered in a mosaic setting, leading to EIEE9.

1.2.2 Neurosteroid hypothesis

Another pathogenic mechanism that has recently been proposed offers an alternative, although not mutually exclusive theory. Tan *et al*. showed that heterozygous mutations in *PCDH19* cause dysregulation in neurosteroid levels, hypothesising that this leads to the pathology in EIEE9 (Tan *et al.* 2015). Neurosteroids are steroid hormones that play a vital role in the modulation of brain excitability through interactions with certain neuronal membrane receptors and ion channels, including $GABA_A$ receptors (Reddy 2010). Neurosteriods also modulate neurogenesis, neurite outgrowth, and neuronal survival (Charalampopoulos *et al.*

2008). They are also anti-convulsive and have sexual dimorphic effects, which correlates with the pathology of EIEE9 (Tan *et al.* 2015). Interestingly, *PCDH19* heterozygous females and mosaic males have reduced levels of the neurosteroid allopregnanolone and dysregulation of aldo-keto reductase family 1-member C1-C3 (AKR1C1-3) genes, which encode crucial steroid hormone-metabolizing enzymes (Tan *et al.* 2015). A reduction in other neuroactive steroids has subsequently been confirmed, including pregnenolone sulphate, 17OH-progesterone, progesterone and cortisol (Trivisano *et al.* 2017). Remarkably, an analysis of the upstream regulatory regions of 73 dysregulated genes in EIEE9 showed 22% to be regulated by nuclear steroid hormone receptors (Tan *et al.* 2015).

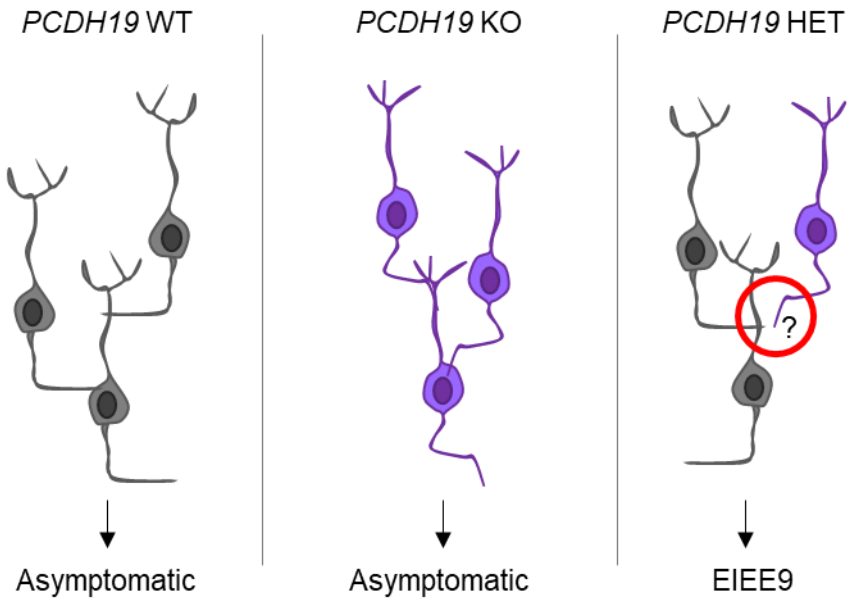

Figure 1.2: Cellular interference model (adapted from (Depienne et al. 2009). Representation of PCDH19 WT cells in a healthy individual, PCDH19 KO cells in hemizygous males, and PCDH19 WT and KO cells in heterozygous females and mosaic males. WT, wild-type; KO, knock-out; HET, heterozygous; EIEE9, Early Infantile Epileptic Encephalopathy 9.

1.3. Protocadherin 19 (PCDH19)

1.3.1. Structure and function of PCDH19

PCDH19 encodes a 1,148-amino acid, δ2 non-clustered protocadherin. It has a total of six exons. Exon 1 spans approximately 2000 bp, coding for six EC repeats and the transmembrane domain; exons 2 to 6 code for the cytoplasmic domain, with two highly conserved regions CM1 and CM2, as well as the WRC interacting receptor sequence (WIRS) (Wolverton and Lalande 2001; Redies et al. 2005). Several protein binding partners have recently emerged in the literature revealing multiple functions of the extracellular domain, with its cell adhesive properties, and the cytoplasmic domain, with its intracellular signalling and trafficking properties. **Figure 1.3** (adapted from (Gerosa *et al.* 2018)) highlights the interacting partners and approximate binding sites that are described in more detail below.

Like many other non-clustered protocadherins, PCDH19 is weakly adhesive. Crystallographic structures from zebrafish revealed that PCDH19 EC1-4 repeats are the adhesive units that form a trans-adhesive interface, interacting to generate an antiparallel PCDH19 dimer (Cooper *et al.* 2016). These dimers involve the full overlap of EC1-4 repeats, which is described as a “forearm handshake” (Cooper et al. 2016). Studies in chick and zebrafish have also looked at the function and adhesiveness of PCDH19. In chick retina, PCDH19 expressing (+) cells aggregate; however, when mixed with PCDH10+ cells, they segregate from one another, suggesting that PCDH19 has a stringent adhesive specificity (Tai et al. 2010). Reinforcing this adhesive specificity, Bisogni *et al.* found that PCDH19+ cells segregate from PCDH19+PCDH7+ cells; however, PCDH7 cells intermix with PCDH19+PCDH7+ cells. Similarly, PCDH19+ cells intermix with PCDH19+PCDH9+, but PCDH9+ cells segregate from PCDH19+PCDH9+ cells (Bisogni *et al.* 2018). Interestingly, it was also found in zebrafish that PCDH19+ cells in the optic tectum segregate into radial columns of neurons, and loss of PCDH19 disrupts this columnar organisation (Cooper et al. 2015). This study also observed that PCDH19 mutants exhibited increased cell proliferation in the optic tectum as well as impaired visual guided behaviours (Cooper et al. 2015).

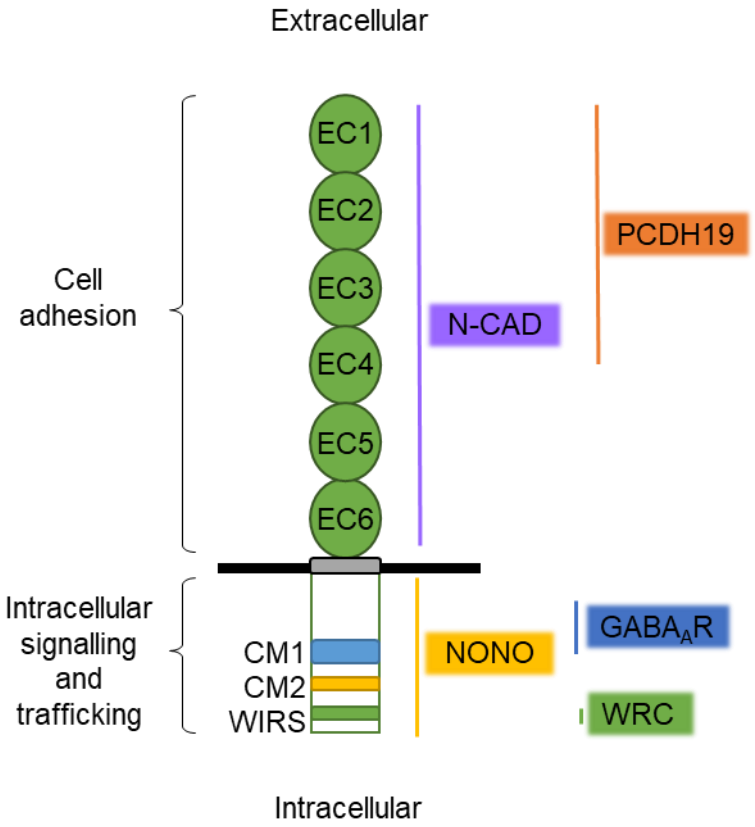

Figure 1.3: PCDH19 protein binding partners (adapted from (Gerosa et al. 2018)). Structural features of PCDH19, including the extracellular, transmembrane and cytoplasmic domains of the protein, their general functions and published protein interacting partners. EC, extracellular repeat; PCDH19, protocadherin 19; N-cad, N-cadherin; CM, cytoplasmic domain; WIRS, WAVE interacting regulatory sequence; NONO, non-POU domain-containing octamer binding protein; $GABA_AR$, gamma-aminobutyric acid, type A, receptors; WRC, WAVE regulatory complex.

Interestingly, PCDH19 can form cis-complexes with the classical cadherin, N-cadherin to synergistically control cell movement during morphogenesis in zebrafish (Biswas et al. 2010). The PCDH19-N-cadherin complex displays different adhesive properties to those of individual N-cadherin or PCDH19, with PCDH19 exerting a dominant role in forming this robust adhesion (Emond et al. 2011). Like many protocadherins, N-cadherin is known to have a multitude of roles during brain development due to its ability to act both as an adhesion and a signalling molecule. Some of these roles include: (1) regulating neuronal progenitor cell proliferation and differentiation during neurogenesis (Miyamoto *et al.* 2015); (2) controlling neuronal attachment to radial glial fibres and nucleokinesis during radial migration (Shikanai *et al.* 2011; Martinez-Garay *et al.* 2016); (3) regulating synapse formation (Bruses 2006), and (4) regulating dendritic spine morphogenesis during synapse plasticity (Togashi *et al.* 2002; Bruses 2006). As PCDH19 is a binding partner of N-cadherin, it is possible that when these two cadherins are co-expressed, PCDH19 could play a role in these processes and mechanisms during brain development.

As mentioned above, all δ2 protocadherins, including PCDH19, have a WIRS binding domain at its C-terminus that interacts with the WRC. The WRC is comprised of the hematopoietic stem/progenitor cell protein 300 (HSPC300), cytoplasmic interactor of FMRP 1 and 2 (CYFIP1/2), Nck-associated protein (NAP1) and Abelson interactor 1 (Abi-1), which together regulate actin cytoskeleton dynamics through the stimulation of the Arp2/3 complex (Chen *et al.* 2014a). Pull-down assays have identified NAP1 and CYFIP2 as interacting partners of PCDH19 in chick embryos (Tai *et al.* 2010). Moreover, Hayashi *et al*. found that PCDH19 co-localises with 57% of Abi-1 puncta in hippocampal neurons, suggesting that PCDH19 may be partly regulating cell-cell contact through the WAVE complex and potentially influencing actin cytoskeleton dynamics (Hayashi *et al.* 2017). Recently, Bassani *et al.* found that down-regulation of *Pcdh19* affects dendritic morphology in hippocampal neurons and postulated that this could be mediated through the control of actin cytoskeleton organisation (Bassani *et al.* 2018). This is particularly interesting as cytoskeletal arrangements are crucial during brain development, modulating the morphology of early neural precursors during neurogenesis and migration, as well as affecting neurite branching, extension and retraction later in development (Compagnucci *et al.* 2016).

PCDH19 was recently found to interact with a nuclear paraspeckle protein involved in gene expression regulation, called, non-POU-domain-containing octamer binding protein p54nrb/NONO (NONO). The interaction between NONO and PCDH19 led to the positive co-regulation of gene expression via estrogen receptor alpha (ERα), the nuclear steroid hormone receptor (Pham *et al.* 2017). Complementing the neurosteroid hypothesis, ERα is involved in the metabolism of neurosteroids, including those neurosteroids that are dysregulated in EIEE9 (Tan *et al.* 2015; Pham *et al.* 2017; Trivisano *et al.* 2017). Moreover, estrogen signalling is generally pro-convulsant and has epileptogenic properties in humans and animal models (Veliskova 2007). It is not yet clear where within the cell PCDH19 and NONO interact; however, work in the Martinez-Garay laboratory has shown that upon neuronal activation in ESC-derived cortical neurons, cytoplasmic fragments of PCDH19 are cleaved and may translocate to the nucleus, which provides a possible site of interaction.

The proximal and central regions of PCDH19's cytoplasmic domain bind to the TM3-4 loop of the $GABA_A$ receptor alpha subunits to regulate receptor surface availability, suggesting a possible role of this complex in intracellular signalling (Bassani *et al.* 2018). Additionally, using shRNA-mediated downregulation, loss of PCDH19 was found to affect GABAergic signalling, causing a lower frequency of miniature post-inhibitory post-synaptic currents (mIPSCs) in hippocampal neurons (Bassani *et al.* 2018). GABAergic signalling is vital for inhibitory neurotransmission in the adult brain and also during development, and its trophic excitatory effects also play a role in neuronal migration, maturation and synapse formation (Deidda *et al.* 2014). Furthermore, neurosteroids including allopregnanolone, which is deficient in EIEE9, are positive allosteric modulators of $GABA_A$ receptors (Wang 2011).

1.3.2 Mammalian expression of PCDH19

Pcdh19 mRNA has previously been shown to have tissue-specific expression during mouse embryogenesis in both neural and non-neural tissue (Gaitan and Bouchard 2006). Early in development, at embryonic day (E)9 in mouse embryos, expression originates from the presomitic mesoderm and is found in the midbrain, forebrain, and discretely in the hindbrain (Gaitan and Bouchard 2006). By E12.5 expression is apparent in several neural tissues including the cortex, lateral ganglionic eminences, neural retina, and spinal cord. Regarding non-neuronal expression, *Pcdh19* is present in regions of the renal and digestive systems and in hair follicles (Gaitan and Bouchard 2006). The expression of *Pcdh19,* particularly in the developing and adult mammalian brain, was found to be spatially and temporally regulated, indicating that PCDH19 has multiple roles during development.

As described in **Section 1.2**, mutations in *PCDH19* cause intellectual disability and epilepsy in humans, with most seizures originating from the frontotemporal limbic system (Marini *et al.* 2012). It is therefore not surprising that the predominant expression of *Pcdh19* is found in the cortex, hippocampus, and hippocampal connecting regions (lateral septum and basolateral amygdaloidal complex, entorhinal cortex, prefrontal cortex) (Dibbens *et al.* 2008; Kim *et al.* 2010; Hertel and Redies 2011). In the developing hippocampus, *Pcdh19* is highly expressed in the *cornus ammonis* (CA)1 and CA3 regions, compared to the dentate gyrus (DG). However, in adult hippocampus, expression is highest in the DG, compared to CA1 and CA3 regions, suggesting a potential role in adult neurogenesis (Kim *et al.* 2010). A recent characterisation of *N-cadherin* and *Pcdh19* expression in the postnatal mouse limbic system has also revealed robust overlapping expression, particularly in the amygdala, hippocampus, and ventral hypothalamus (Schaarschuch and Hertel 2018).

Western blot analysis of mouse lysates from hippocampal and cortical regions, shows that PCDH19 is expressed as early as E10.5, throughout development, and in adulthood, peaking at developmental time points that correlate with the onset of neurogenesis and synaptogenesis (Hayashi *et al.* 2017). *In situ* hybridisation data from the Allen Brain Atlas indicate that *Pcdh19* is transiently expressed in the proliferative regions of the developing cortex. At E10 and E12, PCDH19 expression is apparent in the proliferative zone of the cortex, co-localising with mitotic cell

marker pHH3, and radial glial cell marker Sox2 (Fujitani *et al.* 2017). Later at E18.5, *Pcdh19* has restricted mediolateral bands of expression in a subset of neurons in the deep part of layer IV and layer Va in the primary somatosensory, cingulate and motor cortex (Dibbens *et al.* 2008; Hertel and Redies 2011; Krishna-K *et al.* 2011). In addition, in the adult somatosensory cortices the layer-specific expression observed at E18.5 is maintained in both rat and mouse cortices (Hertel and Redies 2011; Krishna-K *et al.* 2011). Hayashi *et al.* also found PCDH19 to be expressed in layer II and in layer Va cells of the mouse somatosensory cortex (Hayashi *et al.* 2017).

In differentiated cultures of mouse neural stem progenitor cells (NSPCs) there is expression of *Pcdh19* mRNA in neurons, progenitors, astrocytes, and oligodendrocytes (Homan *et al.* 2018). Although there is limited human expression data available, human PCDH19 has been localised in human induced pluripotent stem cells (iPSCs) in neural rosettes and mature neurons (Compagnucci *et al.* 2015; Homan *et al.* 2018). Regarding synapse localisation, Pederick *et al.* used chemical fractionation and primary hippocampal neuronal cultures to characterise subcellular localisation of PCDH19 in synaptosome fractions *in vivo* and synapses *in vitro* (Pederick *et al.* 2016). Hayashi *et al.* also examined the localisation of PCDH19 in primary hippocampal neurons and found that endogenous PCDH19 is expressed in dendrites but is not a constituent component of synapses. It was revealed that there was minimal co-localisation with a pre-synaptic marker, Synapsin-1/2 and a post-synaptic marker, Homer-1 and even less co-registered synapse localisation (Hayashi *et al.* 2017). PCDH19 was also shown to be expressed in GABAergic hippocampal neurons but was found not to be a constituent component of the GABAergic synapses either (Bassani *et al.* 2018).

Using overexpression of Myc-tagged PCDH19 in HeLa cells, hippocampal neurons and Madin-Darby Canine Kidney (MDCK) cells, it was speculated that PCDH19 or at least a cleaved fragment of PCDH19 could be found in the nucleus, where it plays a role in neurosteroid gene transcription (Pham *et al.* 2017). However, this would need to be confirmed as the tag used to detect PCDH19 was located at the N-terminus, where it could interfere with the signalling peptide required for transport to the plasma membrane.

As previous PCDH19 specific antibodies have proven to be non-specific for immunohistochemistry (IHC), there is limited data on protein expression and on

the characterisation of PCDH19-expressing cells in the developing mammalian system, hence further studies are required to characterise the expression patterns in more detail to elaborate on the potential roles of PCDH19 during mammalian brain development.

1.4 Cortical development

The mammalian cortex is an interconnected six-layered structure central to the mammalian nervous system, controlling the most sophisticated cognitive and motor functions. Cortical development can be separated into three main stages; neurogenesis, migration, and synaptogenesis (**Figure 1.4**). Its development is complex and finely-tuned and interestingly, cortical neurons are generated in an "inside-out" manner, with early born-neurons populating the deep layers of the cortex, and later-born neurons migrating past them to form the superficial layers. Corticogenesis will be summarised below with particular emphasis on the development of excitatory cortical projection neurons. As neurogenesis and synaptogenesis are important processes that contribute to the main aims and hypothesises of this thesis, they will be discussed in more depth in **Sections 1.4.1** and **1.4.2**, respectively.

Before the start of neurogenesis, a proliferating pool of NSCs called neuroepithelial (NE) cells line the dorsal telencephalic wall. At the onset of neurogenesis, NE cells transition into highly polarised progenitor cells, called radial glial cells (RGC) that populate the ventricular zone (VZ) and have apical and basal structures that span the width of the developing cortex (Ramon Y Cajal 1952; Rakic 1971). RGCs undergo multiple divisions to proliferate and give rise to neurons throughout cortical development (**Figure 1.4A**). To increase neuronal output, RGCs divide to generate a different type of progenitor cell, called intermediate progenitor cell (IPC), which delaminates from the ventricular surface and migrates basally. The region where the IPCs accumulate is called the subventricular zone (SVZ). Within this region, IPCs divide symmetrically to proliferate (only rarely in mouse) and to generate neurons. Another level of complexity and a further increase in neuronal output and neocortical size is provided in larger and gyrencephalic brains when RGCs produce outer or basal RGCs, giving rise to the outer SVZ (Hansen *et al.* 2010).

Once born, excitatory projection neurons detach and migrate away from the VZ to accumulate in the lower SVZ, termed the multipolar-accumulation zone (MAZ). Here they convert from multipolar to bipolar cells, extending thin axons and thick leading processes to aid radial migration (Takano *et al.* 2015). Initially, early-born neurons are able to extend their processes and attach to the basal surface, followed by shortening of the process and subsequent movement of the neuronal cell bodies to the cortical plate (CP) via a process termed "somal translocation"

(Nadarajah *et al.* 2001). Later in neurogenesis as the cortex expands, neurons undergo RGC-guided locomotion where they use the RGC basal processes as a scaffold for migration (**Figure 1.1B**) (Kawauchi *et al.* 2010). Once the neurons are close enough to the marginal zone (MZ), they transiently pause and detach from the RGC basal process, switching migration mode and anchoring to the basal surface in a process called terminal translocation (Sekine *et al.* 2011). It is important to note that some excitatory neurons migrate tangentially into the developing cortex. Cajal Retzuis (CR) cells for example are generated at E10.5 in mouse and stem from multiple embryonic structures, including the cortical hem, ventral hem, and the caudomedial telencephalon and thalamic eminence (Takiguchi-Hayashi *et al.* 2004; Bielle *et al.* 2005; Meyer 2010; Gu *et al.* 2011). CR cells migrate tangentially to form the preplate (PP) at the basal surface of the developing cortex (Hevner *et al.* 2003) and play an integral role in the regulation of radial migration through the secretion of the extracellular matrix protein, reelin (Ogawa *et al.* 1995; Franco *et al.* 2011; Gil-Sanz *et al.* 2013; Sekine *et al.* 2014). Projection neurons generated later in the VZ and SVZ migrate radially, invade the PP and split it into the subplate (SP) and the MZ. The SP contains a hetergenous population of the earliest generated neurons from cortical and extracortical origins and is transient in nature as many of the neurons in this region undergo apoptosis during postnatal development (Price *et al.* 1997; Pedraza *et al.* 2014). As more neurons settle between the SP and MZ, the space between these two structures becomes the cortical plate (CP) which gives rise to layers II to VI of the mature cortex. A region called the intermediate zone (IZ) is also generated between the SVZ and the CP; a cell-sparse region that neurons traverse to reach the CP.

As migration proceeds, neurons extend axons that elongate throughout the developing brain to form cell-specific synaptic connections (**Figure 1.1C**). Generally, the axons of deep layer neurons (layer V and VI) predominantly project sub-cortically, to regions in the thalamus (layer VI), hindbrain and spinal cord (layer V). Superficial layer neurons (layers II, III and IV) have predominantly intracortical axonal targets.

A number of signalling molecules and “priming” factors, such as cell adhesion molecules (CAMs), are required to initiate synapse formation between specific axonal and dendritic structures. CAMs can trigger axonal target recognition and initiate the assembly of pre-synaptic axonal and post-synaptic dendritic

specializations (Dalva *et al.* 2007; Südhof 2018). Specific pre- and post-synaptic molecules shuttle towards these specialized domains, forming the pre-synaptic active zone (PAZ) and post-synaptic density (PSD), respectively. Once synapses are assembled changes in morphology, functional properties, and cellular composition occur over time. Activity-dependent processes determine whether these synapses stabilize or are eliminated during development, ensuring the correct number and type of connections are made for effective neurotransmission throughout the brain (Waites *et al.* 2005).

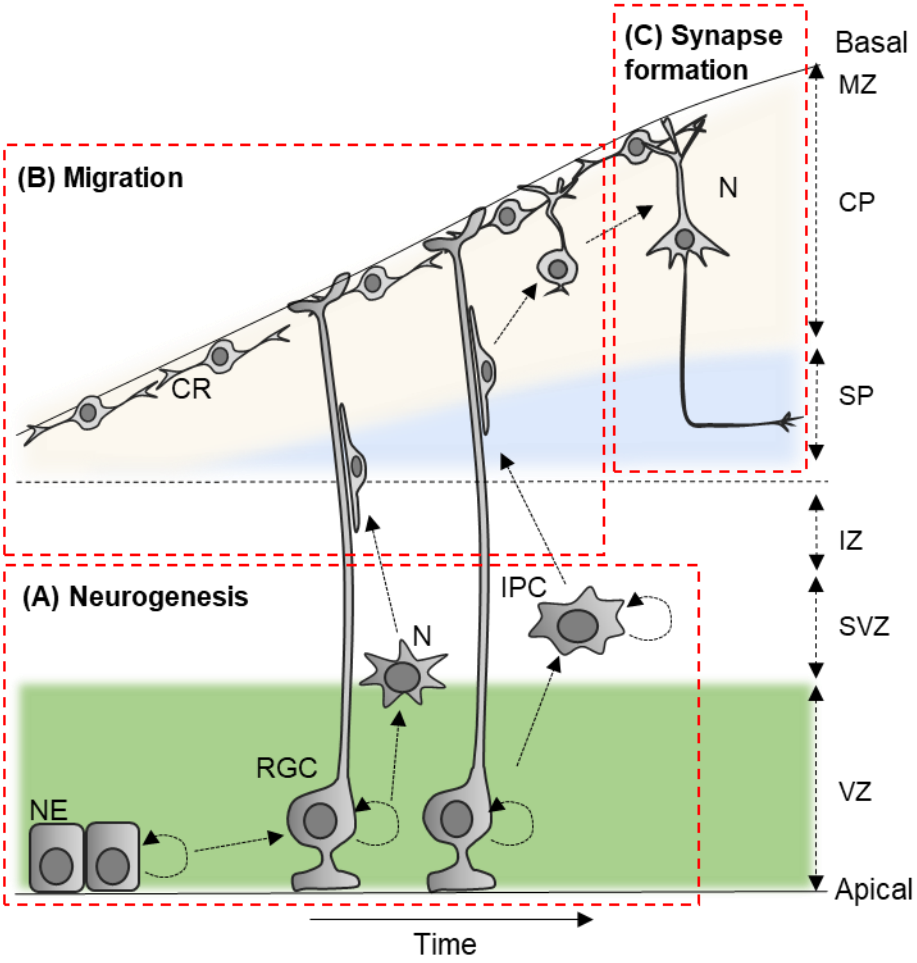

Figure 1.4: Mouse cortical development. Summary of the three phases of mouse cortical development over time: **(A)** neurogenesis, **(B)** migration, and **(C)** synapse formation. NE, neuroepithelial cells; RGC, radial glial cells; N, neurons' IPC, intermediate progenitor cells; CR, Cajal-Retzuis cells; VZ, ventricular zone; SVZ, subventricular zone; IZ, intermediate zone; SP, subplate; CP, cortical plate.

1.4.1. Neurogenesis

During early corticogenesis, at approximately E9 in mouse and gestational week 5-6 in humans, NE cells line the dorsal telencephalic wall in the neural tube, dividing symmetrically to produce a pool of proliferative cells (Rakic 1995). These cells are highly polarised, with tight junctions and adherens junctions at the apical end of the plasma membrane that maintain cell polarity (Aaku-Saraste *et al.* 1996; Manabe *et al.* 2002; Götz and Huttner 2005). As NE cells divide, they undergo a process called interkinetic nuclear migration (INM), where the nuclei migrate from the basal membrane to the apical surface when transitioning from S phase to mitosis (Sauer 1935) and back to the basal surface during G_1. This INM is responsible for the pseudostratified appearance of what becomes the VZ of the developing cortex (Sauer 1935).

At the onset of neurogenesis, NE cells transition into highly polarised progenitor cells called RGCs. These progenitor cells attach to the apical surface of the VZ via end-foot structures that contain adherens junctions and extend long radial fibres that span the thickness of the developing cortex (Götz and Huttner 2005). During the transition of NE cells to RGCs, there is an upregulation of adhesion molecules such as N-cadherin, and glial markers such as glutamate-aspartate transporter (GLAST) and brain lipid-binding protein (BLBP). At the same time, certain epithelial features such as occludin expression and tight junctions disappear (Aaku-Saraste *et al.* 1996; Kriegstein and Alvarez-Buylla 2009; Martynoga *et al.* 2012). RGCs like NEs, undergo INM, but their nuclear migration does not extend through the entire width of the cortical primordium and is restricted to a portion of the cell, which defines the boundary of the VZ (Götz and Huttner 2005).

RGCs can divide in different ways, initially undergoing proliferative symmetric divisions to expand their pool (Takahashi *et al.* 1996). RGCs can also switch from symmetric to asymmetric divisions, to produce a daughter RGC and a daughter cell that differentiates into a post-mitotic neuron (Iacopetti *et al.* 1999; Haubensak *et al.* 2004). It is this division mode that allows for the production of the first cohort of projection neurons via a process termed direct neurogenesis. Individual RGCs directly produce a small number of neurons; approximately one or two neurons per cycle (Noctor *et al.* 2001; Noctor *et al.* 2004) and 8 to 9 neurons altogether (Gao *et al.* 2014). RGCs can also asymmetrically divide to generate a daughter RGC, and an IPC, that delaminates from the apical ventricular surface and migrates

basally to establish the SVZ. Finally, RGCs shift towards a self-consumption symmetric division mode to produce astrocytes and oligodendrocytes at the end of neurogenesis, at approximately E17.5 in the mouse cortex (Malatesta *et al.* 2000; Tamamaki *et al.* 2001; Toma and Hanashima 2015; Winkler *et al.* 2018).

IPCs do not maintain any contact with basal or apical surfaces and therefore lack apicobasal polarity. Following their generation, IPCs can expand their proliferative pool and the SVZ by dividing symmetrically to form two daughter IPCs (Noctor *et al.* 2004), although these proliferative divisions occur more frequently in the human than in the rodent cortex (LaMonica *et al.* 2013). Normally, mouse IPCs undergo self-consuming symmetric divisions to form two neurons (Haubensak *et al.* 2004; Kowalczyk *et al.* 2009). In larger and gyrencephalic cortices, the SVZ further subdivides into the inner and outer SVZ, which contains IPCs and a large number of basal RGCs that contribute to the increase in size and complexity of the cortex (Hansen *et al.* 2010; Dehay *et al.* 2015). The generation of neurons via IPCs, is termed indirect neurogenesis. Indirect neurogenesis is slower than direct neurogenesis due to the intermediate progenitor step; however, the neuronal output is greater (Kriegstein *et al.* 2006).

For the purpose of this thesis I will be referring to the main progenitor cell types as RGCs and IPCs; however, these progenitors can also be categorised broadly as apical and basal progenitors, respectively. Taverna *et al.* provided an excellent review referring to the progenitor types, dependent on three criteria; (1) location of mitosis, (2) cell polarity, and (3) proliferative capacity, allowing for the further categorisation of the progenitor cell types, the identification of new progenitor cells types (such as the subapical progenitor cell (Pilz *et al.* 2013) and for better evolutionary comparisons (Taverna *et al.* 2014).

As mentioned above, neurogenesis occurs in an “inside-out” manner, with neurons destined for certain cortical layers being generated from progenitor cells in a temporal sequence. Early-born neurons mainly reside in the deep cortical layers and later-born neurons reside in the superficial layers. However, it has been suggested that progenitor cells are more heterogenous than originally thought. Genetic lineage-tracing experiments have shown that regardless of birthdate, some progenitors are specified to generate upper layer neurons (Nieto *et al.* 2004; Zimmer *et al.* 2004; Franco *et al.* 2012; Gil-Sanz *et al.* 2015). However, these studies remain controversial (Eckler *et al.* 2015). Other studies have revealed that

neuronal fate is more dynamic and individual progenitors can give rise to a full diversity of excitatory neuronal subtypes. Using Mosaic Analysis with Double Markers (MADM), neuronal output from single RGCs could be measured via Cre recombination. Using this technique, progenitors at E10 to E13 were found to produce all neuronal cell layers in the developing cortex (Gao *et al.* 2014). Moreover, fate-mapping studies have shown that IPC's have the ability to contribute to all cortical layers (Vasistha *et al.* 2015). A detailed quantitive assessment using retroviral tracing, MADM, and genetic lineage tracing supports the notion that cortical neurogenesis is dynamic, and only a limited number of cell identities are required to generate the full diversity of the mature cortex (Llorca *et al.* 2018).

Interestingly, another level of neurogenic complexity has been recently highlighted using Flash-Tag pulse labelling. Neurons born between E11.5 and E13.5 were found to be distributed broadly within the deep cortical layers and were largely heterogeneous in their molecular expression of deep and superficial layer markers (Magrinelli *et al.* 2018). In contrast, neurons generated between E14.5 and E16.5 were found to have more restricted neurogenic potential and the time of birth became a strong determinant of their final location (Magrinelli *et al.* 2018). These results suggest that early neurogenesis has a less determined fate potential than later neurogenesis and encompasses the idea that progenitor cells gradually become fate-restricted as corticogenesis proceeds.

1.4.1.1. Regulation of neurogenesis

Many cell intrinsic and extrinsic factors regulate neurogenesis and the balance between cell proliferative and neurogenic divisions. This is vital for normal brain development, as dysregulation in these divisions can alter neuron and glia output later in development and lead to a number of disorders, including micro- and megalocephaly. These disorders lead to underlying conditions including epilepsy, cognitive decline, and other neurological symptoms (Winden *et al.* 2015; Hanzlik and Gigante 2017). Factors that regulate neurogenesis include, but are not limited to, (1) cleavage plane and mitotic spindle orientation, (2) signalling pathways, (3) cell cycle length, (4) transcription factors, and (5) epigenetic mechanisms.

1.4.1.1.1. Cleavage plane and mitotic spindle orientation

It has been proposed that the orientation of the cleavage plane during mitosis directly affects daughter cell fate, due to the distribution of certain cell fate determinants. Typically, in mouse dividing RGCs, upon apical domain-bisecting of the cleavage plane (vertical cleavage) the daughter cells receive equal determinants and are likely to divide symmetrically. In contrast, upon apical domain bypassing or even when there is a slight tilt of the cleavage plane (oblique cleavage) the two daughter cells will receive unequal determinants and the division is asymmetric (Kosodo *et al.* 2004; Konno *et al.* 2008; Matsuzaki and Shitamukai 2015). Mitotic spindle orientation can largely govern cleavage plane orientation and genes involved in the modulation of centrosomes, astral microtubules, and other proteins at the cell cortex can affect whether progenitor cells divide symmetrically or asymmetrically (Lancaster and Knoblich 2012; Delaunay *et al.* 2014). For example, *Nde1,* a LIS1-interacting protein that is essential during centrosome duplication and mitotic spindle assembly, causes mispositioning of mitotic chromosomes and abnormal mitotic orientation when deleted in *Nde1* knock-out (KO) mouse cortices, leading to an increase in the number of mitotic progenitor cells and the number of cells leaving the cell cycle (Feng and Walsh 2004). The inheritance of polarity proteins located at the apical ventricular end feet also contribute to daughter cell fate. For example, inheritance of the par-complex proteins PAR3 and PAR6 is involved in the maintenance of self-renewing asymmetric divisions via Notch signalling (Costa *et al.* 2008; Bultje *et al.* 2009; Dong *et al.* 2012).

1.4.1.1.2. Signalling pathways

There are many signalling pathways that have been found to play a role in neurogenic fate. Arguably the most studied is the Notch signalling cascade, which has a dual role during cortical neurogenesis, promoting the transition of NEs to RGCs and also inhibiting the generation of IPCs from RGCs by suppressing pro-neural genes such as *Ngn2* and *Mash1* (Gaiano *et al.* 2000; Mizutani *et al.* 2007). Newly differentiated neurons, IPCs, and RGCs have been shown to undergo lateral inhibition; a process where differentiating cells with high expression of Notch ligands, such as Delta-like (Dll1) and Jagged activate Notch signalling to prevent the differentiation of neighbouring cells (Kawaguchi *et al.* 2008; Li *et al.* 2008; Nelson *et al.* 2013). More recent work has shown that different combinations of

Notch signalling molecules further diversifies the progenitor pool (Nelson *et al.* 2013). Other molecules can work in conjunction with Notch signalling, such as Neuregulin 1 through its ErB2 receptor. Downregulation of *ErB2* led to the transformation of RGCs to astrocytes and *Notch1* was found to upregulate *ErB2* in RGCs (Schmid *et al.* 2003). In addition, increased *Slit/Robo* signalling in amniotes led to decreased levels of *Dll1*, leading to impaired IPC formation and the promotion of direct neurogenesis (Cárdenas *et al.* 2018). Another example of a pathway that governs progenitor fate is fibroblast growth factor (FGF) signalling, by promoting RGC identity and a reduction in the progression of RGCs to IPCs (Yoon *et al.* 2004; Kang *et al.* 2009; Martynoga *et al.* 2012). In particular, FGF2 has been found to shorten the G_1 phase of the cell cycle by regulating the expression of cyclin D1 and cyclin-dependent kinase (CDK) inhibitor p27(kip1) (Lukaszewicz *et al.* 2002).

1.4.1.1.3. Cell cycle length

It is known that cell cycle length increases in neural progenitors as neurogenesis proceeds (Takahashi *et al.* 1993). Interestingly, asymmetrically-dividing neurogenic progenitors have a longer cell cycle duration than symmetrically-dividing proliferative progenitors (Haubensak *et al.* 2004; Calegari *et al.* 2005). Furthermore, G_1 lengthening and S-phase shortening are associated with the transition of neural stem cells into IPCs (Arai *et al.* 2011). Using experimental alterations of G_1 length, an increase in length caused premature neurogenesis and a reduced number of IPCs (Calegari and Huttner 2003), whereas a decrease in length caused an expansion of self-renewing progenitors and a rise in IPC number (Pilaz *et al.* 2009), indicating that the cell cycle is highly regulated and dynamic during corticogenesis.

1.4.1.1.4 Transcription factors

In addition to those factors described above, several transcription factors including *Pax6*, and pro-neural factors such as *Ascl1* and *Ngn2* also regulate progenitor fate (as reviewed by (Martynoga *et al.* 2012)). *Pax6* has been found to promote RGC symmetric proliferate divisions by regulating spindle orientation (Asami *et al.* 2011). Lack of *Pax6* leads to premature delamination of progenitor cells from the VZ with an unequal distribution and reduced number of adherens junction proteins (N-cadherin, aPKC and β-catenin) and the Par complex protein, PAR3 (Asami *et al.* 2011). *Pax6* also interacts with other neurogenic regulators such as the Notch

signalling target *Hes1*, and with *Ngn2* and *Asc1*, to control the balance between self-renewal and neurogenesis (Sansom *et al.* 2009). Interestingly, pro-neural genes such as *Ngn2* and *Asc1* appear during the transition of NE's to RGC's and *Ngn2*:*Asc1* double mutants failed to undergo neurogenic divisions and instead excessively proliferated and generated astrocytes (Nieto *et al.* 2001).

1.4.1.1.5 Epigenetic mechanisms

Epigenetic modifications including DNA methylation and histone modifications have also been shown to control the expression of certain genes during neurogenesis, as well as to regulate neurogenic divisions (reviewed by (MuhChyi *et al.* 2013). For example, modifications of the BAF170 subunit of the chromatin-remodelling complex suppress the expression of *Pax6* target genes, such as *Tbr2*, *Cux2,* and *Tle2,* leading to a premature switch to indirect neurogenesis, through an increased generation of IPCs (Tuoc *et al.* 2013).

Taken together, there is a high number of studies that have implicated multiple intrinsic and extrinsic components in the control of neurogenesis and ultimately the generation of the precise number and neuronal cell types of the mature cortex. However, the fundamental mechanism that integrates many of these factors and explains how the switch from proliferative and neurogenic divisions is controlled is still unknown.

1.4.2 Synaptogenesis

Synapses are asymmetric intercellular junctions that allow for the transfer of information from one neuron to another, forming highly complex networks and bi-directional communication between areas of the developing and mature brain. These junctions are composed of: (1) a pre-synaptic terminal that contains synaptic vesicles filled with neurotransmitters, as well as structures involved in neurotransmitter release, (2) a post-synaptic terminal, that has various ion channels, scaffolding proteins, and signalling molecules that can be activated by chemical and electrical stimuli, and (3) a synaptic cleft that separates and aligns the pre- and post-synaptic specializations. The majority of synapses formed can be categorised as excitatory or inhibitory, where transmission is mainly mediated by ionotropic glutamate receptors (NMDA, AMPA and KA receptors) and ligand-gated ion channels ($GABA_A$ and glycine receptors), respectively. Synapse formation can be broadly split into four main stages; initial contact, induction, synaptic terminal differentiation and maturation. Each of the main stages are graphically represented in **Figure 1.5** and are described below.

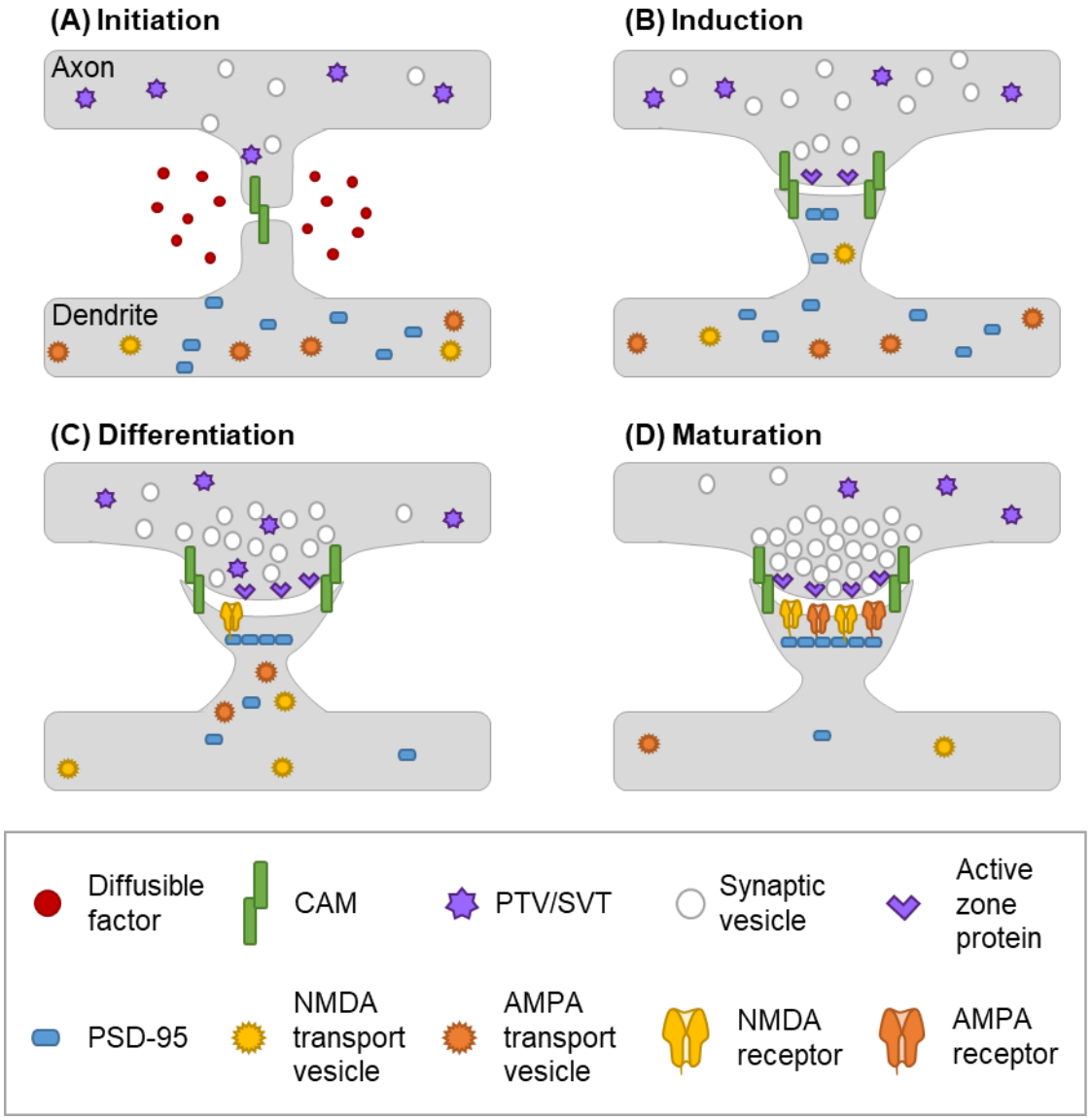

Figure 1.5: Excitatory synapse formation (adapted from (Garner *et al.* 2002)). **(A)** Synapse formation via diffusible synaptogenic factors and CAMs. **(B)** Induction of pre-synaptic and post-synaptic assembly due to further CAM interactions. **(C)** Synaptic terminal differentiation where synaptic vesicle proteins and active proteins are shuttled to the developing PAZ via PTVs/SVTs and transport vesicles and PSD components are shuttled sequentially to the PSD. **(D)** Maturation as the synapse stabilises and differentiates via an activity-dependent process. CAM, cell adhesion molecule; PTV, piccolo transport vesicles; SVT, synaptic transport vesicle; PSD-95, post-synaptic density protein 95; NMDA, N-methyl-D-aspartate; AMPA, α-amino-3-hydroxy-5-methyl-4-isoxazolepropionic acid.

1.4.2.1 Synapse initiation and induction

Initially, a neuron's axonal growth cone elongates, developing into a presynaptic site. Simultaneously, dendrites project from the cell soma to develop into a potential postsynaptic site. Once a presynaptic terminal and a complementary post-synaptic partner come into contact, these synaptic sites assemble into highly motile filopodia structures from the growth cones and shafts, exhibiting protrusive and exploratory behaviour (Ahmari *et al.* 2000; Chen *et al.* 2014b). Functional synapses form at axonal-dendritic, axonal-somatic, axonal-axonal or dendro-dendritic contact sites. Interestingly, most excitatory synapses onto pyramidal neurons occur on dendritic spines, whereas inhibitory synapses specifically target axon, soma or alternative dendritic domains (Spruston 2008).

It has been suggested that synapse initiation and preliminary contact is stimulated by several diffusible synaptogenic factors, such as brain-derived neurotrophic factor (BDNF), FGF, and thrombospondins (TSP) (McAllister 2007). Astrocytes have also been found to secrete ions and neuroactive molecules such as cholesterol and TSP to facilitate the maturation of incoming axonal and dendritic processes (Farhy-Tselnicker and Allen 2018). Furthermore, interacting trans-synaptic cell adhesion molecules (CAMs), such as neurexins and their ligands, cadherins, Ephrins/Eph receptors and synaptic CAMs coordinate axonal target specification and the precise and cell-specific alignment of pre- and post- synaptic terminals (reviewed by (McAllister 2007)). Interestingly, it is believed that the vast array of cadherin interactions are required for correct connections between specific neurons and certain combinations of cadherin clusters are required for molecular identity in neurons (Mountoufaris *et al.* 2017).

Once synaptic targets are recognised, CAMs can induce synapse formation, causing certain pre- and post- synaptic cytoplasmic and membrane-associated protein precursors to be packaged into dense vesicular structures and shuttled along the cell's axon or dendrite towards the newly formed synaptic sites to form the PAZ and PSD (**Figure 1.2B**). Several CAMs are known to be involved in synapse induction, including those described above that initiate synapse formation (Dalva *et al.* 2007; Südhof 2018). For example, N-cadherin is required for the recruitment of three synaptic organisers: neuroligin 1, leucine-rich repeat transmembrane protein 2 (LRRtm2), and Cell Adhesion Molecule 1

(Cadm1/SynCAM), and the recruitment of neurexin1β, inducing pre- and post-synaptic terminal differentiation (Yamagata *et al.* 2018).

1.4.2.2 Synapse differentiation

During pre-synaptic differentiation, proteins involved in vesicle release and synaptic proteins continue to be transported to the pre-synaptic terminal to generate the PAZ. Instead of being transported individually many proteins are packaged and transported in large aggregates (**Figure 1.2B-C**). Two types of presynaptic transport vesicles have been identified to be involved in this shuttling; piccolo transport vesicles (PTVs) and synaptic vesicle proteins transport vesicles (SVTs) (McAllister 2007). Both PTVs and SVTs can move in anterograde and retrograde directions (Ahmari *et al.* 2000; Shapira *et al.* 2003), with periods of saltatory movement that correlate with increased synapse formation (Sabo *et al.* 2006). Microtubule components, such a kinesin superfamily motor proteins are essential for the coordinated movement and arrangement of these vesicles (Hirokawa *et al.* 2009).

At the post-synaptic site, post-synaptic protein 95 (PSD-95) and glutamatergic receptors (NMDA and AMPA receptors) are delivered sequentially to form the post-synaptic density (**Figure 1.2B-C**) (Friedman *et al.* 2000). There have been a number of suggestions for possible transport mechanisms involved in shuttling these components. They can be shuttled in transport packages, but it has also been observed that NMDA and AMPA receptors are transported independently along microtubules (Washbourne *et al.* 2002; Washbourne *et al.* 2004). Moreover, NMDA receptors and other scaffolding proteins have been found to be recruited from diffuse pools (Bresler *et al.* 2004). In addition, it has been reported that pre-assembled PSD scaffolding complexes have appeared at predefined sites before synapse formation and that they can induce presynaptic differentiation and stabilisation, suggesting there may be pre-determined sites for synapse formation (Gerrow *et al.* 2006).

1.4.2.3. Synapse maturation

As the synaptic terminals differentiate and stabilize, they start to mature. Maturation is activity-dependent, and leads to changes in receptor composition, ion channels, and transporters. During maturation, synaptic vesicles increasingly cluster at the PAZ, and PSD proteins accumulate to become a more complex

assembly (**Figure 1.2D**) (McAllister 2007). Structurally, dendritic protrusions become more defined, forming “neck” and “head” structures that can develop into mushroom-shaped or stubby spines (**Figure 1.2D**) (Vicente-Manzanares *et al.* 2009).

During maturation, silent synapses that contain NMDA but not AMPA receptors require an activity-dependent mechanism to upregulate AMPA (Anggono and Huganir 2012). Additionally, there are changes in the expression of voltage-gated calcium channels (VGCCs). At the onset of synaptogenesis, there is an upregulation of N-type and L-type neuronal VGCCs in pre- and post-synaptic membranes, respectively (Vigers and Pfenninger 1991). There is also a switch from the expression of N-type to the more active Q-type VGCCs (Scholz and Miller 1995). Interestingly, vesicular glutamate transporters (vGLUT) are also altered during maturation (Berry *et al.* 2012). Downregulation of vGLUT2 and upregulation of vGLUT1 promotes presynaptic terminal differentiation in cortical neurons, correlating with the accumulation of synaptic proteins such as synapsin and synaptophysin (Berry *et al.* 2012).

Finally, synapses have been shown to be dynamic structures, contributing to remodelling of neural circuits (Alsina *et al.* 2001). They can be eliminated and reformed as axonal branches and dendritic spines increase their complexity (Alsina *et al.* 2001; Trachtenberg *et al.* 2002). A number of theories have been considered to instruct synapse elimination, such as the retraction of a synapse through an active reconstruction process or the elimination through microglia or astrocyte phagocytosis, but further research is required to confirm the general mechanisms and signalling pathways involved (Südhof 2018).

1.5 PCDH19 in cortical development

Protocadherin 19 has been shown to be highly expressed with a specific spatial and temporal pattern throughout cortical development in both human and rodent brains (Gaitan and Bouchard 2006; Dibbens *et al.* 2008; Hertel and Redies 2011; Pederick *et al.* 2016). In the rodent, low expression of *Pcdh19* was found as early as E9 (Gaitan and Bouchard 2006). Quantification of RNA levels in mouse cortical tissue revealed that *Pcdh19* levels peak at E12.5 and diminish during later embryonic development. Following birth, expression levels peak again during early post-natal development, before diminishing during adulthood (Fujitani *et al.* 2017). Interestingly, cortical neurogenesis onset occurs at approximately E11.5/E12.5 in mice, while synapses start to form during the first postnatal week, peaking at P14, before stabilising between P21 and P28 (Farhy-Tselnicker and Allen 2018). This highlights two distinctive developmental time windows in which *Pcdh19* is expressed: at the onset of neurogenesis and during synapse formation.

Recent studies have supported the hypothesis that PCDH19 is involved in cortical neurogenesis. It has been found that miR-484, involved in 16p13.11 microduplication syndrome, can control neurogenesis by binding to a specific sequence of the 3'-untranslated region of *Pcdh19* mRNA, inhibiting *Pcdh19* translation and mRNA stabilization (Fujitani *et al.* 2017). Using shRNA, *Pcdh19* was found to increase RGC proliferation and decrease the differentiation of RGCs into IPCs (Fujitani *et al.* 2017). Furthermore, Homan *et al.* used the differentiation of NSPCs from mouse and human patient-derived cell lines to uncover that loss of PCDH19 function led to enhanced neurogenesis, premature maturation of cells and loss of progenitor cell polarity (Homan *et al.* 2018). In *Pcdh19* KO mouse NPSC differentiations there was also an increase in the number of neurons generated at the expense of oligodendrocytes (Homan *et al.* 2018). Together, it has been suggested that PCDH19 KO cells are undergoing premature neurogenesis and therefore PCDH19 may be involved in the maintenance of proliferative progenitor divisions.

Further studies have looked at PCDH19 mosaicism during cortical neurogenesis. Pederick *et al.* recently generated a mouse line using CRISPR/Cas9 genome editing to insert a hemagglutinin (HA)-FLAG epitope sequence at the C terminus of PCDH19 to identify all PCDH19-expressing cells (Pederick *et al.* 2018). By crossing this mouse line with a *Pcdh19* KO line that expressed a β-galactosidase

(β-gal) reporter cassette, replacing exons 1-3 of the *Pcdh19* gene, Pederick and colleagues generated a *Pcdh19* HET mouse. As the HET mouse co-expressed HA-tagged PCDH19-expressing cells and β-gal-expressing PCDH19 KO (non-expressing) cells, individual populations could be traced. Interestingly, a segregated and "columnar-like" expression pattern was seen in the developing cortices (Pederick *et al.* 2016; Pederick *et al.* 2018). This expression pattern was not present in the HA-tagged PCDH19 WT control mice, indicating that it was not due to random X-chromosome inactivation, but that it had to be related to the tissue mosaicism (Pederick *et al.* 2018). As this segregation was seen as early as E10.5 in the mouse cortex, it is important to assess how this striking pattern could affect progenitor behaviour and neuronal output during cortical neurogenesis.

Interestingly, an electrocorticogram analysis was performed on *Pcdh19* wild-type (WT), knock-out (KO) and HET young adult mice. It was found that neuronal activity in WT and KO cortices was similar. Remarkably, HET mice had a dramatic increase in amplitude and duration of neuronal activity (Pederick *et al.* 2018). Furthermore, Pederick *et al.* went on to rescue the aberrant changes in network activity seen in *Pcdh19* HET mice by deleting the functional *Pcdh19* allele in the HET model (Pederick *et al.* 2018). This observation indicates that the aberrant changes in network activity are due to the mosaic expression of PCDH19. Whether this change in network activity is a consequence of alterations in synaptic function and connections remains to be determined.

The data presented in both *in vitro* and *in vivo* systems suggests that PCDH19 is playing a role in cortical neurogenesis, particularly in the maintenance of proliferating progenitor cells. As those experiments were carried out in an *in vitro* system, the structural architecture of the brain is lost, and the striking cell sorting arrangement found in the *Pcdh19* HET cortices could not be studied. Therefore, it is vital that this hypothesis is investigated *in vivo* to elaborate on PCDH19's physiological and pathophysiological role during neurogenesis. Additionally, although *Pcdh19* has not yet been studied in synapse formation, the aberrant network activity in the *Pcdh19* HET mouse, the peak expression during synaptogenesis and localisation at the synapse (described in **Section 1.3.2**) points towards a role of PCDH19 in this process.

1.6 Hypothesis and aims

Investigating the role of PCDH19 in cortical development is vital to better understand the function of this protein, and to determine the pathophysiology of EIEE9. Although recent publications have advanced in deciphering the role of PCDH19 at a fundamental biological level, there are still limited studies that thoroughly characterise its function during cortical development. With limited expression data and evidence confirming the pathogenetic mechanism that underlies EIEE9, it is important that the results observed thus far in animal models and stem cell culture systems are investigated further.

Based on the spatial and temporal expression pattern of *Pcdh19* in the developing mammalian cortex, the current studies using *Pcdh19* KO mouse models, the early onset of EIEE9, and the phenotypic symptoms of the disorder, the fundamental hypothesis for this thesis is that PCDH19 plays a role in neurogenesis and synapse formation. To test this hypothesis and to answer the outstanding questions that expand on the current research, the following aims were formulated:

- Characterise the cells that express PCDH19 during neurogenesis by combining RNA *in situ* hybridisation with immunohistochemistry.
- Assess the role of PCDH19 in neurogenesis using birth dating markers and immunohistochemistry to assess cell cycle parameters and the quantitative levels of certain cell types.
- Generate an *in vitro* system and develop a co-culture system to study *Pcdh19* mosaicism as a disease model of EIEE9.
- Assess the role of PCDH19 in synaptogenesis using this *in vitro* system.

Chapter 2: Materials and methods

2.1 Animal husbandry

Experiments were conducted in accordance to local ethical approval and Home Office approval under the UK Animals (Scientific Procedures) Act 1986. Mice were held in a 12-hour light /dark cycle and received food and water *ad libitum.* Mice were weaned four/five-weeks post-birth and kept in cages with a maximum of five animals per cage.

2.2 Mouse lines

C57BL/6 (B6) mice were purchased from Charles River Laboratories, *Pcdh19* knock-out (KO) mice (TF2108) from Taconic Biosciences, D4/XEGFP (X-GFP) were kindly provided by Prof. Ros John's research group at Cardiff University, and the Tis21GFP mice were kindly provided by Prof. Wieland Hüttner at the Max Planck Institute of Molecular Cell Biology and Genetics in Dresden, Germany. The *Pcdh19* KO mouse line was maintained on a B6 background.

In the *Pcdh19* KO mouse line, the *Pcdh19* allele has a β-galactosidase (β-gal)/neomycin (neo) reporter cassette replacing exons 1-3 of the gene, which is therefore expressed under the control of the endogenous *Pcdh19* promoter (**Figure 2.1**; modified from (Pederick *et al.* 2016)). This mouse line was recently validated and tested to confirm the activity of the cassette (Pederick *et al.* 2016).

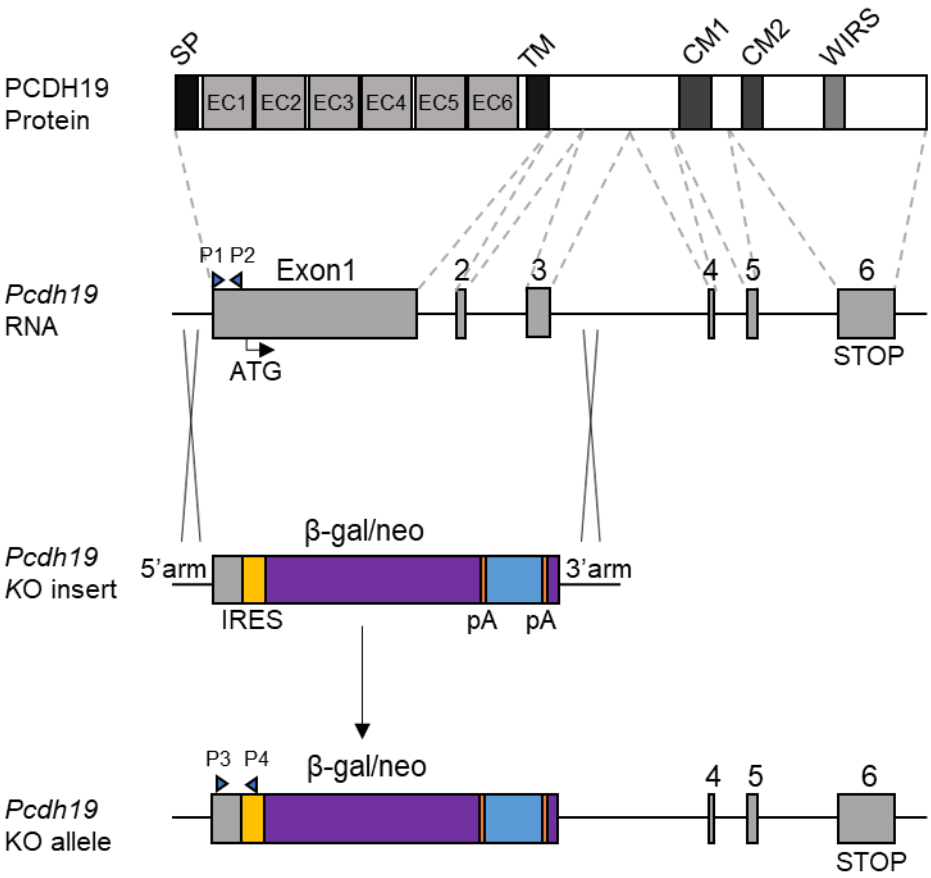

Figure 2.1: *Pcdh19* KO mouse model (modified from (Pederick *et al.* 2016)). Diagrammatic representation of the *Pcdh19* KO line, where a β-galactosidase/neomycin fusion reporter cassette replaces exons 1-3 of the *Pcdh19* gene, ablating the entire extracellular domain and transmembrane domain of the protein. P1 and P2 blue arrows represent primers TF2108-F2 and TF2108-R2, respectively, used for genotyping the WT allele. P3 and P4 blue arrows represent primers TF2108-10 and GT-IRES, used for genotyping the KO allele. SP, signal peptide; EC, extracellular cadherin repeat; TM, transmembrane domain; CM, cytoplasmic domain; WIRS; WAVE regulatory complex-interacting receptor sequence; β-gal, β-galactosidase; Neo, neomycin; KO, knock-out; 5'arm, 5 homology arm; IRES, internal ribosome entry site; pA, polyA; 3'arm, 3' homology arm. Not drawn to scale.

2.3 Mouse genotyping

To genotype the animals, ear notches from adult mice and tail clips from embryonic mice were obtained and stored at -20°C for subsequent extraction.

2.3.1 DNA extraction

Genomic DNA was extracted from tissue samples using the Mouse Direct PCR kit as per manufacturer's instructions (Biotool, cat no. B4001). Briefly described, a pre-made lysis buffer (Buffer L) and Protease Plus mixture was added to the samples and incubated at 55°C for 30 minutes for effective digestion. Once digested, the mixture was incubated for a further 5 minutes at 95°C for protease inactivation. Digested solution was used directly as a DNA template in the polymerase chain reaction (PCR).

2.3.2 Polymerase chain reaction (PCR)

For PCR, 2x M-PCR OPTI^{TM} mix (obtained from the Mouse Direct PCR kit and containing optimised Taq DNA polymerase, dNTPs, $MgCl_2$, and reaction buffer), distilled water (ddH_20), specific primer pairs (10 µM), and extracted DNA, was combined and loaded into a BIORAD T100 Thermal Cycler. All primer pairs for specific reactions are shown in **Table 2.1**. For all PCR's, the following steps were performed: (1) initial denaturation of genomic DNA, at 94°C for 4 minutes, followed by 35 cycles of steps 2 to 4 which are (2) DNA denaturation at 94°C for 20 seconds, separating the two DNA strands after every synthesis, (3) primer annealing to the DNA at a primer-specific temperature (shown in **Table 2.1**) for 30 seconds, (4) DNA synthesis at 72°C, and at a time dependent on product size (2 kb/min). Finally, (5) once all cycles had been performed, there was a final DNA synthesis at 72°C for 5 minutes. PCR products were stored at 4°C until separated on a 1-1.5% agarose gel by electrophoresis and visualised using ethidium bromide.

2.3.2.1 Genotyping for Pcdh19 KO animals

Genotyping for *Pcdh19* wild-type (WT), KO, and heterozygous (HET) animals was conducted using two PCR reactions following the instructions from Taconic and described previously by (Pederick *et al.* 2016). In brief, one PCR reaction was WT specific and absent in the targeted allele (WT oligos; TF2108-F2 and TF2108-R2), and the other was mutation specific and absent in the wild-type allele (Mutant Oligos; TF2108-10 and GT-IRES). Therefore, WT, KO and HET genotypes could

be determined. WT animals would have an amplified WT-specific 123 bp band and no product from the mutant-specific PCR. KO animals would have an amplified mutant-specific 437 bp band, and no product from the WT-specific PCR. Finally, both a WT-specific 123 bp band from the WT PCR and mutant-specific 437 bp band from the mutant PCR would be present for a HET genotype. Targeted sequences and primer locations are illustrated in **Figure 2.1**.

2.3.2.2 Genotyping for X and Y chromosome gene Jardid1d

Sex determination was conducted as described by (Clapcote and Roder 2005). Primers used in this reaction detected sequences in the *Jarid1d* gene that were X-chromosome and Y-chromosome specific. The *Jarid1d* gene is 29 bp longer on the X chromosome compared to the Y chromosome, therefore a X-specific 331 bp and Y-specific 331 bp long product was detectable in males and X-specific 302 bp product was detectable in females.

Primer Name	Direction	Product size (bp)	Annealing temp (°C)	Primer Sequences (5’ to 3’)
WT Oligos (TF2108 genotyping):				
TF2108-F2	F	123 bp	56.5°C	TAGAGGTTCTTGCTGAAGACTTCC
TF2108-R2	R			TCAACTGTTTCGATGAGACACTGC
Mutant Oligos (TF2108 genotyping):				
TF2108-10	F	437 bp	57.2°C	GTGCGTACCAGGCGGGAGC
GT-IRES	R			CCCTAGGAATGCTCGTCAAGA
Sex Determination Oligos:				
Jardid1c	F	331 bp, 302 bp	54°C	CTGAAGCTTTTGGCTTTGAG
Jardid1d	R			CCACTGCCAAATTCTTTGG
***Pcdh19* Probe Oligos:**				
Exon1	F	987 bp	72°C	CACCAAGCAGAAGATTGACCGAG
Exon 1	R			GCCTCCCATCCACAAGAATAGTG
Exon 6	F	810 bp	66.8°C	GGATTCTTGGCCACTCTGATAG
Exon 6	R			CTCTGTTTCCCCAACATCAAG
***Ctnnd1* Probe Oligos:**				
p120 catenin	F	988 bp	65°C	ATGGACGACTCAGAGGTGGA
p120 catenin	R			GCACCTCTTCACCAATCATG

Table 2.1: Primers for genotyping and probe generation. bp, base pair; temp, temperature; WT, wild-type; F, forward; R, reverse.

2.4 *In situ* hybridisation (ISH)

Three probes were designed for RNA *in situ* hybridisation (ISH); two for *Pcdh19* mRNA at sites specific to exon 1 and exon 6, and one for *Ctnnd1* mRNA as a positive control. **Figure 2.2** summarises the ISH procedure, including the probe generation, ISH procedure and probe detection.

2.4.1 Probe generation

Fragments specific to each probe were amplified by PCR. Primers used to generate the fragments are shown in **Table 2.1**. PCR products were cloned into a pCRII-Blunt-TOPO vector using the TOPO cloning reaction kit as per manufacturer's instructions (Thermo Fisher Scientific, cat no. K280002). To deliver the plasmid in to bacterial cells, the TOPO cloning mixture was transformed into one 50 µl vial of TOP10 competent cells and incubated on ice for 30 minutes before a heat shock was performed for 30 seconds at 42°C. 250 µl S.O.C medium was added to the competent cells aseptically, which were incubated at 37°C for 1 hour at 200 rpm, allowing for bacterial growth. Subsequently, the mixture was spread on to LB plates (Sigma; 17.5 g in 500 ml ddH_20 at 121°C for 15 minutes) with kanamycin (1:1000 dilution) and incubated overnight at 37°C. The next day bacterial colonies were picked and inoculated into LB broth, incubating them overnight at 37°C with 180 rpm shaking. Plasmid DNA was extracted from the bacterial culture using QIA Quick Midiprep Kit (Qiagen, cat no.12143) as per the manufacturer's instructions. To confirm that the recovered plasmid contained the correct insert, a restriction digest was conducted. In brief, 2 µl DNA, 15.5 µl ddH_20, 0.5 µl of an appropriate restriction enzyme (see **Section 3.2.1.1**), and 2 µl reaction buffer were mixed and incubated for 1 hour at 37°C. Product was run on a 1% agarose gel and visualised with ethidium bromide. Plasmids were sequenced (Eurofin Genomics) to confirm no mutations were introduced during PCR amplification or cloning. Following the confirmation of the correct sequence, 50 µg of the plasmid DNA was linearized using an appropriate restriction enzyme to generate both antisense and sense probes. Plasmid DNA was incubated with 4 µl of the appropriate restriction enzyme (see **Section 3.2.1.1)** over-day and an additional 4 µl of the restriction enzyme over-night at 37°C to ensure the vector was linearised. DNA was then purified using QIA Quick PCR Purification Kit (Qiagen; cat no.28104) to eliminate residual salt and enzymes. Next, the linearized vector was transcribed using T7 or SP6 RNA polymerase (New England-Biolabs,

cat no. M0251S and M0207S, respectively) combined with a digoxigenin (DIG) - dUTP nucleotide mix (Sigma Aldrich, cat no.11277073910) to generate DIG-labelled antisense and sense probes. Linearized product was added to the DIG-dUTP nucleotide mix, transcription buffer, the appropriate RNA polymerase and RNase free ddH_20, and incubated for 2 hours at 37°C. Once the probe was transcribed, the unincorporated DIG-labelled nucleotides were eliminated using illustra MicroSpin G-50 columns as per the manufacturer's instructions (GE Healthcare Life Sciences; cat no. 27533001).

2.4.2 Tissue preparation

Embryonic day (E)11.5, E12.5, and E13.5 embryonic heads, and E14.5 brains were dissected and fixed in 4% paraformaldehyde in 1x phosphate-buffer saline (PBS; 10x PBS in ddH_20; 137 mmol/L NaCl, 2.7 mmol/L KCL, 8 mmol/L Na_2HPO_4, 1.46 mmol/L KH_2PO_4) overnight, then cryoprotected in 30% sucrose in ddH_2O overnight at 4°C before being frozen on dry ice in Optimal Cutting Medium (OCT) medium (Fisher Scientific; cat no. 23730571). All tissue samples were stored at -80°C and treated in an RNase free environment throughout the tissue preparation and ISH procedure. Tissue was sectioned at 12 µM using a cryostat (Leica Biosystems, cat no. CM3050) and mounted on to polysine microslides (VWR International Ltd, cat no. 6311560).

2.4.3 ISH procedure

Sections were post-fixed in 4% paraformaldehyde, endogenous peroxidases were quenched in 3% hydrogen peroxidase in PBS, and acetylated (acetic anhydride in 0.1 M triethanolamine/PBS) at room temperature (RT) before pre-hybridisation in hybridisation buffer (50% formamide, 0.1% tween-20, 0.25% CHAPS, 250 µg/ml yeast tRNA, 500 µg/ml herring sperm, 5x Denhardts, 5x SSC, 50 µg/ml heparin, 2.5mM EDTA) for 1 hour at 65°C. Between each of these steps, sections were washed with 1x PBS (3x 5-minutes). After pre-hybridisation, all probes were denatured at 80°C for 5 minutes and added to the samples in fresh hybridization buffer (2 µl probe per 750 µl buffer) and incubated at 65°C overnight in an enclosed humid chamber containing 50% formamide and 50% 5x SSC. The next day, excess probe was washed out with 0.2x SSC (5x SSC in ddH_2O) solution at 65°C (3 x 20-minutes). After sections were washed, 0.5% blocking reagent in TN buffer (100 mM Tris-HCL (pH 7.5), 150 mM NaCl) was added for 30 minutes to prevent unspecific binding. Next, sections were washed in 1x PBS (3 x 5-minute washes)

and anti-DIG-horseradish peroxidase (HRP; 1:2000, Thermo Fisher Scientific) was applied for a further 30 minutes at RT, binding to the DIG labelling mix on the probes.

2.4.4 Probe detection

After 3x 5-minute washes in 1x PBS, sections were incubated in Cy3-Tyramide using the TSA^{TM} Plus Cy3 Fluorescence kit (Perkin Elmer, cat no. NEL744001KT). With the addition of a small concentration of H_2O_2, HRP catalyzes the formation of oxidized TSA free radicals. These TSA free radicals bind covalently with tyrosine residues proximal to HRP and the fluorophore, and Cy3 can be visualized. Sections were then washed in 1x PBS (3x 5-minutes) and stained with 4',6 diamidino-2-phenylindole dihydrochloride (DAPI; 1:4000 in PBS; Sigma). Sections were mounted with coverslips using DAKO mounting medium (DAKO North America, USA) and then stored at 4°C before imaging.

2.4.5 ISH combined with immunohistochemistry (IHC)

To visualize *Pcdh19* mRNA alongside the detection of cell markers, combined ISH and immunohistochemistry (IHC) was performed. ISH was conducted similar to that described above with some minor changes. Once the excess probe was washed off on the second day of the ISH protocol, IHC staining was performed as described in **Section 2.6** and anti-DIG-HRP was subsequently added to detect the probe once the IHC was complete. Antibodies used are shown in **Table 2.2**.

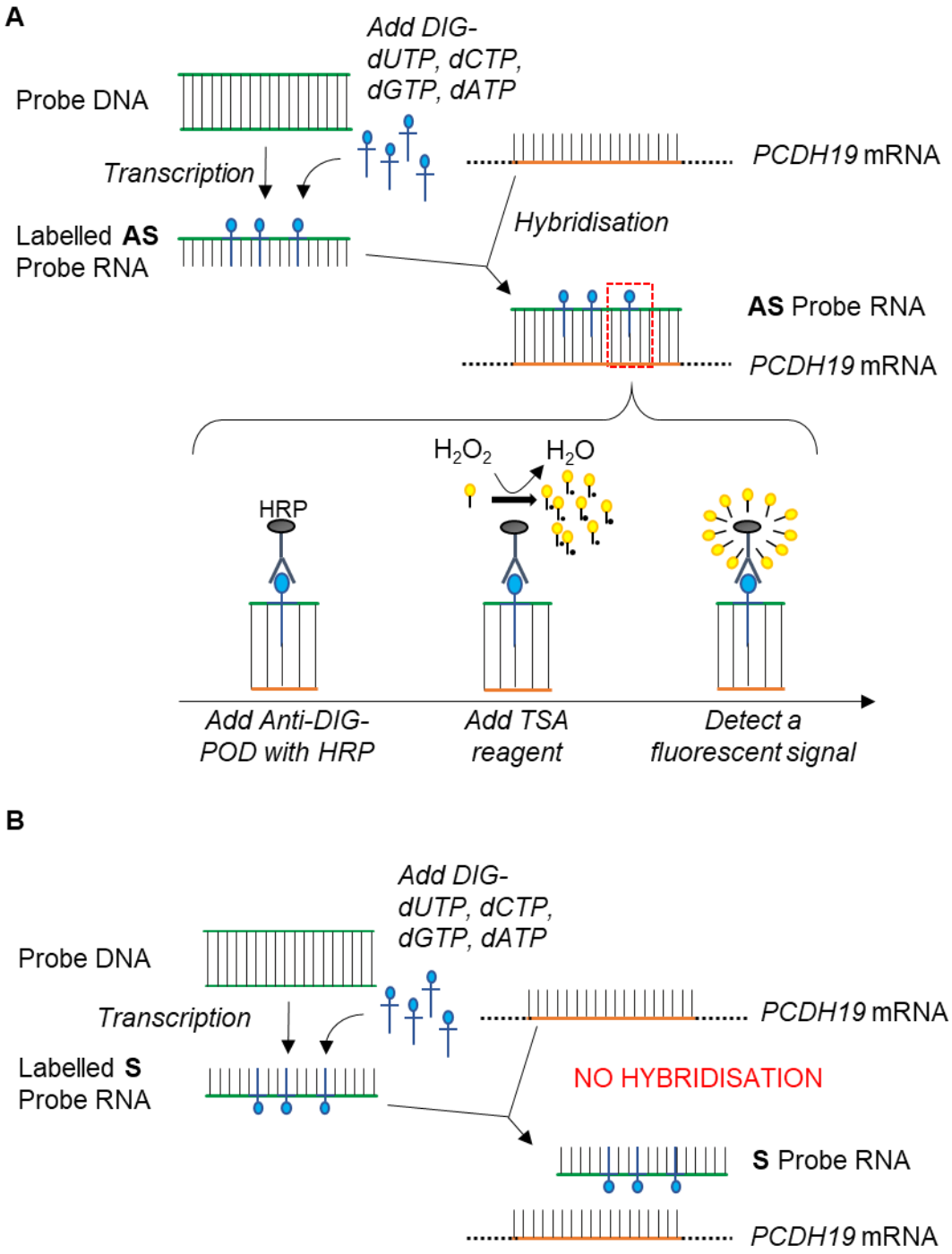

Figure 2.2: *In situ* hybridisation (ISH). Diagrammatic representation of **(A)** antisense (AS) and **(B)** sense (S) probes used to detect endogenous *Pcdh19*. DNA was transcribed, labelled with the DIG labelling mix and purified to form labelled AS and S probes that target *Pcdh19* mRNA and can be visualised in the AS procedure using the Cy3-Tyramide amplification reaction. The AS probe complementarily binds and hybridises to the endogenous *Pcdh19* mRNA to produce a signal, whereas the S probe is unable to bind to the endogenous *Pcdh19* mRNA and no signal is detected.

2.5 Ethynyl-2′-deoxyuridine (EdU) labelling

5-Ethynyl-2′-deoxyuridine (EdU) is a nucleoside analogue of thymidine and can be incorporated into new DNA during active DNA synthesis (S-phase). Therefore, with a fluorescent label it can be effectively used as a birth dating marker.

2.5.1 EdU injection

To measure certain cell cycle parameters EdU (Thermo Fisher Scientific, cat no. A10044) was administered intraperitoneally to pregnant mice at 10 mg/kg at E11.5 and E12.5. At either 2 hours or 24 hours after injection, embryonic brains were dissected and fixed overnight in 4% paraformaldehyde. A minimum of 3 different litters were used for each parameter measured using EdU. Tail clips were used to verify genotype and gender as described in **Section 2.3**.

2.5.2 EdU detection

Fixed brain tissue was cryoprotected in 30% sucrose, and frozen on dry ice in OCT medium. Tissue was sectioned coronally at 12 µm using a cryostat and mounted on polysine slides ready for subsequent EdU detection and IHC. EdU was detected using the Click-iT® EdU Alexa Fluor® 594 Imaging Kit (Thermo Fisher Scientific, cat no. C10339). Sections were permeabilized in 0.5% Triton™ X-100 (Sigma) before the addition of the Click-iT reaction cocktail according to the manufacturer's instructions. EdU detection was combined with IHC (described in **Section 2.6)** to be used for subsequent cell cycle analysis. By combining these two techniques, the EdU labelling index (number of cells in S phase; EdU+$^{(2hrs)}$ Ki67+ / Total Ki67+) and the quitting fraction (number of cells that left the cell cycle, EdU+$^{(24hrs)}$ Ki67- / Total EdU) were calculated as described in more detail in Chapter 4.

2.6 Immunohistochemistry (IHC)

Sections were washed in 1x PBS (3x 5-minutes) and incubated for 1 hour at RT in blocking solution (10% donkey serum in PBS + 0.1% Triton™ X-100 (PBS-T)). Primary antibodies (**Table 2.2**) were diluted in blocking solution, applied to the sections and incubated overnight at 4°C in a humidified chamber. Sections used as no primary controls were incubated with blocking solution only. The next day, sections were washed with 1x PBS (3x 5-minutes) and secondary antibodies (**Table 2.3**; 1:1000, donkey, Thermo Fisher Scientific) were also diluted in blocking solution, applied to the sections and incubated for 1 hour at RT in a dark chamber.

Sections were then washed and counterstained with DAPI (1:4000 in PBS). Finally, sections were mounted with coverslips using DAKO mounting medium.

For the detection of anti-PCDH19, an additional antigen retrieval step was taken. Sections were incubated in citrate buffer (10 mM citric acid in ddH_20; pH adjust to 6.0 using NaOH; Sigma) at 95°C for 20 minutes and allowed to cool for 30 minutes. Then they were washed in 1x PBS (3x 5-minutes) before the IHC procedure was conducted.

2.7 Imaging

2.7.1 Acquisition

Whole brain images and higher magnification 1024 x 1024-pixel images were acquired using confocal microscopy (Carl Zeiss, LSM 780) together with Zen Black software (version 2.0, Carl Zeiss) for ISH, IHC, EdU detection and ICC.

2.7.2 Image analysis

Images were processed and analyzed using the imaging software FIJI. For manual cell counting, images were analyzed using the “Cell Counter” plug-in, and for co-localisation experiments, images were analyzed using the “Puncta Analyzer” plug-in as previously described by (Ippolito and Eroglu 2010).

Primary Antibody	Type	Dilution	Species	Distributor	Cat no.
anti-KI67	mab	1/100	mouse	BD Bioscience	ab15580
anti-PHH3	mab	1/300	rat	Abcam	ab10543
anti-PAX6	pab	1/500	rabbit	Biolegend	PRB-278P
anti-TBR2	pab	1/400	rabbit	Abcam	ab23345
anti-Hippocalcin (HPCA1)	pab	1/1000	rabbit	Abcam	ab24560
anti-PCDH19	pab	1/100	rabbit	Bethyl Laboratories	A304-468A
anti-TBR1	pab	1/500	rabbit	Abcam	ab31940
anti-β-galactosidase (β-GAL)	pab	1/500	chicken	Abcam	ab9361
anti-βTUB3	pab	1/1000	rabbit	Abcam	ab78078
anti-MAP2	pab	1/1000	chicken	Abcam	ab5392
anti-CTIP2	mab	1/250	rat	Abcam	ab18465
anti-SATB2	mab	1/400	mouse	Abcam	ab51502
anti-CUX1	mab	1/200	rabbit	Proteintech	11733
anti- GAD65/67	pab	1/200	rabbit	Abcam	ab11070
anti-GFP	pab	1/500	chicken	Fisher Scientific	10524234
anti-Homer	mab	1/500	rabbit	Synaptic Systems	160003
anti-Synaptophysin	mab	1/1000	mouse	Abcam	ab32127

Table 2.2: Primary antibodies used for IHC and ICC. mab, monoclonal antibody; pab, polyclonal antibody.

Secondary Antibody	Primary antibody used
anti-mouse Alexa 488	KI67
anti-mouse Alexa 555	Synaptophysin
anti-rat Alexa 594	PHH3
anti-rabbit Alexa 488	PAX6, TBR2, HPCA1, PCDH19, TBR1, TUJ1
anti-rabbit Alexa 555	PAX6, TUJ1, GAD65/67
anti-rabbit Alexa 647	Homer
anti-chicken Alexa 488	GFP
anti-chicken Alexa 647	β-GAL

Table 2.3: Secondary antibodies used for IHC and ICC.

2.8 Neuronal differentiation procedure

2.8.1 Derivation of Pcdh19 KO embryonic stem cells (ESCs)

Pcdh19 KO embryonic stem cells (ESCs) were obtained from *Pcdh19* KO mouse embryos. A day before mating, *Pcdh19* KO females were exposed to male pheromones by coming into contact with male bedding, inducing the natural oestrous cycles in females. *Pcdh19* KO females were mated with *Pcdh19* KO males. Females that carried a plug were sacrificed four days later and embryos were flushed from oviducts at the 8-cell stage using a mouth pipette. Obtained embryos were incubated at 37°C and a concentration of 7% CO_2 in organ culture dishes containing KSOM medium (Millipore, cat.no.MR-020P-5D) with 2 MEK inhibitors, 1 μM PDO325901 (Axon Medchem, cat.no.1408-B5v) and 3 μM CHIR99021 (Axon Medchem, cat.no.1386-B8) (2i). After 2 days, embryos were transferred to N2B27 medium (50% Dulbecco's Modified Eagle Medium (DMEM)/F12-N2 (DMEM/F12; Life Technologies, cat no. 11540566) + 25 mg/ml N2 medium (Life technologies, cat no. 17502048) + 2.5 mg/ml insulin (Sigma, cat no. 11376497001) + 50 mg/ml bovine serum albumin (BSA; Sigma, cat no. A9647-10G) medium + 50% Neurobasal/B27 medium + 200 mM L-Glutamine (Life Technologies, cat no. 25030024) + 0.1mM β-mercaptoethanol (Life technologies, cat no. 11528926) with 2i and 1000 U/ml Leukemia Inhibitory Factor (LIF; Millipore, cat.no. ESG1106) and incubated until the *zonae pellucidae* hatched. Blastocysts were incubated with 20% anti-mouse serum (Sigma- Aldrich; cat.no. M5774) for an hour to induce apoptosis of the outer trophoblastic cell mass, and then 20% rat serum (made in house) for 10 minutes, to provide complement to enhance the apoptotic process and sustain the survival of the cells within the inner cell mass (Solter and Knowles 1975). Individual blastocysts were placed in a drop of N2B27 medium under paraffin oil and each epiblast was isolated from the remnants of the trophoblastic cells and placed in a gelatinised 96-well plate using a glass mouth pipette. After 7-9 days of culture, colonies were identified, and outgrowths were passaged with a small drop of accutase (Millipore) and disaggregated with a glass pipette into a new gelatinised 96-well plate. The cells were tested for mycoplasma using the 'LookOut® Mycoplasma PCR Detection Kit' (Sigma; cat no. MP0035) as per the manufacturer's instructions.

For genotyping, trophectoderm lysate was taken from individual blastocysts. DNA was prepared from each sample as described in **Section 2.3.1**. Subsequent PCR

genotyping was conducted to determine sex and confirm the presence of the targeted allele (described in **Section 2.3.2)**. Subsequently, the selected cell lines that had a confirmed *Pcdh19* KO genotype were expanded and frozen at -80°C in N2B27 medium with 10% foetal bovine serum heat inactivated (FBS; 30 minutes at 60°C; Biological Industries, cat no. 040021A) and 10% dimethyl sulfoxide (DMSO; Sigma, cat no. D2650).

2.8.2 Isolation of mouse embryonic fibroblasts (MEFs)

A pregnant B6 female mouse was culled and embryos were collected at E15. Embryos were kept on ice in 1x PBS. Each embryo was removed from the uterus and washed in fresh 1x PBS. Using dissection tools and a dissection microscope, embryos were decapitated, and all internal organs were carefully removed, and the remaining embryo cadavers were pooled together in a falcon tube containing DMEM (Life Technologies; cat no. 11500596). The tissue was subsequently washed twice in DMEM and transferred to a Petri dish on ice to be cut in to small pieces ready for dissociation. The tissue was then transferred to a clean falcon tube and 20ml of 0.05% trypsin (Life Technologies; cat no. 11580626) and 20 µg/ml DNase (Roche; cat no. 79254) was added and subsequently incubated in a water bath at 37°C for 30 minutes, with agitation every 5 minutes. The suspension was pipetted up and down using a 1000 µl pipette, while an additional 20 ml of 0.05% trypsin was added. The previous step was repeated, and the suspension was incubated and re-suspended as described above. Trypsinisation was stopped by the addition of 10 ml of 10% heat inactivated FBS. The suspended tissue was passed through a 40 µm nylon strainer (BD Falcon) before centrifugation at 1000 rpm for 15 minutes. The supernatant was removed, and the pellet re-suspended in cellular aggregate (CA) medium (DMEM + 1% non-essential amino acids (Life Technologies, cat no. 11140035) + 1% L-Glutamine + 10% FBS heat inactivated + 1.43 mM β-mercaptoethanol). Mouse embryonic fibroblasts (MEFs) were counted using a NucleoCounter ® NC-100™ (Chemometec) and $1.75x10^4$ cells/cm^2 were plated on 0.2% gelatin-coated dishes (0.2% gelatin in ddH_2O). Once the cells were confluent they were passaged again. Cells were tested for mycoplasma using the 'LookOut® Mycoplasma PCR Detection Kit' by following the manufacturer's instructions, before freezing cells in CA medium and 10% DMSO in liquid nitrogen.

2.8.3 Culture of ESCs

The protocol generated by (Bibel *et al.* 2004) was followed to differentiate mouse ESCs into neurons. The 5 main steps are described below. Mouse derived *Pcdh19* KO ESCs and Tau-EGFP knock-in ESCs (Wernig *et al.* 2002) were used in these experiments.

MEFs were plated at a density of $1.5x10^6$ on gelatin coated-dishes (60mm; Nunc) and left to grow in CA medium over night at 37°C under an atmosphere of 5% CO_2 and 95% air. Once confluent, 1 ug/ml of mitomycin C (Sigma; cat no. M4287) was added to the medium to inactivate the MEFs. MEFs were subsequently washed after 2 hours, left to recover for a minimum of 1 hour, before plating ESCs at an approximate density of $3x10^6$ per dish on top of the MEFs. ESCs were sub cultured every other day at a ratio between 1:7 and 1:10 in ES medium (DMEM + 1% non-essential amino acids + 1% L-Glutamine + 10% FBS heat inactivated + 1,43 mM β-mercaptoethanol + 1000 U/ml LIF) until a homogenous population of defined colonies were seen, that were proliferating at a high rate (usually five to six passages were required). ESCs were sequentially passaged on gelatin-coated dishes (100 mm; Nunc) and deprived of MEFs for 2-3 passages in ES medium, at a splitting ratio between 1:5 and 1:7.

2.8.4 Formation of cellular aggregates

ESCs were suspended at a density of $4x10^6$ in CA medium on non-adherent bacteriological dishes (100mm; Greiner) for eight days to form cellular aggregates (CAs). CA medium was changed on Day 2, 4 and 6 with the addition of 5 μM retinoic acid (Sigma, cat no. R2625) on Day 4 and 6 to drive the differentiation of ESCs to excitatory cortical neurons. Medium was changed by transferring the CAs and medium into a 50 ml Falcon tube using a 25 ml pipette. Once the CAs had settled on the bottom of the falcon tube, supernatant was carefully removed, and CAs were resuspended in fresh CA medium (15 ml per dish).

2.8.5 Dissociation of cellular aggregates and neuronal differentiation

At Day 8 CAs were dissociated in 1 ml of 0.05% trypsin in 0.05% Ethylenediaminetetraacetic acid (EDTA)/PBS. Disintegration of CAs was readily observed after 3 minutes at 37°C. Trypsin was inactivated by the addition of CA medium and CAs were re-suspended. Dissociated aggregates were passed through a 40 μm nylon strainer and centrifuged. Supernatant was removed, and

cells were re-suspended in N2 medium (DMEM/F12 medium + 1% N2 supplement + 1% non-essential amino acids + 1mM L-Glutamine, 2.5 µg/ml insulin + 100 µM 2-β-mercaptoethanol + 100 U/ml Pen/Strep (Life Technologies, cat no. 15140122)). Cells were counted using NucleoCounter ® NC-100™ and plated at densities ranging from $1.75x10^5$ to $1.5x10^6$ per well on pre-coated poly-DL-ornithine (Sigma, cat no. P8638; stock as 0.5 mg/ml in borate buffer (150 mM BH_3O_3, pH 8.3 adjusted with NaOH) diluted 1:5 with ddh_20) / laminin (1 mg/ml; Life Technologies, cat no. 23017015) plates (4-well, 12-well, and 24-well plates; Thermo Fisher Scientific). The day of plating dissociated aggregates is represented as Day *in vitro* 0 (DIV0). After 24 hours, medium was replaced with fresh N2 medium. On DIV2, media was changed to complete medium (**Table 2.4**; made in house) with 5 µg/ml 5-Fluorodeoxyuridine (5-FdU; Sigma, cat no. 856657) to prevent the growth of mitotic cells. Fresh complete medium was added at DIV4, 8 and 12. After this medium was only changed if exhausted.

A

Components	100x stock (µg/ml)	200ml stock of 100x (mg)	Suspension	
L-Alanine	200.00	40.0000	Dissolved in 26.6ml ddH_20	Added to 172ml DMEM
Biotin	10.00	2.0000		
L-Carnitine	200.00	40.0000		
Ethanolamine	100.00	20.0000		
D-Galactose	1500.00	300.0000		
L-Proline	776.00	155.2000		
Putrescine	1610.00	322.0000		
Na-Pyruvate	2500.00	500.0000		
Na-Selenite	1.60	0.3200		
Vitamin B12	34.00	6.8000		
Zinc sulfate	19.40	3.8800		
Catalase	256.00	51.2000		
Glutathione	100.00	20.0000		
Linoleic acid	100.00	20.0000	Dissolved in 1.4ml EtOH	
Linolenic acid	100.00	20.0000		
Progesterone	0.63	0.1260		
All-trans retinol	10.00	2.0000		
Retinylacetate	10.00	2.0000		
Tocopherol	100.00	20.0000		
Tocopherolacetate	100.00	20.0000		

B

BSA/transferrin/insulin mix	Added to 30ml of DMEM [mg]
BSA	1000.00
Transferrin	20.00
Insulin	16.00

C

Final Mix**	(ml)
100x Complete medium stock (A)	4.00
BSA/transferrin/insulin mix (B)	30.00
2.5mg/ml superoxidase dismutase	0.40
100x Penicillin/streptomycin	4.00
DMEM	358.00

**Before use 10 µl/ml of 1 mM Glutamax

Table 2.4: Components and preparation of complete medium. (A) 100x concentrated stock medium was prepared and stored in 5 ml aliquots for subsequent use. **(B)** BSA/transferrin/insulin mix was prepared fresh. **(C)** 4 ml of the 100x complete medium mix (A), the 30 ml BSA/transferrin/insulin mix (B) were combined with the final mix components to make complete medium. Before use 10 µl/ml of 1 mM Glutamax was added. Once made complete medium was stored at 4°C for a maximum of one month.

2.9 Coverslip treatment

13 mm nitric-acid treated glass coverslips were prepared for subsequent ICC. Coverslips (VWR) were treated with 70% Nitric Acid (Sigma) overnight to remove excess dirt. After rinsing in ddH_20, coverslips were placed in 1 M hydrochloric acid (HCl; Sigma) and heated at 100 °C for 4 hours. HCl was rinsed off with ddH_20, and coverslips were incubated overnight in pure ethanol before being stored in 70% ethanol at RT. Before use, coverslips were washed twice with ddH_20 and coating substrates were added as described in **Section 2.8.5**.

2.10 Immunocytochemistry (ICC)

ESC-derived neurons were cultured on top of 13 mm coverslips in a 24-well plate and were fixed for 7 minutes in 4% paraformaldehyde in 1x PBS. Immunocytochemistry (ICC) was conducted as described for IHC in **Section 2.6**, with the minor difference of PBS-T (PBS with 0.1% Triton ™ X-100) being used instead of PBS for the wash steps. Once the ICC was completed, cells were washed with ddH_20 and coverslips were mounted on to polysine microslides using DAKO mounting medium. Imaging was conducted as described in **Section 2.7.**

2.11 RNA extraction

2.11.1 RNA lysis and quantification

Total RNA was extracted from ESC's, and ESC-derived progenitors and neurons at different time points. ESC's and neurons were washed twice with 1x PBS and lysed using RLT lysis buffer (from RNeasy Mini kit; Qiagen, cat no. 74104) containing 1% β-mercaptoethanol. Lysate was either frozen immediately at -80°C or processed using the RNeasy Mini kit per the manufacturer's instructions, with DNase treatment.

2.11.2 Reverse transcription

RNA was quantified using a BioSpectrometer® (Eppendorf) and complementary DNA (cDNA) was prepared from 1250 ng of RNA. RNA was primed with 1 mM dNTP mix (Promega, cat no. U1511) and 0.025 µg/µl random hexamers (Promega, cat no. C1181) at 65°C for 5 minutes. Next, using Superscript III first strand synthesis system, 5x First Strand Buffer (Thermo Fisher Scientific, cat no. 18080044), 0.1 M dithiothreitol (DTT; Invitrogen, cat no. D1532), RNasin®

ribonuclease inhibitor (Promega, cat no N2111) and SuperScript® III reverse transcriptase (Thermo Fisher Scientific, cat no. 18080044), was mixed and added to the samples to be reverse transcribed for 2 hours at 50°C. The reaction was inactivated at 70°C for 15 minutes, and cDNA was stored at -20°C or used directly for real-time quantitative polymerase chain reaction (RT-qPCR) to measure relative expression of certain genes.

2.12 Real-time quantitative polymerase chain reaction (RT-qPCR)

2.12.1 FAST SYBR® Green RT-qPCR

All RT-qPCR experiments were performed using the FAST SYBR® Green master mix (Applied Biosystems, cat no. 10556555) with primers specific to the genes of interest and a house-keeping gene (β-actin) (**Table 2.5**). Primer pairs were either manually designed or taken from previous publications and the efficiency of the primers was determined to check they qualified when using the $2^{-\Delta\Delta CT}$ method (see **Section 2.12.2** for primer efficiency test). The reaction mix containing 12 µl FAST SYBR® Green master mix, 0.625 µl of 10 µM selected primer pairs, and ddH_20 was loaded on to a MicroAmp® Fast Optical 96-well plate (Thermo Fisher Scientific) and 60 ng of cDNA was added per well (i.e. per reaction). Biological triplicates were made for each cDNA sample, alongside the internal control (β-actin). The StepOnePlus™ Real-Time PCR system (Applied Biosystems, Invitrogen) was used for the PCR reaction. cDNA was amplified and underwent 40 cycles of PCR using an annealing temperature of 60°C for all primer combinations. The accumulation of fluorescent signal was calculated automatically using the StepOne™ Software. The signal was calculated as the cycle threshold (Ct), defined as the number of cycles required to cross the threshold, which is inversely proportional to the amount of target nucleic acid in the sample. Additionally, a melting curve was generated by increasing the temperature by 1°C per minute up to 99°C to detect fluorescent signal released from the denatured product. The curve was checked to ensure there was no unspecific fluorescence signal detected that would indicate unspecific product amplification. Once the RT-qPCR was complete the raw data was extracted for RT-qPCR analysis (**Section 2.11.2**).

2.12.2 RT-qPCR analysis

Relative levels of cDNA were calculated using the $2^{-\Delta\Delta CT}$ method (Schmittgen and Livak 2008). The normalised ΔCt values were calculated by subtracting the Ct

value of the housekeeping gene from the gene of interest. As biological triplicates were made this value was averaged. To analyze target gene expression changes relative to expression levels at a given time point, the ΔCt was further divided from the ΔCt of this given time point to obtain the ΔΔCt value. The ΔΔCt was then converted to its linear form to represent the fold change difference ($2^{-\Delta\Delta Ct}$).

For the $2^{-\Delta\Delta CT}$ method to be applied, the amplification efficiencies of the target and housekeeping gene must be approximately equal. Thus, efficiency was measured by measuring the variation in ΔCt values with template dilutions. Serial dilutions of cDNA of a known concentration were amplified with target and housekeeping primer pairs, using RT-qPCR to obtain Ct values. The ΔCt was calculated, subtracting the amplified housekeeping gene (β-actin) from the gene of interest. These values were plotted against the log cDNA dilution. The absolute slope was calculated, and values close to zero meant that the efficiency of the target and housekeeping gene were similar, thus the $2^{-\Delta\Delta CT}$ method could be used.

Target Gene	Primer Direction	Primer Sequence (5' to 3')
β-actin	F	CTGCCTGACGGCCAGG
	R	GATTCCATACCCAAGAAGGAAGG
PCDH19	F	TGGCAATCAAATGCAAGCGT
	R	ACCGAGATGCAATGCAGACA
vGlut1	F	GGAGGAGCGCAAATACATTGAGG
	R	CATAGACGGGCATGGACGTAAAG
vGlut2	F	TGCAAAGCATCCTACCATTACAG
	R	GCAGAAGTTGGCAACAATTATCG

Table 2.5: Primers used for SYBR® Green RT-qPCR. F, forward; R, reverse.

2.13. Protein extraction

2.13.1 Protein lysis

Protein lysates were taken from ESCs, neural progenitors (NPs) and neurons. Cells were washed twice with 1x PBS before the addition of RIPA buffer (50 mM Tris base, 150 mM NaCl, 1 mM EDTA, 1% Triton X100, 0.2% sodium deoxycholate, 0.1% SDS, pH to 7.4 adjusted with HCl, and inhibitors (1% phosphatase inhibitor cocktail 3 (Sigma), 1% protease inhibitor cocktail (Sigma), 100 mM 6-aminohexanoic acid, 1.5 mM aprotinin, 1 mM DTT, 100 mM 1,10-phenanthroline and 1 mM phenylmethylsulphonyl fluoride (PMSF)). Cells were scraped from the dish, kept on ice for 30 minutes and vortexed every 5 minutes before centrifugation at 4°C for 10 minutes at 10,000 rpm. Protein lysate (the supernatant) was collected and stored at -80°C and the remaining pellet was discarded.

2.13.2 Protein quantification

For protein quantification, the Pierce™ bicinchoninic acid (BCA) Assay Protein Kit (Thermo Fisher Scientific, cat no. 23235) was used according to the manufacturer's instructions. Briefly, a standard curve was prepared by diluting 2 mg/ml BSA with ddH_20. Subsequently a dilution series was performed. Next, protein lysate was diluted 1:50 with ddH_20 and again a dilution series was performed. 100 ul of BCA reagent was added to the sample and the standard curve. The plate was incubated for 30 minutes at 37°C, then a FLUOstar® Omega Microplate Reader was used to measure the absorbance at 562 nm. 40 µg of sample was calculated and loaded for western blot.

2.14 Western blot

Quantified protein lysates were mixed with 1x lithium dodecyl sulphate (LDS) buffer (1 M glycerol,140 mM Tris Base, 106 mM Tris HCl, 0.5 mM EDTA, 0.22 mM Brilliant Blue G-250, 0.175 mM Phenol Red, 74 mM LDS, pH 8.5) and 50 mM DTT. Next, lysates were centrifuged, boiled at 70°C for 10 minutes and centrifuged again, before being loaded on a NuPAGE™ Novex™ 4-12% Bis-Tris gel (Thermo Fisher Scientific, cat no. NP0321BOX) with a given ladder (Novex Sharp). The gel was run at 120 V for 90 minutes in 2-(N-morpholino) ethanesulfonic acid (MES) running buffer (50 mM MES, 50 mM Tris base, 0.1% SDS, 1 mM EDTA, pH 7.4).

Subsequently, a wet transfer technique was used to pass the proteins to a nitrocellulose membrane. The gel and membrane were placed between two blotting papers and encased in a cassette before being submerged in 1x NuPAGE transfer buffer (25 mM Bicine, 25 mM Bis-Tris, 1 mM EDTA, 20% MeOH) diluted with isopropanol and ddH_20, and subjected to 100 V for 2 hours at 4°C. After transfer, the membrane was cut horizontally at approximately 35 kDa and used to detect the loading control antibody as described below. Total protein was detected using Ponceau Red (Sigma, cat no. P7170) staining. Following Ponceau staining, the membrane and loading control membrane were washed with ddH_20, and 5% blotting-grade blocker (Bio-Rad, cat no. 1706404) in tris-buffered saline with 0.1% Triton ™ X-100 (TBS-T) was added and incubated at RT for one hour. The membranes were next incubated with anti-PCDH19 (rabbit,1:100, Bethyl Laboratories), or a loading control antibody, anti-HH3 (histone H3; rat; 1:1000; Sigma, cat no. H0164) in the same blocking reagent and incubated overnight at 4°C.

The following day, the membranes were washed (3 x 15-minutes) with TBS-T, before incubation with anti-rabbit (for PCDH19 detection) and anti-rat (for HH3 detection) HRP-conjugated secondary antibody (1:20,000, Promega) for one hour at RT. The membrane was again washed (3x 15-minutes) with TBS-T at RT. To develop the membranes, LumiGLO® Reserve Chemiluminescent Substrate kit (Seracare, cat no. 54300049) was used as per manufacturer's instructions. The membrane was covered with the provided substrate and incubated at RT for one minute. The substrate was then removed, and chemiluminescent signal was detected using the ChemiDoc™ MP system with the Image Lab™ software (Bio-Rad).

2.15 Multi-electrode array (MEA)

To study spontaneous electrical activity in neuronal networks, NPs were plated on a 24-well Multiwell Micro Electrode Array (MEA) gold electrode epoxy (24W700/100F-288) plate (Multichannel Systems). Prior to plating, wells were submerged in 10% heat inactivated FBS to aid attachment of progenitors, washed twice with ddH_20 and coated with poly-DL-ornithine/laminin as described in **Section 2.8.5**. Progenitors were plated at a density of 5 $x10^5$ per well and cultured as described in **Section 2.8.5**. Activity was measured from DIV10, DIV12, DIV14, and DIV16 neurons on a Multiwell-MEA Headstage (Multichannel Systems), for

signal amplification, interfaced through a MCS-IFB Interface Board (Multichannel Systems). Each well contained 12 electrodes which simultaneously recorded activity over a 2-minute phase duration, absent of any stimulation. Raw data, spikes per second histograms and spike waveforms were collected. Spike activity was determined as that activity above or below five standard deviations of the mean noise. Data was visualised using the Multiscreen and Multi-Channel Suite computer programmer (Multichannel Systems). Timestamps of spike and burst data were extracted and imported into MATLAB where custom-written analysis routines were coded. All codes used were kindly written by Oliver Steele.

2.16 Calcium imaging

Calcium imaging experiments were conducted using the calcium chelating indicator, Fura-2-AM (Fura-2; Life Technologies, cat no. F1201). Cells were plated at a density of $2.5x10^5$ per well, on 13 mm nitric-acid treated glass coverslips in 4-well dishes and recordings were taken from coverslips at DIV14-16. Before imaging, 1 µM of Fura-2 was added to the culture medium and incubated at 37°C for 30 minutes. Next, coverslips were mounted on an Olympus IX71 inverted microscope connected to a monochromator-based fluorimeter system (Cairn Research, Faversham, Kent, UK) and continuously perfused with an extracellular solution (ECS; 135 mM NaCl, 5 mM KCL, 5 mM HEPES, 10 mM glucose, 1.2 mM $MgCl_2$, 1.25 mM $CaCl_2$) at RT (22 ± 0.5°C). Using an Orca CCD camera, Fura-2-AM was alternately excited with light at 340 nm and 380 nm and re-emission was captured at 510 nm. Regions of interest were selected as well as a background region, and images were taken every 3 seconds. Using an automated rapid solution changer (RSC), cells were subjected to 30 second pulses of high potassium chloride (KCl) solution (75 mM NaCl, 10-60 mM KCl, 5 mM HEPES, 10 mM glucose, 1.2 mM $MgCl_2$, 1.5 mM $CaCl_2$) at RT (22 ± 0.5°C) before a subsequent wash with ECS for 300 seconds.

Ratio of emission intensities (i_{340}/i_{380}) evoked by each excitation wavelength was acquired using the OPTOFLuor computer program and recorded automatically on Microsoft Excel. Using Excel, the background ratio of emission recorded was subtracted from the emission intensities. An average was taken from independent experiments and values were normalized to the first 60 seconds of recording.

2.17 Statistical analysis

For statistical analysis, SPSS Statistics® 23 software (IBM) was used. To test for homogeneity of variance a Levene's test of equality of error variances was conducted. Based on the mean value, equal variance was assumed if the p-value was ≥ 0.05. To test for normality a Shapiro-Wilk test was conducted. Data was considered normal if the p-value was ≥ 0.05.

For cell counting, RT-qPCR, puncta counting and calcium imaging analysis, the mean percentage and standard error of the mean (SEM) was calculated from the mean of at least 3 independent experiments. A two-way ANOVA was conducted to test the influence of epigenotype/ cell line and genotype/ age /culture condition, with post-hoc Bonferroni correction for multiple comparisons. Where the data was not normally distributed a logarithmic transformation was conducted and statistical tests were conducted using transformed data.

For the cortical width and MEA analysis, the mean and SEM were calculated from the mean of at least 3 independent experiments. A one-way ANOVA was conducted to test for differences between cultures/genotype, followed by a Bonferroni correction for multiple comparisons. Where normality was not determined equal a non-parametric Kruskal-Wallis test was used.

For comparisons between two groups, a two-tailed t-test was used to compare means. Unless otherwise stated, the number n stands for the number of independent experiments.

Chapter 3: Characterisation of Protocadherin 19 in early cortical development

3.1 Introduction

The early expression of protocadherin 19 in the mammalian brain, along with the early onset of early infantile epileptic encephalopathy 9 (EIEE9) suggests that PCDH19 plays a role in brain development. *Pcdh19* has previously been shown to have a tissue-specific expression during mouse embryogenesis, in neural and non-neural tissue (Gaitan and Bouchard 2006). Of particular interest, in the developing mouse central nervous system (CNS), predominant expression was seen in the cortex, hippocampus and hippocampal connecting regions (lateral septum and basolateral amygdaloidal complex, entorhinal cortex, prefrontal cortex) that play a role in cognitive function and are affected in epileptic patients (Dibbens *et al.* 2008; Kim *et al.* 2010; Hertel *et al.* 2012).

The information available in the Allen Brain Atlas shows that *Pcdh19* is expressed throughout cortical development, including robust expression in early stages, at the onset of neurogenesis. However, as previous PCDH19 antibodies have proven to be non-specific, there is limited data on protein expression and characterisation of PCDH19-expressing cells in the developing mammalian cortex. Hence, further studies are required to characterise this in more detail.

There are two main proliferative zones in the cortex; the ventricular zone (VZ) and subventricular zone (SVZ). Within these regions, neural stem cells (NSC) of a particular lineage generate different cell types at specific time points. Specific proteins or transcription factors can be used as markers to distinguish certain cell types during cortical neurogenesis. To study cells that are proliferating, nuclear protein markers such as Ki67 and phosphohistone H3 (pHH3) are frequently used. Ki67 is a nuclear protein that can be detected during all active phases of the cell cycle (G_1, S, G_2, and mitosis), but not during resting phase (G_0), early phases of G_1 or in quiescent cells (Zacchetti *et al.* 2003). It is commonly used to measure proliferative activity and as a diagnostic tool in many cancers (Shepherd *et al.* 1988; Scholzen and Gerdes 2000). Moreover, pHH3, a nuclear core histone protein of chromatin, is a marker of the four phases of mitosis (prophase,

metaphase, anaphase, and telophase) and late G_2 (Hendzel *et al.* 1997), offering a clear distinction of the cycling cells in mitosis.

As mentioned in Chapter 1, there are two main progenitor types in the rodent cortex, namely radial glial cells (RGC) that produce neurons and glia, and intermediate progenitor cells (IPC) that are derived from RGCs and produce only neurons. The transcription factors paired box 6 (*Pax6*) and T-box brain factor 2 (*Tbr2*) are used to detect those progenitor cells, respectively. When RGCs transition to IPCs there is a downregulation of PAX6 and complementary upregulation of TBR2 (Englund *et al.* 2005). Furthermore, when neurons are generated from IPCs, there is a subsequent downregulation of TBR2 and upregulation of T-box brain factor 1 (TBR1). Additionally, preplate neurons transiently co-express TBR2 and TBR1, whereas neurons generated directly from RGCs either express TBR2 briefly or not at all (Englund *et al.* 2005).

Although the majority of the cells in the early developing cortex are progenitor cells or post-mitotic neurons, there are also other cell types present. These include other post-mitotic cells that migrate tangentially into the developing cortex, including future sub-plate (SP) cells, glutamatergic Cajal-Retzius (CR) cells and interneurons. During early cortical development, the preplate is formed from the earliest-generated neurons. The preplate later separates due to the rise of later-born radially migrating neurons, generating the superficial marginal zone (MZ) and the SP area that is located below the developing cortical plate (CP). Early in cortical development, future SP cells can be detected using Hippocalcin (HPCA1) (Osheroff and Hatten 2009), a neuronal calcium sensor protein, known to induce neurogenesis and inhibit the formation of astrocytes (Park *et al.* 2016). CR cells generated from the developing pallial-subpallial border aid excitatory cortical migration (Bielle *et al.* 2005) and express a number of factors that could be used as markers for detection, including reelin, a secretory factor specific to CR cells, and the calcium-binding protein, calretinin (Huntley and Jones 1990; del Río *et al.* 1995; Alcántara *et al.* 1998; Hevner *et al.* 2003).

Together these cell markers can distinguish stages of the cell cycle and specific cell-types that populate the developing cortex at a given time. In combination with the detection of *Pcdh19,* the cell-specific role of PCDH19 during cortical neurogenesis could be characterised.

3.1.1 Aim

The main aim of chapter was to conduct a descriptive characterisation of protocadherin 19-expressing cells during early cortical neurogenesis by detecting *Pcdh19* mRNA using in situ hybridisation (ISH) and cell-type specific markers using immunohistochemistry (IHC). Cycling cells (KI67+) and mitotic cells (PHH3+), the two main progenitor cells in rodent neurogenesis: PAX6+ RGCs and TBR2+ IPCs, and cells residing in the preplate during early neurogenesis: Cajal-Retzius (CR) cells (Reelin+ or Calretinin+) and future subplate cells (HPCA1+) were to be detected alongside *Pcdh19* mRNA. As the commercially available anti-PCDH19 antibodies have previously been described not to work in immunohistochemistry (IHC), it was further aimed to test an anti-PCDH19 antibody and optimise the detection, validating any signal using a *Pcdh19* knock-out (KO) mouse model as a negative control.

3.2 Results

3.2.1 In situ hybridisation (ISH) probe generation to detect Pcdh19

A fluorescent ISH technique was established, and cRNA probes were successfully generated to detect *Pcdh19* exon 1, *Pcdh19* exon 6 and *Ctnnd1* (p120 catenin). *Pcdh19* probes amplified a region that coded for part of the extracellular domain (exon 1 probe) and cytoplasmic domain (exon 6 probe) of the protein. The cRNA probe for *Ctnnd1* (p120 catenin) was used as a positive control. P120 catenin is a regulator of cadherin stability and modulator of RhoGTPase activity (Reynolds 2007) and is highly expressed in the developing cortex as early as E11.5, according to the information available in the Allen Brain Atlas. Hence, it was an appropriate control gene to ensure the efficiency of the ISH technique.

3.2.1.1 Probe generation

A diagrammatic representation of *Pcdh19* exon 1 and 6 probe generation, amplification of exon 1 and exon 6 inserts, and clarification of correct insertion by restriction digestion is shown in **Figure 3.1A-C**. In brief, using mouse genomic DNA and specific primers for *Pcdh19* exon 1 (previously described by (Gaitan and Bouchard 2006)) and *Pcdh19* exon 6 (used in the Allen Brain Atlas), inserts were amplified using polymerase chain reaction (PCR) and visualised on an agarose gel using electrophoresis and ethidium bromide (**Figure 3.3B**). Inserts of the correct size (exon 1, 987 bp; exon 6, 810 bp) were purified and ligated to the pCR II TOPO vector. A restriction digest of the plasmid DNA (minipreps) using Sac1 and EcoR1 enzymes was conducted and visualised to confirm product insertion for *Pcdh19* exon 1 (Sac1, 250 bp product) and exon 6 (EcoR1, 800 bp product), respectively (**Figure 3.3C**; arrowheads represent minipreps selected for subsequent sequencing and linearization). Once the sequence of the selected minipreps was confirmed, DNA was linearized using Not1 and Spe1 restriction enzymes for sense and antisense probes, respectively. Once linearized, DNA was transcribed using SP6 polymerase and T7 polymerase combined with a DIG labelling mix for sense and antisense probes, respectively. The *Ctnnd1* insert was amplified from plasmid DNA and directly ligated into the pCR II TOPO vector, following the same protocol as described above.

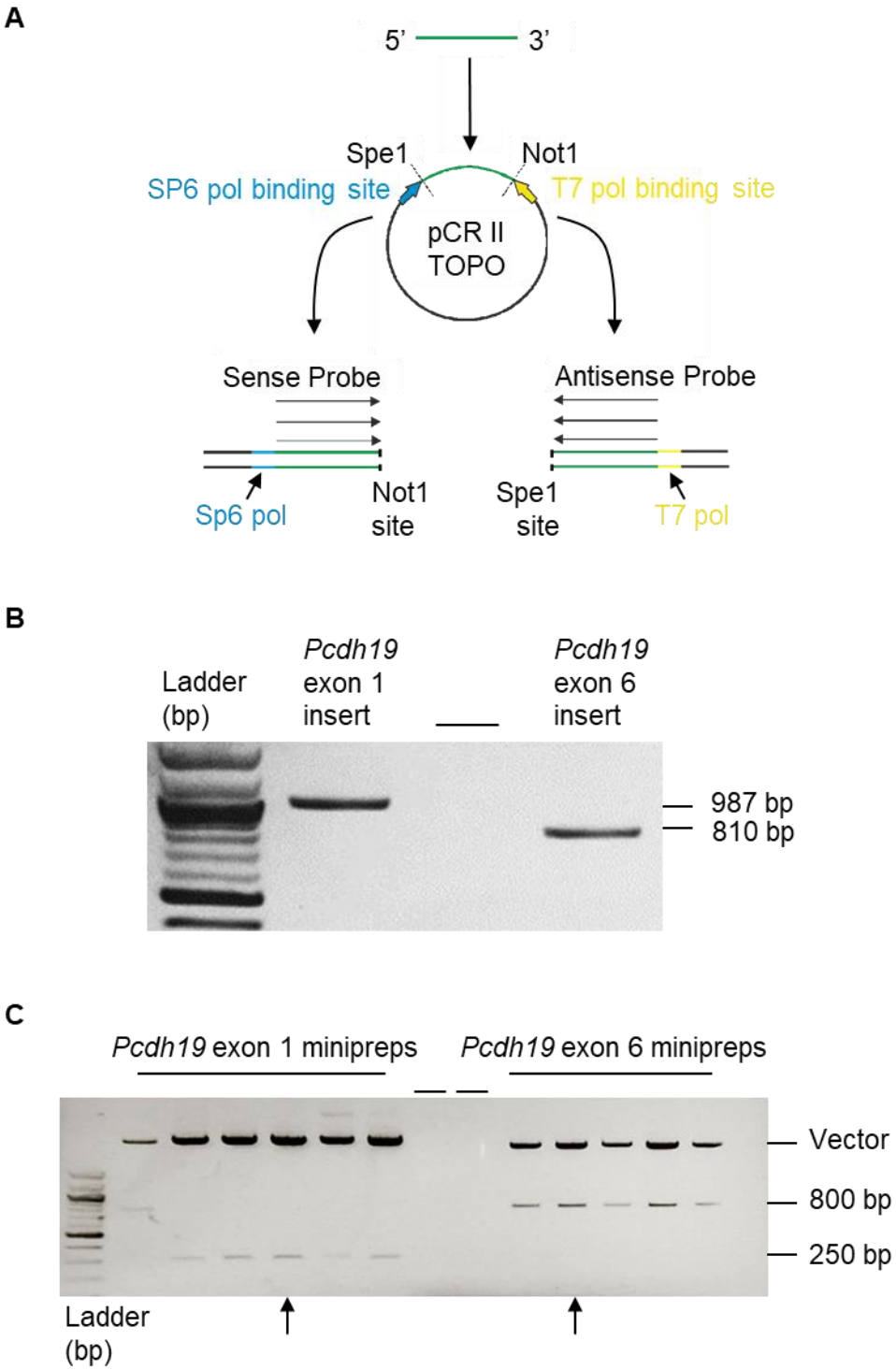

Figure 3.1: *Pcdh19* probe generation steps. (A) Diagrammatic representation of the generation of *Pcdh19* exon1/6 probes. **(B)** Amplification of *Pcdh19* exon 1 (987 bp) and exon 6 (810 bp) inserts. **(C)** Restriction digest of extracted plasmid DNA from *Pcdh19* exon 1 miniprep (Sac1 enzyme; 250 bp product) and exon 6 miniprep (EcoR1 enzyme; 800 bp product) both visualised on a 1.5% agarose gel with ethidium bromide. Arrowheads indicate selected minipreps. DNA Ladders: (A) 100 bp; (B) 1 kb. pol, polymerase; bp, base pair.

3.2.1.2 Probe detection

The antisense probes, complementary to *Pcdh19* and *Ctnnd1* mRNA, could bind and hybridise to the endogenous mRNA and a Cy3-Tyramide amplification reaction allowed for the visualisation of the specific probes.

Different concentrations of each probe were tested to gain an optimal signal and a concentration of 1:375 was chosen for all subsequent experiments. Antisense probes were hybridised onto cryostat sections of wild-type (WT) embryonic day (E)12.5 mouse heads. All three antisense probes gave a signal in the developing cortex (**Figure 3.2**). As sense probes cannot hybridise to the endogenous *Pcdh19* mRNA all three sense probes gave no signal in the WT E12.5 developing cortex (**Figure 3.2**). *Pcdh19* exon 1 and exon 6 cRNA probes displayed similar patterns of expression, therefore for consistency throughout the rest of this chapter, *Pcdh19* exon 1 probe was used for all ISH experiments.

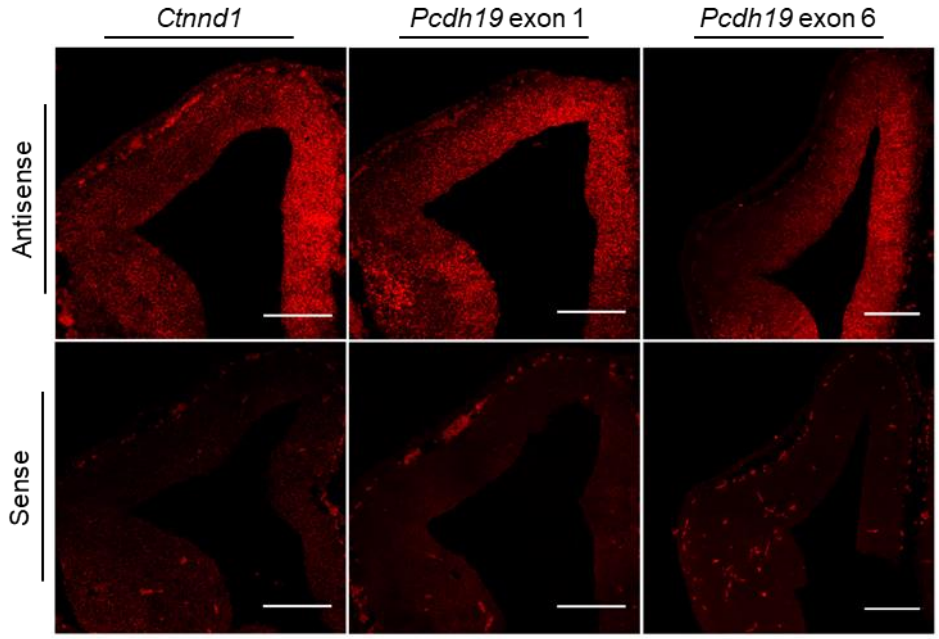

Figure 3.2 *Pcdh19* and *Ctnnd1* could be detected in WT E12.5 cortices using specific antisense probes. Representative *in situ* hybridisation images using an antisense probe to detect *Ctnnd1*, *Pcdh19* exon 1, *Pcdh19* exon 6 in E12.5 WT cortices. Specific sense probes were used as probe-specific controls. Scale bars: 200 μM.

3.2.2 Pcdh19 is highly expressed in early stages of cortical development

To understand whether *Pcdh19* levels and pattern of expression change during early cortical development, WT embryonic brains at E11.5 up to E14.5 were fixed and cryosectioned coronally for subsequent ISH to detect *Pcdh19* mRNA (using the exon 1 probe). Representative rostral and caudal sections from each indicated age were imaged and revealed a high transient expression of *Pcdh19* (**Figure 3.3**). At E11.5, in both rostral and caudal regions of the cortex, robust expression of *Pcdh19* extended across the VZ, from the apical to basal surface, with a high lateral to low medial gradient (**Figure 3.3A and E**). This expression progressively changed, becoming low lateral to high medial at E12.5 and E13.5 (E12.5, **Figure 3.3B and F**; E13.5, **Figure 3.3C-G**). By E14.5, there was a diminished expression in the lateral VZ and the SVZ, and high expression was restricted very medially to the hippocampal primordium (**Figure3.3D and H**). Interestingly, the spatiotemporal pattern of expression of *Pcdh19* was reminiscent and opposed of the latero-medial neurogenic gradient. Additionally, at E13.5, a distinctive band of expression appeared at the basal surface where the PP and developing CP became apparent. This expression became more visible at E14.5 (**Figure 3.3C', D', G', H'**; white dotted line), indicating *Pcdh19* may be expressed in projection neurons. Asides from the cortical expression pattern explained, there were also other distinctive areas of the brain that highly expressed *Pcdh19*. At E12.5 and E13.5, a defined boundary of high *Pcdh19* expression was distinguishable in the lateral ganglionic eminence (LGE) VZ, the birthplace of interneurons, as well as in the intermediate (IZ) zone of the LGE which develops into the future striatum (**Figure3.3B and F**; white arrows). Strong expression was also in the bed nucleus of the stria terminalis at E12.5 (**Figure 3.3F**; white asterisks), a region which connects to the amygdaloid nucleus, coordinating activity involved in autonomic, neuroendocrine and motor systems (Dumont 2009). Complementary to this site of expression, high levels of *Pcdh19* were present in the amygdala at E14.5 (**Figure 3.5D**; white arrow).

As the region and cell-type specific *Pcdh19* levels could only be assumed by location using this method, a cell-type and region-specific analysis of *Pcdh19* expression in the developing cortex was to be conducted, using different markers and combining ISH with IHC.

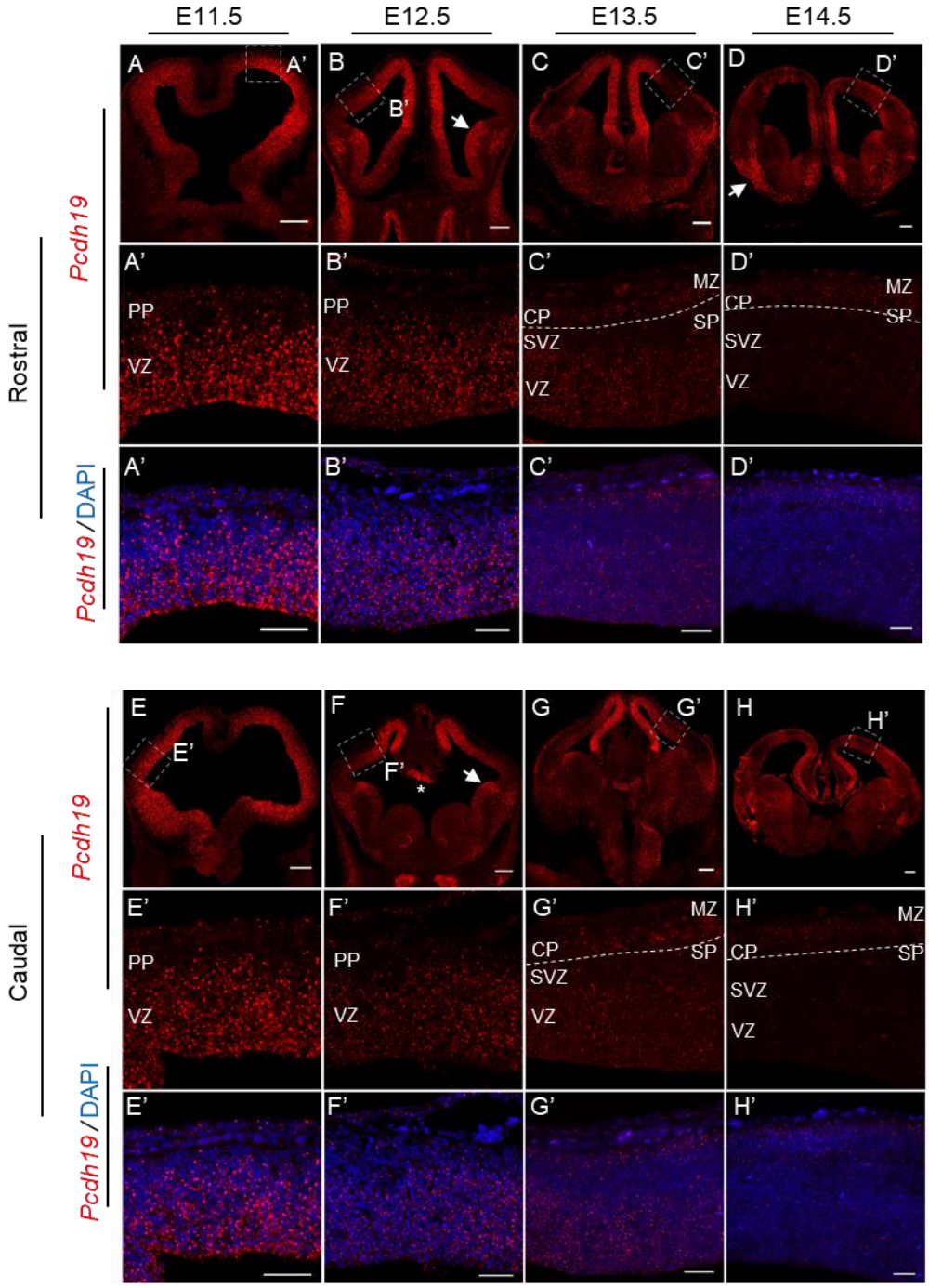

Figure 3.3: *Pcdh19* changes its expression pattern during early cortical development. *Pcdh19* mRNA (red) detection in representative rostral **(A, B, C, D)** and caudal **(E, F, G, H)** coronal sections at embryonic day 11.5 **(A, E)**, 12.5 **(B, F)**, 13.5, **(C, G)** and 14.5 **(D, H)**. **A'-D'** and **E'-H'** represent higher magnification images of regions highlighted by the white dashed boxes, emphasising the temporal expression of *Pcdh19*. Nuclei are counterstained with DAPI (blue). VZ, ventricular zone; PP, preplate; SVZ, subventricular zone; SP, subplate; CP, cortical plate; MZ, marginal zone. Scale bars: 200 µM; 50 µM.

3.2.3 Combination of RNA in situ hybridisation and immunohistochemistry to characterise Pcdh19 during early cortical neurogenesis

To further characterise *Pcdh19* expression in a cell-type and region-specific manner, ISH against *Pcdh19* was combined with IHC to detect different markers in WT cortices. As shown in **Section 3.2.2**, *Pcdh19's* spatiotemporal expression pattern changed in the developing cortex over time. Therefore, the assessment of *Pcdh19* expression in combination with the different markers was conducted at E11.5, E12.5, and E13.5. Antibodies to distinguish cycling cells (KI67+), mitotic cells (PHH3+), RGCs (PAX6+), IPCs (TBR2+), and future subplate cells (HPCA1+) were used and are displayed in combination with *Pcdh19* mRNA detection. An additional antibody was tested to detect CR cells (reelin); however, the antibody did not work in combination with this ISH method or when tested in IHC alone.

3.2.3.1 Pcdh19 is expressed in regions of high proliferation during early neurogenesis

At each embryonic age assessed, the majority of the cells in the VZ were cycling and expressed KI67, while most mitotic PHH3+ cells were localised at the ventricular surface of the developing cortex, with only a few cells in more basal positions (**Figure 3.4**). At E11.5, amongst the KI67+ proliferating cells there was a high expression of *Pcdh19,* which continued to be observed at E12.5 (E11.5, **Figure 3.4A-B**; E12.5, **Figure 3.4E-F**). At E13.5, lower expression of *Pcdh19* was found in regions containing a high proportion of KI67+ cells relative to that seen at E11.5 and E12.5 (**Figure 3.4I-J**).

Moreover, a relatively high expression of *Pcdh19* mRNA was juxtaposed to apical PHH3+ cells at E11.5 and E12.5 (E11.5, **Figure 3.4C-D**; E12.5, **Figure 3.4G-H**). At E13.5, lower expression of *Pcdh19* was found in regions where PHH3+ cells resided compared to E11.5 and E12.5 (**Figure 3.4K-L**). Furthermore, at each embryonic age, basally positioned pHH3+ cells had lower *Pcdh19* mRNA expression than apically positioned pHH3+ cells.

Taken together, *Pcdh19* is highly expressed in the proliferative regions of the VZ between E11 and E12 and diminishes by E13, suggesting PCDH19 may be playing a specific role in the proliferation of progenitor cells.

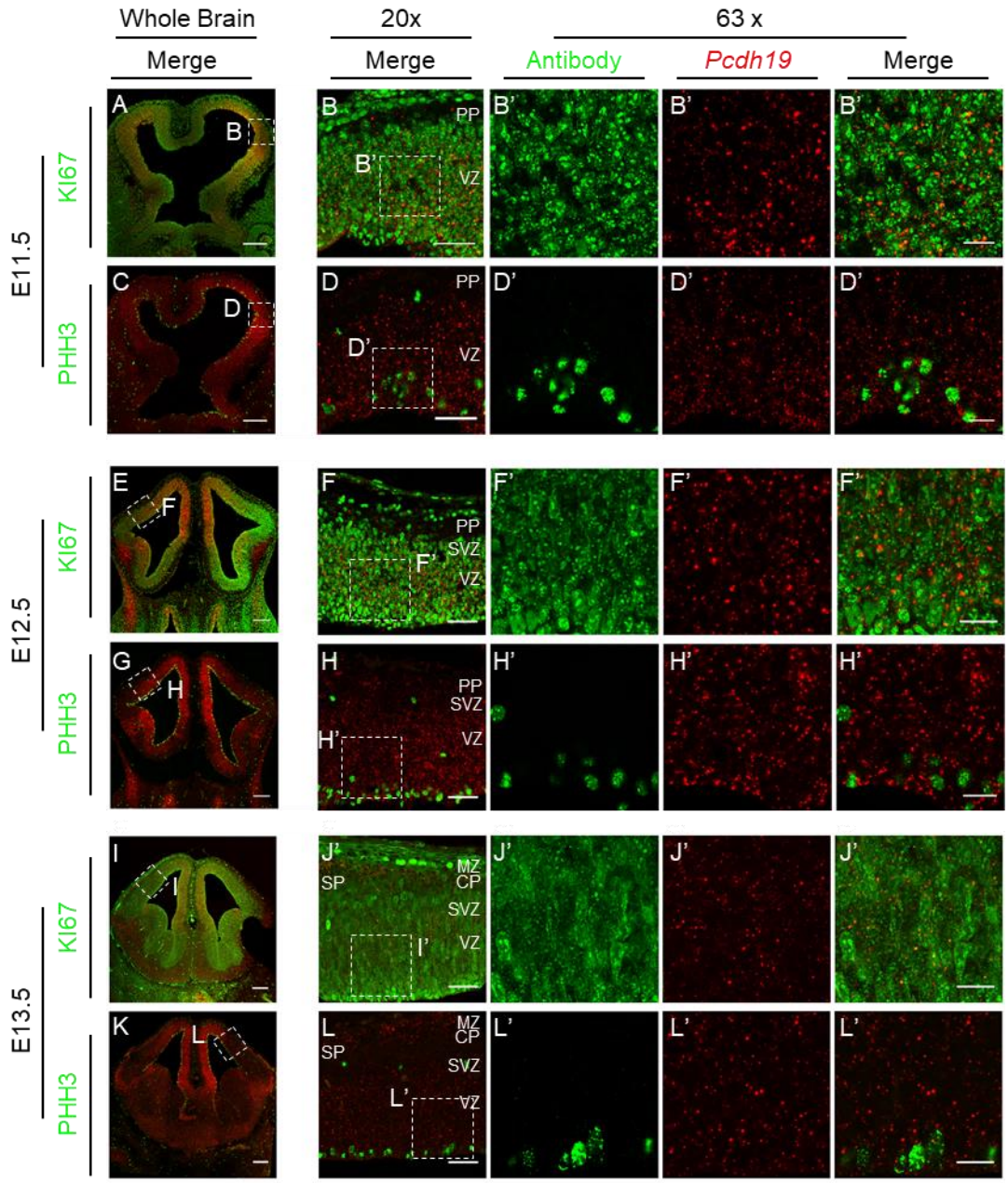

Figure 3.4: *Pcdh19* mRNA is expressed in proliferative regions of the developing cortex. Representative images of E11.5 **(A-D)**, E12.5 **(E-H)** and E13.5 **(I-L)** coronal brain sections, detecting *Pcdh19* mRNA (red) and immunostaining with antibodies (green) against KI67 **(A, B, E, F, I, J)** and PHH3 **(C, D, G, H, K, L)**, to study cycling cells and mitotic cells, respectively. VZ, ventricular zone; PP, preplate; SVZ, subventricular zone; SP, subplate; CP, cortical plate; MZ, marginal zone. Scale bars: (whole brain) 200 μM; (20x) 50 μM; (63x)10 μM.

3.2.3.2 Pcdh19 is expressed highly in RGCs and downregulated in IPCs

To distinguish between the two main proliferating progenitor cells (RGCs and IPCs) at early embryonic ages, *Pcdh19* mRNA was detected alongside PAX6 and TBR2 immunostaining, respectively. As expected, upon detection of the progenitors expressed at E11.5 to E13.5, it was found that the majority of the cells in the VZ were PAX6+ RGCs. Moreover, TBR2+ cells started to appear as a small population of progenitor cells that bordered the basal surface of the VZ and were denser in the lateral cortex, compared to the medial cortex at E11.5. By E13.5 the SVZ was forming above the VZ and was populated by TBR2+ cells that spanned the width of the SVZ.

At E11.5, it was observed that in the PAX6+ cell regions, there was a high expression of *Pcdh19* (**Figure 3.5A-B**). A proportion of the PAX6+ cells had a co-localised expression with *Pcdh19*, while other PAX6+ cells existed in close proximity to *Pcdh19* mRNA (**Figure 3.5B'**; white bordered arrow and white filled arrow, respectively). At E12.5, *Pcdh19* was also highly expressed in the VZ where PAX6+ RGCs were expressed (**Figure 3.5E-F**). However, at E13.5 PAX6+ RGCs had a diminished expression of *Pcdh19* in comparison to the earlier ages (**Figure 3.5I-J**).

Interestingly, at E11.5 it appeared that *Pcdh19* expression was downregulated in regions where TBR2+ cells resided, relative to regions that did not express TBR2 (**Figure 3.5C-D**; **Figure 3.5D'**, compare above and below the white dotted lines). However, some expression of *Pcdh19* was seen in the uppermost TBR2+ cell populations (**Figure 3.5D'**; white filled arrow). As TBR2 is expressed transiently in CR cells between E10.5 and E12.5 (Englund *et al.* 2005), it is possible that *Pcdh19* was expressed in CR cells at this time point, but this would need to be clarified with CR-specific cell markers. As the SVZ became more apparent, there was an increased proportion of TBR2+ cells at E12.5 and E13.5 (E12.5, **Figure 3.5G-H**; E13.5, **Figure 3.5K-L**). The downregulation of *Pcdh19* expression in these regions populated by TBR2+ cells was particularly striking across the length of the VZ at E12.5 (**Figure 3.5H'**; compare above and below the white dotted lines) and by E13.5, more TBR2+ cells were generated, and little to no *Pcdh19* was detectable in the TBR2+ cell regions (**Figure 3.5K-L**).

Overall, it was demonstrated that *Pcdh19* is expressed in PAX6+ RGCs and its expression is downregulated in TBR2+ IPCs between E11.5 and E12.5. Proliferating RGCs showed juxtaposed and co-localised expression of *Pcdh19,* leading to the hypothesis that PCDH19 could be playing a functional role in maintaining RGCs in a proliferative state.

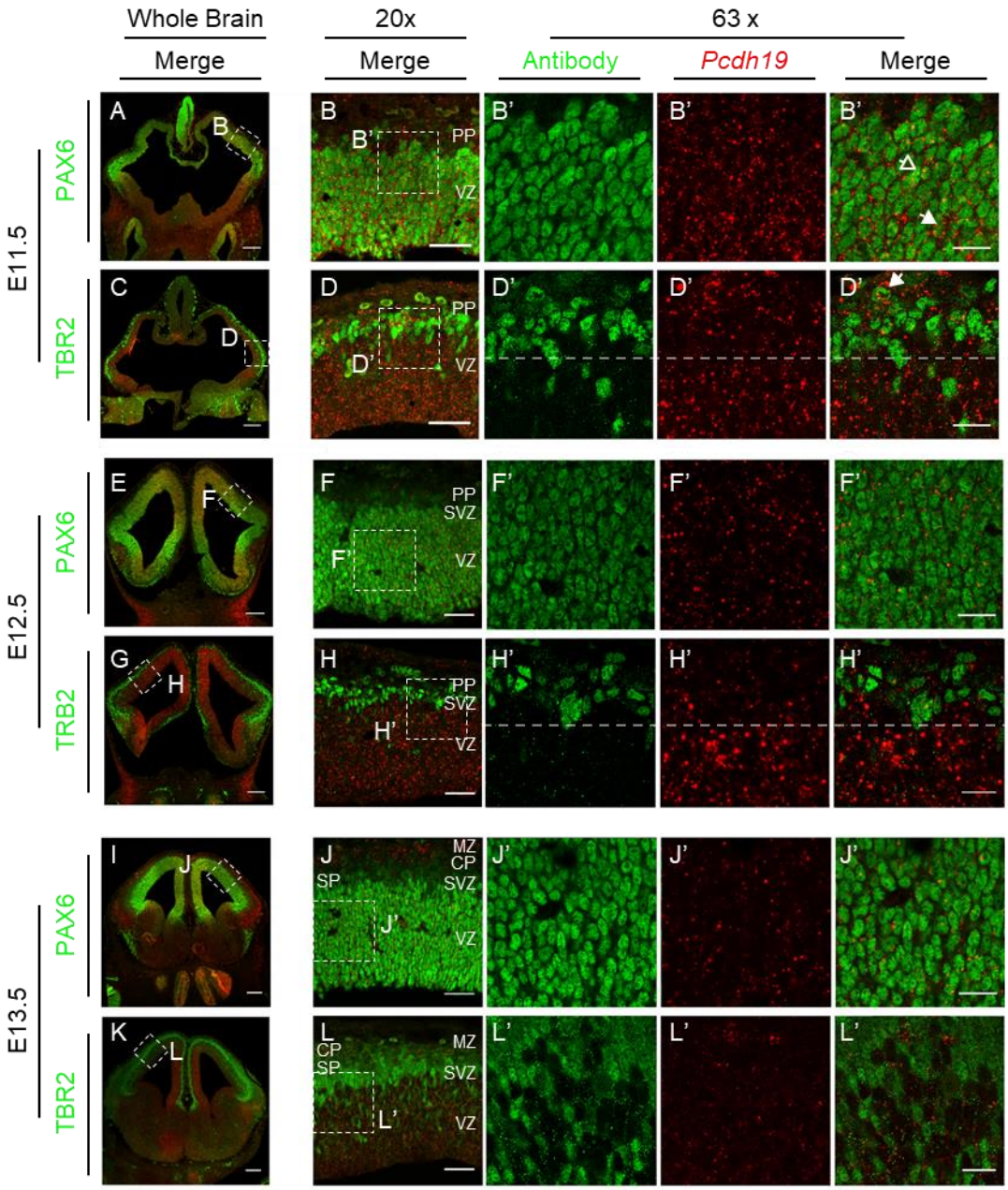

Figure 3.5: *Pcdh19* mRNA is expressed highly in RGCs and declines in IPCs. Representative images of E11.5 **(A-D)**, E12.5 **(E-H)** and E13.5 **(I-L)** coronal brain sections, detecting *Pcdh19* mRNA (red) and immunostaining with antibodies (green) against PAX6 **(A, B, E, F, I, J)** and TBR2 **(C, D, G, H, K, L)** to study RGCs and IPCs, respectively. VZ, ventricular zone; PP, preplate; SVZ, subventricular zone; SP, subplate; CP, cortical plate; MZ, marginal zone. Scale bars: (whole brain) 200 μM; (20x) 50 μM; (63x) 10 μM.

3.2.3.3 Pcdh19 may be expressed in newly migrated future subplate neurons

Before the splitting of the pre-plate into the MZ and SP, future subplate cells migrate tangentially and radially towards the basal surface of the developing cortex from the rostromedial telencephalic wall and the cortical germinative zone, respectively. It has been shown that specific genes can be used to detect future subplate neurons in the earliest stages of their development, one of which is *Hpca1* (Osheroff and Hatten 2009). HPCA1 is located in the cytoplasm of future subplate cells and has been reported to populate an area adjacent to and just below the migrating CR cells (Osheroff and Hatten 2009). To determine whether *Pcdh19* mRNA was expressed in a region where future subplate cells resided, ISH was combined with IHC to detect *Pcdh19* and HPCA1, respectively.

At E11.5, it was found that there was no expression of HPCA1 in the developing cortex (data not shown), but at E12.5 and E13.5, HPCA1 lined the basal surface of the developing cortex (**Figure 3.6**). In combination with *Pcdh19* detection, it was observed that *Pcdh19* co-localised with HPCA1 at E12.5 (**Figure 3.6A-B**; **Figure3.6B'**; white filled arrow). Further observations at E13.5 showed little to no colocalised expression of *Pcdh19* and HPCA1 (**Figure 3.6C-D**). This suggested that *Pcdh19* may be expressed transiently in future subplate cells that reside in the preplate region at E12.5. However, as HPCA1 is a cytoplasmic marker and there was high background staining detected when using this antibody, co-expression in other cell-types or structures at the preplate, such as RGC basal end foot structures and CR cells could not be ruled out.

3.2.3.4 Reelin+ Cajal Retzuis cells could not be detected using ISH or IHC

To distinguish CR cells, detection of *Pcdh19* mRNA was combined with IHC against the secreted factor reelin. However, when conducting this procedure, the reelin antibody did not give any specific signal. This antibody was also tested alone using IHC with standard procedures and with antigen retrieval, and again no specific signal was detected, indicating that the antibody was incompatible with IHC. Therefore, an alternative reelin antibody, optimisation of methods, or different markers would be required to assess *Pcdh19* expression in CR cells.

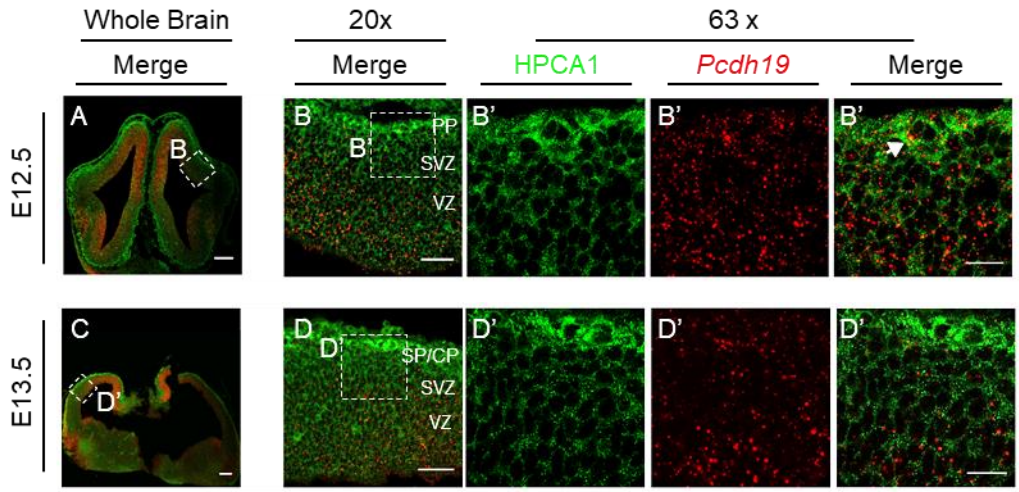

Figure 3.6: *Pcdh19* mRNA may be expressed transiently in future subplate cells. Representative images of E12.5 **(A-B)** and E13.5 **(C-D)** coronal brain sections, detecting *Pcdh19* mRNA (red) and immunostaining with an antibody against HPCA1 (green) to study subplate cells. VZ, ventricular zone; PP, preplate; SVZ, subventricular zone; SP, subplate. Scale bars: (whole brain) 200 µM; (20x) 50 µM; (63x) 10 µM.

3.2.4 Optimising a PCDH19 antibody to study expression during early cortical neurogenesis

3.2.4.1 PCDH19 can be detected using IHC

The commercially available antibodies used to detect PCDH19 have been described as unspecific and not compatible with IHC. Hence, a thorough characterisation of cell- and region-specific protein expression in mammalian tissue is lacking. To determine whether it was possible to optimise PCDH19 IHC, WT and *Pcdh19* KO embryonic brains were fixed and cryosectioned as previously conducted in **Section 3.2.2** and the standard IHC procedure described in Chapter 2 was conducted. A few minor changes were conducted to optimise the protocol specifically for the detection of PCDH19 using an anti-PCDH19 antibody from Bethyl Laboratories.

IHC was optimised using different blocking reagents (donkey serum, and BSA), antibody concentrations (1:100 to 1:1000), and antigen retrieval steps (heat and chemical). It was found that by using heat antigen retrieval (95°C for 20 minutes), BSA blocking solution (3% donkey serum, 4% BSA, 0.1% Triton X-100 in 1xPBS), and a 1:100 antibody dilution in the standard IHC procedure, a PCDH19 signal was detectable at E11.5 to E14.5 (**Figure 3.7** and **3.8**). By comparing WT brain sections to *Pcdh19* KO, the specificity of the antibody was determined (**Figure 3.7B and D** and **Figure 3.8B and D**). Strong background and a punctate signal was present in both WT and KO samples, making it difficult to study expression at a higher resolution. Using no primary antibody control, it was concluded that the background and unspecific signal seen in the WT and KO samples, was not due to the secondary antibody used (**Figure 3.7E** and **Figure 3.8E**). A distinct WT-specific expression pattern was distinguished that was not visible in the KO sections, which allowed for a descriptive analysis of PCDH19.

At E11.5 there was strong expression throughout the VZ, particularly at the apical ventricular surface (**Figure 3.7A**). This signal looked most specific, as it was clearly not visible in the KO brain section (**Figure 3.7B**). At E12.5, expression diminished laterally, and PCDH19 expression presented a low lateral to high medial gradient (**Figure 3.7C**; gradient shown in **Figure 3.7C'** when counterstained with DAPI). Additionally, at E12.5 there was a strong expression in the lateral ganglionic eminence (LGE) (**Figure 3.7C**; white filled arrow). At E13.5 and E14.5 there was

little to no visible expression of PCDH19 in the VZ of the developing cortex (**Figure 3.8**). However, a strong band of expression was present in the marginal zone (MZ) and developing CP (CP), presenting as a high lateral to low medial gradient. Although a signal in the KO cortices was also detectable in these regions, higher magnification images show that PCDH19 expression was specific when compared to KO sections (**Figure 3.8A''-D''**).

In summary, PCDH19 detection was sub-optimally achieved using IHC. Complementary to the ISH, PCDH19 was found to be transiently expressed in the VZ at E11.5 and E12.5. By E13.5 and E14.5 this expression had diminished, and a distinctive band of expression at the basal surface of the developing CP appeared. However, due to the high background signal and unspecific staining present in the KO sections, it was difficult to conduct a descriptive analysis at a cellular level. Therefore, the PCDH19 detection would require further optimisation to study expression reliably.

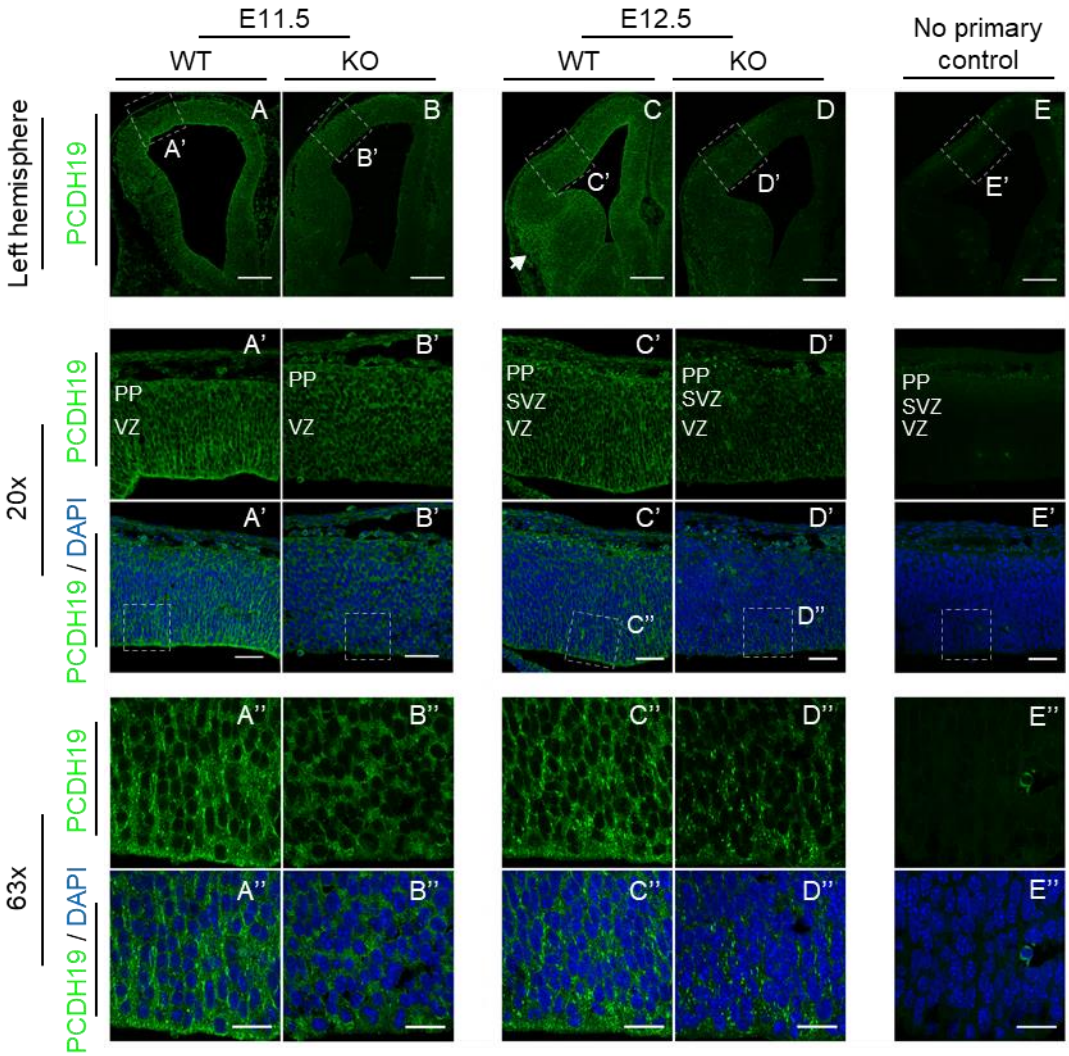

Figure 3.7: PCDH19 can be detected by IHC at E11.5 and E12.5. Representative images of PCDH19 (green) staining in WT and KO coronal sections at E11.5 **(A and B)** and E12.5 **(C and D)** compared to a no primary control (E). Nuclei counterstained with DAPI (blue). WT, wild-type; KO, knock-out; VZ, ventricular zone; PP, preplate; SVZ, subventricular zone; SP, subplate; CP, cortical plate; MZ, marginal zone. Scale bars: (whole brain) 200 μM; (20x) 50 μM; (63x) 20 μM.

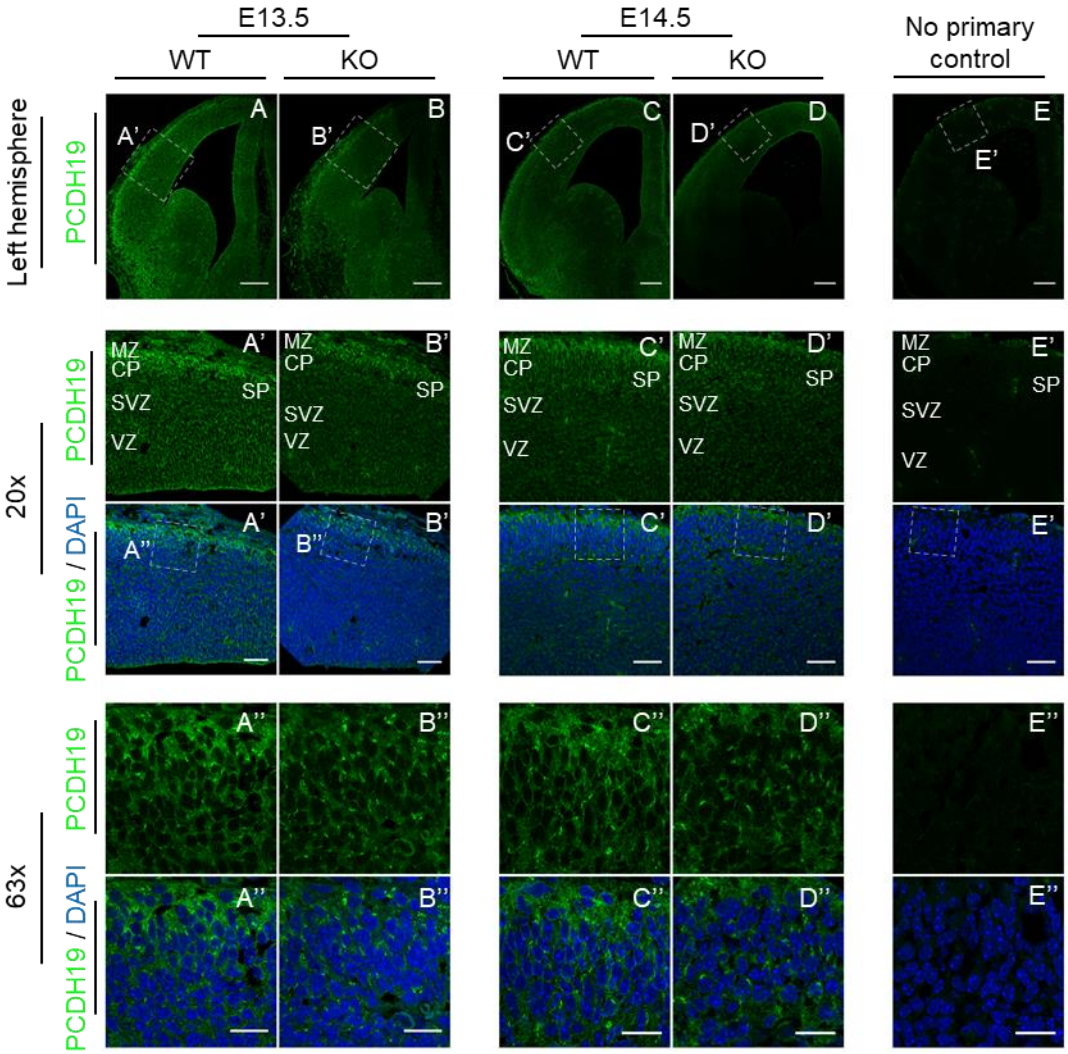

Figure 3.8: PCDH19 can be detected by IHC at E13.5 and E14.5. Representative images of PCDH19 (green) staining in WT and KO coronal sections at E13.5 **(A and B)** and E14.5 **(C and D)** compared to no primary control (E). Nuclei counterstained with DAPI (blue). WT, wild-type; KO, knock-out; VZ, ventricular zone; PP, preplate; SVZ, subventricular zone; SP, subplate; CP, cortical plate; MZ, marginal zone. Scale bars: (whole brain) 200 μM; (20x) 50 μM; (63x) 20 μM.

3.2.4.2 PCDH19 may be expressed in calretinin+ CR cells

As explained in **Section 3.2.3.4**, the reelin antibody did not work in combination with ISH or using IHC alone. Therefore, an alternative approach was taken to try to detect CR cells during early cortical development. As the calcium binding protein calretinin is expressed in CR cells, it was considered as an appropriate marker to conduct ISH in combination with IHC. However, previous attempts to use this antibody alongside ISH did not work. As anti-calretinin had worked when using IHC, it was proposed that the harsh conditions used during the ISH (e.g., treatment with formamide) prevented the antibody from working.

In an attempt to detect CR cells, and to decipher whether PCDH19 was expressed in CR cells, IHC was conducted as described in **Section 3.2.4.1.**, combined with calretinin staining. *Pcdh19* KO brain sections were also immuno-stained with PCDH19 and calretinin and used as a negative control (**Figure 3.9G-H**). At E11.5, E12.5 and E13.5 calretinin was found to be expressed strongly at the LGE, with sparse calretinin expression bordering the basal surface of the developing cortex (**Figure 3.9**). Although PCDH19 was expressed in the areas were calretinin+ cells resided and appeared to co-localise with calretinin staining at each age, the strong background staining made it difficult to conclude whether PCDH19 was expressed in calretinin+ cells (**Figure 3.9A-F**). Moreover, as calretinin and PCDH19 are not nuclear markers, the cell-specific expression could not be determined.

Taken together, although PCDH19 could be detected using IHC, the antibody detection could not be reliably used to characterise cell-specific expression due to unspecific and high background staining. CR-specific expression could not be determined using this method; however, it was concluded that PCDH19 was expressed in the preplate where calretinin+ CR cells and interneurons reside alongside future subplate cells.

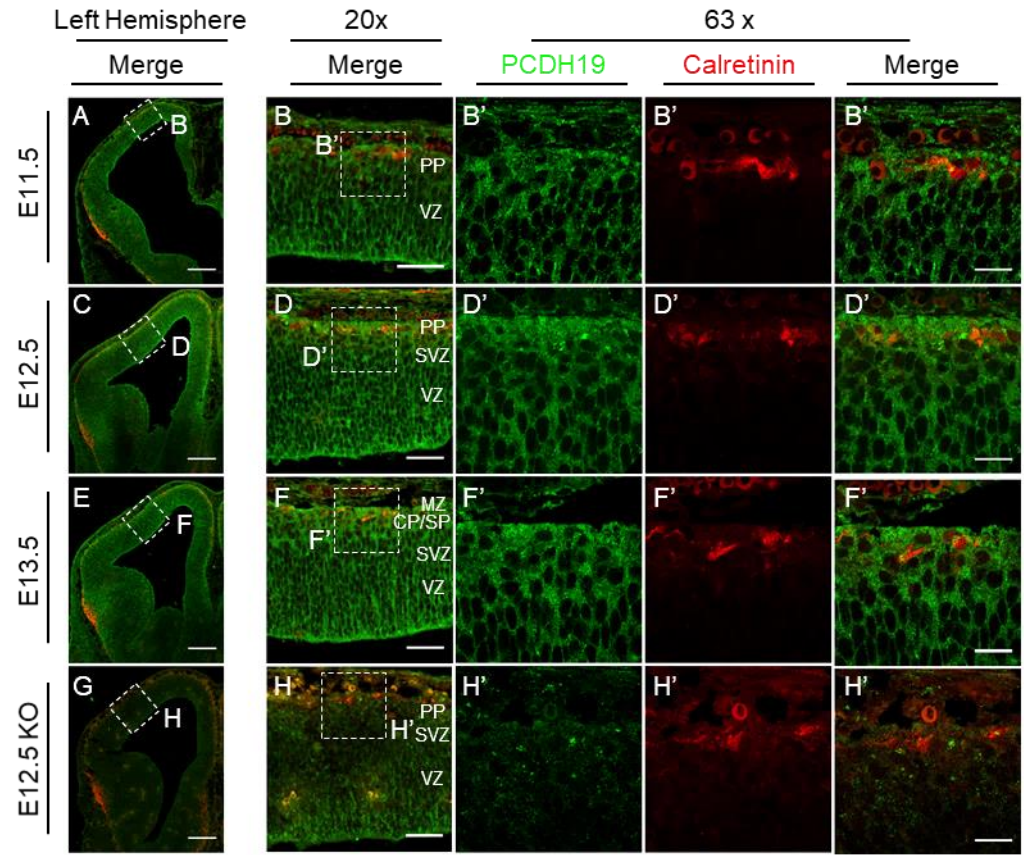

Figure 3.9: PCDH19 may be expressed in calretinin-positive neurons. Representative images of E11.5, E12.5 and E13.5 WT coronal (**A-F**), and E12.5 KO brain sections (**G-H**), immuno-stained with antibodies against PCDH19 (green) and calretinin (red). Images were taken of whole hemispheres (20x tile scan; **A, C, E, G**), single coronal sections (20x; **B, D, F, H**) and high magnification regions of interest (63x; **B', D', F', H'**). Scale bars: (left hemisphere) 200 µM; (20x) 50 µM; (63x) 10 µM.

3.3 Discussion

In this chapter, region-specific expression of protocadherin 19 was determined during early cortical neurogenesis. Transient expression of *Pcdh19* was observed in the proliferative regions of the developing cortex, with a pattern that was reminiscent of and opposed/complementary to the latero-medial neurogenic gradient. Further characterisation of *Pcdh19* expression in a cell- and region-specific manner revealed that there was high expression in regions populated by RGCs and downregulated expression in regions populated by IPCs. At E12.5, *Pcdh19* mRNA co-localised transiently with HPCA1, a future SP cell marker. Furthermore, PCDH19 signal was detected in a region populated by calretinin+ cells, suggesting that a subset of cells within the PP express PCDH19. Importantly, this initial characterisation complements the aim of understanding PCDH19 during cortical neurogenesis and supports the hypothesis that PCDH19 may be functioning in RGCs during the time in which progenitor cells switch from symmetric to asymmetric divisions.

3.3.1 Pcdh19 has a spatiotemporal expression pattern that complements/opposes the neurogenic gradient

A detailed analysis was conducted to expand on *Pcdh19* expression data published in the Allen Brain Atlas. More ages were studied (E11.5-E14.5), using coronal sections rather than sagittal, alongside a characterisation of the cells present in regions that express *Pcdh19.*

It was confirmed using ISH that *Pcdh19* is highly expressed in the proliferative region of the VZ, where the cell bodies of progenitors are located. Although *Pcdh19* was not studied earlier than E11.5, previously published data has shown that PCDH19 is expressed already at E9.5 in mouse embryos and in developing cortices (Gaitan and Bouchard 2006; Pederick *et al.* 2018), just before the onset of cortical neurogenesis. Neurogenesis progresses in a spatiotemporal manner, from rostro-lateral to caudo-medial regions, and is regulated by a number of factors, including, but not limited to, morphogens such as fibroblast growth factors (FGF) (Cholfin and Rubenstein 2008) and canonical Wnt signalling (Machon *et al.* 2007). Interestingly, from E11.5 to E14.5, *Pcdh19* expression followed a latero-medial gradient; the lateral expression of *Pcdh19* diminished from E11.5 to E12.5, and by E14.5 there was only very restricted expression medially in the VZ at the

hippocampal primordium. FGF2 has previously been shown to interact with PCDH19 (communication at the Cortical Development Conference 2017); therefore, it is possible that PCDH19 expression is being regulated by FGF signalling.

3.3.2 Pcdh19 is expressed transiently in regions populated by RGCs and in the PP during early cortical neurogenesis

In regions of the cortex that were populated by cycling cells (KI67+) and cells undergoing mitosis at the ventricular surface (apical PHH3+), high expression of *Pcdh19* was observed. Furthermore, *Pcdh19* was highly expressed in close proximity to PAX6+RGCs in the VZ and dropped where TBR2+IPCs appeared. Fujitani *et al.* found that knockdown of *Pcdh19* increased RGC proliferation and decreased IPC generation (Fujitani *et al.* 2017). Furthermore, it has been shown that RGCs transition from symmetric divisions to asymmetric divisions around E11-E12 (Gao et al. 2014) which correlates with the disappearance of *Pcdh19*. Taken together, the data suggest that PCDH19 could be playing a role in RGCs proliferative behaviour during the switch from symmetric to asymmetric divisions.

As the PP at the early stages of cortical development is a densely packed region containing the future SP cells, CR cells, other early-born neurons, interneurons, and RGC basal endfeet structures, it was difficult to determine PCDH19's cell-type specific expression. At E12.5 and E13.5 it was observed that *Pcdh19* co-localised transiently with HPCA1, which indicates that future SP cells might express *Pcdh19*. This would be of particular interest as neurons destined for the SP pioneer the first sub-cortical and contralateral projections in the developing brain (McConnell *et al.* 1994). Initially, these neurons extend their axons to the corticothalamic regions of the developing brain (Jacobs *et al.* 2007), and it is known that a cortical-thalamic-cortical loop is critical in initiating seizures (Bertram 2013). To study CR cells in the PP, the reelin antibody was considered as a suitable marker. However, the antibody did not work using ISH or IHC alone; therefore, calretinin was used as an alternative. It is important to note that there is an initial stream of interneurons that migrate from the medial ganglionic eminence (MGE) at approximately E11.5 to reside in the PP, which also expresses calretinin (Marin and Rubenstein 2001). Therefore, calretinin expression could only confirm the regional expression of *Pcdh19* at the PP to complement that found in close proximity to the future SP cells. The calretinin antibody was only compatible with IHC alone; therefore, the

PCDH19 antibody was used for double IHC to determine protein-specific expression. It was found that calretinin appeared to partially co-localise with PCDH19 in early cortical development, indicating that PCDH19 could be expressed in CR cells or interneurons or both. However, non-nuclear staining and high PCDH19 background staining made it difficult to determine whether this expression was reliable. It would be important to use other markers in combination with those already used to eliminate cells or structures that do or don't express PCDH19 at the PP. For example, TBR1 could be used to detect early-born neurons above the PP in the developing CP, and brain lipid binding protein (BLBP) could be used to detect RGC endfeet structures. In addition, as the PCDH19 antibody gave high background and non-specific staining further optimisation is required to reliably trust the protein expression data.

3.3.3 Alternative methods to determine Pcdh19 cell-type specific expression

Ideally, a PCDH19-specific antibody would be used in combination with compatible markers to conduct a thorough characterisation during early cortical neurogenesis. However, as shown in this chapter and described previously, PCDH19 antibodies are often unreliable. Alternatively, there are other methods to analyse cell type-specific gene expression. For example, using a transgenic mouse line, where PCDH19 is tagged with a fluorescent protein, such as GFP, would allow for a cell-specific characterisation of PCDH19. This would be especially useful if a nuclear GFP was used to indicate whether PCDH19 is expressed in a particular cell. Using a reporter line, cells could also be physically isolated using fluorescently-activated cell sorting (FACs), and entire mRNAs or proteins could be extracted, and levels could be measured using RNA sequencing or mass spectrometry, respectively. This approach could eliminate the complications that arise with antibody reliability and diversity and provide a high output of data for further analysis of cell types. This technique could also include an analysis of more sparse populations of progenitor cells, such as subapical progenitor cells and basal RGCs (Wang *et al.* 2011; Pilz *et al.* 2013; Vaid *et al.* 2018). However, the purification procedure may affect gene expression profiling and PCDH19 expression could not be studied at a single cell level using this technique. Double ISH could also be used, generating probes to detect markers of interest such as reelin and calretinin, combined with the *Pcdh19*-specific probes used in this chapter.

3.3.4 Concluding remarks

A characterisation of PCDH19 has been lacking in the literature due to poor antibody efficiency for IHC. Knowing that *Pcdh19* is highly expressed during early cortical development from the data accessible in the Allen Brain Atlas, this chapter complemented and expanded on this expression data, to try and understand the function of PCDH19 in certain cell- and region-specific areas during early cortical neurogenesis. It was found that *Pcdh19* expression was complementary to the neurogenic gradient, that *Pcdh19* was highly expressed in regions expressing proliferating RGCs and in cells populating the PP but was downregulated in regions expressing IPCs. *Pcdh19 mRNA* diminished during the time RGCs switch from symmetric proliferative to asymmetric neurogenic divisions and previous *Pcdh19* knockdown data complements the hypothesis that PCDH19 is playing a role in neurogenesis, possibly by modulating the symmetrically dividing RGCs. Although this characterisation has shed light on the possible role of PCDH19 in neurogenesis, a thorough and perhaps alternative technique may be required to understand cell-type specific expression further.

Because the results of this chapter suggest a role for PCDH19 in neurogenesis the next chapter investigated whether the lack of PCDH19 affects specific cell numbers and progenitor divisions during early neurogenesis. As a *Pcdh19* heterozygous mouse was used as a disease model, this data could be used to further understand the pathophysiological function of PCDH19.

Chapter 4: The role of PCDH19 in cortical neurogenesis

4.1 Introduction

Since 2006, there have been several publications documenting the expression pattern of protocadherin 19 in the developing mouse brain, confirming a predominant expression in the early developing cortex (Gaitan and Bouchard 2006; Dibbens *et al.* 2008; Pederick *et al.* 2016; Hayashi *et al.* 2017; Pederick *et al.* 2018; Schaarschuch and Hertel 2018). In Chapter 3, it was shown that *Pcdh19* mRNA was transiently expressed in the proliferative regions of the cortex as early as E11.5. There was expression throughout the ventricular zone (VZ) following a pattern complementary/opposed to the neurogenic gradient. *Pcdh19* was expressed highly in radial glial cells (RGCs) but diminished in intermediate progenitor cells (IPCs). This expression pattern suggests that PCDH19 may be playing a functional role in a subpopulation of progenitor cells during cortical neurogenesis. In particular, it has been hypothesised that PCDH19 is playing a role in RGC maintenance during the switch between symmetric and asymmetric divisions.

Alterations in the timing of proliferative and neurogenic divisions, neuronal output, and neuronal subtypes can be detrimental for later brain development. As mentioned in the introduction, dysregulation of overall neuron and glia number can lead to epilepsy and cognitive impairment (Winden *et al.* 2015; Hanzlik and Gigante 2017). The cell cycle is key to the regulation of the expansion and development of the cortex and its complex molecular machinery directs progenitor proliferation and differentiation (Ohnuma *et al.* 2001; Nguyen *et al.* 2006; Dehay and Kennedy 2007), determining laminar fate via the coordinated birth of a neuron and timing of progenitor cell cycle exit (Caviness 1982; McConnell and Kaznowski 1991). Together, this highlights the importance of determining whether PCDH19 has an impact on progenitor behaviour via cell cycle regulation during neurogenesis.

Evidence has been published to indicate that PCDH19 is affecting cortical neurogenesis. ShRNA knock-down of *Pcdh19* decreased RGC proliferation and increased IPC production *in vivo* and PCDH19 promoted neurogenesis in human induced pluripotent stem cells (iPSC)-derived neurons *in vitro* (Fujitani *et al.* 2017; Homan *et al.* 2018). Moreover, Pederick *et al*. reported striking segregation of PCDH19-expressing and non-expressing progenitors in heterozygous mice during

the time of neurogenesis which was later thought to underly the pathogenesis of EIEE9 by causing aberrant neuronal activity *in vivo* (Pederick *et al.* 2018). As shRNA experiments are limited by potential off-target effects and *in vitro* studies are unable to mimic the development of the 3-D cortical structure, how this abnormal cell sorting has an impact on neurogenesis *in vivo* is yet to be determined. It is possible that the mechanism involved could shed light on new factors affecting progenitor fate in certain cellular environments and elucidate the potential cause of the phenotypic features leading to EIEE9.

4.1.1 Aim

The aim of this chapter was to decipher the role of PCDH19 in cortical neurogenesis using the commercially available *Pcdh19* knock-out (KO) mouse model, EdU labelling, and cell-type markers to determine if there are any potential differences in cell cycle parameters, progenitor cell number, and neuronal cell number at the onset of neurogenesis. In the *Pcdh19* KO mouse line, *Pcdh19* exons 1-3 are replaced by a β-galactosidase (β-gal)/neomycin reporter cassette. Therefore, in the heterozygous (HET) mice, it was possible to detect the β-gal on the KO allele to distinguish between the PCDH19 expressing (PCDH19+) and (PCDH19-) non-expressing cell populations. It was further aimed to use this model to confirm PCDH19's role in cell sorting and extend the neurogenic analysis conducted in WT and KO cortices, to study the different cell populations **within** the HET cortex. Finally, an objective was to conduct a preliminary assessment of the effect that PCDH19 may have on direct and indirect neurogenesis.

4.2 Results

4.2.1 PCDH19 is involved in cell sorting during early cortical neurogenesis

4.2.1.1 A Pcdh19 KO mouse model is used to study PCDH19 mosaicism

The *Pcdh19* KO mouse has a β-gal /neomycin reporter cassette replacing exons 1-3 of *Pcdh19*, providing a reporter allele for cells that would normally express PCDH19 (see **Section 2.2**). By using an antibody against β-GAL to detect the reporter, WT E11.5 cortices did not show any β-GAL+ staining, but KO brains did (**Figure 4.1A and B**, respectively). PCDH19-negative (PCDH19-) cells in the KO cortex show strong β-GAL expression across the whole VZ (**Figure 4.1B**). The *Pcdh19* HET female mice had mosaic expression of PCDH19, carrying one WT allele and one KO allele. Cells could be distinguished as either expressing or not expressing PCDH19 since they were negative and positive for β-GAL, respectively (**Figure 4.1C**). In these HET cortices, striking alternating patterns of PCDH19+ (β-gal-) and PCDH19- (β-gal+) areas were seen throughout the developing cortex at E11.5 and E12.5 (E11.5, **Figure 4.2D-F**; E12.5, **Figure 4.1G-I**). These patterns were unique in each brain and varied significantly from brain to brain, revealing distinctive stripes and patches that were of different width and height.

4.2.1.2 Aberrant cell sorting arrangements were found using a PCDH19 antibody

To visualise PCDH19+ cells and to confirm that there is a distinctive segregation of PCDH19+ and PCDH19- cells, E11.5 HET brains were stained with PCDH19 and β-GAL (**Figure 4.2A and B** respectively). As described in Chapter 3, after initial difficulties with unspecific staining of the commercially available PCDH19 antibodies, the staining procedure was partially improved using heat antigen retrieval (**Section 3.2.4**). When combining the PCDH19 immunostaining with β-GAL, an antibody-specific signal was detectable, and a complementary, non-overlapping staining pattern of PCDH19+ and β-GAL+ columns were seen in the HET cortices. Therefore, it was concluded that the two progenitor populations were segregated. Moreover, this immunostaining supported the notion that the PCDH19 antibody staining was specific (**Figure 4.2C**).

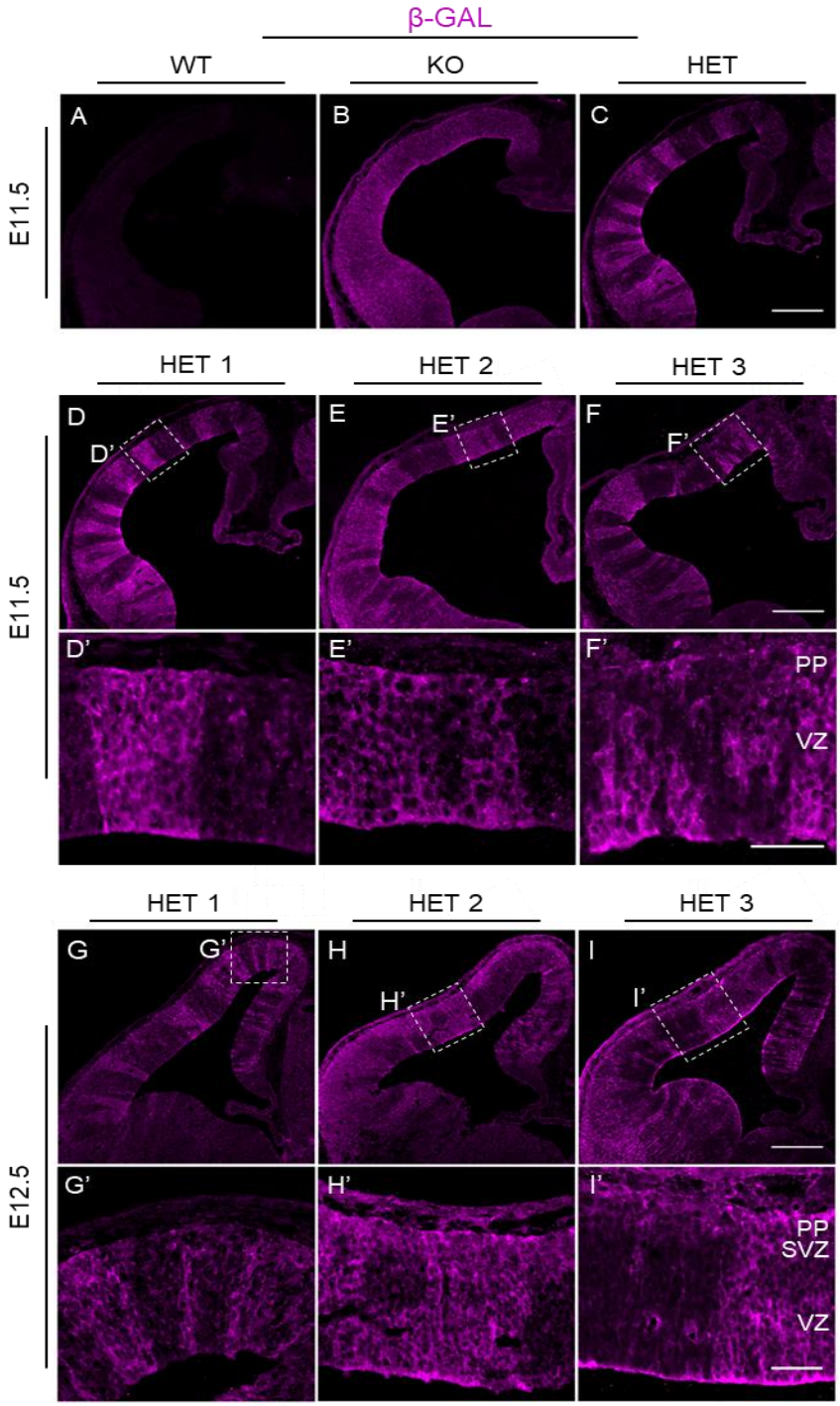

Figure 4.1: PCDH19+ and PCDH19- cells segregate in the developing cortex. (A-C) Representative coronal sections of *Pcdh19* WT, KO and HET brains collected at E11.5 and stained with anti-β-GAL. Example *Pcdh19* HET cortices stained with anti-β-GAL at E11.5 **(D-F)** and E12.5 **(G-I)** with higher magnification images (20x). β-GAL, β-galactosidase; WT, wild-type; KO, knock-out; HET, heterozygous; VZ, ventricular zone. SVZ, subventricular zone; PP, preplate. Scale bars: 200 µM; 50 µM.

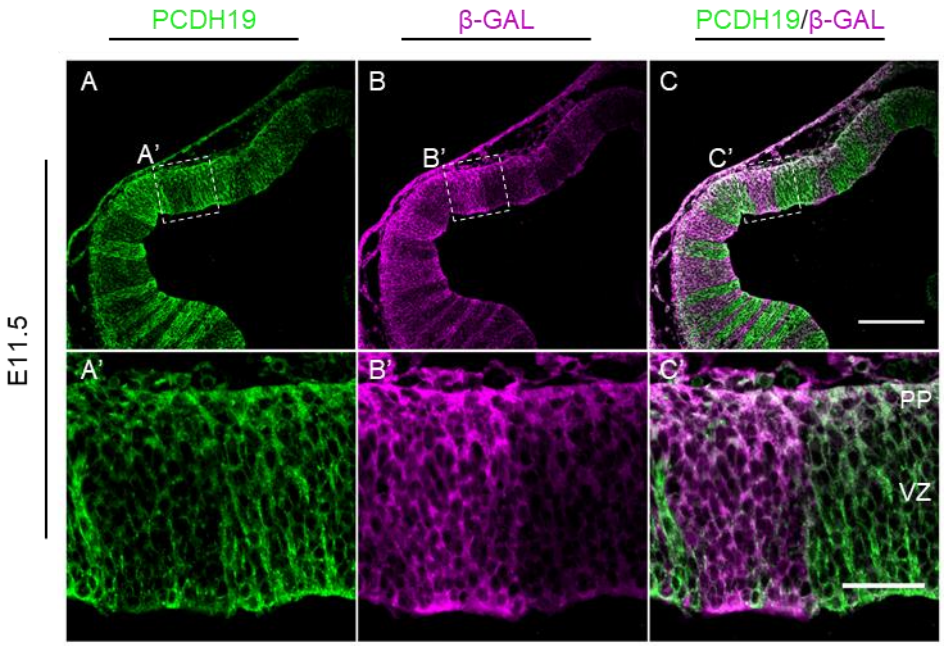

Figure 4.2: PCDH19+ and β-GAL+ cells have a complementary non-overlapping cell segregation arrangement. Representative coronal images of E11.5 *Pcdh19* HET brain stained with anti-PCDH19 (**A and C)** and anti-β-GAL **(B and C)**. Higher magnification images were taken at 20x objective. β-GAL, β-galactosidase; VZ, ventricular zone; PP, preplate. Scale bars: 200 μM; 50 μM.

4.2.1.3 Cell sorting in the Pcdh19 HET mice is due to PCDH19 mosaicism

As *Pcdh19* is subject to X-inactivation (Dibbens *et al.* 2008), the cell sorting pattern seen in the *Pcdh19* HET brains could have been due to random X-inactivation and subsequent clonal expansion. D4/XEGFP (X-GFP) animals carry an X-linked GFP expressing transgene (Hadjantonakis *et al.* 1998); therefore, by mating X-GFP male mice with either *Pcdh19* WT or *Pcdh19* KO females, cell sorting differences could be determined between X-GFP/WT ($X\text{-}GFP^{19\text{-}wt}X^{19\text{-}wt}$) and X-GFP/PCDH19 HET ($X\text{-}GFP^{19\text{-}wt}X^{19\text{-}ko}$) animals (**Figure 4.3**).

E11.5 brains were extracted and counterstained with DAPI and representative sections from X-GFP/WT and X-GFP/*Pcdh19* HET females are depicted in **Figure 4.4**. In the X-GFP/WT cortex, WT progenitors and their descendants from the X-GFP allele expressed GFP and WT cells from the WT allele did not express GFP. The distribution of GFP+ and GFP- cells appeared random with some sparse clustering of GFP+ cells throughout the cortical region (**Figure 4.4A**). In the X-GFP/*Pcdh19* HET females, WT progenitors and their descendants expressed GFP, while *Pcdh19* KO progenitors and their progeny did not (**Figure 4.4B**). It was evident that there were distinctive columns and striking segregation of GFP+ and GFP- cells. By measuring the fluorescent intensity over a defined length of the cortical VZ (600 µM length; **Figure 4.4A and B**; white arrows) GFP+ cell clustering was found to be randomly dispersed in the X-GFP/WT cortex with no clear segregation pattern. In the X-GFP/HET cortex, distinctive and organised clustering of GFP+ cells was seen with large patches of GFP- cells expressing little to no GFP (**Figure 4.4C and D**, respectively).

At E11.5, X-GFP/HET brains were also stained with GFP and β-GAL. It was evident that the two progenitor populations were segregated as distinctive columns of β-GAL+ cells and GFP+ cells segregated with no overlapped expression (**Figure 4.4E**).

Taken together, using the PCDH19 antibody, β-GAL antibody and X-GFP mouse line, it was confirmed that the cell sorting seen in the *Pcdh19* HET females during early cortical development was not due to random X-inactivation alone, but PCDH19 mosaicism, by a mechanism that remains to be elucidated.

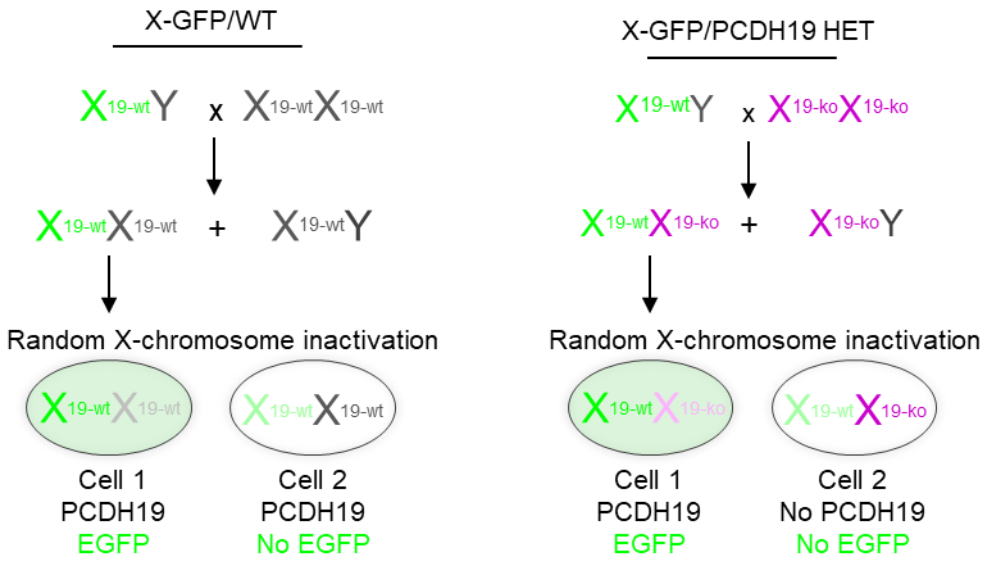

Figure 4.3: Schematic representation of X-GFP/WT and X-GFP/PCDH19 HET mating scheme and the outcome of random X-inactivation. WT, wild-type; HET, heterozygous. EGFP, enhanced green fluorescent protein; 19, PCDH19.

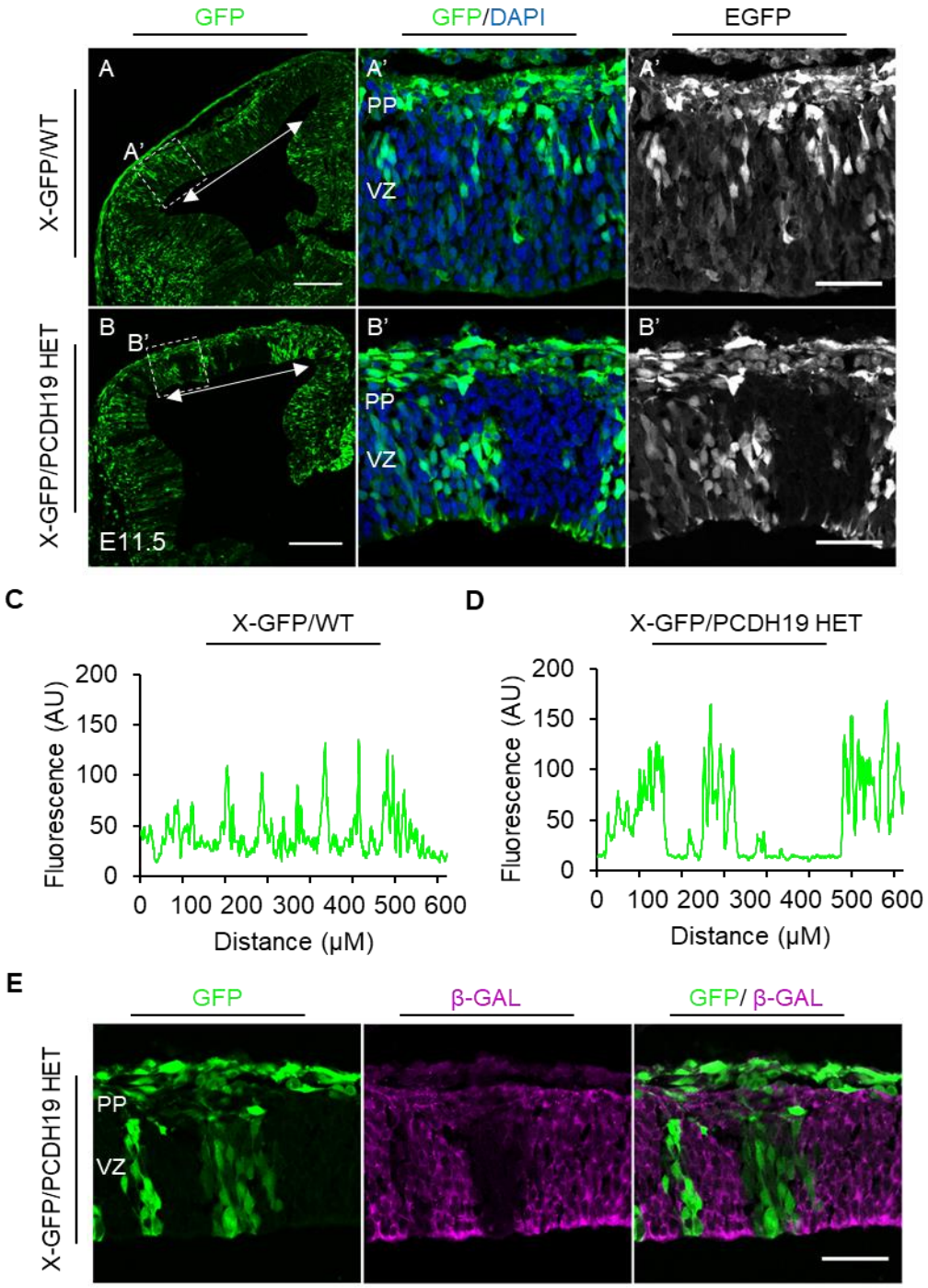

Figure 4.4: PCDH19 is involved in cell sorting during cortical neurogenesis. **(A)** E11.5 X-GFP/ WT and **(B)** X-GFP/ PCDH19 HET coronal sections expressing GFP (green/greys) and counterstained with DAPI (blue). White arrows indicate approximate length of region selected for fluorescent intensity measurement. **(C, D)** Surface plot quantification of the fluorescent intensity across the VZ from X-GFP/WT **(C)** and X-GFP/PCDH19 HET **(D)** coronal section. **(E)** E11.5 X-GFP/ PCDH19 HET expressing GFP and stained with anti-β-GAL. WT, wild-type; HET, heterozygous; β-GAL, β-galactosidase; VZ, ventricular zone; PP, preplate; AU, arbitrary unit. Scale bars: 200 μM; 50 μM.

4.2.2 A Pcdh19 KO mouse model to study cortical neurogenesis

To study the role of PCDH19 in cortical neurogenesis, an approach was needed to determine whether there were differences between *Pcdh19* wild-type (WT), KO and HET developing cortices, and, due to the mosaicism in the HET brain, whether there were differences in PCDH19+ and PCDH19- cell populations **within** the HET cortex. Firstly, experimental matings ($X^{19\text{-}ko}X^{19\text{-}wt}$ x $X^{19\text{-}wt}Y$) were set up to give litters composed of HET females, KO males, WT males and WT females (**Figure 4.5A**). Secondly, a system was designed to analyse the cortex rostro-caudally and latero-medially: three coronal slices were chosen to represent a rostral, medial and caudal section for each genotype (**Figure 4.5B-C**). Then, three regions of a pre-defined size were selected from these sections that spanned the radial thickness of the cortex, to include lateral (1), middle (2) and medial (3) regions (**Figure 4.5C**) These sections were then averaged to represent the corresponding value for the whole brain in the quantifications.

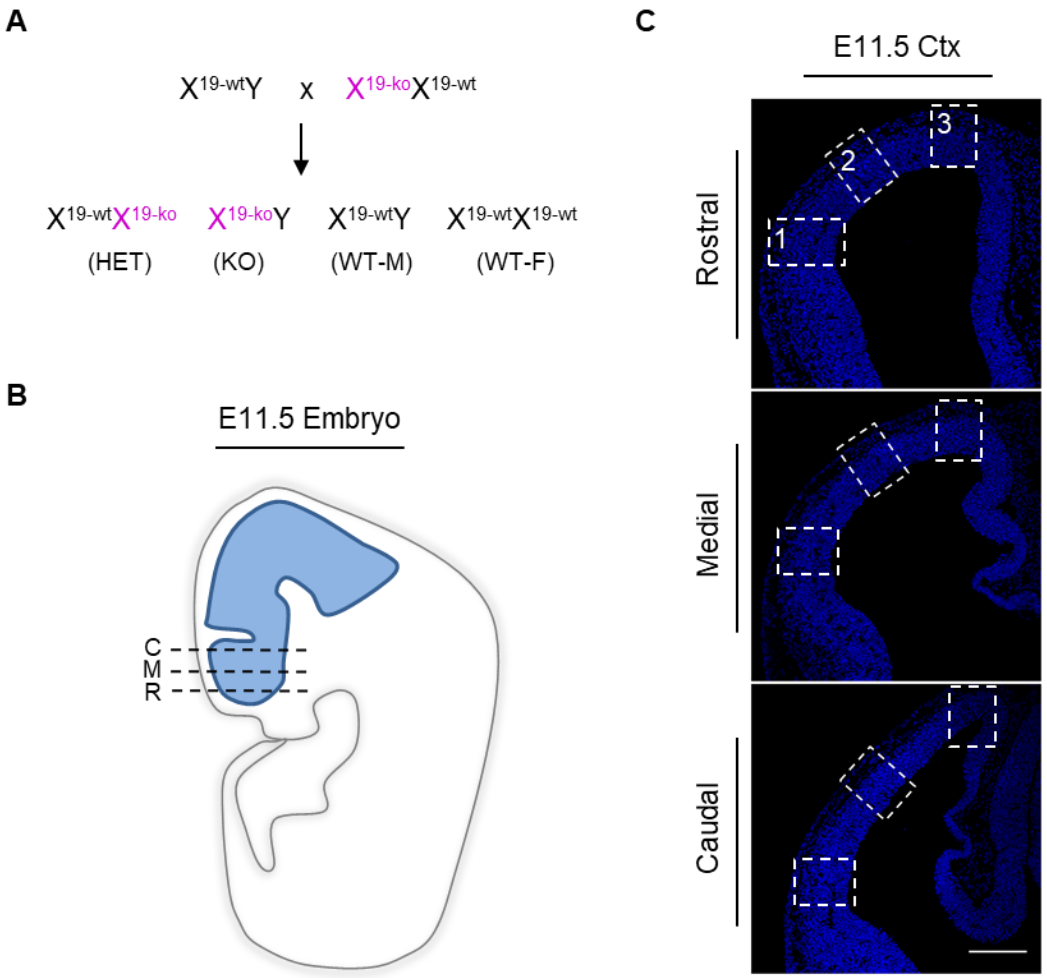

Figure 4.5: Experimental plan (A) Scheme of the experimental mating used for all neurogenesis experiments, generating *Pcdh19* HET female ($X^{19\text{-wt}}X^{19\text{-ko}}$), KO males ($X^{19\text{-ko}}Y$), WT-M ($X^{19\text{-wt}}Y$), and WT-F ($X^{19\text{-wt}}X^{19\text{-wt}}$). Purple text indicates the KO allele. **(B and C)** Cortical regions of interest. **(B)** Schematic representation of an E11.5 embryo. Black dashed lines indicate sections selected for analysis. **(C)** Representative E11.5 rostral, medial and caudal sections selected for analysis, counterstained with DAPI. White dashed boxes indicate regions of interest selected for quantification where 1 = lateral, 2= middle, and 3= medial. WT-M, wild-type male; WT-F, wild-type female; KO, knock-out; HET, heterozygous; Ctx, cortex; R, rostral; M, medial; C, caudal. Scale bar: 200 µM.

4.2.3 PCDH19+ and PCDH19- progenitors have differential cell cycle properties in the developing HET cortex during early cortical neurogenesis

To determine whether different cell cycle parameters were regulated by PCDH19, WT, KO and HET cortices were analysed. Importantly, the analysis of the HET cortex took into consideration PCDH19+ and PCDH19- progenitors **within** the HET brain. Therefore, the analyses presented below not only compare the genotype (WT, KO and HET brains), but also the epigenotype, comparing WT and KO cells in WT and KO cortices and WT and KO cells within the HET cortex (HET-WT and HET-KO).

4.2.3.1 Mitotic Cell Number

To determine the fraction of cells undergoing mitosis at E11.5, WT, KO, and HET brain sections were stained with the mitotic cell marker, phosphohistone H3 (PHH3), β-GAL to detect the reporter cassette, and counterstained with the nuclear marker DAPI (**Figure 4.6B**). The percentage of cells undergoing mitosis over the total cell number (PHH3+/total DAPI+) was calculated for each genotype (**Figure 4.6A and C**). The percentage of PHH3+ cells in WT and KO cells **within** the HET was calculated over the total number of DAPI+ β-GAL- and DAPI+ β-GAL+ cells, respectively.

Firstly, to ensure there were no differences caused by gender within the WT group, female and male cortices were analysed separately. It was found that gender did not affect the mitotic cell number, and the groups were pooled together for subsequent analysis (WT-F, 2.8% (n=3) vs. WT-M, 3.1% (n=3); *P=0.536*; unpaired t-test).

The effect of epigenotype and genotype on the percentage of mitotic cells was then assessed using a two-way ANOVA. This analysis revealed that both epigenotype and genotype significantly influenced the fraction of mitotic cells present at E11.5 (**Figure 4.6C**; Genotype: *F (2,15) =6.275, P=0.010*; Epigenotype: *F (1,15) =23.631, P=0.000;* two-way ANOVA). Post-hoc analysis revealed that there were no differences between WT, KO, and HET cortices overall (WT vs. KO vs. HET: *F (2,15) =0.091, P=0.913;* Bonferroni post hoc). However, **within** the HET cortices, HET-KO cells had a significantly higher fraction of mitotic cells than HET-WT cells (HET-WT, 1.6% (n=5) vs. HET-KO, 4.3% (n=5); *P=0.000*; Bonferroni post-hoc). Interestingly, HET-WT cells had a significantly lower mitotic cell number compared to WT cells from WT cortices (WT, 2.9% (n=6) vs. HET-WT, 1.6% (n=5); *P=0.023*; Bonferroni post-hoc) and HET-KO cells had a

significantly higher mitotic cell number than KO cells in KO cortices (KO, 2.7% (n=6) vs. HET-KO, 4.3% (n=5); *P=0.023*; Bonferroni post-hoc).

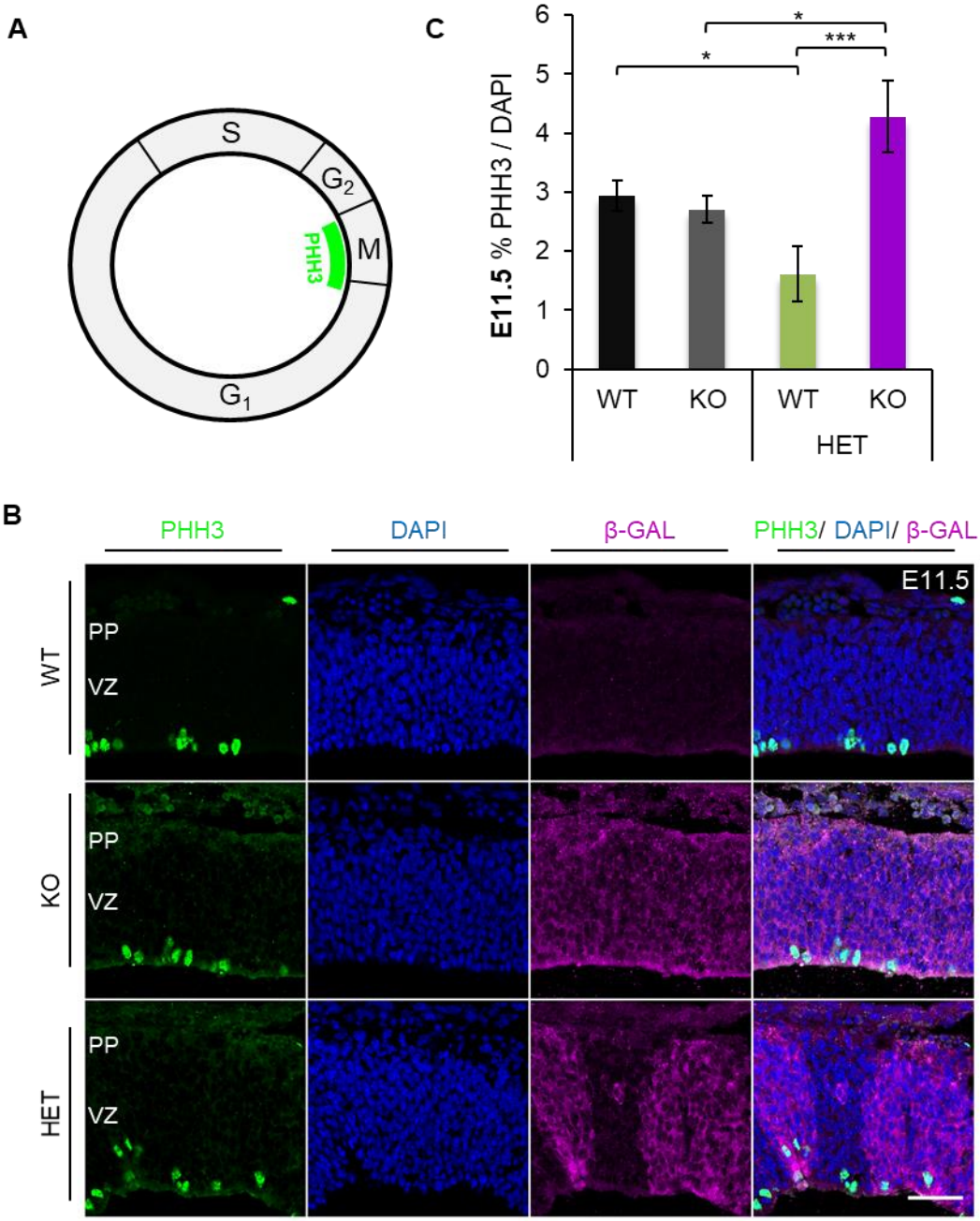

Figure 4.6: PCDH19+ and PCDH19- cells have altered mitotic cell numbers within the HET cortex. (A) Schematic representation of PHH3 staining in the cell cycle. **(B)** Representative E11.5 sections, stained with PHH3 (green), and β-GAL (magenta), and counterstained with DAPI (blue) for each genotype. **(C)** Quantification of the percentage of cells undergoing mitosis at E11.5 calculated as the percentage of pHH3+ cells over the total cell number (DAPI+). HET-WT and HET-KO groups refer to β-GAL- (PCDH19+) and β-GAL+ (PCDH19-) regions **within** the HET brain, respectively. WT-F, wild-type female; WT-M, wild-type male; KO, knock-out; HET, heterozygous; β-GAL, β-galactosidase; VZ, ventricular zone; *, $p<0.05$; ***, $p<0.001$. Data are represented as mean ± SEM. Scale bars: 50 µM.

4.2.3.2 EdU Labelling Index

To determine what fraction of cells were in S-phase at E11.5, the EdU labelling index was calculated. E11.5 pregnant dams were injected with EdU, and after 2 hours embryonic brains were dissected, fixed, and cryosectioned. EdU was detected using the Click-iT reaction and sections were stained with the cycling cell marker KI67, and β-GAL (**Figure 4.7B**). The EdU labelling index was calculated as the percentage of dividing cells (KI67+ cells) that were in S-phase (EdU labelled 2 hours post-injection) over the total number of dividing cells (KI67+; EdU+$^{(2hrs)}$) / Total KI67+) (**Figure 4.7A-C**). The percentage of EdU+KI67+ cells in WT and KO cells **within** the HET was calculated over the total number of KI67+β-GAL- and KI67+β-GAL+ cells, respectively.

Initially, it was found that gender did not affect the EdU labelling index within the WT group; therefore, WT female and male groups were pooled together for subsequent analysis (WT-F, 47.4% (n=3) vs. WT-M, 45.1% (n=3); *P=0.536*; unpaired t-test).

The effects of epigenotype and genotype were then assessed using a two-way ANOVA. This analysis revealed that, at E11.5, there were differences in the fraction of cells in S-phase that was significantly influenced by epigenotype but not genotype (**Figure 4.7C**; Genotype: *F (2,15) =2.609, P=0.107*; Epigenotype: *F (1,15) =7.034, P=0.018;* two-way ANOVA). Post-hoc analysis revealed that WT, KO, and HET whole cortices had similar numbers of cells in S-phase overall (WT vs. KO vs. HET: *F (2,15) =0.091, P=0.913;* Bonferroni post hoc). Further post-hoc analysis revealed that HET-KO cells had a significantly higher fraction of cells in S-phase than HET-WT cells (HET-WT, 46.8% (n=5) vs. HET-KO, 56.11% (n=5); *P=0.018*; Bonferroni post-hoc). Additionally, HET-KO cells had a significantly higher fraction of cells in S-phase when compared to KO cells in KO cortices (KO, 46.8% (n=5) vs. HET-KO, 56.1% (n=5); *P=0.038*; Bonferroni post-hoc), but differences were not seen between WT cells from different genotypes (WT, 46.3% (n=5) vs. HET-WT, 46.8% (n=5); *P=0.883*; Bonferroni post-hoc).

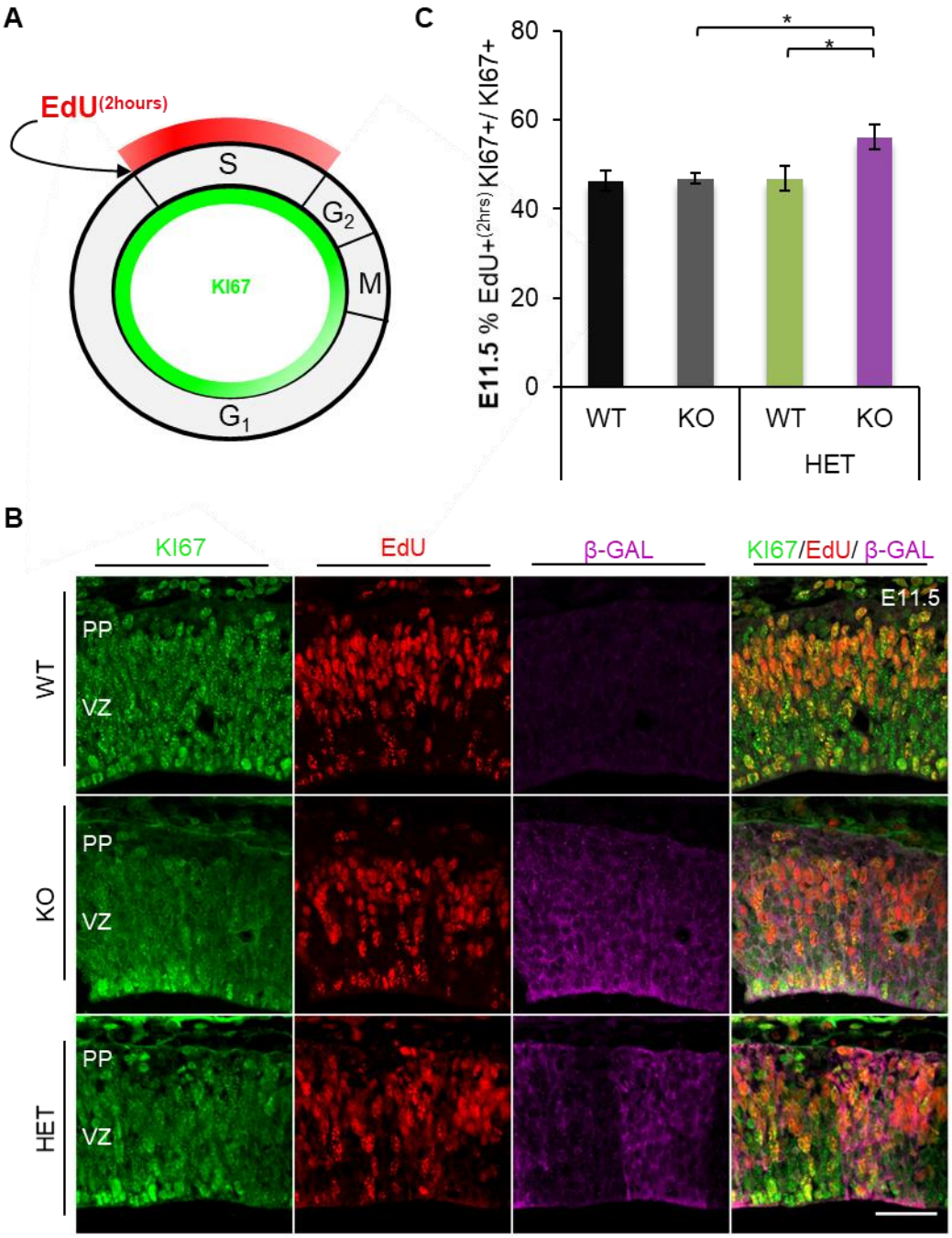

Figure 4.7: PCDH19- cells have an increased fraction of cells in S-phase within the developing HET cortex. (A) Schematic representation of EdU detection after 2 hours combined with Ki67 staining within the cell cycle. **(B)** Representative E11.5 sections labelled with EdU (red) and stained with KI67 (green) and β-GAL (magenta) for each genotype. **(C)** Quantification of the percentage of cells in S-phase of the cell cycle at E11.5, calculated as the percentage of cycling (Ki67+), EdU labelled cells after 2 hours. HET-WT and HET-KO groups refer to the β-GAL- (PCDH19+) and β-gal- (PCDH19-) regions **within** the HET brain, respectively. WT-F, wild-type female; WT-M, wild-type male; KO, knock-out; HET, heterozygous; β-GAL, β-galactosidase; VZ, ventricular zone; *, $p<0.05$. Data are represented as mean ± SEM. Scale bars: 50 µM.

4.2.3.3 Quitting fraction

To quantify the number of cells leaving the cell cycle (entering terminal G_0 phase to become a post-mitotic neuron), the quitting fraction was calculated. EdU was injected at E11.5 into pregnant dams, and after 24 hours, embryonic brains were dissected, fixed and cryosectioned. EdU was detected, and sections were stained with KI67and β-GAL (**Figure 4.8B**). By calculating the percentage of EdU+ cells that were no longer cycling (KI67-) over the total number of EdU+ cells (EdU+$^{(24hours)}$; KI67-/Total EdU+$^{(24hours)}$), the number of cells leaving the cell cycle after 24 hours was determined (**Figure 4.8A-C**). The percentage of EdU+KI67- cells in WT and KO cells **within** the HET was calculated over the total number of EdU+ β-GAL- and EdU+ β-GAL+ cells, respectively.

When comparing WT female and male cortices, no differences were observed in the fraction of cells leaving the cell cycle; therefore WT-F and WT-M groups were analysed as one group (WT-F, 11.5% (n=3) vs. WT-M, 11.8% (n=3); *P=0.862*; unpaired t-test).

The fraction of cells leaving the cell cycle varied significantly, depending on genotype and epigenotype (**Figure 4.8**; Genotype: *F (2,15) =8.425, P=0.107*; Epigenotype: *F (1,15) =35.930, P=0.000;* two-way ANOVA). Post-hoc analysis revealed that differences were not seen in WT, KO, or HET cortices overall (WT vs. KO vs. HET: *F (2,15) =0.292, P=0.751;* Bonferroni post hoc). However, the HET-KO population had a significantly higher fraction of cells leaving the cell cycle, compared to HET-WT (HET-WT, 5.1% (n=5) vs. HET-KO, 16.5% (n=5); *P=0.000*; Bonferroni post-hoc). In addition, there was a trend towards HET-KO cells having an increased quitting fraction compared to KO cells in KO cortices and a significant decrease in the quitting fraction in HET-WT cells when compared to WT cells in WT cortices (KO, 12.2% (n=3) vs. HET-KO, 16.5% (n=5); *P=0.065*; WT, 11.7% (n=5) vs. HET-WT, 5.1% (n=5); *P=0.003*; Bonferroni post-hoc).

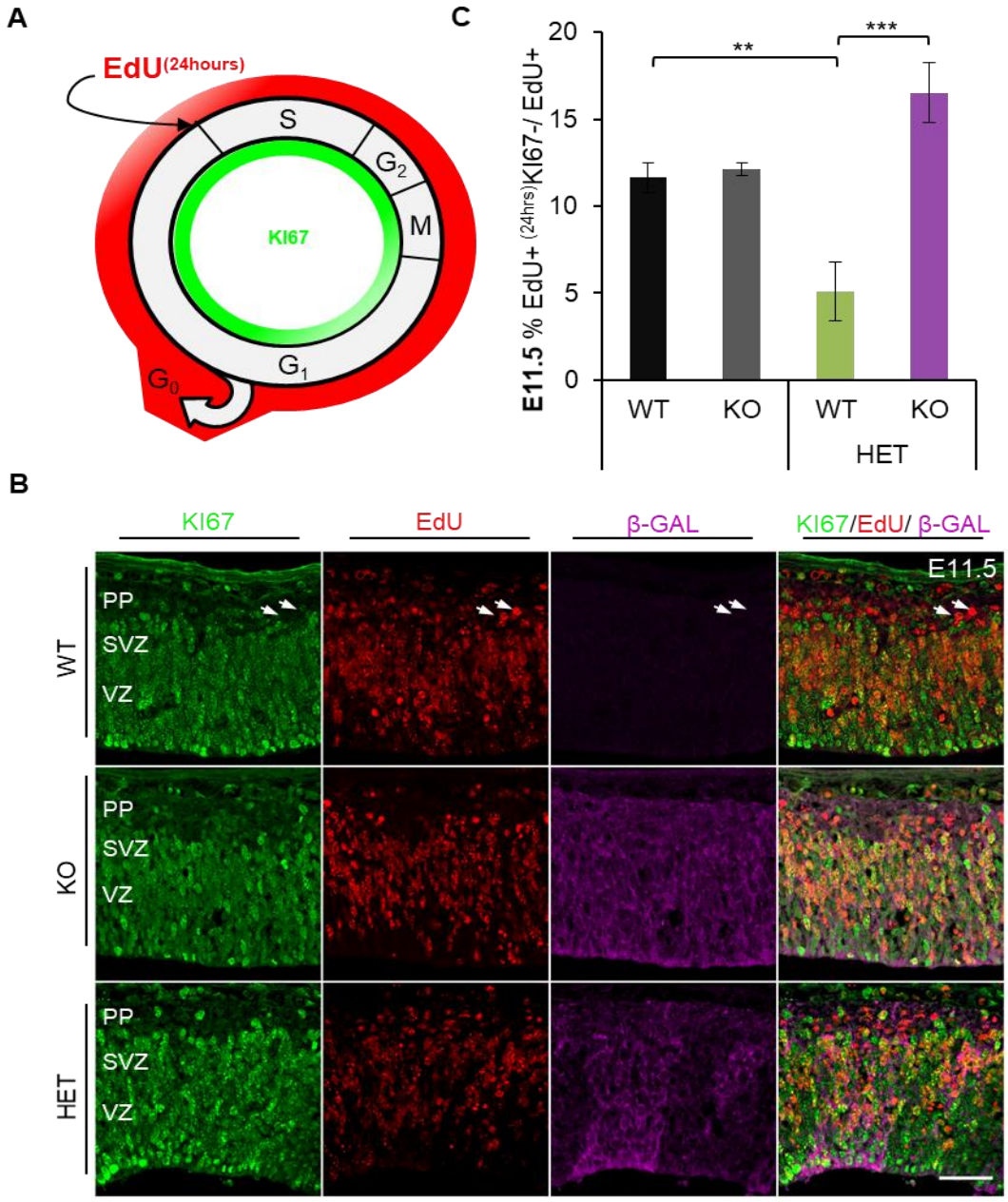

Figure 4.8: Mosaic expression of PCDH19 influences cell cycle exit in the developing cortex. (A) Schematic of EdU and KI67 after 24 hours in the cell cycle. **(B)** Representative E11.5 sections, labelled with EdU (red), and stained with KI67 (green) and β-galactosidase (magenta) for each genotype. **(C)** Quantification of the percentage of cells leaving the cell cycle at E11.5 after 24 hours, calculated as the percentage of EdU labelled cells that are Ki67- after 24 hours. PCDH19- and PCDH19+ refer to the β-GAL+ and β-GAL- regions of the HET brain, respectively. White arrowheads show example EdU+/KI67- cells. N, neuron; WT-F, wild-type female; WT-M, wild-type male; KO, knock-out; HET, heterozygous; β-GAL, β-galactosidase; VZ, ventricular zone; PP, preplate; ns, not significant; **, p<0.01. Data represented as the mean ± SEM. Scale bars: 50 µM.

4.2.3.4 Summary of PCDH19's role in cell cycling during early cortical neurogenesis

In summary, PCDH19 altered cell cycling **within** the HET cortices, presumably due to their cellular environment. It was observed that lack of PCDH19 did not affect the mitotic cell number, EdU labelling index or quitting fraction overall in KO brains. However, WT and KO cells behaved differently within the HET brain. Surprisingly, more HET-KO cells proliferated and left the cell cycle than KO cells in a KO brain. Furthermore, HET-KO cells had a higher fraction of proliferating cells, cells in S-phase and cells leaving the cell cycle, compared to HET-WT cells. Reflective of this, less HET-WT underwent mitosis and left the cell cycle than WT cells from a WT brain.

This unusual divergence of cell cycle behaviour within the HET cortex may reflect and influence the proportion of progenitor cells and/or early-born neurons being present in PCDH19+ and PCDH19- cell regions. Hence, it was of interest to next analyse the percentage of the most common progenitors in rodents: RGCs and IPCs, as well as the percentage of early-born neurons to understand if the cellular composition of the developing cortex is altered due to PCDH19 mosaicism.

4.2.4 PCDH19+ and PCDH19- regions of the HET cortex have opposing and complementary progenitor cell compositions

As it has been observed that PCDH19+ and PCDH19- cells **within** the HET cortex behave differently to one another and differ from those in WT and KO cortices, respectively, it was important to assess whether these changes correlated with a change in progenitor cell number. As RGCs and IPCs are the two main progenitor cells found in rodent, the percentages of these progenitors were assessed. The analysis was conducted as explained in **Sections 4.2.2** and **4.2.3**. The genotype (WT, KO and HET brains) and the epigenotype (WT and KO cells in WT and KO cortices and WT and KO cells within HET cortices) were compared.

4.2.4.1 Radial glial cell (RGC) percentage

To determine whether there were differences in the proportion of RGCs in WT and KO cortices, as well as WT and KO cells populations within the HET cortex, sections from each genotype were stained with the RGC marker PAX6, β-GAL, and counterstained with DAPI (**Figure 4.9A-B**). Once stained and imaged, the percentage of PAX6+ cells over the total number of cells (DAPI+) (PAX6+/Total DAPI+) was determined (**Figure 4.9C**). For the within HET analysis, the percentage of PAX6+ cells in WT and KO cells within the HET was calculated over the total number of DAPI+ β-GAL- and DAPI+ β-GAL+ cells, respectively. In the developing mouse cortex, there are significant differences in progenitor fate and neuronal output over 24 hours; therefore, the analysis was expanded and E11.5 and E12.5 cortices were assessed.

To ensure gender did not influence RGC number in WT brains, WT female and male brains were assessed separately. At both E11.5 and E12.5 it was determined that gender did not affect RGC number (E11.5: WT-F, 85.2% (n=3) vs. WT-M, 89.5% (n=3); *P= 0.371*; E12.5: WT-F, 80.1% (n=3) vs. WT-M, 73.4% (n=3); *P= 0.269*; unpaired t-tests).

At E11.5, the effects of epigenotype and genotype were assessed using a two-way ANOVA. It was found that there were differences in the fraction of RGCs between groups that were influenced by epigenotype but not by genotype (**Figure 4.9C**; Genotype: *F (2,15) =1.498, P=0.255*; Epigenotype: *F (1,15) =7.906, P=0.013;* two-way ANOVA). Post-hoc analysis revealed that there were no differences in WT, KO, and HET cortices overall (WT vs. KO vs. HET: *F (2,15) =0.378, P=0.378;* Bonferroni post hoc). However, within the HET cortices, HET-KO cells had a significantly lower fraction of RGCs than

HET-WT (HET-WT, 89.6% (n=5) vs. HET-KO, 80.5% (n=5); *P=0.013*; Bonferroni post-hoc). Although there was a significant difference within the HET cortex, this difference was not present when comparing KO and HET-KO cells or WT and HET-WT cells (KO, 86.4% (n=6) vs. HET-KO, 80.5% (n=5); *P=0.138*; WT, 87.3% (n=6) vs. HET-WT, 89.6% (n=5); *P=0.473*; Bonferroni post-hoc).

At E12.5, differences were observed between WT, KO, HET-WT, and HET-KO cell populations that was influenced by genotype and epigenotype (Genotype: *F (2,15) =7.407, P=0.006*; Epigenotype: *F (1,15) =25.444, P=0.000;* two-way ANOVA). Although post-hoc analysis revealed that there was no significant differences between WT, KO, and HET genotype overall (WT vs. KO vs. HET: *F (2,15) =1.401, P=0.277;* Bonferroni post hoc), within the HET cortices, a significant decrease in RGC number was observed in HET-KO cells compared to HET-WT cells (HET-WT, 83.9% (n=5) vs. HET-KO, 60.2% (n=5); *P=0.013*; Bonferroni post-hoc). Interestingly, HET-KO cells had a lower fraction of RGCs than KO cells in KO cortices, while HET-WT cells did not differ from WT cells in WT cortices (KO, 79.2% (n=6) vs. HET-KO, 60.2% (n=5); *P=0.003*; WT, 76.7% (n=6) vs. HET-WT, 83.9% (n=5); *P=0.130*; Bonferroni post-hoc).

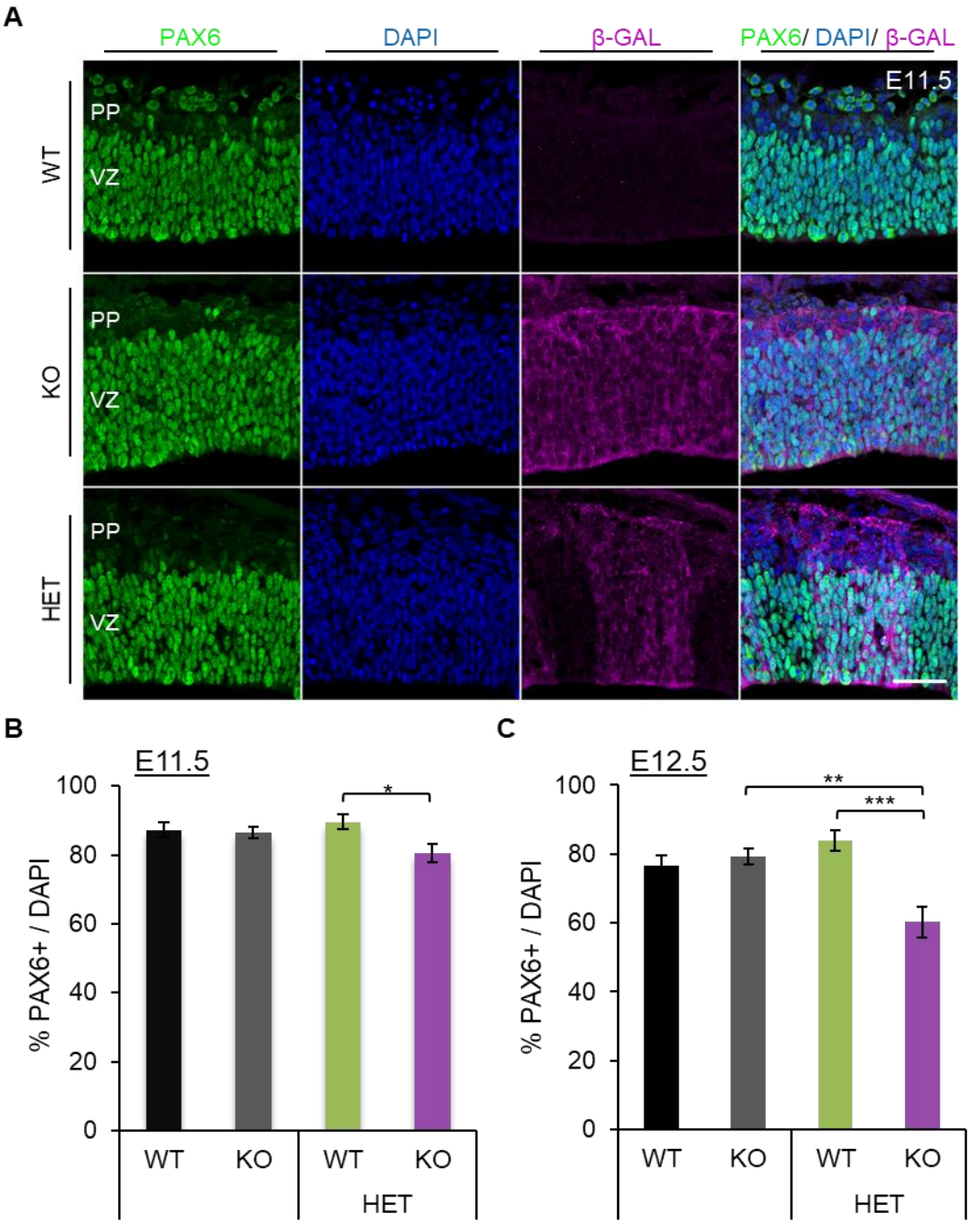

Figure 4.9: PCDH19+ and PCDH19- cells within the developing HET cortex have an increased and decrease fraction of RGC's, respectively. (A) E11.5 sections stained with PAX6 (green), β-GAL (magenta) and counterstained with DAPI (blue) for indicated genotypes. HET-WT and HET-KO cells refer to the β-GAL- (PCDH19+) and β-GAL- (PCDH19+) regions of the HET brain, respectively. **(B and C)** Quantification of the total number of RGC's at E11.5 **(B)** and E12.5 **(C)**, calculated as the percentage of PAX6+ cells over the total cell number (DAPI+). WT-F, wild-type female; WT-M, wild-type male; KO, knock-out; HET, heterozygous; β-gal, β-galactosidase; VZ, ventricular zone; *, $p<0.05$ **, $p<0.01$; ***, $p<0.001$. Data are represented as mean ± SEM. Scale bar: 50 µM.

4.2.4.2 Intermediate progenitor cell (IPC) percentage

To study whether the proportion of IPCs differ in WT and KO cortices and WT and KO populations within the HET cortex, sections were stained with IPC marker TBR2, β-GAL, and counterstained with DAPI (**Figure 4.10A**). The proportion of IPCs was calculated as the percentage of TBR2+ cells over the total number of cells (DAPI+) (TBR2+/Total DAPI+) (**Figure 4.10B-C**). Similar to the RGC quantifications, the percentage of TBR2+ cells in HET-WT and HET-KO cells was calculated over the total number of DAPI+β-GAL- and DAPI+β-GAL+ cells, respectively. Furthermore, the analysis was again expanded to E12.5.

It was firstly determined that gender of WT cortices did not influence IPC number at either E11.5 or E12.5. Therefore, WT female and WT male groups were pooled together for subsequent comparative analysis (E11.5: WT-F, 21.5% (n=3) vs. WT-M, 20.5% (n=3); *P= 0.114*; E12.5: WT-F, 26.5% (n=3) vs. WT-M, 26.7% (n=3); *P= 0.910*; unpaired t-tests).

At E11.5, differences were found in the proportion of WT, KO, HET-WT, and HET-KO cells expressing TBR2. Furthermore, a two-way ANOVA revealed that this difference was significantly influenced by genotype and epigenotype (**Figure 4.10B**; Genotype: *F (2,15) =37.348, P=0.000*; Epigenotype: *F (1,15) =140.583, P=0.000*; two-way ANOVA). Upon post-hoc analysis of WT, KO, and HET cortices overall, it was found that there was a trend towards a significantly lower proportion of TBR2 cells in the HET cortices when compared to WT cortices, and a significantly lower proportion of TBR2+ cells when compared to KO cortices (WT, 21.0% (n=6) vs. HET, 17.7% (n=5), P=0.077; KO, 22.4% (n=3) vs. HET, 17.7% (n=5), *P=0.025*; Bonferroni post-hoc). However, no differences were seen between WT and KO cortices (WT, 21.0% (n=6) vs. KO, 22.4% (n=3); Bonferroni post-hoc). Interestingly, the HET-WT cells had a significantly lower percentage of IPCs when compared to HET-KO and WT cells in the WT cortex (HET-WT, 10.9% (n=5) vs. HET-KO, 26.0% (n=5); *P=0.000*; HET-WT, 10.9% (n=5) vs. WT, 21.0% (n=6), *P=0.000*; Bonferroni post-hoc). Moreover, HET-KO cells had a significantly higher number of IPCs when compared to KO cells within the KO cortex (HET-KO, 26.0% (n=5) vs. KO, 22.4% (n=3), P=0.030; Bonferroni post-hoc).

At E12.5, differences were also found between the groups. A two-way ANOVA revealed that both genotype and epigenotype significantly influenced this difference (**Figure 4.10C**; Genotype: *F (2,15) =4.093, P=0.038;* Epigenotype: *F (1,15) =9.578, P=0.007*;

two-way ANOVA). Unlike the analysis at E11.5, when comparing WT, KO and HET cortices overall, no significant difference was observed (WT vs. KO vs. HET, *F (2,15) =1.705, P=0.215*; Bonferroni post-hoc). When comparing cell populations within the HET cortex, HET-KO cells had a significantly higher proportion of IPCs compared to HET-WT. In addition, HET-WT cells did not differ from WT cells in WT cortices (HET-WT, (n=5) vs. HET-KO, (n=5); *P=0.007* HET-WT, (n=5) vs. WT, (n=6), *P=0.618*; Bonferroni post-hoc). Unlike at E11.5, no differences were observed between KO and HET-KO cells (KO, (n=6) vs. HET-KO, (n=5), *P=0.013*; Bonferroni post-hoc).

4.2.4.3 Summary of PCDH19's effect on progenitor cell number

Overall, it has been shown that **within** the HET developing cortex there is a different composition of progenitor cells at E11.5 and E12.5 between PCDH19+ and PCDH19- cells. There were fewer RGCs and more IPCs in the PCDH19- compared to the PCDH19+ cell populations within the HET cortex. This suggests that PCDH19- cells have an increased rate of neurogenesis. Interestingly, the proportion of IPCs is lower in HET cortices overall when compared to WT and KO cortices, but only at E11. In addition, the difference in progenitor cell composition within the HET is bigger at E11.5 when considering the proportion of IPCs but is bigger at E12.5 when considering the proportion of RGCs.

At E11.5, a small proportion of early-born neurons are generated from progenitor cells. This neurogenic behaviour progresses over time, either directly from RGCs or indirectly from IPCs (mainly from IPCs in later neurogenesis). In **Section 4.2.3.3**, an increased quitting fraction was observed in PCDH19- cells, which was compensated by a decreased quitting fraction in PCDH19+ cells, making the overall quitting fraction within the HET cortex similar to that seen in KO and WT cortices. This difference within the HET cortex implies that PCDH19- cells contribute to the generation of more early post-mitotic neurons than PCDH19+. Therefore, assessing the fraction of early-born neurons is necessary to determine whether there is a difference in neuronal output in the HET cortex.

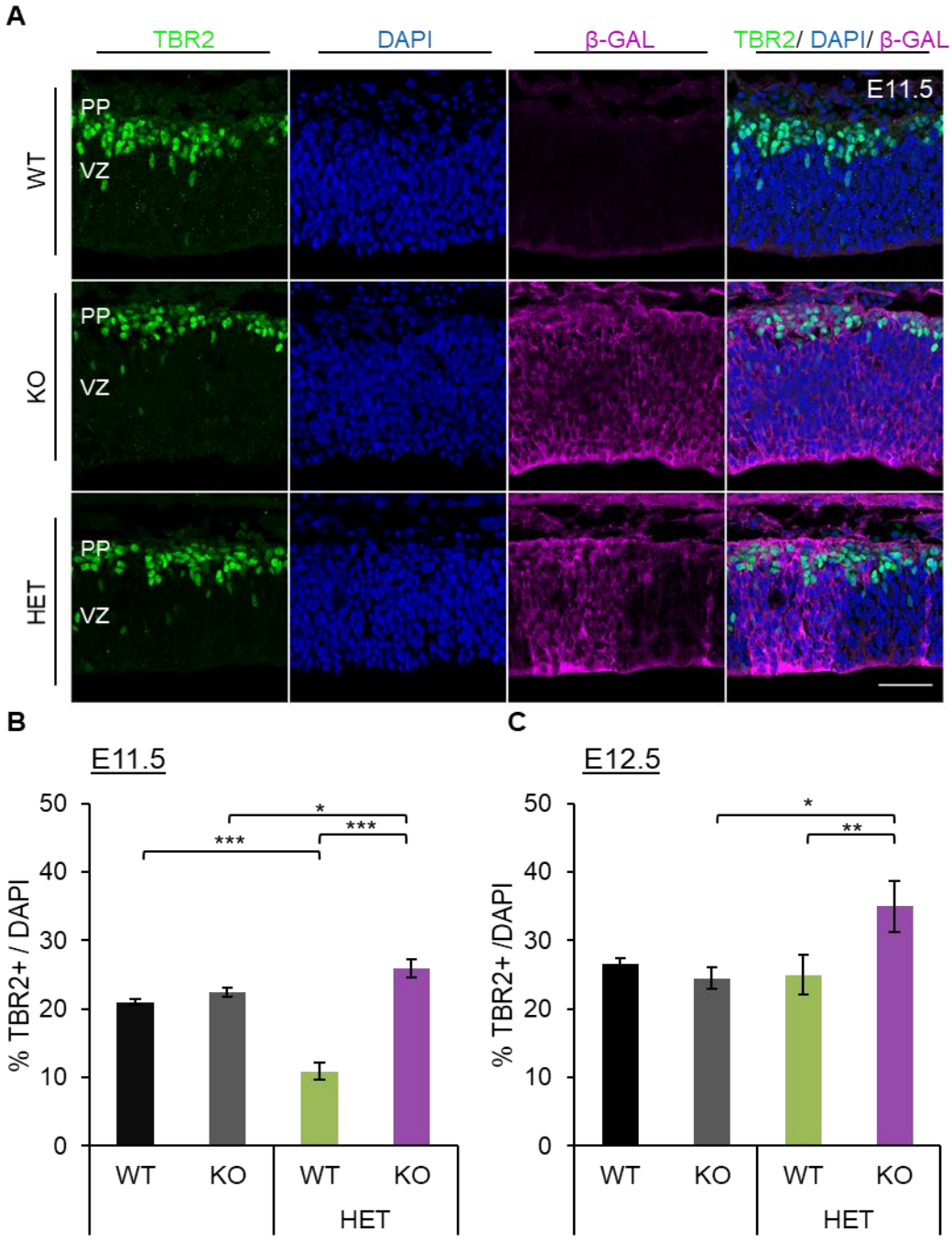

Figure 4.10: PCDH19 mosaicism causes an alteration in IPC number in the developing HET cortex. (A) E11.5 sections stained with TBR2 (green), β-GAL (magenta) and counterstained with DAPI (blue) for indicated genotypes. HET-WT and HET-KO cell populations refer to the β-GAL- (PCDH19+) and β-GAL- (PCDH19-) regions of the HET brain, respectively. **(B and C)** Quantification of the total number of IPC's at E11.5 **(B)** and E12.5 **(C)**, calculated as the percentage of TBR2+ cells over the total cell number (DAPI+). WT-F, wild-type female; WT-M, wild-type male; KO, knock-out; HET, heterozygous; β-GAL, β-galactosidase; VZ, ventricular zone; PP, preplate; *, $p<0.1$; **, $p<0.01$, *** $p<0.001$. Data represented as mean ± SEM. Scale bar: 50 µM.

4.2.5 PCDH19+ and PCDH19- cells have a decreased and increased neuronal output in the developing HET cortex, respectively

4.2.5.1. Early-born neuron percentage

Due to the differing ratios of RGCs and IPCs found between WT and KO cell populations **within** the HET developing cortex, and differences in the fractions of cells leaving the cell cycle, it was hypothesised that there would be differences in the number of neurons generated during this time. Therefore, the proportion of early-born neurons was assessed at E11.5 and E12.5 in WT, KO and HET cortices. Sections were stained with the early-born neuronal cell marker TBR1, β-GAL, and counterstained with DAPI (**Figure 4.11A**). The proportion of early-born neurons was calculated as the percentage of TBR1+ cells over the total number of cells (DAPI+) (TBR1+/Total DAPI+) (**Figure 4.11B-C**). For the within HET analysis, the percentage of TBR1+ cells in WT and KO regions was calculated over the total number of DAPI+ β-GAL- and DAPI+ β-GAL+ cells, respectively.

Firstly, no significant differences were observed between WT-F and WT-M cortices at E11.5 or E12.5 (E11.5: WT-F, 8.7% (n=3) vs. WT-M, 10.2% (n=3); *P= 0.078*; E12.5: WT-F, 8.6% (n=3) vs. WT-M, 7.5% (n=3); *P= 0.375*; unpaired t-tests). Therefore, the two groups were pooled together for subsequent analysis at each age.

At E11.5, it was found that epigenotype, but not genotype, significantly affected the proportion of TBR1+ cells present in WT, KO, HET-WT, and HET-KO regions (**Figure 4.11B**; Genotype: *F (2,15) =1.961, P=0.170*; Epigenotype: *F (1,15) =7.922, P=0.011*; two-way ANOVA). Post hoc analysis confirmed that overall in the WT, KO, and HET cortices, there were no differences in the percentage of TBR1+ cells (WT vs. KO vs. HET, *F (2,15) =0.033, P=0.989*; Bonferroni post-hoc). However, HET-KO cells had a higher proportion of TBR1+ cells compared to HET-WT (HET-WT, 7.4% (n=5) vs. HET-KO, 11.5% (n=5), *P=0.011*; Bonferroni post-hoc), emphasising that HET-KO cells are proliferating faster and undergoing premature neurogenesis, relative to HET-WT cells. Finally, HET-WT cells were not significantly different from WT (HET-WT, 7.4% (n=5) vs. WT, 9.73% (n=6), *P=0.111*; Bonferroni post-hoc) and neither were HET-KO and KO (HET-KO, 11.5% (n=5) vs. KO, 9.6% (n=3), *P=0.306*; Bonferroni post-hoc).

At E12.5, a difference was seen in the fraction of TBR1+ cells expressed in WT, KO, HET-WT, and HET-KO regions. By conducting a two-way ANOVA, it was revealed that the difference was significantly influenced by epigenotype, but not genotype (**Figure 4.11C**; Genotype: *F (2,15) =2.202, P=0.145*; Epigenotype: *F (1,15) =14.972, P=0.002*; two-way ANOVA). Post-hoc analysis revealed there were no significant differences between WT, KO, or HET cortices overall (WT, 8.0% (n=6) vs. KO, 9.6% (n=3) vs. HET, 9.8% (n=5); *F (2,15) =0.598, P=0.563;* Bonferroni post-hoc). However, HET-KO cells had a significantly higher percentage of TBR1+ cells than HET-WT (HET-WT, 5.9% (n=5) vs. HET-KO, 13.8% (n=5), *P=0.002*; Bonferroni post-hoc). These differences did not cause there to be variations in TBR1+ percentage when comparing HET-WT and WT or HET-KO and KO (HET-WT, 5.9% vs. WT, 8.0%, *P=0.287*; HET-KO, 13.8% vs. KO, 9.6%, *P=0.095*; Bonferroni post-hoc).

4.2.5.2 Summary of changes in early-born neuronal number in the developing cortex

Taken together, this analysis has shown that **within** the HET cortices, there is an increased number of neurons born in HET-KO regions compared to HET-WT at E11.5 and E12.5; the time of deep layer neuron generation. These differences did not affect the overall number of neurons generated in the HET cortex and the HET-WT, and HET-KO cells did not significantly differ from cells in WT and KO cortices.

The changes in neuronal number may be due to direct or indirect neurogenesis. By using certain markers to determine which progenitors and their progeny underwent direct neurogenesis, it was possible to assess whether the proportions differed within the HET cortex.

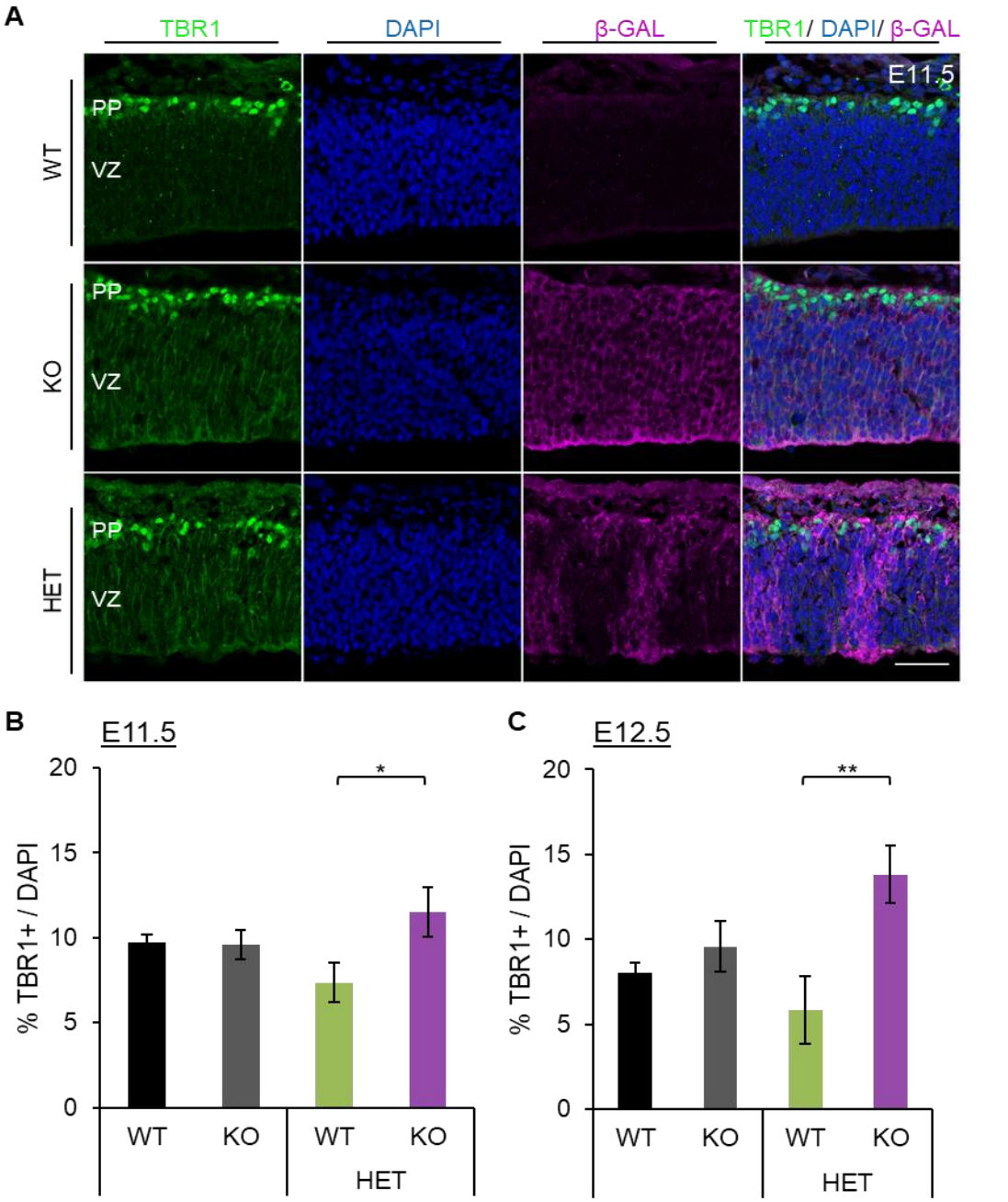

Figure 4.11: PCDH19+ and PCDH19- have a decreased and increased neuronal output within the HET cortex, respectively. (A) Representative E11.5 sections stained with TBR1 (green), β-GAL (magenta), and counterstained with DAPI (blue) in indicated genotypes. HET-WT and HET-KO cell populations refer to the β-GAL- (PCDH19+) and β-GAL+ (PCDH19-) regions of the HET brain, respectively. **(B and C)** Quantification of the total number of early-born neurons at E11.5 **(B)** and E12.5 **(C)**, calculated as the percentage of TBR1+ cells over the total cell number (DAPI+). Data represented as the mean ± SEM. WT-F, wild-type female; WT-M, wild-type male; KO, knock-out; HET, heterozygous; β-GAL, β-galactosidase; VZ, ventricular zone; PP, preplate; *, $p<0.05$; **, $p<0.01$. Scale bars: 50 µM.

4.2.6 Altered progenitor behaviour is not due to direct neurogenesis at E11.5

As neurogenesis can occur via a direct or indirect pathway (**Figure 4.12**) it was important to determine whether the alterations in neuronal output within the HET cortices came from a direct route as opposed to an indirect route. *Tis21* is an anti-proliferative, pro-neuronal gene used to distinguish progenitors whose fate is neurogenic (Iacopetti *et al.* 1999; Haubensak *et al.* 2004; Calegari *et al.* 2005). By crossing a *Tis21* GFP mouse (Iacopetti *et al.* 1999) with a *Pcdh19* HET mouse; *Pcdh19* WT, KO, and HET embryos were generated, and the *Tis21* gene was detectable in all genotypes using the GFP reporter. In combination with *Tis21* GFP, IHC was conducted, staining for β-GAL, PAX6 and counterstaining with DAPI. *Tis21* GFP labelled all neurogenic progenitors as well as newly born neurons (**Figure 4.12**; Tis21+; green cells), and neurogenic RGCs were distinguished as Tis21+PAX6+ cells (**Figure 4.12**; green and red cells).

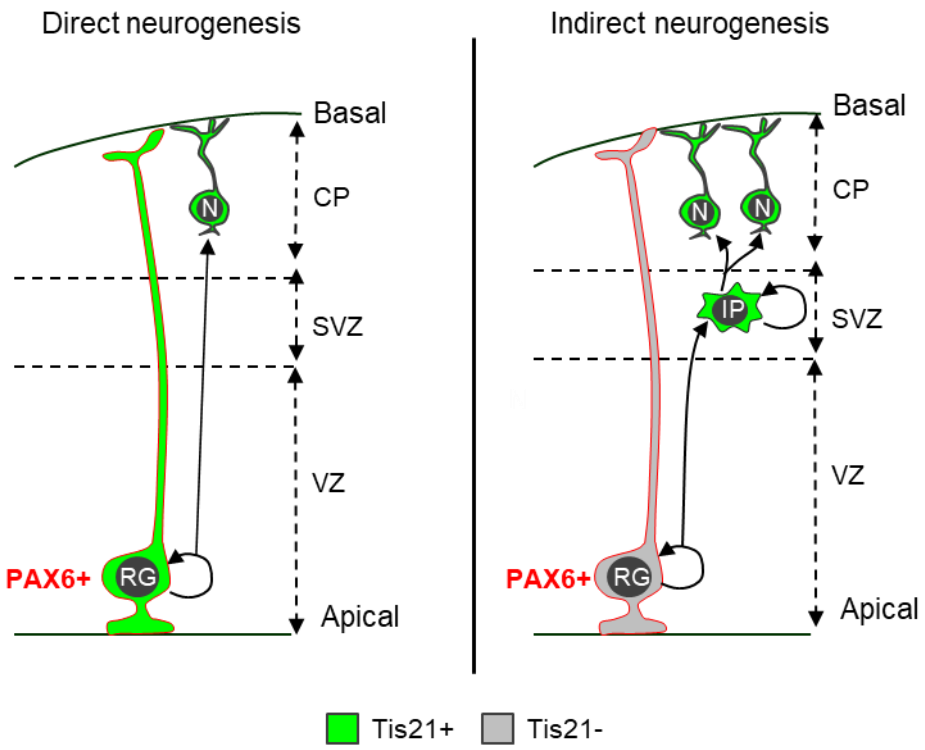

Figure 4.12: Tis21 GFP mouse line as a tool to study direct neurogenesis. Schematic representation of direct and indirect neurogenesis, with *Tis21* GFP+ (Tis21+) cells (green) and Tis21- cells (grey). Red border represents PAX6+ cells. RG, radial glial cell; N, neuron; IP, intermediate progenitor cell; VZ, ventricular zone; SVZ, subventricular zone; CP, cortical plate.

4.2.6.1 Percentage of Tis21 GFP+ cells

Tis21 GFP/*Pcdh19* WT (WT), *Tis21* GFP/*Pcdh19* KO (KO) and *Tis21* GFP/*Pcdh19* HET (HET) brains were immunostained with β-GAL and counterstained with DAPI, and coronal sections were imaged as represented in **Figure 4.13A**. A preliminary analysis was conducted at E11.5 to assess the percentage of Tis21+ cells over the total cell number (DAPI+) (Tis21+/Total DAPI+) (**Figure 4.13B**). For the within HET analysis, the percentage of Tis21+ cells in HET-WT and HET-KO cells was calculated over the total number of DAPI+ β-GAL- and DAPI+ β-GAL+ cells, respectively.

It was first concluded that gender had no impact on the fraction of Tis21+ cell expressed in WT-F and WT-M cortices, and therefore these groups were pooled together for subsequent analysis (WT-F, 7.4% (n=3) vs WT-M, 7.8% (n=3); *P= 0.782;* unpaired t-test).

By conducting a two-way ANOVA, it was determined that neither epigenotype or genotype caused a significant change in the percentage of Tis21+ cells being expressed in WT, KO, HET-WT, and HET-KO regions (**Figure 4.13B**; Genotype: *F (2,15) =0.396, P=0.680;* Epigenotype*: F (1,15) =1.856, P=0.193*; two-way ANOVA). However, within the HET cortices, there was a trend towards a significantly higher percentage of Tis21+ cells in the HET-KO regions compared to HET-WT (HET-WT, 6.8% (n=5) vs. HET-KO, 8.1% (n=5)).

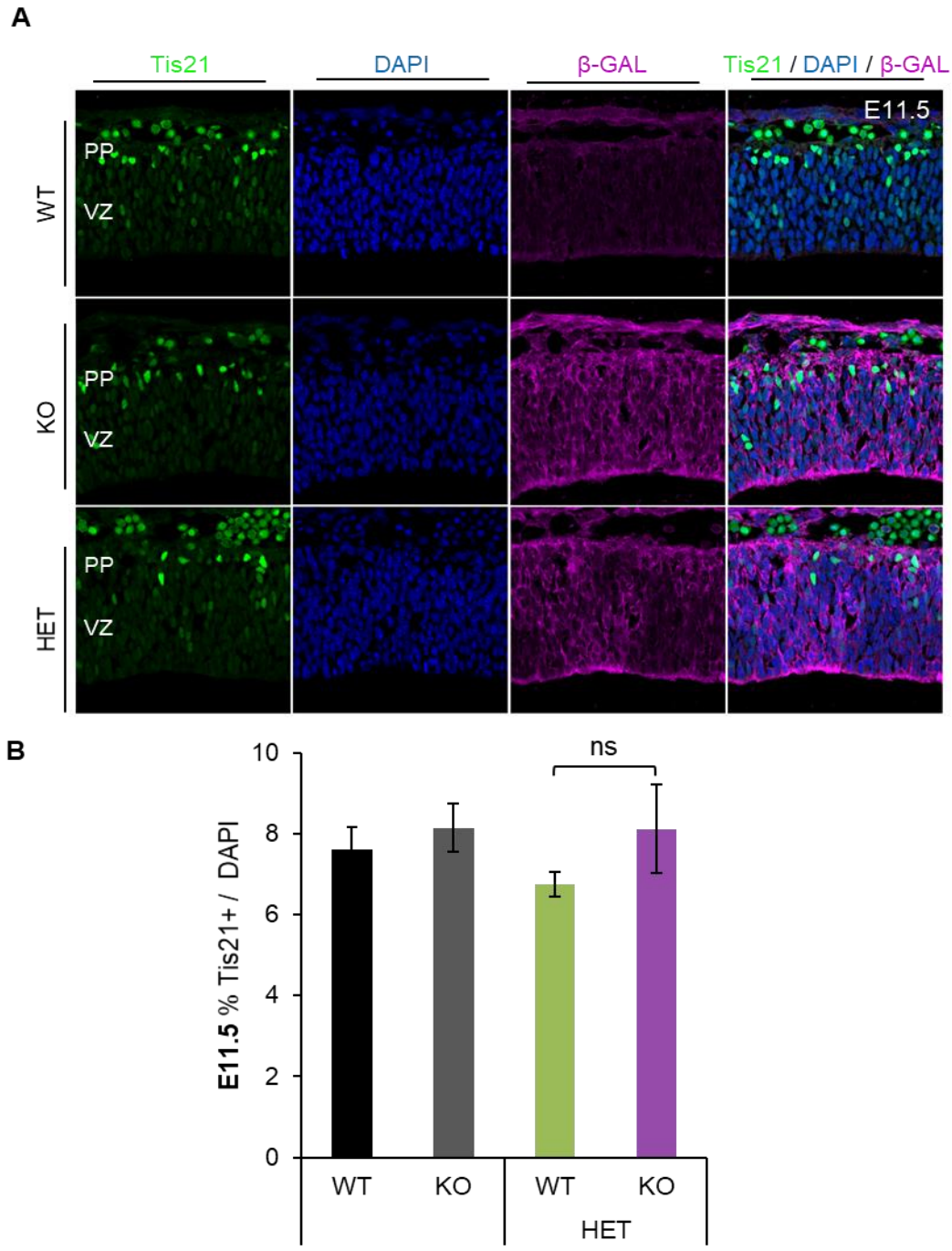

Figure 4.13: Tis21 GFP expression does not significantly change in the developing cortices at E11.5. (A) Images of E11.5 *Tis21* GFP/*Pcdh19* WT (WT), *Tis21* GFP/*Pcdh19* KO (KO) and *Tis21* GFP/*Pcdh19* HET (HET) cortices. Visualisation of *Tis21* GFP (green), combined with β-GAL (magenta), and DAPI counterstaining (blue). **(B)** Quantification of the total number of Tis21+ (green) cells over the total cell number (DAPI+). WT-F, wild-type female; WT-M, wild-type male; KO, knock-out; HET, heterozygous; β-GAL, β-galactosidase; VZ, ventricular zone; PP, preplate. Scale bar: 50 µM.

4.2.6.2 Percentage of RGCs (PAX6+)

To clarify that the genetic background of the mouse had no impact on the differential behaviour of HET-WT and HET-KO progenitors (*Tis21* GFP and C57BL6), the number of RGCs (PAX6+) over the total number of cells (DAPI+) (PAX6+/Total DAPI+) was calculated as conducted in **Section 4.2.4.1**. *Tis21* GFP/ PCDH19 WT, KO and HET cortices were immunostained against PAX6 and β-GAL (**Figure 4.14**), and counterstained with DAPI.

Firstly, gender was evaluated to ensure PAX6+ RGC percentage was not affected in WT-F and WT-M groups; however, unexpectedly there was a significant difference observed (WT-F, 83.6% (n=3) vs. WT-M, 86.8%(n=3); *P=0.026*; unpaired t-test). As the difference was not deemed significant for any other measurements using the *Tis21* GFP mouse line or when assessing PAX6+ cells in C57BL6 mice (**Section 4.2.5.1**), it is believed that this result is a false positive and it may be due to slight variations in age of the cortices analysed. Therefore, for subsequent analysis the two groups were pooled together.

Upon assessment of the fraction of cells expressing PAX6 in each group (Tis21-GFP/Pcdh19 WT (WT), Tis21-GFP/Pcdh19 KO (KO) and Tis21-GFP/Pcdh19 HET WT (HET-WT) cells and KO (HET-KO) cells), it was found that there were significant differences influenced by both genotype and epigenotype (**Figure 4.15A**; Genotype: *F (2,15) =8.425, P=0.004;* Epigenotype: *F (1,15) =35.930, P=0.000*; two-way ANOVA). Post-hoc analysis revealed that there were no differences between WT, KO and HET cortices overall (WT, 85.1% (n=6) vs. KO, 82.9% (n=3) vs. HET, 84.6% (n=5); *F (2,15) =0.469, P=0.635*; Bonferroni post-hoc). However, HET-KO cells expressed a significantly lower fraction of PAX6+ cells than HET-WT (HET-WT, 91.3% (n=5) vs. HET-KO, 77.9% (n=5); *P=0.000*; Bonferroni post-hoc), similar to that seen in the C57JI/B6 background (**Section 4.2.4.1**). Moreover, there was a significantly higher fraction of PAX6+ cells in HET-WT cells compared to WT and a significantly lower fraction of PAX6+ cells in HET-KO cells compared to KO (WT, 85.1% (n=6) vs. HET-WT, 91.3% (n=5); *P=0.006*; KO, 82.9% (n=3) vs. HET-KO, 77.9% (n=3); *P=0.050*; Bonferroni post-hoc).

Overall, there appeared to be a similar effect in both mouse lines, where HET-KO cells had a significantly lower proportion of RGCs compared to HET-WT. Although there was a greater difference using the *Tis21* GFP mouse line, this may be due to slight differences

in age or genetic background. It was concluded that the analysis using this technique was appropriate in determining whether direct neurogenesis was affected in the HET cell populations.

4.2.6.3 Percentage of neurogenic RGCs (Tis21+PAX6+)

At E11.5 the fraction of RGCs that were neurogenic (Tis21+PAX6+), hence following the direct neurogenic route, was calculated as the percentage of Tis21+PAX6+ cells over the total number of PAX6+ cells (Tis21+PAX6+/PAX6+) (**Figure 4.15B**). Therefore, within the HET cortices, the percentage of Tis21+PAX6+ cells in WT and KO cells was calculated over the total number of PAX6+β-GAL- and PAX6+β-GAL+ cells, respectively.

As previously conducted, gender of WT cortices was confirmed not to influence the number of Tis21+PAX6+ cells expressed (WT-F, 3.3% (n=3) vs. WT-M, 4.3%(n=3); *P=0.300*; unpaired t-test). Interestingly, a two-way ANOVA analysis showed no significant differences in the number of RGCs that were undergoing direct neurogenesis when comparing WT, KO, HET-WT, or HET-KO cells (**Figure 4.15B**; WT, (n=6); KO, (n=3); HET-WT, (n=5); HET-KO, (n=5); Genotype: *F (2,15) =0.483, P=0.626*; Epigenotype: *F (1,15) =0.760, P=0.397*; two-way ANOVA).

Together these results showed that PCDH19's effect on progenitor behaviour and neuronal output within the HET developing cortex at E11.5 may not be due to direct neurogenesis, but more likely to indirect neurogenesis, through IPCs.

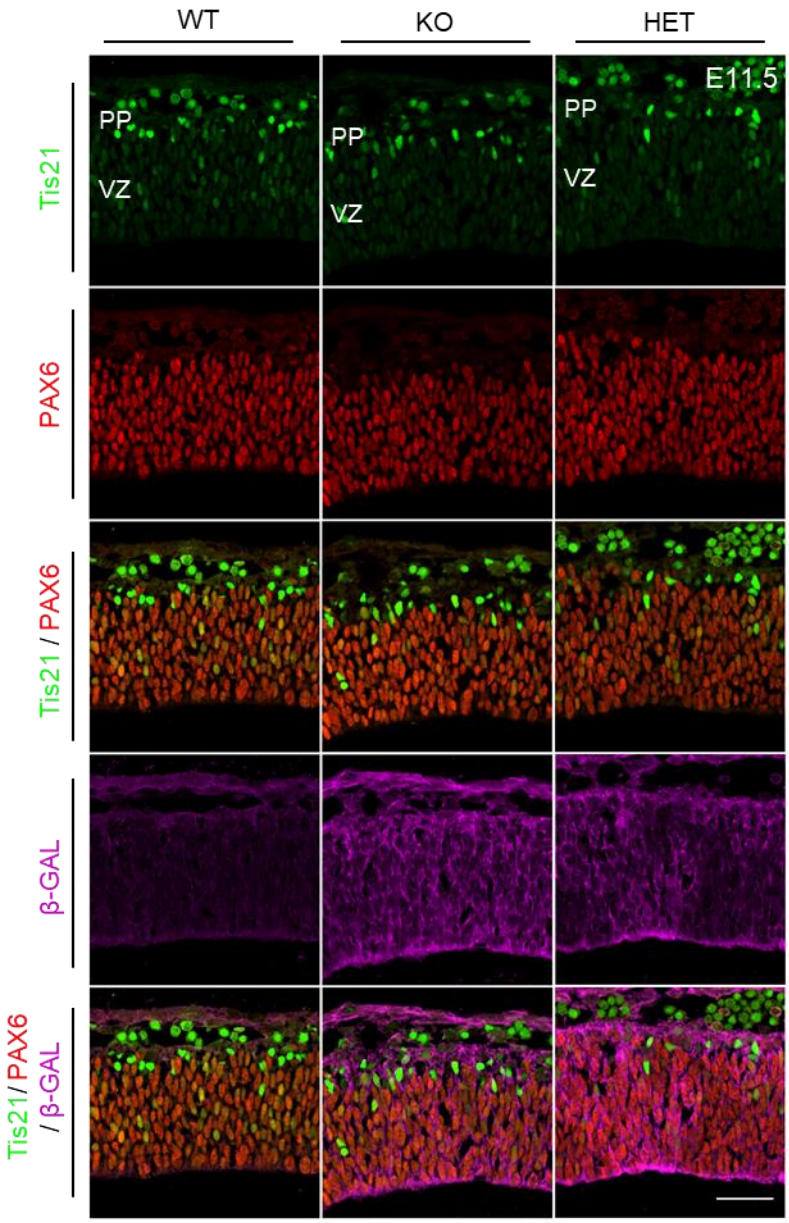

Figure 4.14: *Tis21* GFP combined with PAX6 detection to trace RGCs undergoing direct neurogenesis Images of E11.5 *Tis21* GFP/*Pcdh19* WT (WT), *Tis21* GFP/*Pcdh19* KO (KO) and *Tis21* GFP/*Pcdh19* HET (HET) cortices. Visualisation of *Tis21* GFP (green), combined with PAX6, (red) and β-GAL (magenta). β-GAL, β-galactosidase; VZ, ventricular zone; PP, preplate. Scale bar: 50 µM.

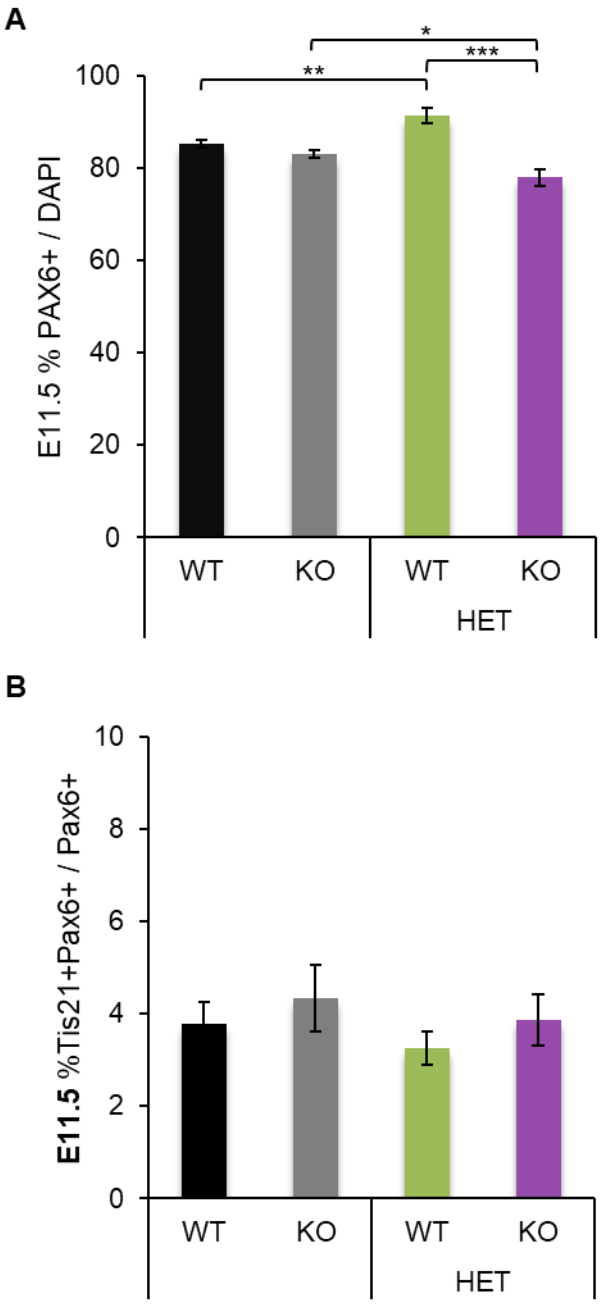

Figure 4.15: No differences in the fraction of RGCs undergoing direct neurogenesis. (A) Quantification of the total number of RGC's at E11.5, calculated as the percentage of PAX6+ cells over the total cell number (DAPI+). **(B)** Quantification of the percentage of Tis21+PAX6+ progenitors over the total number of PAX6+ progenitors. PCDH19- and PCDH19+ cell populations refer to the β-GAL+ and β-GAL- regions of the HET brain, respectively. WT-F, wild-type female; WT-M, wild-type male; KO, knock-out; HET, heterozygous; *, p<0.1; **, p<0.01, *** p<0.001. Data are represented as mean ± SEM.

4.2.7 PCDH19 has no effect on cortical width in KO or HET developing cortices.

As the HET brain had no overall differences in progenitor or neuronal cell number (asides from a difference in the fraction of IPCs at E11.5) it is unlikely that the cortical structure is altered at these ages. To confirm that there was no overall impact on the developing cortical structure, the cortical width was measured in WT, KO and HET brains at E11.5 and E12.5. A one-way ANOVA was used to compare the effect of genotype on the cortical width at E11.5 and E12.5. It was revealed that there was no significant effect of genotype on cortical width in WT, KO and HET cortices at either E11.5 or E12.5 (**Figure 4.16**; E11.5; WT, 137.2 (n=8); KO, 137.8 (n=4); HET, 132.4 (n=6); *F (2,15) = 0.474, P=0.631;* E12.5, WT, 174.2 (n=9); KO, 177.7 (n=5); HET, 179.4 (n=5); *F (2,16) =0.491, P=0.621*; one-way ANOVA). Therefore, it was concluded that PCDH19 does not affect the cortical width in early neurogenesis.

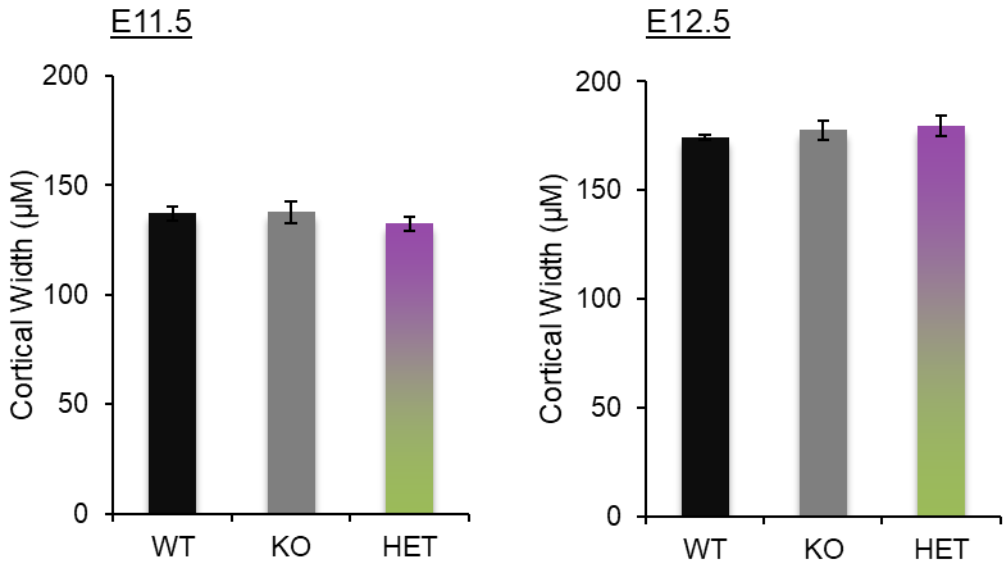

Figure 4.16: No overall differences are seen in early developing PCDH19 WT, KO, or HET cortices. Quantification of the average cortical width in WT, KO and HET cortices at E11.5 and E12.5. Data represented as the mean ± SEM. WT, wild-type; KO, knock-out; HET, heterozygous, µM, micrometer.

4.3 Discussion

In this chapter and recent publications, a remarkable cell sorting arrangement of PCDH19 expressing and non-expressing cells has been discovered within the developing *Pcdh19* HET mouse cortex (Pederick *et al.* 2016; Hayashi *et al.* 2017; Pederick *et al.* 2018). Furthermore, with the use of a commercial *Pcdh19* KO reporter mouse line it has been determined that PCDH19 plays a role in cortical neurogenesis; regulating progenitor fate within heterozygous animals that have co-existing PCDH19+ and PCDH19- cells. No differences were found in cell cycle parameters or neuronal output when analysing PCDH19+ and PCDH19- progenitors in WT and KO cortices, respectively. However, a striking difference was seen between the two cell populations **within** the HET cortices. PCDH19- cells within the HET cortex proliferated more, had an increased fraction of IPCs at the expense of RGCs, and greater neuronal output. Remarkably, PCDH19+ progenitors behaved oppositely. These alterations in cell behaviour meant that progenitor cell number, neuronal cell number, and cortical width was similar in WT, KO and HET cortices overall. Despite the lack of differences when considering the cortex as a whole, the differential neurogenic behaviour of progenitor cells suggests putative alterations in the proportion of WT and KO neuronal progeny generated over time. A higher proportion of KO neurons in deep layers and WT neurons in upper layers could lead to alterations in connectivity in the postnatal period. The mechanism behind this interesting finding remains to be discovered; however, a preliminary assessment of the direct and indirect modes of neurogenesis revealed that altered neuronal output within the developing HET cortex may not stem from direct neurogenesis.

4.3.1 PCDH19 is involved in cell sorting during early cortical development

As previously described by Pederick *et al.*, the β-gal/neomycin cassette in the *Pcdh19* KO mouse provides a reporter allele for cells that would normally express PCDH19 (Pederick *et al.* 2016; Pederick *et al.* 2018). In the HET brains, generated from the KO mouse, a mosaic pattern of PCDH19+ and PCDH19- cells was seen, with striking segregation and columnar organisation. Each HET brain had a different pattern given that *Pcdh19* undergoes random X chromosome inactivation (XCI) (Dibbens et al. 2008). It is believed that the cellular environment and random XCI mosaicism leads to EIEE9 (Dibbens *et al.* 2008; Pederick *et al.* 2018). Due to XCI mosaicism, distinctive and unique

cell-type and region-specific segregation of the two cell populations have been shown throughout the CNS, including spatial heterogeneity in the cerebral cortex (Wu *et al.* 2014). Additionally, reports showing inactivation of an X-linked lacZ transgene revealed striking columnar organization (Tan *et al.* 1995), similar to what was seen in the *Pcdh19* HET cortices. Therefore, it was possible that the initial differences due to random XCI would be magnified by subsequent clonal expansion of the progenitors, leading to the unusual cell sorting. However, when mating *Pcdh19* WT and KO mice with a mouse carrying an X-linked GFP expressing transgene (X-GFP), it was clear that the sparse segregation due to random XCI in the WT was different to that seen in the X-GFP/ *Pcdh19* HET, and segregation of WT and KO progenitors and their descendants was clearly defined in the HET brain. Pederick *et al.* also confirmed this finding by comparing *Pcdh19* HA-FLAG/KO (HET) brains with *Pcdh19* HA-FLAG/WT (Pederick *et al.* 2018). Additionally, it was found that the abnormal cell sorting correlated with altered network activity. By deleting PCDH19 completely from the HET mouse, abnormal cell sorting was abolished, and normal network activity was restored (Pederick *et al.* 2018). This supports the notion that PCDH19 is playing a role in the abnormal cell sorting behaviour and indicates that the pathogenesis seen in EIEE9 could stem from this cell sorting during early cortical development.

N-cadherin is highly expressed in RGC adherens junctions and is vital in the maintenance of the strong adhesion between progenitor cells. It is known that PCDH19 forms a strong complex in cis with N-cadherin and that this PCDH19-N-cadherin complex exclusively binds with the same complex in trans, and not PCDH19 or N-cadherin alone (Emond *et al.* 2011). It is hypothesised that within the HET cortex where there is a mixture of PCDH19+ and PCDH19- cells, alterations in binding affinities at the adherens junctions could be the cause of progenitor cell segregation. PCDH17 has also been shown to form a similar complex with N-cadherin. However, that complex cannot bind to a PCDH19-N-cadherin complex in trans (Emond *et al.* 2011), so even if PCDH17 was to compensate in the PCDH19 KO cells, the adhesive imbalance would not be repaired in the HET animals. As it is not known whether PCDH17 is expressed in RGCs, this would be an important experiment to prove that PCDH19 is compensated for in this manner. In conclusion, it is possible that a mosaic absence of PCDH19 could be disruptive in the HET brain, even if compensated by a different protocadherin, causing the abnormal

formation of segregated progenitor cell populations due to incompatible adhesion affinities.

Furthermore, it has been shown that N-cadherin regulates neuronal progenitor self-renewal and the switch from proliferating to neurogenic divisions (Miyamoto *et al.* 2015). Interestingly, downregulation of N-cadherin has been reported to cause the detachment of apical processes (Rousso *et al.* 2012), while N-cadherin knock-out cortical progenitors undergo premature neurogenesis (Zhang *et al.* 2010; Miyamoto *et al.* 2015). Therefore, alterations in adhesiveness of N-cadherin due to changes in PCDH19 mosaicism could influence the neurogenic properties of the progenitor cells.

There are assays that could be used to further study PCDH19-mediated cell sorting behaviour. For example, a so-called “fish-ball” assay where injected mRNAs encoding for certain receptors and their ligands have been previously used in zebrafish embryos to visualise whether bi-directional signalling is necessary for cell segregation (Mellitzer *et al.* 1999). In the case of PCDH19, it would be interesting to study cell sorting using this method with injected RNA encoding for PCDH19, N-cadherin, other protocadherins such as PCDH17, as well as truncated versions of each. Alternatively, using a similar approach but with HEK293 cells selectively expressing these cadherins and mutant forms, cell segregation assays could be performed where cell clusters and boundary sharpness could be measured to understand what mechanism regulates the aberrant cell behaviour as previously conducted (Taylor *et al.* 2017).

4.3.2 PCDH19 mosaicism affects cell proliferation and neuronal output by altering progenitor behaviour

The cell cycle is linked to progenitor cell fate in the developing brain and defects in the cell cycle can lead to changes in progenitor behaviour and neuron production (Vernon *et al.* 2003; Arai *et al.* 2011). Certain cell cycle parameters were investigated to determine whether PCDH19 affects mitotic cell number, S-phase or cell cycle exit and ultimately alters cell fate. In WT, KO, and HET cortices overall, there were no differences in the number of progenitors that were in mitosis, in S-phase or leaving the cell cycle. Remarkably, PCDH19+ and PCDH19- cells behaved differently **within** the HET cortex, deviating from WT and KO brains, respectively. More PCDH19- cells were undergoing mitosis, and leaving the cell cycle than PCDH19+ cells, indicating that PCDH19- cells were proliferating faster and driving towards a neurogenic fate. Furthermore, at the

expense of RGCs, there was an increase in the fraction of IPCs and early-born neurons in the PCDH19- cells when compared to the PCDH19+ cells in the HET cortex. In support of this result, Fujitani *et al*. demonstrated that *Pcdh19* inhibition by shRNA knockdown caused an increase in the transition of RGCs to IPCs (Fujitani *et al.* 2017). Homan *et al.* also demonstrated in human induced pluripotent stem cell (hiPSC)-derived neurons, that PCDH19 inhibition increased neurogenesis, with evidence of reduced apical-basal polarity in the progenitor cells *in vitro* (Homan *et al.* 2018).

One of the important findings to highlight is that both PCDH19+ and PCDH19- cells significantly alter their behaviour within the HET environment, but these changes cause no overall differences in cell cycle parameters and neuronal output. Therefore, cell-cell communication must be an integral factor that regulates these differential responses that seem to balance each other out. There are two possible reasons for the differential behaviour between WT and KO progenitors within the same environment: (1) direct communication of the two progenitor populations may cause these changes and (2) WT and KO cells may respond differently to external signals due to alterations in their cellular characteristics.

There are factors known to be implicated in the switch between symmetric and asymmetric divisions and that could contribute to the differential behaviour. These include; (1) mitotic spindle orientation/asymmetry and cleavage plane positioning, (2) inherited fate determinant factors and (3) signalling pathways. As described above, it is hypothesised that incompatible binding affinities at RGC adherens junctions may partly cause the cell segregation within the HET cortex. This effect on adherens junctions and on N-cadherin's adhesive properties could in turn lead to changes in cleavage plane orientation, changing the distribution of fate determinant genes and/or the activation/downregulation of certain signalling pathways in the two daughter cells, ultimately leading to altered neurogenic behaviour. If the cellular characteristics are altered immunohistochemical approaches could be taken to assess the differences between PCDH19+ and PCDH19- cells. For example, N-cadherin and Prominin could be detected to analyse both apical domain size and changes in distribution of N-cadherin, while combining N-cadherin and Anillin could be used to assess spindle orientation (Kosodo *et al.* 2004). If an external signal is causing the differentially neurogenic behaviours, there are some signalling pathways that could be considered to cause altered effects in each progenitor cell population. Interestingly, N-cadherin and Slit-Robo

signalling have been found to regulate apical process retraction in developing retinal ganglion cells (Wong *et al.* 2012). Furthermore, the Notch ligand Delta-like1 (DII1) localises at adherens junctions in apical endfeet of progenitors and early born neurons, and N-cadherin is required for active Notch signalling (Hatakeyama *et al.* 2014). A very recent study has shown that low levels of Robo and high levels of DII1 are favoured for indirect neurogenesis while high Robo and low DII1 drive direct neurogenesis (Cárdenas *et al.* 2018). As it has been shown that the increased neurogenesis in PCDH19- cells of the HET cortex may not come directly from neurogenic RGCs, it is possible that PCDH19- cells have an increased neuronal output through indirect neurogenesis. Therefore, PCDH19- cells could be subject to low Robo signalling. Another candidate pathway that may be differentially signalling in the presence and absence of PCDH19 could be FGF signalling, as a communication to the 2017 Cortical Development Conference described an interaction between PCDH19 and FGF2. Single-cell RNA sequencing could be conducted as an unbiased approach to study differential molecular pathways in the different cell-types and cell populations. X-GFP/PCDH19 HET cortices (**Section 4.2.2.3**) could be used and RNA could be extracted for subsequent RNA sequencing. Using the GFP reporter that is found in all of the PCDH19+ cells, FACS sorting could separate the KO and WT cell populations and the identification of *Pax6*, *Tbr2*, and *Tbr1* would allow for the separate analysis of RGCs, IPCs, and neurons, respectively.

It is also important to consider the cell cycle length, as neurogenesis changes with time. Early progenitor cell expansion is followed by gradual loss of proliferative capacity and increased commitment to neuron production (Arai *et al.* 2011), with an increased proportion of RGCs dividing to produce IPCs (Haubensak *et al.* 2004). It is known that asymmetric divisions have longer cell-cycle durations than symmetric divisions (Calegari and Huttner 2003) and G_1 lengthening is associated with the transition of stem cell progenitors to IPCs (Arai *et al.* 2011). Conversely, a reduction in G_1 lengthening promotes the proliferation of progenitor cells and causes a transient delay in neurogenesis (Pilaz *et al.* 2009). Surprisingly, proliferating progenitor cells also have a longer S-phase than those that are committed to neuron production (Arai et al. 2011). If PCDH19 is involved in the transition from symmetric to asymmetric divisions in RGCs, it could be doing so by affecting cell cycle length. It would be interesting to look at total cell cycle, G_1, and S phase length to see whether PCDH19- cells within the HET have a

longer total cell cycle length, longer G_1 and shorter S-phase than PCDH19+ cells. Total cell cycle length could be calculated using double injections of birth dating markers such as EdU and BrdU which would allow for the identification of progenitors entering and leaving the cell cycle, as well as the S-phase length (Martynoga *et al.* 2005). Alternatively, to calculate the length of all cell cycle phases, cumulative labelling (EdU labelling index) in combination with immunostaining to detect mitotic cells could be used as described by (Arai *et al.* 2011).

No differences have previously been reported in the cortical thickness of KO or HET adult brains (Pederick *et al.* 2016) and in this chapter is has been shown that there are no differences in the cortical thickness at E11.5 or E12.5. Therefore, changes in neurogenic behaviour within the HET cortex do not increase overall neuron number and the difference in the number of progenitors and neurons may cancel each other out later in development. Firstly, this highlights the necessity in continuing the analysis conducted so far at later ages to determine whether the effects seen change over time. Secondly, as projection neurons are born sequentially (layer VI neurons at approximately E11, up to layer II neurons at E15 onwards), there could be cortical lamination defects in the HET cortices at post-natal ages. By using cortical cell markers to distinguish the different layers, work from the Martinez-Garay laboratory has found that there are no differences in the overall number of deep and superficial layer neurons in WT, KO and HET cortices at post-natal ages. However, PCDH19- progenitors within the HET cortex could be contributing more to deep layer neurons (VI and V) than to superficial neurons (layers IV, II and III). This could also mean that the layers that express PCDH19 in the mature cortex (Va and II) could have an unequal distribution of PCDH19 expressing and non-expressing cells. These alterations in distribution could therefore influence synapse formation and connectivity within the HET cortices. As mentioned above, alterations in network activity have already been recorded in Pcdh19 HET mice (Pederick *et al.* 2018), however, whether these changes are due to the differential contribution of progenitor cell progeny and subsequent alteration in connections, remains unknown. This could be studied by combining the use of the X-GFP/ PCDH19 HET mouse and cortical-layer markers to determine whether post-natal neurons stem from PCDH19+ or PCDH19- progenitor progeny. Additionally, electrophysiological recordings of X-GFP/ PCDH19 HET adult brain slices could shed light on whether connectivity is altered in PCDH19 expressing and non-expressing neuronal progeny.

4.3.3 PCDH19 mosaicism may not affect neuronal output by direct neurogenesis

During early cortical development, a proportion of neurons are produced through direct neurogenesis, from neuroepithelial cells and RGCs, but the majority are derived from indirect neurogenesis, through the symmetric self-consuming divisions of IPCs (Noctor *et al.* 2001; Haubensak *et al.* 2004; Noctor *et al.* 2004). To begin to elucidate the mechanism behind the differential neurogenic behaviour of PCDH19- and PCDH19+ progenitor cells within the HET cortex, the proportion of RGCs undergoing direct neurogenesis was assessed. By using the anti-proliferative gene, *Tis21*, progenitors that had switched from a symmetric proliferative division to neurogenic division could be detected (Iacopetti *et al.* 1999; Haubensak *et al.* 2004; Attardo *et al.* 2008). It was observed that the increased proliferation and neuronal output found within the PCDH19- cells in the HET did not come from direct neurogenesis at E11.5. This indicates that alterations in neuronal output may largely be due to IPCs undergoing symmetric consumptive divisions. Additionally, changes in neuronal output at E11 could come from progenitor alterations earlier in development, highlighting the need to assess cell cycle parameters and cell numbers at E10.5. As there has been an increase in the number of IPC's in PCDH19- regions of the HET cortex, it would not be so surprising that the neuronal output is affected due to neurogenic IPC's. However, to monitor whether this change in neuronal output is compensated for or amplified later in neurogenesis it is important to validate this finding at later and early embryonic ages.

4.3.4 Concluding remarks

This unusual phenomenon where the two progenitors alter their behaviour depending on their cellular environment is unlike any in the literature so far. It is important to note that, even though there is an altered behaviour in the PCDH19 expressing and non-expressing populations within the HET, the HET brain taken as a whole shows no differences when compared to the WT and KO brains. With a preliminary assessment indicating that direct neurogenesis is not affected by PCDH19, further experiments looking at indirect neurogenesis and certain cell intrinsic and extrinsic factors will help decipher the mechanism controlling this altered behaviour. Additionally, the X-GFP line could provide an interesting tool to determine whether PCDH19- and PCDH19+ progenitor progeny contributes to certain neuronal subtypes in certain cortical layers and whether an unequal distribution or number of these cell types in a given layer and cell population could potentially play a role in the pathogenesis in humans.

Chapter 5: Establishing an *in vitro* system to study PCDH19

5.1 Introduction

As individuals with Early Infantile Epileptic Encephalopathy 9 (EIEE9) have a mosaic expression of PCDH19, Dibbens *et al.* hypothesised that the disorder may be caused by a phenomenon called "cellular interference", stating that coexistence of PCDH19 expressing and non-expressing neurons result in cell-cell communication disruption that leads to the distinctive epileptic phenotype in EIEE9. It has been shown that PCDH19 is highly expressed in cortical neurons during the time of synaptogenesis (Fujitani *et al.* 2017), however the theory of cellular interference is yet to be proven. Therefore, an experimental approach to study cortical neurons is necessary to demonstrate that synapses and communication could be altered in a PCDH19 mosaic environment.

Protocols have been developed to differentiate mouse embryonic stem cells (ESCs) into "cortical-like" neurons *in vitro* (Bibel *et al.* 2004; Gaspard *et al.* 2009; Alsanie *et al.* 2017; Gazina *et al.* 2018). As primary culture is limited by cell number and cellular heterogeneity, these ESC-based protocols offer the advantage of generating a homogenous population of mainly glutamatergic "cortical-like" neurons that have a defined phenotype and synchronous development. These protocols allow for the study of cell-specific gene functions using biochemical and physiological approaches. As detailed in Chapter 2 Material and Methods, and described in Chapter 3, a *Pcdh19* KO mouse model has been generated and used previously in some *in vivo* and *ex vivo* studies (Pederick *et al.* 2016; Hayashi *et al.* 2017; Pederick *et al.* 2018). It is possible to derive ESCs from the inner cell mass of the *Pcdh19* KO blastocysts for subsequent expansion and differentiation into "cortical-like" neurons using a method previously established (Bibel *et al.* 2004). This particular ESC-based method is unique due to its generation of mainly excitatory neurons. In addition, the progenitor cells generated using this protocol have been characterised as being PAX6+, and relatively similar to the endogenous PAX6+ RGCs found in the primary cortex (Bibel *et al.* 2004; Gotz and Barde 2005). This method provides a relevant *in vitro* model that could be manipulated to study PCDH19's function in a knock-out (KO) and mosaic environment.

5.1.1 Aims

Before considering the functionality of PCDH19 or the theory of cellular interference, it was important to first establish a suitable *in vitro* system. Hence, the first aim of this chapter was to use the *in vitro* technique described by Bibel *et al*. to generate “cortical-like” neurons from a well-established wild-type (WT) cell line. The expression of PCDH19 then needed to be confirmed in these neurons to ensure the culture system was appropriate for further experiments. If the cultures expressed PCDH19, the second aim was to derive *Pcdh19* KO ESCs directly from the *Pcdh19* KO mice and to determine whether it was possible to differentiate these cells into “cortical-like” neurons. If so, the final aim of this chapter was to conduct an initial comparison of WT and *Pcdh19* KO ESC-derived neurons using immunohistochemical and quantitative real-time polymerase chain reaction (qRT-PCR) approaches.

5.2 Results

5.2.1 Generating mouse ESC-derived neurons

To ensure the feasibility of generating ESC-derived “cortical-like” neurons, a WT ESC line expressing green fluorescent protein (GFP) from the *Mapt (tau)* locus (Tau-GFP (WT)) (Tucker *et al.* 2001; Bibel *et al.* 2004) was differentiated using the procedure described briefly in **Figure 5.1** and in Chapter 2 **Section 2.8**. Upon plating of the ESC’s on to mouse embryonic fibroblasts (MEFs), oval, shiny colonies with clear boundaries were formed (**Figure 5.1A**). These ESC’s divided and proliferated effectively over 5-6 passages. Once the ESC’s were rapidly dividing, they were deprived of MEFs and split on to gelatin-coated dishes. After two passages on gelatin, cells started to flatten, showing single cells with a uniform morphology (**Figure 5.1B**). Cellular aggregates were then formed by passaging ESCs on non-adherent dishes (**Figure 5.1C**). ESCs were able to form aggregates effectively, and after 4 days of aggregating, neural induction was initiated using retinoic acid. After a further 4 days, aggregates were dissociated, and cells acquired spindle-shaped morphology 2 hours after plating (**Figure 5.1D**). Once plated, cells sprouted processes that started to form intricate neurite networks (**Figure 5.1E**). These progenitors were allowed to grow and mature into neurons up until day *in vitro* (DIV)20.

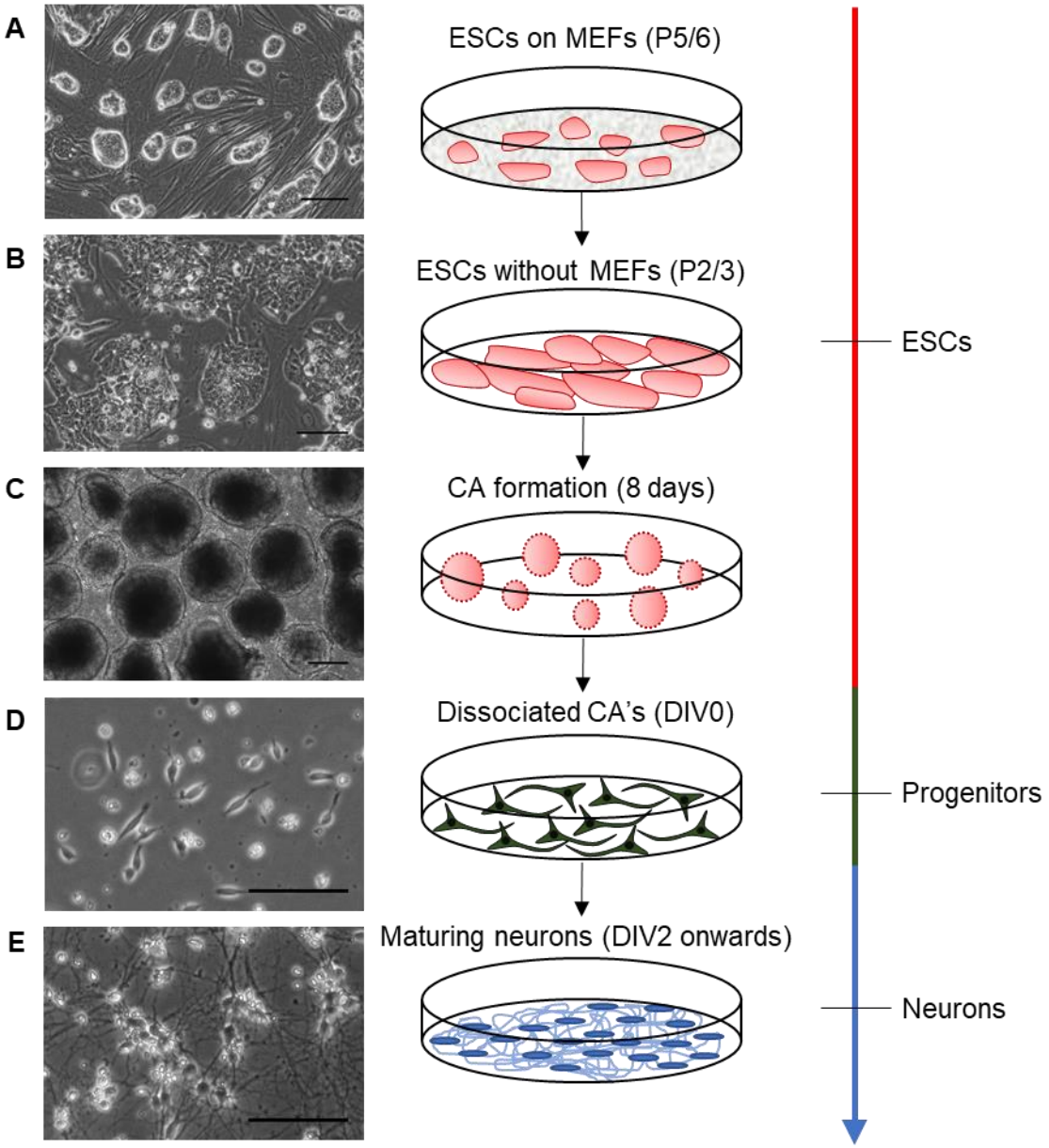

Figure 5.1: Differentiation of ESCs into "cortical-like" neurons. Schematic representation of the differentiation protocol adapted from (Bibel *et al.* 2004). **(A)** Colonies of ESC's plated on MEFs. **(B)** ESC's deprived of MEFs on gelatin-coated dishes. **(C)** Formation of cellular aggregates at CA6, two days after the addition of retinoic acid. **(D)** Neuronal progenitors 2 hours after plating dissociated aggregates. **(E)** Neurons 8 days after plating dissociated aggregates. ESC, embryonic stem cell; MEF, mouse embryonic fibroblast; P, passage number; CA, cellular aggregates, DIV, days in vitro. Scale bars: (A, B, D, E) 100 µM; (C) 200 µM.

5.2.2 Expression of PCDH19 in mouse ESC-derived neurons

Given that the main aim of this chapter was to establish a system to study PCDH19 in cortical neurons, it was essential to determine if PCDH19 was expressed in mouse ESC-derived neurons using the protocol described above. To ensure *Pcdh19* RNA and PCDH19 protein were detectable, WT neural progenitors were plated at a high density. RNA and protein were extracted from the WT ESC-derived neurons at different time points. Endogenous *Pcdh19* mRNA and PCDH19 protein were detected via qRT-PCR and Western blot, respectively (**Figure 5.2A and B**).

RNA was reverse transcribed, and 60 ng of cDNA was used for qRT-PCR analysis using the ΔCt method described in Chapter 2 **Section 2.13.2**. There was a consistent increase in the level of *Pcdh19* mRNA expressed (relative to β-actin) from neural progenitors at the day of plating (DIV0) up until DIV16 (**Figure 5.2A**). Furthermore, extracted protein from WT progenitors (DIV2) and neurons (DIV12) was quantified and 40 µg of protein was used to detect PCDH19 by Western blot (**Figure 5.2B**). PCDH19 was detectable at 110 kDa in both neural progenitors and neurons. Histone H3 (HH3), a histone protein ubiquitously expressed in eukaryotic cells, was used as a loading control and was also detectable in neural progenitors and neurons at about 15 kDa.

As WT ESC-derived neurons were successfully generated and expressed PCDH19, it was concluded that if *Pcdh19* KO ESC-derived neurons could also be generated using this protocol, then it would be used for subsequent experiments.

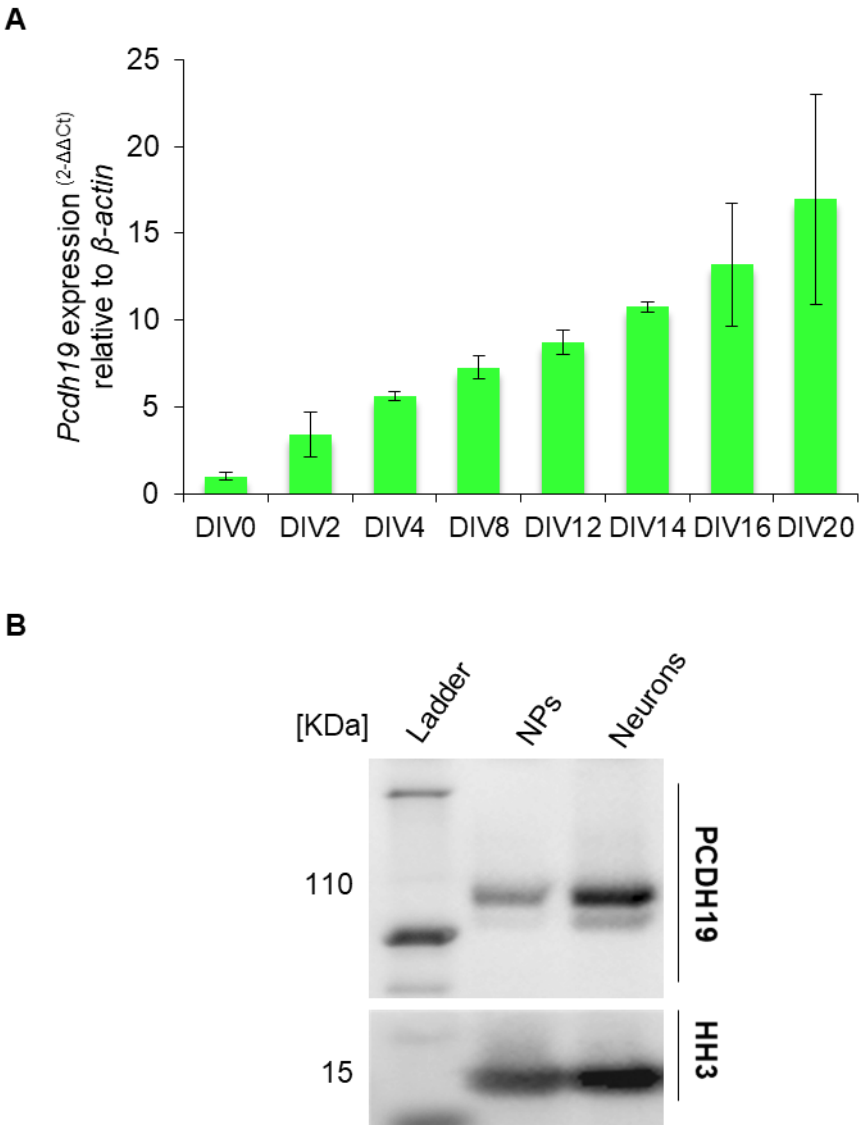

Figure 5.2: Endogenous *Pcdh19* mRNA and PCDH19 protein can be detected in mouse WT ESC-derived neurons. (A) qRT-PCR quantification of the levels of *Pcdh19* normalised to β-actin, calculated as the $2^{-\Delta\Delta Ct}$ at different days *in vitro* **(B)** Western blot to detect PCDH19 at 110 kDa and histone H3 at approximately 15 kDa as a loading control in NP's (DIV2) and neurons (DIV12). Data represented as the mean ± standard error of the mean. DIV, day *in vitro*; NPs, neuronal progenitors; HH3, histone H3; kDa, kilodaltons.

5.2.3 Successful derivation of a mouse ESC line from a Pcdh19 KO mouse model

To assess the function of *Pcdh19* in ESC-derived neurons, a cell line needed to be generated that lacked *Pcdh19*. Therefore, the *Pcdh19* KO mouse model was utilised, and *Pcdh19* KO ESCs were harvested. In brief, *Pcdh19* KO mice were bred, and female mice sacrificed after four days to harvest blastocysts. From four pregnant female mice, a total of 30 blastocysts were isolated and left to grow in serum-free medium (**Figure 5.3A**). Once the *zona pellucidae* had hatched, epiblasts were separated from the trophectoderm and cultured in 96-well plates until they were ready for expansion (**Figure 5.3A**). The remaining trophectoderm was lysed, and DNA was extracted from four lysates that stemmed from rapidly growing ESCs. DNA lysate was used in polymerase chain reaction (PCR) experiments, to confirm the gender and genotype of the ESCs. As X-inactivation cannot be mimicked *in vitro* using this protocol and XX (female) mouse ESCs do not survive and cannot be propagated efficiently (Barakat and Gribnau 2010), XY (male) ESCs were selected for further experiments. Sex determination genotyping was conducted via PCR as described in Chapter 2 **Section 2.3.2.2**, using gel electrophoresis and ethidium bromide to detect amplicons specific to the X and Y chromosome (**Figure 5.3B**). Bands were detectable in all 4 samples selected. ESC lines 1, 2 and 4 were considered XY, as the *Jarid1d* (X) 331 bp band and *Jarid1d* (Y) 302 bp band was detectable, and ESC line 3 was considered XX as only a *Jarid1d* (X) 331 bp band was detectable. Following on from XY selection, ESC lines 2 and 4 were tested to validate the *Pcdh19* KO genotype, conducting a WT-allele specific and mutant-allele specific PCR as described in Chapter 2 **Section 2.3.2.1** (**Figure 5.3C**). It was confirmed that a mutant amplicon was present in both cell lines at 437 bp. No band was expected to be seen using the WT-allele specific PCR; however, a faint band was present at 123 bp when detecting the WT amplicon in ESC line 2, but not in ESC line 4. The reason for this WT-specific band being present in ESC line 2 remains unknown; however, a possible explanation could be contamination of this sample. As ESC line 4 was male (XY) and had the *Pcdh19* KO genotype it was further cultured and expanded for storage in liquid nitrogen.

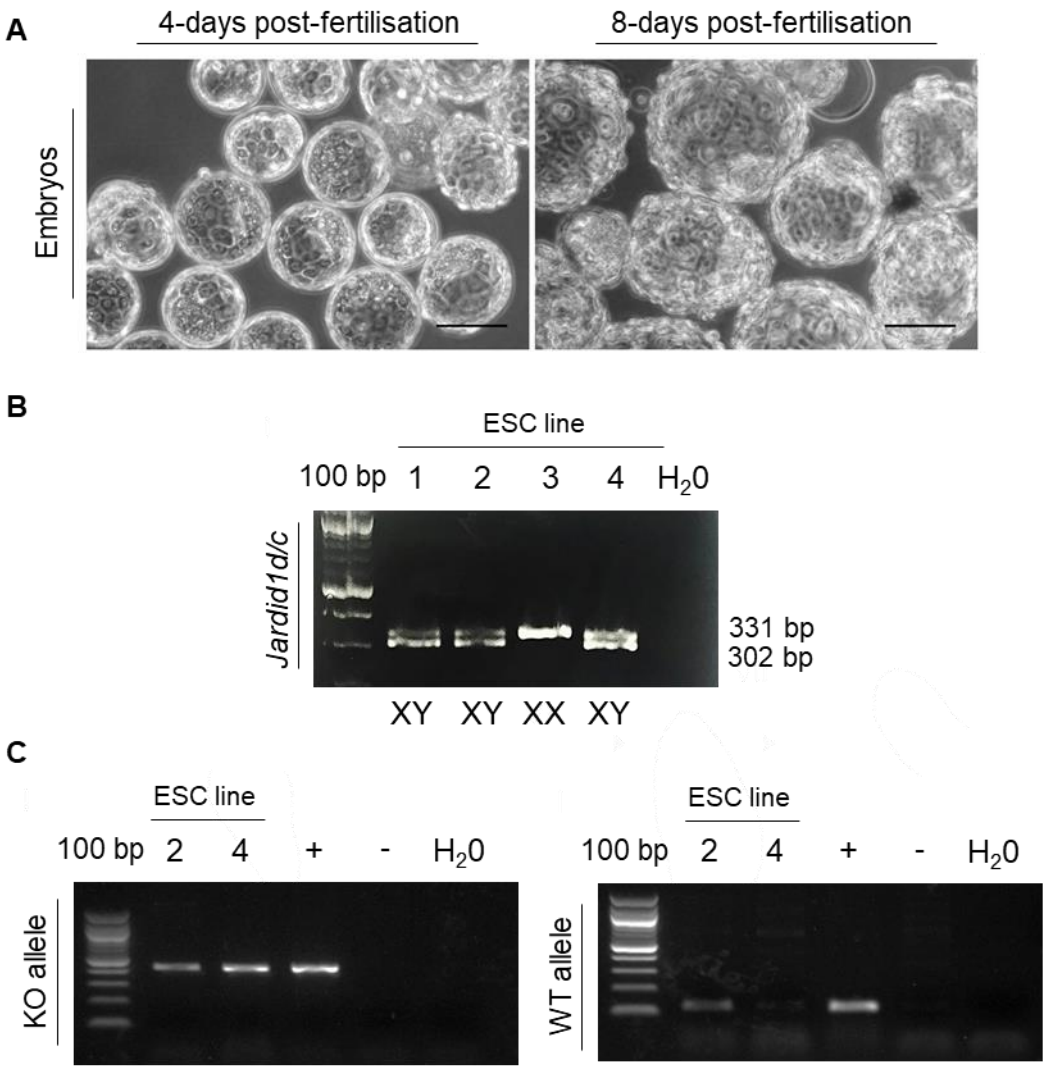

Figure 5.3: Successful derivation of *Pcdh19* KO ESCs. (A) Embryos flushed from oviduct 4 days post-fertilisation (left panel). Embryo outgrowth in serum-free media (right panel). **(B)** Sex determination PCR amplicons from ESC line 1 - 4, detecting 331 bp and 302 bp amplicons specific to the X and Y chromosome, respectively. WT-specific and mutant-specific PCR from ESC line 2 and 4, detecting 123 bp and 437 bp amplicons, respectively. All PCR amplicons were separated by gel electrophoresis on a 1.5% agarose gel and visualised with ethidium bromide. Distilled water was used as a negative control. ESC, embryonic stem cell; Bp, base pair; H_20, distilled water. Scale bars: (left panel) 200 µM; (right panel) 100 µM.

5.2.4 Differentiation of Pcdh19 KO ESC-derived neurons

To determine whether *Pcdh19* KO ESC line 4 could differentiate into neurons the protocol described by Bibel *et al.* was followed as previously conducted with WT ESCs in **Section 5.2.1**. ESCs were passaged on MEFs 5 to 6 times and were found to be rapidly dividing and formed defined colonies (**Figure 5.4A**). Next, ESCs were deprived of MEFs and continued to grow on gelatin-coated dishes for another 2 to 3 passages and formed flat uniform colonies (**Figure 5.4B**). ESCs were split and visible aggregates formed after 24 hours (**Figure 5.4C**). Neural induction was initiated at aggregate day 4. By day 8 dense cellular aggregates formed with clearly defined boundaries (**Figure 5.4D**). Aggregates were dissociated successfully, and neural progenitors (NPs) were plated, forming bipolar spindle-like cells 2 hours after plating (**Figure 5.4E**). Progenitors were cultured over 20 days *in vitro* and were able to develop into neurons with extensive neurite connections that were visible at DIV6 (**Figure 5.4F**). At DIV20, multi-polar cell bodies with extensive processes formed intricate connections (**Figure 5.4G**).

To further confirm that there was no residual PCDH19 expression during the differentiation, protein lysates were taken from KO ESCs, NPs (DIV2) and neurons (DIV12). 40 µg of protein was taken from each KO sample and DIV12 WT neurons as a control, and endogenous PCDH19 was detected by Western blot (**Figure 5.5**). There was no detection of PCDH19 at any stage of the differentiation of *Pcdh19* KO ESCs but the loading control, HH3, was detected in all samples at 15 kDa, validating the presence of protein. Also, as a positive control, PCDH19 was detectable at 110 kDa in DIV12 WT neurons.

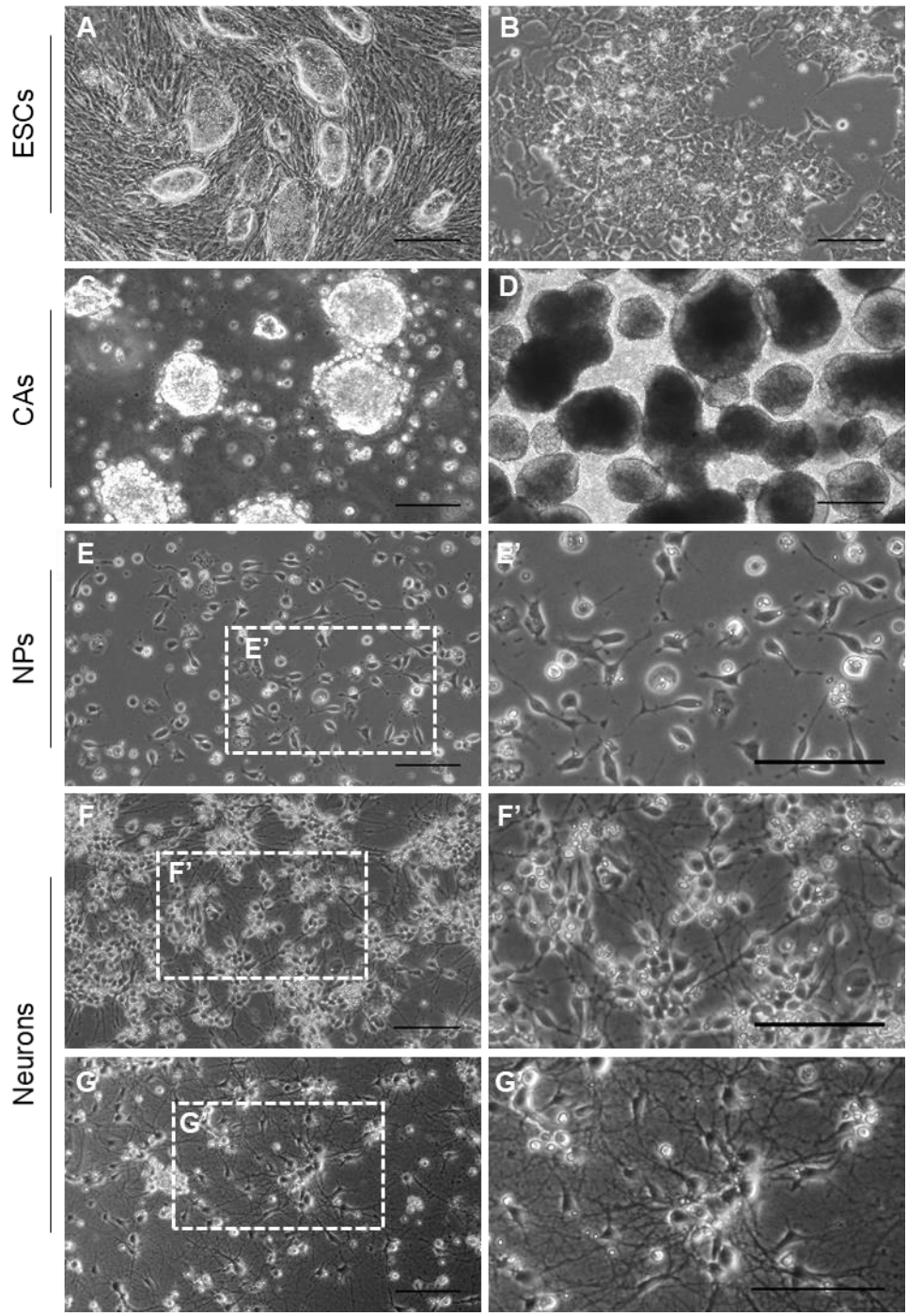

Figure 5.4: *Pcdh19* KO ESCs could be differentiated into neurons. (A) Colonies of established *Pcdh19* KO ESC's plated on MEFs for neuronal differentiation. **(B)** ESC's deprived of MEFs on gelatin-coated dishes. Formation of CAs at **(C)** CA day 1 and **(D)** CA day 8. **(E)** Neuronal progenitors 2 hours after plating dissociated CAs. **(F)** DIV6 neurons after plating dissociated aggregates. **(G)** DIV20 neurons after plating aggregates. KO, knock-out; ESC, embryonic stem cell; MEF, mouse embryonic fibroblasts; CA, cellular aggregate. Scale bars: (A, B, C, E, F, G) 100 µM; (D) 200 µM.

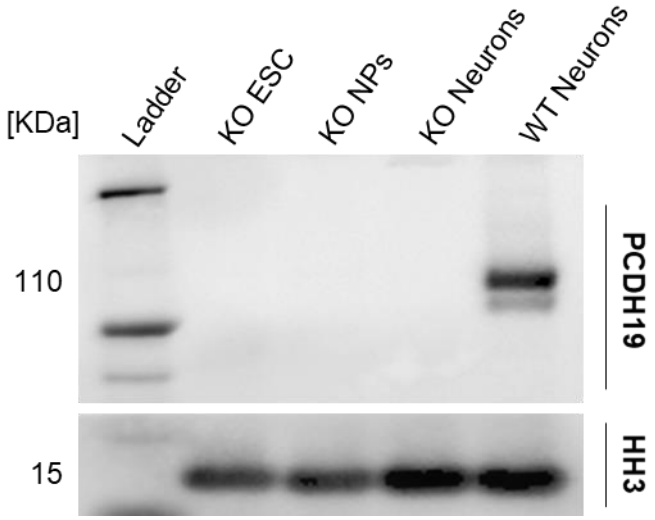

Figure 5.5: PCDH19 is not expressed in KO ESC-derived neurons. Western blot against PCDH19 (110 kDa) in KO ESCs, NPs (DIV2) and neurons (DIV12) compared to the positive control of WT neurons (DIV12). Histone H3 (HH3) detected at 15 kDa as a loading control. WT, wild-type; KO, knock-out, ESC, embryonic stem cells; NPs, neuronal progenitors; kDa, kilodaltons.

5.2.5 Less Pcdh19 KO progenitors were generated during cellular aggregation than WT

During the neuronal differentiation procedure, when WT and KO ESCs were ready for cellular aggregate formation, 4 million ESCs were passaged per aggregate dish (CA0). At the final day of aggregation (CA8), cells were dissociated, and the cell number was calculated for subsequent plating. As a high rate of proliferation was expected during this time (Bibel *et al.* 2007), the absolute number of cells per aggregate dish was recorded in WT and KO cells. Unexpectedly, there were significantly less KO than WT cells at the end of the aggregation process (**Figure 5.6**; *P=0.000*; n=10; unpaired t-test). On average there was an overall KO progenitor cell loss (from 4 million to 2.5 million cells per dish), while WT cells proliferated (from 4 million to 9.65 million cells per dish). Irrespective of the cell loss, KO neural progenitors were still able to be plated and generated a uniform population of neurons as shown in **Figure 5.4E-G**.

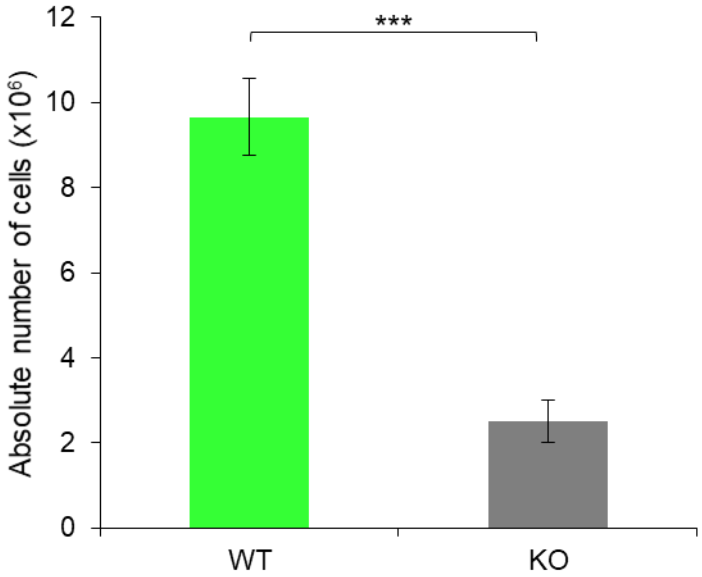

Figure 5.6: *Pcdh19* KO ESC-derived cellular aggregates gave rise to less progenitor cells than WT. Absolute number of WT and KO cells calculated at the day of dissociation and plating (CA8). Starting cell number at CA0 was always 4 million cells per dish. Data represented as the mean ± standard error of the mean. ESC, embryonic stem cell; CA, cellular aggregate; WT, wild-type; KO, knock-out; ***, $p<0.001$.

5.2.6 Characterisation of Pcdh19 KO mouse ESC-derived neurons

To confirm that *Pcdh19* KO ESCs were capable of differentiating into "cortical-like" neurons, similar to the WT cell line and as described previously (Bibel *et al.* 2004; Bibel *et al.* 2007), a characterisation of the cortical cell types present within the culture was required. WT and KO neural progenitors were plated on coverslips and cultured for 12 days. DIV12 neurons were fixed using paraformaldehyde and immunocytochemistry (ICC) was used to detect cortical layer markers, TBR1 (layer VI), CTIP2 (layer V), SATB2 (callosal projection neurons), and CUX1 (layers II-IV), in combination with neuron-specific markers MAP2 (dendritic marker) and β-tubulin 1 (TUJ1). Also, as a 5% population of GABAergic neurons had previously been reported in WT cultures (Bibel *et al.* 2004) the inhibitory neuronal marker GAD65/67 was also used. All cells were counterstained with DAPI and mounted on to slides for subsequent imaging. Maximum intensity projection images were taken of WT and KO coverslips (**Figure 5.7**).

The number of marker-positive cells over the total number of cells (DAPI+) was calculated (e.g., TBR1+/Total DAPI+) to determine what fraction of cells expressed each cell marker. A minimum of 10 images were taken per differentiation, and an average percentage was calculated from these images and presented in **Figure 5.7F**. The "n" number defines the number of differentiations used per quantification. Upon observation and a preliminary quantification, it was found that all cell-specific markers described above were expressed in *Pcdh19* WT and KO mouse ESC-derived neurons at DIV12, including the inhibitory marker GAD65/67. (**Figure 5.7F**; TBR1, WT= 58.0% (n=1), KO= 64.5% (n=2); CTIP2, WT= 12.2% (n=3), KO= 11.6% (n=2); SATB2, WT= 6.6% (n=2), KO= 7.9% (n=2); CUX1, WT= 36.1% (n=1), KO= 50.3% (n=1); GAD65/67, WT= 5.6% (n=2), KO= 10.3% (n=1)). Due to difficulties with antibody detection that may have arisen due to fixing procedures or different antibody batches, some of the quantifications were not repeated or had to be calculated from less than 3 independent differentiations. Therefore, statistical comparisons between WT and KO neurons could not be done and it was not possible to conclude whether there were differences between cell lines. However, it can be concluded that both lines expressed all cortical cell markers tested.

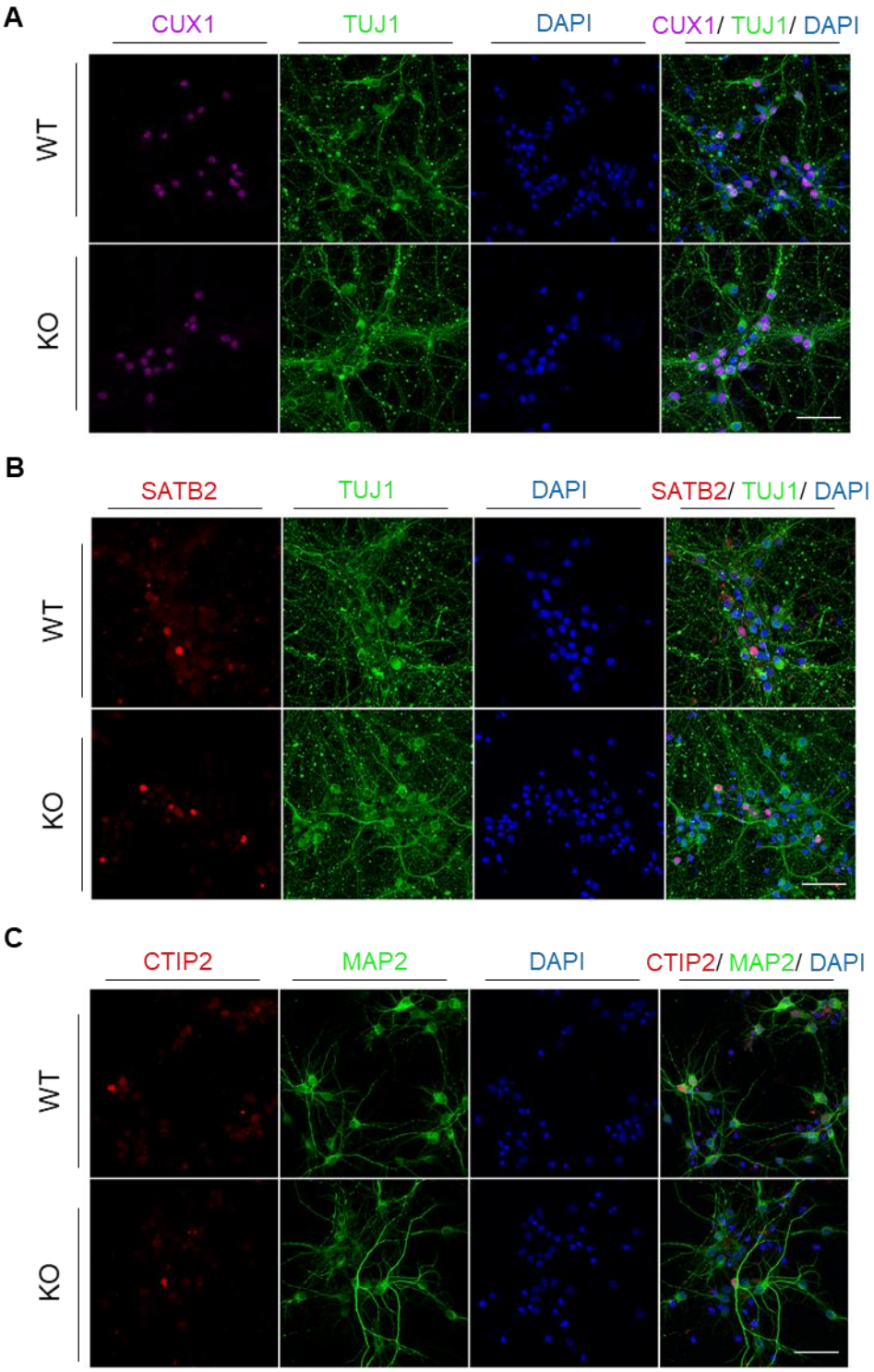

Figure 5.7: Cortical layer and GABAergic markers are detectable in *Pcdh19* KO ESC-derived neurons. Immunocytochemical staining to detect cortical layer markers, CUX1 **(A)**, SATB2 **(B)** and CTIP2 **(C)** combined with neuron-specific markers, TUJ1 **(A and B)** MAP2 (**C**). Nuclei counterstained with DAPI. WT, wild-type; KO, knock-out. Scale bars: 20 µm.

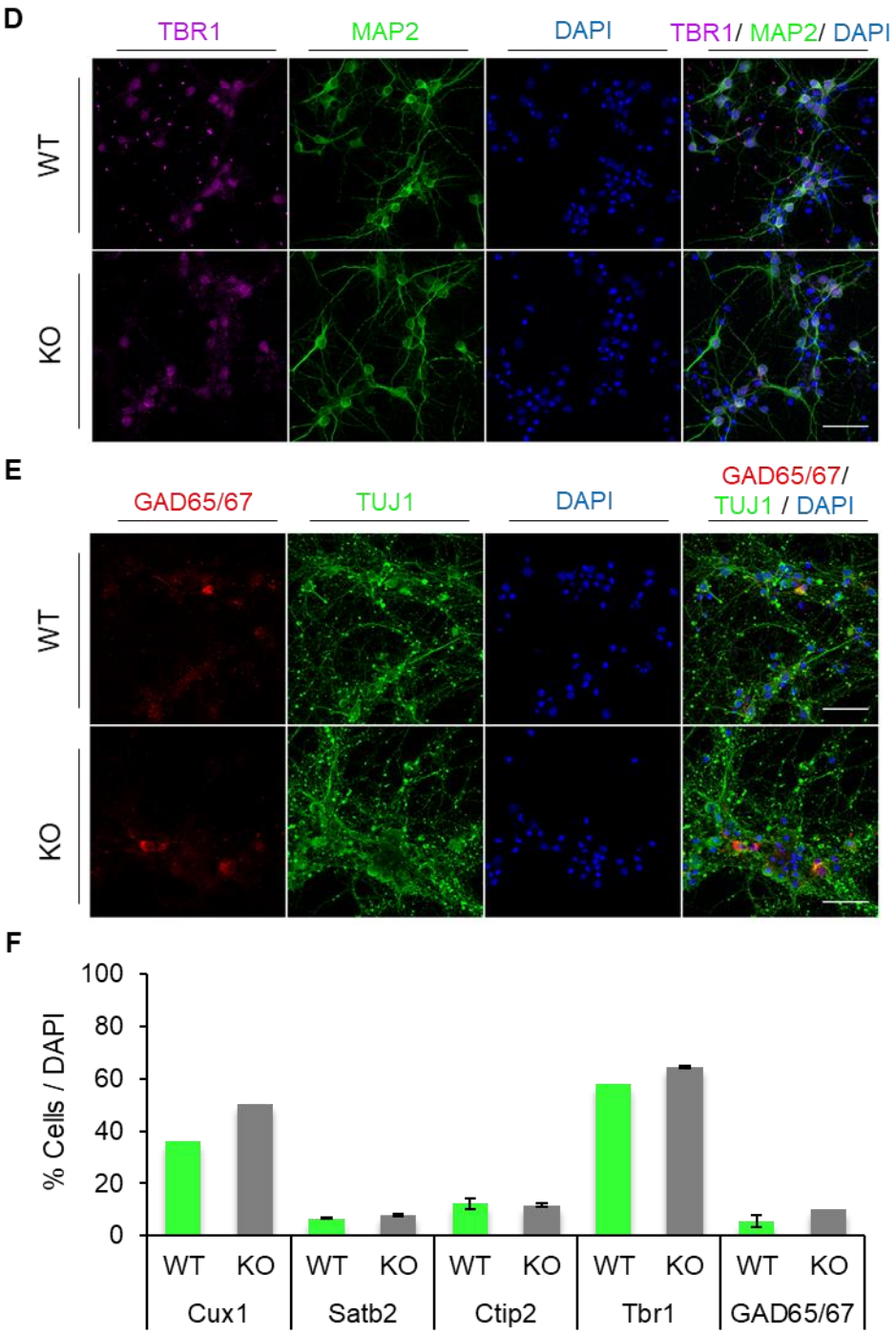

Figure 5.7 (continued): Cortical layer and GABAergic markers are detectable in *Pcdh19* KO ESC-derived neurons. Immunocytochemical staining to detect cortical layer marker TBR1 **(D)** and GABAergic marker GAD65/67 **(E)**, combined with neuron-specific marker MAP2 **(D)** and TUJ1 **(E)**. Nuclei counterstained with DAPI. **(F)** Quantification of the average number of cells positive for cortical/GABAergic markers over the total cells number (DAPI+). Data represented as the mean ± standard error of the mean for n<1. WT, wild-type; KO, knock-out. Scale bars: 20 µm.

5.2.7 Pcdh19 WT and KO neurons form synapses

Using this neuronal differentiation procedure, previous reports have indicated that synapses form as early as DIV9 (Bibel *et al.* 2004). To ensure that pre- and post-synaptic proteins were present in WT and KO cultures and that synapses were forming, DIV12 WT and KO neurons were grown on coverslips, fixed, and immunostained to detect the presynaptic vesicular protein synaptophysin, and postsynaptic scaffolding protein homer (**Figure 5.8**). Nuclei were counterstained with DAPI, and to visualise cell morphology, Tau-GFP was imaged in the WT cells and phase contrast images were taken of the KO cells. It was found that synaptophysin puncta were distributed in the processes and around the cell bodies of both WT and KO neurons and homer was concentrated at the postsynaptic cell bodies and processes of both WT and KO neurons. Co-localised yellow puncta (**Figure 5.8A and B**; white arrows) were visible in both cell lines, indicating that synapses were formed at DIV12. As it is aimed to quantify the number of synapses formed in these cultures in Chapter 6, it was particularly important to establish that synapses were being formed in both cell lines.

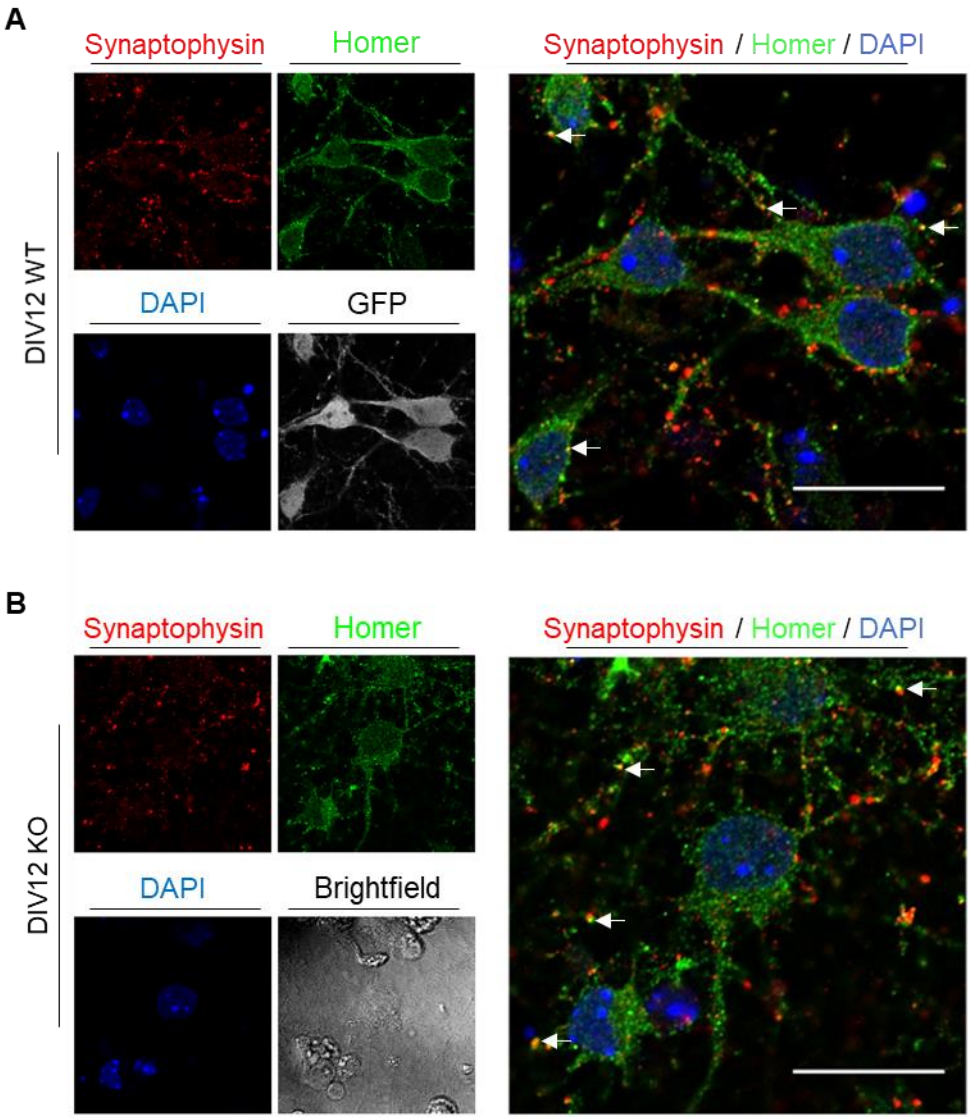

Figure 5.8: *Pcdh19* KO and WT ESC-derived neurons form synapses by DIV12. Representative images of DIV12 WT-ESC derived neurons **(A)** and *Pcdh19* KO ESC-derived neurons **(B)**, immuno-stained with synaptophysin (red), homer (green), and counterstained with DAPI (blue). GFP (grayscale) and bright field imaging were used to study cell morphology in WT and KO neurons, respectively. Examples of co-localised synaptophysin/homer puncta are labelled with white arrowheads to highlight the formation of synapses. DIV, day in vitro; WT, wild-type; GFP, green fluorescent protein; KO, knock-out. Scale bars: 20 µM.

5.2.8 vGlut1 and vGlut2 expression in Pcdh19 KO and WT ESC-derived neurons

Vesicular glutamate transporters (vGLUT) ensure the packaging of glutamate into vesicles for subsequent release from excitatory synapses and are commonly used as a marker of excitatory neurons. Using ICC, vGLUT1 expression was determined to support the excitatory nature of both cell lines. DIV12 WT and KO neurons were fixed on coverslips and stained with antibodies to detect vGLUT1, β-tubulin (TUJ1), and were counterstained with DAPI (**Figure 5.9A**). vGLUT1 was detectable around the cell bodies and in the axonal processes of both WT and KO neurons, indicating that a proportion of the cultured neurons were excitatory. For reasons that are unknown, there was unspecific nuclear staining present in both cell lines.

As changes in vesicular glutamate transporters 1 and 2 (*vGlut1* and *2*) expression correlate with neuronal maturity, their transcriptional levels were assessed in *Pcdh19* KO and WT ESC-derived neurons. NPs were plated and cultured at a high density and RNA was extracted from WT and KO NPs (DIV2) and neurons (DIV12). Quantitative RT-PCR was used to determine the transcriptional levels of *vGlut1* and *vGlut2* relative to *β-actin* (**Figure 5.9B and C**).

A two-way ANOVA was conducted to assess the influence of genotype and age on *vGlut1* and *2* expression. When assessing *vGlut1*, there was a significant difference between KO and WT neurons (**Figure 5.9A**; Genotype, *F (1,8) =2.187, P=0.023*; two-way ANOVA). Upon post hoc analysis, it was determined that WT cells significantly increased their levels of *vGlut1* from DIV2 to DIV12, while KO cells remained at a similar level in DIV2 and DIV12 neurons (WT DIV2, 1 (n=3) vs. WT DIV12, 2.0 (n=3); *P=0.047*; KO DIV2, 0.7 (n=3) vs. KO DIV12, 0.6 (n=3); *P=0.810*; Bonferroni post-hoc). Further analysis revealed that *vGlut1* expression levels were lower in DIV12 KO neurons compared to WT (WT DIV12, 2.0 (n=3) vs. KO DIV12, 0.6 (n=3); *P=0.011*; Bonferroni post-hoc).

When assessing *vGlut2* levels, significant differences were observed that were dependent on age (DIV2 vs. DIV12) and not genotype (**Figure 5.9B**; Genotype, *F (1,8) =0.075, P=0.791*; Age, *F (1,8) =59.831, P=0.000*; two-way ANOVA). Upon post-hoc analysis, both WT and KO cells significantly increased their levels of *vGlut2* from DIV2 to DIV12 (WT DIV2, 1 (n=3) vs. WT DIV12, 29.8 (n=3), *P=0.000*; KO DIV2, 1.4 (n=3) vs. KO DIV12, 27.5 (n=3); *P=0.001*; Bonferroni post-hoc). Additionally, the levels of *vGlut2*

were not significantly different at DIV2 or DIV12 when comparing genotypes (WT DIV2, 1 (n=3) vs. KO DIV2, 1.4 (n=3) *P=0.943*; WT DIV12, 29.8 (n=3) vs. KO DIV12, 27.5 (n=3); *P=0.657*; Bonferroni post-hoc).

In summary, it was observed that *Pcdh19* KO neurons had a reduced level of *vGlut1* when compared to WT neurons at DIV12. No alterations were seen in the levels of *vGlut2* and both WT and KO neurons matured from DIV2 to DIV12, expressing significantly higher levels of *vGlut2* over time.

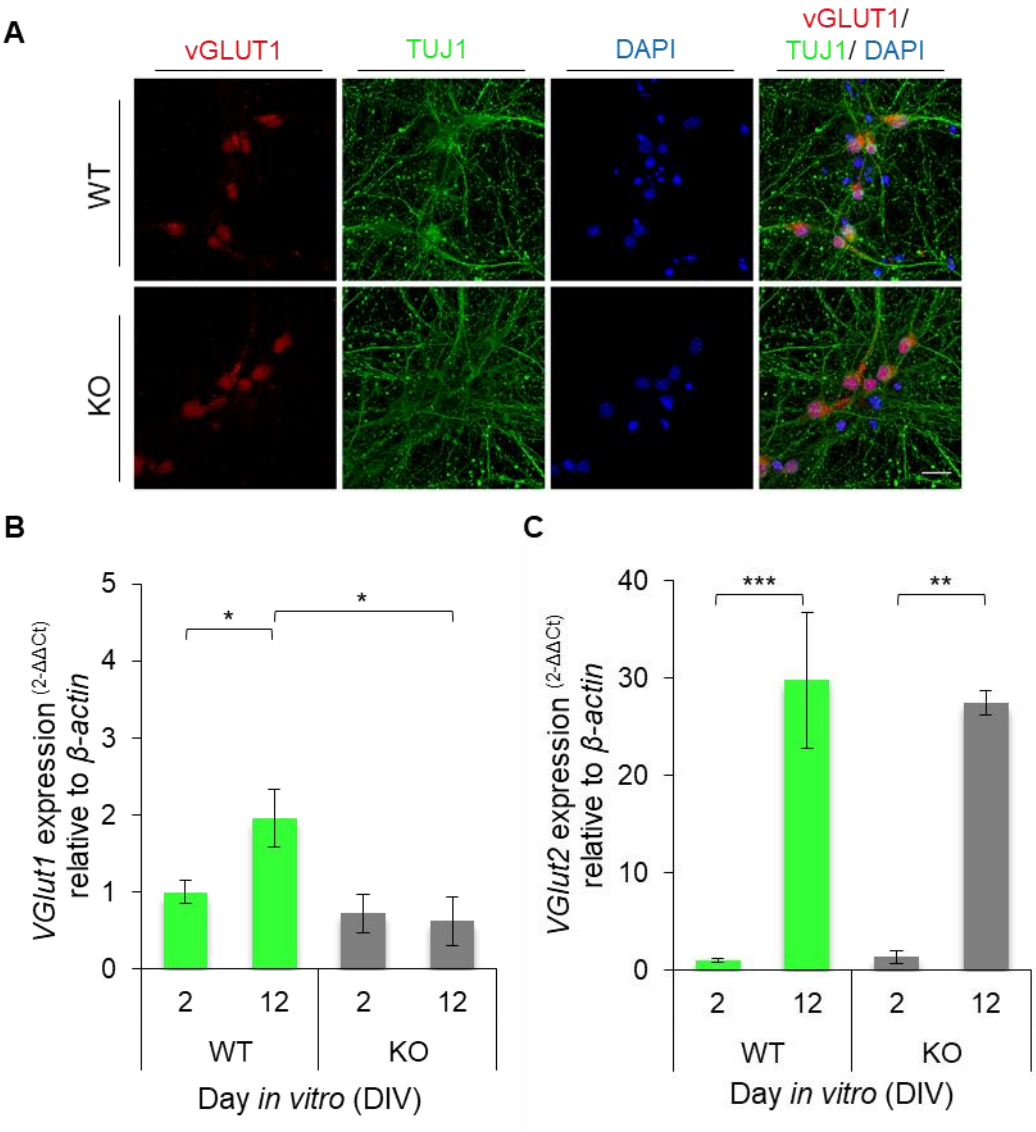

Figure 5.9: *vGlut1* expression is altered in *Pcdh19* KO neurons. (A) Representative images of DIV12 WT and KO neurons immuno-stained with vGLUT1 (red), TUJ1 (green) and counterstained with DAPI (blue). RT-PCR quantification of the levels of *vGlut1* **(B)** and *vGlut2* **(C)** in DIV2 and DIV12 WT and KO neurons. Ct values normalised to β-actin and relative expression levels calculated with the $2^{-\Delta\Delta Ct}$. Data represented as the mean ± standard error of the mean. TUJ1, β-tubulin; WT, wild-type; KO, knock-out; Ct, cycle threshold, *, p<0.05, **, p<0.01, ***, p<0.001. Scale bar: 20 µM.

5.3 Discussion

The primary aim of this chapter was to generate an *in vitro* system that could be used to study the role of PCDH19 in cortical neurons. A homogenous population of WT "cortical-like" neurons could be generated using the protocol described by Bibel *et al.* Furthermore, an increasing level of *Pcdh19* was found in these ESC-derived neurons and it was deemed an appropriate *in vitro* system to be used for subsequent experiments. This chapter also largely focused on deriving *Pcdh19* KO ESC's and on determining that it was possible to generate "cortical-like" neurons that lacked PCDH19. Once KO progenitors were plated, they were able to differentiate into neurons, maturing over time and expressing cell-type markers specific to cortical layers II to VI and GABAergic neurons in the mammalian cortex, similar to WT neurons. KO cells were also able to form synapses by DIV12, as assessed by the co-registration of pre- and post-synaptic markers. At the mRNA level, as KO neurons matured they expressed increasing levels of *vGlut2*. Interestingly though, unlike WT neurons, KO neurons failed to increase their expression levels of *vGlut1* at DIV12, indicating that there may be a possible reduction in the uptake or release of glutamate in these neurons.

5.3.1 The use of mouse ESC-derived neurons to study the role of Pcdh19

The generation of ESC-derived neurons is now a frequently used tool, with the advantage of generating unlimited numbers of cells. This tool is particularly useful in understanding cell-specific gene functions, including that of *Pcdh19*. Many protocols have used mouse ESCs to generate cortical neurons that have varying levels of neuronal culture homogeneity (Ying *et al.* 2003; Bibel *et al.* 2004; Gaspard *et al.* 2009; Alsanie *et al.* 2017; Gazina *et al.* 2018). Bibel *et al.* described a protocol that gives rise to 90-95% glutamatergic cortical-like neurons, with only 5% GABAergic cells and little to no astrocytes and oligodendrocytes. As it is of interest to study the function of *Pcdh19* in cortical neurons, this protocol that generates a homogenous population of cortical neurons was favourable.

Pcdh19 mRNA and protein were shown to be expressed in ESC-derived neurons using this protocol. A progressive increase in the levels of *Pcdh19* mRNA was observed in NPs after plating and as they matured into neurons. In mouse cortical development, the pattern of *Pcdh19* mRNA expression is different from that observed *in vitro*. During early

mouse cortical development, *Pcdh19* mRNA levels peak at embryonic day (E)12 and diminish during later embryonic development. Then, following birth, during early postnatal development expression peaks again before diminishing during adulthood (Fujitani *et al.* 2017). In contrast, it has been found that in induced pluripotent stem cell (iPSC)-derived human neural stem/progenitor cells (hNSPCs), an increasing level of *PCDH19* was expressed upon neural induction, which peaked at neural rosette stage (cultured neural progenitor stage with the establishment of apical-basal polarity being the defined feature) and was maintained in maturing neurons (Homan *et al.* 2018). Using an open RNA sequencing transcriptome database, it was found that more *PCDH19* is expressed in human neurons than *Pcdh19* in mouse neurons; therefore, it may be possible that these variations in expression stem from evolutionary differences between mouse and human brains. Moreover, *in vitro* studies do not directly correlate with *in vivo* studies due to the lack of key developmental cues, maturity, and the loss of the structural integrity of a normal developing brain. Taken together, the differentiation procedure described by Bibel *et al.* appeared to be an appropriate culture system for functional studies of PCDH19. However, due to differences between *in vitro* and *in vivo* development and indeed the differences between mouse and human (see General Discussion), this system cannot be translated directly to human development and should be used only as a tool that can pinpoint functional properties of PCDH19 and lead on to future *in vivo* studies.

5.3.2 Pcdh19 KO ESC's can differentiate into "cortical-like" neurons

The derivation of ESCs from blastocysts has been previously used in combination with this protocol with high success (Bibel *et al.* 2004). Following the same procedure, *Pcdh19* KO ESCs were successfully derived and "cortical-like" neurons were generated.

However, one caveat of this system could be the gender of the cells used. *Pcdh19* KO ESCs were isolated from *Pcdh19* KO mice, and a cell line was selected that was XY (male). X-inactivation cannot be mimicked *in vitro* using this protocol as mouse pluripotent XX ESCs cannot be stably maintained in culture as a result of the lack of X inactivation, a key feature of true pluripotency. Accordingly, as *Pcdh19* is X-linked, it is not possible to determine whether there are sex-specific differences using this culture system. However, when Homan *et al*. found premature neurogenesis in *PCDH19* KO hNSPCs, there were no sex-specific differences. Also, males do present with somatic

mutations of PCDH19 and have EIEE9, and there are reports of “carrier” (KO) males suffering from some behavioural disturbances (van Harssel *et al.* 2013; Perez *et al.* 2017). Therefore, this culture system can still be considered a useful disease model.

An initial difference was seen when comparing KO and WT cell numbers. It was observed that the absolute number after aggregation and neural induction was lower in the KO line when compared to WT. This indicates that KO cells may have a low proliferative rate. As this is not known, to test this, cellular aggregates could be dissociated at different time points and KI67 could be used as a marker to quantify proliferating cells in both KO and WT lines. However, it is likely that these differences are due to differences in the genetic background of the cells. In support of this, work in the Martinez-Garay laboratory has shown that a *Pcdh19* WT and KO cell line of the same genetic background did not have different absolute numbers after aggregation, and KO cells proliferated similarly to WT cells of the same background.

Interestingly, *Pcdh19* KO aggregates were still able to dissociate and develop into neurons. As this was the first time *Pcdh19* KO mouse ESC-derived neurons were generated, it was essential to conduct an initial characterisation of the neuronal cell types produced. A proportion of both KO and WT neurons expressed TBR1 (layer VI), CTIP2 (layer V), SATB2 (callosal projection neurons), CUX1 (layers II-IV), and GAD65/67 (GABAergic neurons). However, due to the low number of repeated differentiations, it could not be determined whether the proportion of these markers differed in each cell line. It is worth noting that *ex vivo* mouse studies conducted in the Martinez-Garay laboratory have revealed no differences in cortical cell markers expressed in adult *Pcdh19* WT (C57BlJ/6), *Pcdh19* KO and *Pcdh19* HET mouse brains. Moreover, studies using iPSC-derived neurons found no differences in the mRNA levels of *SATB2* or *GAD67* (Homan *et al.* 2018). Taken together, *Pcdh19* KO cortical neurons can be generated and used in functional studies.

5.3.3 Alterations in vesicular glutamate transporter mRNA levels in neurons lacking PCDH19 may cause defects in glutamate release

Vesicular glutamate transporters control the amount of glutamate that is packaged into vesicles and subsequently released at an excitatory synapse, therefore regulating neurotransmission efficacy (Wojcik *et al.* 2004). To support the excitatory nature of the

WT and KO neurons generated, expression of vGLUT1 was assessed using ICC. However, unspecific staining prevented a quantitative analysis. *vGlut1* and *vGlut2* mRNA levels were also investigated. A significant increase in *vGlut2* expression was seen from DIV2 to DIV12 in both WT and KO neurons, ensuring both lines were maturing. Surprisingly, although *vGlut1* levels were similar between WT and KO neruons at DIV2, KO neurons expressed significantly less *vGlut1* at DIV12 than WT, which could lead to possible differences in glutamate packaging and release. It is known that a switch from high *vGlut2* and low *vGlut1*, to low *vGlut2* and high *vGlut1* levels marks a developmental time point in neurons which correlates with an increase in presynaptic proteins, such as synapsin and synaptophysin (Berry *et al.* 2012). It was observed that DIV12 WT neurons had a higher level of *vGlut2* than *vGlut1*, supporting the notion that these neurons were not fully matured by DIV12. Therefore, as the difference in *vGlut1* levels between WT and KO neurons was relatively small and in neurons that were not fully matured, it would be interesting to determine whether this difference persists as expression levels shift to high *vGlut1* and low *vGlut2* levels later in neuronal maturation. Furthermore, as mentioned above, differences in genetic backgrounds can cause slight changes in functional milestones (Barth *et al.* 2014). Therefore, confirmation using a cell line of the same genetic background would be necessary to validate the result. Also, contrary to our observations with mouse neurons, Homan *et al.* found an increase in *vGlut1* and a corresponding decrease in *vGlut2* in human iPSC-derived *Pcdh19* KO neurons (Homan *et al.* 2018). This difference could be due to the age of the neurons (DIV70/90) and the species variability. If the differences in *vGlut1* levels are confirmed it would be of interest to study glutamate release to determine whether PCDH19 is affecting neuronal transmission. This could be tested using a glutamate release assay. Neurons could be incubated in ^{3}[H]-labelled glutamate and medium could be collected at different time intervals and upon stimulation of the neurons to determine the amount of glutamate released in both WT and KO neurons as described by (Schrenk-Siemens *et al.* 2008).

5.3.4 Concluding remarks

Taken together, the *in vitro* neuronal differentiation protocol described by Bibel *et al.* and established during this chapter can be applied to *Pcdh19* KO ESCs to generate “cortical-like” neurons that lack PCDH19. This protocol provides a powerful tool to study PCDH19’s function *in vitro*. As this procedure generated comparable “cortical-like” *Pcdh19* KO and WT neurons, the next step was to use this *in vitro* system to generate a

mosaic culture that could act as a possible disease model of EIEE9 *in vitro.* This model could then be used to test the theory of cellular interference. By studying synapse number, and other physiological parameters, in *Pcdh19* WT, KO and, mosaic cultures the physiology and pathophysiological role of PCDH19 could be determined.

Chapter 6: Assessing the role of PCDH19 in synaptogenesis

6.1 Introduction

As stated throughout this thesis, patients with Early Infantile Epileptic Encephalopathy 9 (EIEE9) have a mixture of PCDH19 expressing and PCDH19 non-expressing cells. According to the theory of "cellular interference, it is believed that the co-existence of these two different types of cells causes connectivity deficits that lead to hyperexcitability in neurons and the epileptic phenotype. Due to hemizygous males being asymptomatic, it is further hypothesised that there are no alterations in synapse formation in neuronal networks that completely lack functional PCDH19. However, the pathophysiological mechanisms of EIEE9 and the theory of cellular interference are yet to be tested experimentally. This objective has been difficult to reach, not least because of the lack of suitable antibodies for detailed *in vivo* investigations and of suitable experimental models reflecting mosaicism, a hallmark of this disorder. Therefore, it is of great interest to generate a mosaic ESC culture system to study PCDH19's function during synaptogenesis.

Although no studies have been conducted to look directly at synapse formation thus far, PCDH19 has been localised in synaptosome fractions *in vivo* and synapses *in vitro* using primary hippocampal cultures (Pederick *et al.* 2016; Hayashi *et al.* 2017), suggesting that PCDH19 could be involved in modulating synaptogenesis. Furthermore, neuronal excitability deficits have been found in *Pcdh19* heterozygous (HET) mice and not *Pcdh19* KO using electrocorticogram recordings (Pederick *et al.* 2018), supporting the notion that connectivity is being affected due to PCDH19 mosaicism in the mouse model.

Previous experiments do suggest a role for δ-protocadherins in connectivity. For example, PCDH17 was found to affect axon extension in the amygdala through the recruitment of WAVE complex components, lamellipodin and Ena/VASP (Hayashi et al. 2014). PCDH18b has been shown to promote axon outgrowth and branching in zebrafish motor neurons via Nap1-binding (Biswas et al. 2014). Moreover, protocadherin 11X knockdown caused an increase in dendritic branching in cultured cortical neurons through the activation of PI3K/AKT signalling (Wu *et al.* 2015), while PCDH10 regulates synapse elimination, by initiating the protease degradation of the scaffolding protein, PSD-95 (Tsai *et al.* 2012). Finally, activity-dependent stimulation of PCDH8 regulates

synapse stability, by associating with N-cadherin in cis and binding to TAO2 kinase (TAO2β) which causes endocytosis of N-cadherin and PCDH8 (Yasuda *et al.* 2007).

Additionally, specific combinations of clustered cadherins provide cell surface diversity that is required for circuit assembly, providing a specific molecular identity in neurons that ensures that the correct synaptic partners are connected (Friedman *et al.* 2015; Mountoufaris *et al.* 2017). Specific cadherin combinations have been found to be necessary for axonal arborisation and the generation of correct synaptic connections (Duan *et al.* 2014; Mountoufaris *et al.* 2017), dendrite recruitment (Duan *et al.* 2018) and the recruitment of certain synaptic organisers during synaptic differentiation (Yamagata *et al.* 2018), hence altering synaptic function or signalling. Single mismatched protocadherins can lead to the segregation of particular cell populations, even when several other protocadherins are expressed in common (Thu *et al.* 2014). Co-expression of PCDH19 and other δ2-protocadherins can significantly impact on the binding affinity within a cell (Bisogni *et al.* 2018; Pederick *et al.* 2018). Taken together, it is hypothesised that the mosaic expression of PCDH19 could affect synaptogenesis due to mismatched protocadherins that may not engage in proper cell adhesion. As a result, this could lead to skewing of cell-cell synapse formation, differences in synaptic number or alterations in synaptic function and signalling.

Although biochemistry and histology can provide valuable information about synaptic connections and expressed synaptic components, these approaches fail to provide information about the electrophysiological properties of the synapses that are formed, including synaptic transmission in particular. Two non-invasive approaches that are commonly used to study neuronal activity are multi-electrode array (MEA) and calcium imaging. MEA is a system that is increasingly used in stem cell-derived neurons to study electrical activity (Telezhkin *et al.* 2015). This technique allows for a high throughput assessment of spontaneous electrochemical changes within a network and is particularly useful when studying epileptiform behaviour. Calcium imaging allows for the visualisation and quantification of intracellular calcium signals which is particularly beneficial as it can be a measure of the direct effects of calcium and calcium channels and an indication of the indirect effects of calcium-dependent mechanisms and neurotransmission efficacy. It would be useful to optimise a mosaic co-culture system to be used in combination with these two electrophysiological techniques. These techniques could provide further information on the translatability of this culture system and enable the assessment of

alterations in synaptic function and signalling which may be affected due to PCDH19 mosaicism.

6.1.1 Aims

To study PCDH19 mosaicism and the theory of cellular interference with the WT ESCs and *Pcdh19* KO ESCs that had been differentiated into “cortical-like” neurons in the previous chapter, the main aim was to establish mosaic cultures to understand the basic parameters of synapse formation and synaptic transmission using multielectrode array (MEA) and calcium imaging.

6.2 Results

6.2.1 Successful generation of a mosaic co-culture system

To study the role of PCDH19 in synapse formation, mosaicism was investigated by generating an *in vitro* co-culture system. This system would allow for EIEE9 to be modelled *in vitro*, and for individual cells and cultures to be studied over time. By using the Tau-GFP (WT) and *Pcdh19* KO (KO) ESC's used in Chapter 5, neurons were generated and either cultured separately (WT and KO neurons in single WT and KO cultures (WT-WT and KO-KO, respectively)) or together (**Figure 6.1A**; WT and KO cells in a co-culture (WT-MIX and KO-MIX, respectively)). Using this method, it could be determined whether individual cell populations or cultures acted differently dependent on PCDH19 expression and culture environment.

To ensure there was a homogenous mixture and 1:1 ratio of WT and KO cells, NPs from both cell lines were mixed just before cellular aggregates were dissociated and plated (**Figure 6.1B**). WT and KO cells cultured separately were plated at $2.5x10^5$ cells per well, and WT and KO cells in mixed cultures were plated at $1.25x10^5$ cells per well each for all experiments in this chapter. Mixed cultures were treated the same as WT and KO separate cultures throughout the differentiation procedure. Once mixed, the co-cultures were observed using a bright field microscope and kept in culture until DIV16. Representative images of mixed NPs and developing neurons are shown in **Figure 6.1C**. Upon observation, co-cultured neurons survived in culture, similar to WT and KO neurons in separate cultures, forming multipolar cell bodies with extensive processes that were highly interconnected.

To study differences between cells within the mixed culture, WT and KO neurons needed to be distinguished from one another. By using the Tau-GFP ESC line, the WT neuronal population could be visualised by virtue of GFP inserted into the *tau* locus. As Tau is a neuronal microtubule-associated protein, all neurons and their processes could be detected using GFP detection. GFP was visible in a proportion of the live cells as early as DIV2 (**Figure 6.2A**) and could be seen in the cell bodies and the extended processes as the neurons matured as previously reported (Bibel *et al.* 2004; Bibel *et al.* 2007). Furthermore, in the mixed culture at DIV6, WT GFP+ neurons were easily distinguishable from KO neurons, as only the Tau-GFP neurons fluoresced green (**Figure 6.2B**). Taken

together, a system had been generated to study individual *Pcdh19* WT and KO neurons in separate and mixed cultures, to study cell-specific changes in synapse formation and physiological properties

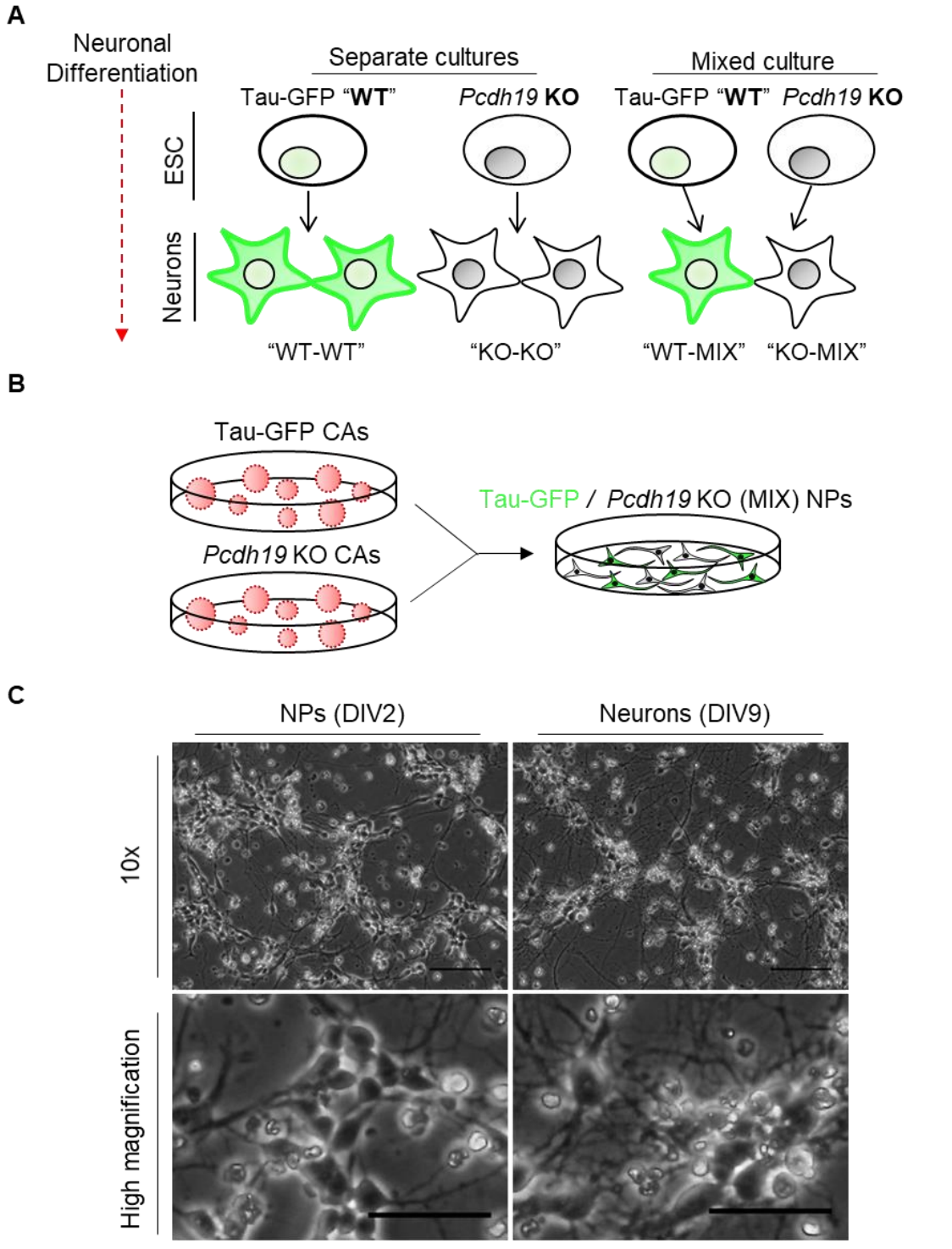

Figure 6.1: Generation of WT and Pcdh19 KO co-cultured ESC-derived neurons. Diagrammatic representation of (A) the experimental plan, and (B) the point of mixing Tau-GFP (WT) and Pcdh19 KO cells. (C) Live images of mixed ESC-derived NPs (DIV2) and neurons (DIV9) at 10x objective and high magnification. GFP, green fluorescent protein; CA, cellular aggregate; NP, neural progenitors. Scale bars: (10x) 100 µM; (High magnification) 50 µM.

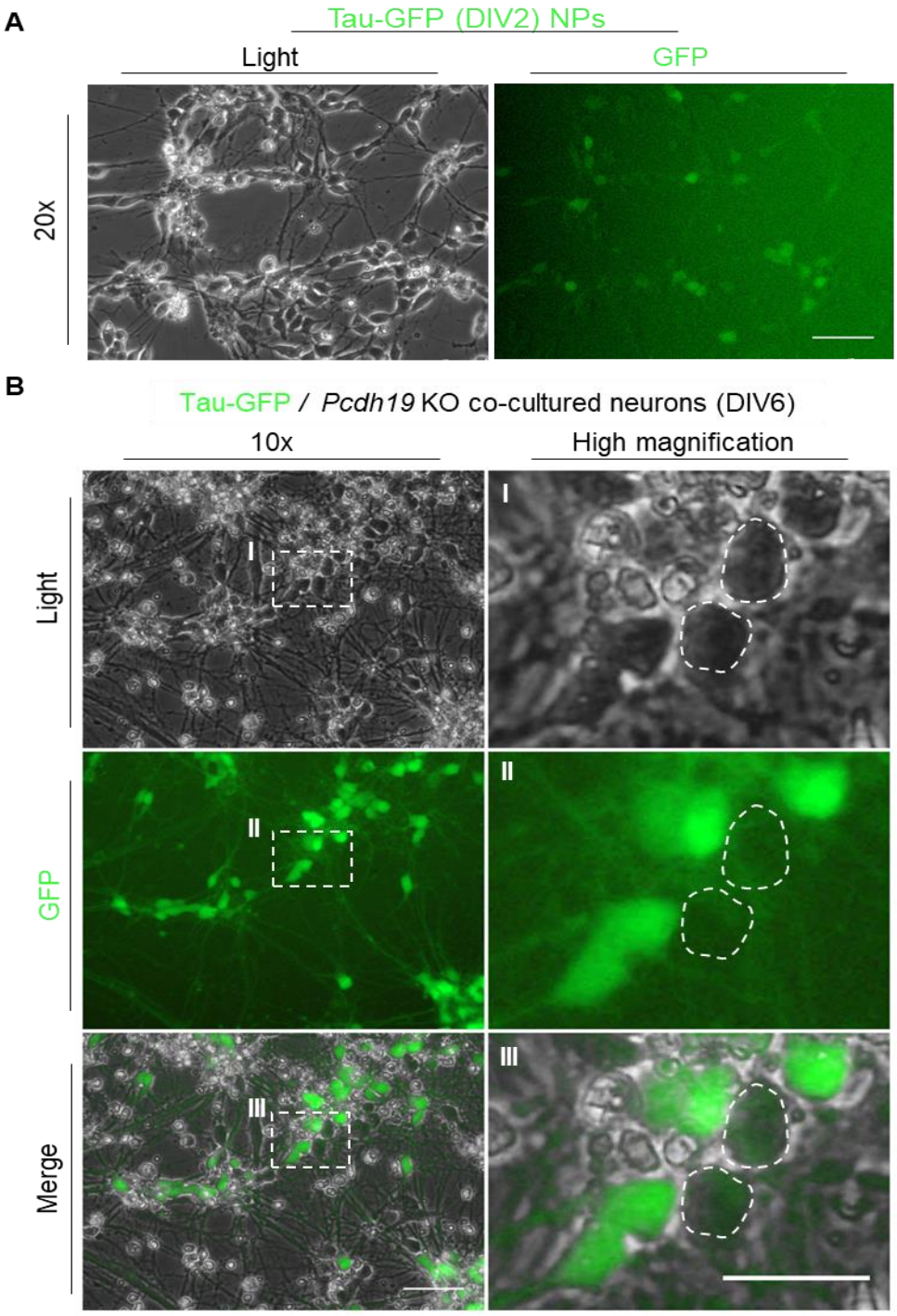

Figure 6.2: WT and *Pcdh19* KO neurons can be distinguished in co-culture using live imaging. (A) Images of Tau-GFP DIV2 NPs. **(B)** Images of Tau-GFP (WT) (GFP+; green) and *Pcdh19* KO (GFP-; non-green; dashed white cell outline) neurons mixed in co-culture. Images were taken at 10x objective and at a high magnification using brightfield and epifluorescence microscopy. GFP, green fluorescent protein; KO, knock-out; DIV, day *in vitro.* Scale bars: (10x) 100 µM; (High magnification) 50 µM.

6.2.2 PCDH19 does not affect synapse number and density in mouse ESC-derived neurons

Using the experimental approach depicted in **Figure 6.1A** to compare WT and KO ESC-derived neurons in separate (WT-WT and KO-KO) and mixed cultures (WT-MIX and KO-MIX), it was aimed to determine whether there were differences in synapse formation. As mentioned above, PCDH19 was shown to be expressed partially in synaptic structures (Hayashi *et al.* 2017). Furthermore, work in the Martinez-Garay laboratory has shown that endogenous PCDH19, labelled *in vivo* through a combination of CRISPR-Cas9 and *in utero* electroporation, can be detected in the cytoplasm around the nucleus in cortical neurons. Taking this expression data into consideration, an analysis of synapse number and density was undertaken in two different areas; around the cell soma and in the neuronal processes (**Figure 6.3-4** and **Figure 6.5-7**, respectively).

DIV14 ESC-derived neurons from WT, KO, and mixed cultures were fixed and immuno-stained with presynaptic vesicular protein synaptophysin, postsynaptic scaffolding protein homer, GFP, and counterstained with DAPI. Z-stack confocal images were taken, and single planes were selected for quantitative analysis at the cell soma and processes (**Figure 6.3** and **Figure 6.5**, respectively). WT-WT, KO-KO, WT-MIX, and KO-MIX postsynaptic sites were assessed, and GFP detection was used to distinguish WT-MIX (GFP+) neurons from KO-MIX (GFP-) neurons within the mixed culture. The absolute number of synaptophysin and homer puncta, co-localised puncta, and co-localised puncta area were calculated automatically using the FIJI Puncta Analyser plug-in. This analysis allowed for the quantification of a presynaptic vesicular protein, a postsynaptic scaffolding protein, overall synapse number, and synapse density, respectively. Three independent differentiations were analysed, with a minimum of 12 cells/processes of interest analysed per differentiation.

Approaches were taken to try to detect and distinguish the KO-MIX processes within the co-culture to be able to determine whether a synapse was made between a WT:WT, KO:KO, WT:KO or KO:WT pre- and post-synaptic partner. A neuronal marker, such as β-tubulin (TUJ1) would have been useful to discriminate between WT-MIX (TUJ1+ GFP+) and KO-MIX (TUJ1+ GFP-) cells. However, as the green, red, and far-red fluorophores were used for GFP, synaptophysin, and homer detection, respectively, and the blue fluorophore secondary antibodies did not work effectively, another approach

was needed. Neurons were transfected with a membrane-bound blue fluorescent protein to attempt to resolve this issue, but, due to high cell death after transfection, this proved to be ineffective. Moreover, a MemBrite™ Fix Cell Surface Staining Kit was used to attempt to visualise the neuronal surface; however, the detection did not work and would need to be optimised further.

As KO neurons were not labelled, KO processes were identified by the background staining of the anti-Homer antibody and were further confirmed through bright field visualisation. However, this method did not allow to easily distinguish specific synaptic connections and it was not possible to differentiate between WT:WT and WT:KO or KO:WT synaptic connections within the mixed culture. Therefore, the co-culture analysis was not extended to assess the proportion of WT:WT, KO:KO, WT:KO or KO:WT synaptic connections formed within a mosaic culture. Only WT and KO neurons from separate and mixed cultures were analysed (WT-WT vs. KO-KO vs. WT-MIX vs. KO-MIX) and overall differences were assessed as WT cells could be distinguished using the GFP signal.

6.2.2.1 Synapse analysis around the cell soma

Postsynaptic cell bodies were selected unbiasedly using DAPI staining, and 40 µM x 40 µM images were selected for quantification. For the within culture analysis, cells were distinguished depending on whether the cell body was GFP+ (WT-MIX) or GFP- (KO-MIX).

A two-way ANOVA was conducted on the influence of culture condition (WT, KO and MIX) and cell type (WT and KO) on synaptophysin puncta number, homer puncta number, co-localised puncta number, and co-localised puncta area. Upon analysis at the cell soma, no significant differences were found in the number of synaptophysin puncta expressed (**Figure 6.4A**; WT-WT, 37.508; KO-KO, 34.627; WT-MIX, 34.904; KO-MIX, 39.3; n=3; Culture condition, *F (2,8) =0.465; P=0.644*; Cell line, *F (1,8) =0.628, P=0.451*; two-way ANOVA). This was also true for the absolute number of homer puncta expressed (**Figure 6.4B**; WT-KO, 57.098; KO-KO, 65.087; WT-MIX, 52.259; KO-MIX, 54.338; n=3; Culture condition, *F (2,8) =0.382, P=0.694*; Cell line, *F (1,8) =0.024, P=0.881*; two-way ANOVA). In addition, it appeared that the number of co-localised puncta at the cell soma was also not significantly different (**Figure 6.4C**; WT-WT, 13.902;

KO-KO, 11.263; WT-MIX, 10.396; KO-MIX, 12.054; n=3; Culture condition, *F (2,8) =1.184, P=0.354*; Cell line, *F (1,8) =0.504, P=0.498*; two-way ANOVA), therefore there were no differences in the number of synapses formed at the cell soma overall. Finally, it was observed that the synaptic area was also not significantly different between cultures or cell types (**Figure 6.4D**; WT-WT, 17.342; KO-KO, 19.049; WT-MIX, 20.479; KO-MIX, 17.363; n=3; Culture condition, *F (2,8) =1.122, P=0.372*; Cell line, *F (1,8) =1.703, P=0.228*; two-way ANOVA).

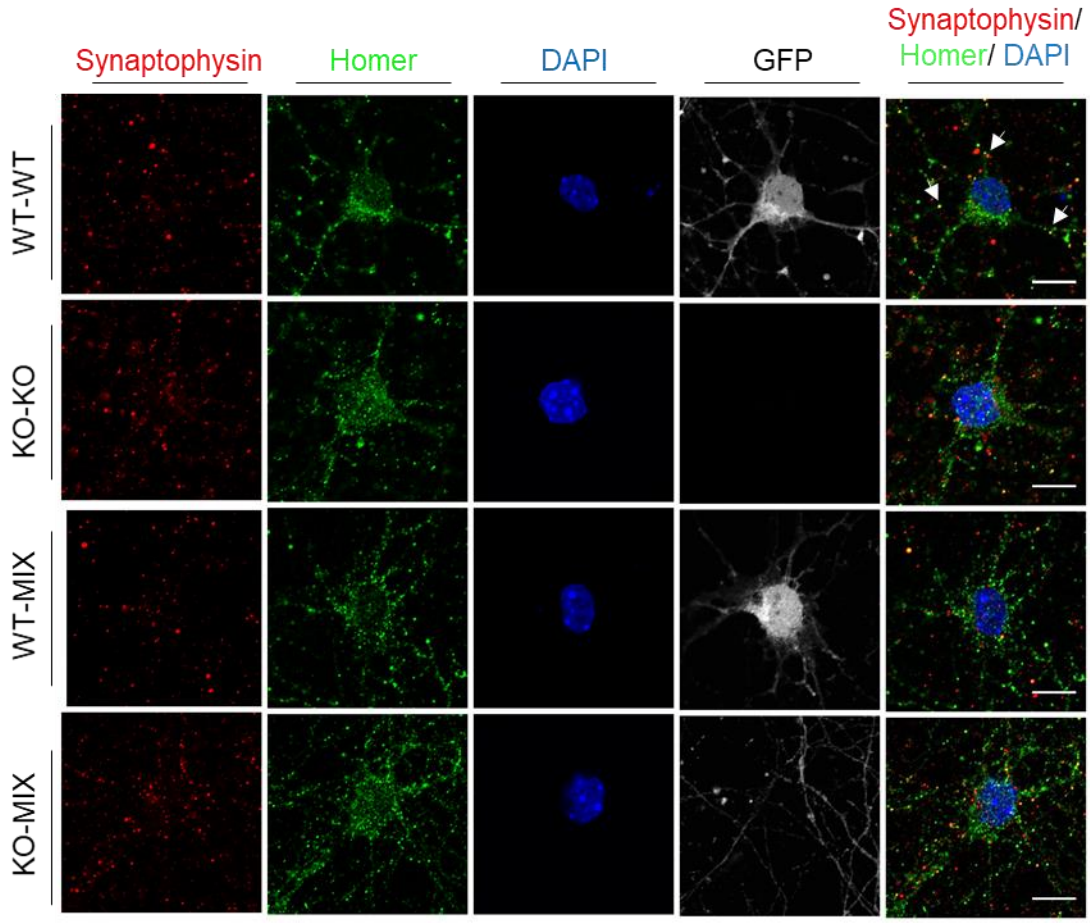

Figure 6.3: Detection of synapses at the cell soma of ESC-derived neurons. Representative single plane images of WT, KO, WT-MIX and KO-MIX neurons immuno-stained with synaptophysin (red), homer (green), and GFP (grey). Nuclei counterstained with DAPI. White arrowheads indicate examples of co-localised puncta (formed synapses). GFP, green fluorescent protein. WT, wild-type; KO, knock-out. Scale bars: 10 µM.

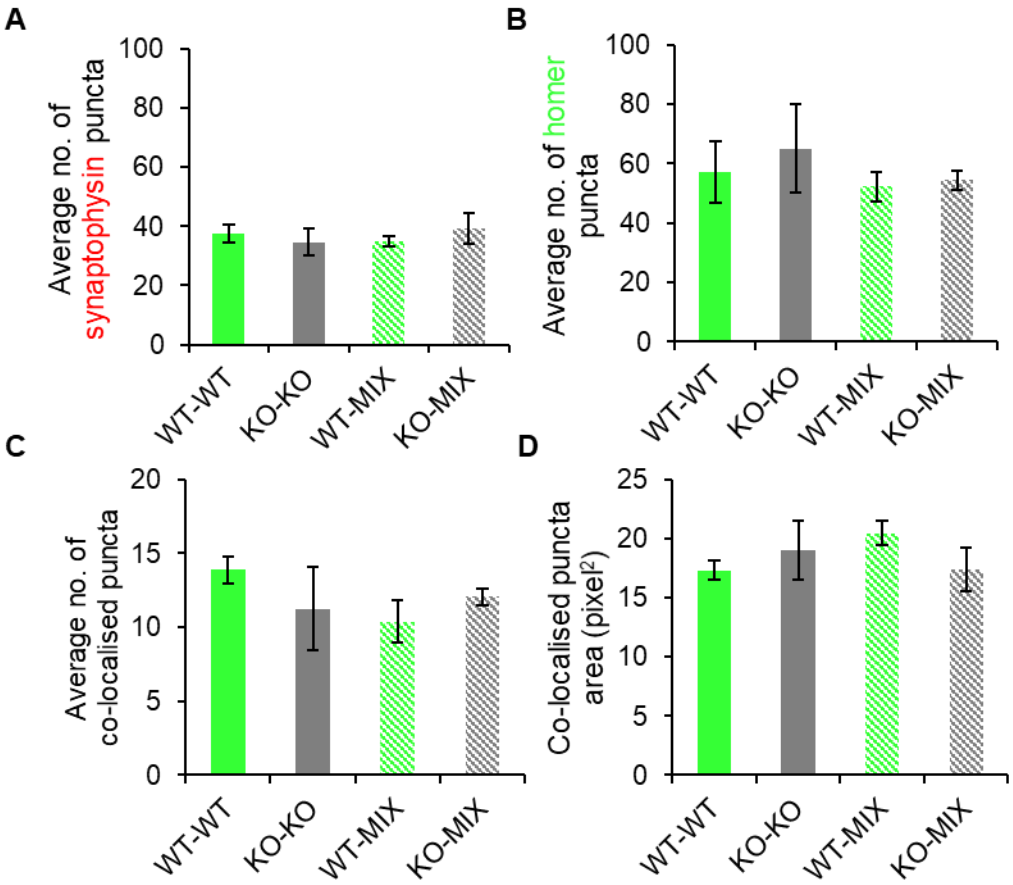

Figure 6.4: PCDH19 does not affect synapse formation at the postsynaptic cell soma in mouse ESC-derived neurons. Synapse analysis of DIV14 Tau-GFP (WT) and *Pcdh19* KO ESC-derived neurons in separate cultures (WT and KO, respectively) and mixed cultures (WT-MIX and KO-MIX, respectively) at the cell soma. **(A)** Quantification of the number of synaptophysin puncta expressed and **(B)** homer puncta expressed per cell soma. **(C)** Quantification of the number of co-localised puncta (Synaptophysin+ Homer+) per cell soma. **(D)** Quantification of the co-localised puncta area (pixel^2). All quantifications were taken from 3 independent differentiations and ≥12 images per differentiation (WT-WT, n=55; KO-KO, n=43; WT-MIX; n=51; KO-MIX, n=43, when n= individual no. of cells analysed). Data represented as the mean ± standard error of the mean. GFP, green fluorescent protein; WT, wild-type; KO, knock-out; MIX, co-culture.

6.2.2.2 Synapse analysis in neuronal processes

When conducting the synapse analysis in neuronal processes, 40 µM x 10 µM regions were selected and quantified. Processes were distinguished using background staining detected when using anti-Homer and verified using bright field visualisation. WT neurons were discriminated from KO neurons by using GFP detection.

Again, a two-way ANOVA was conducted to test the influence of culture condition (WT, KO and MIX) and cell type (WT and KO) on synaptophysin puncta number, homer puncta number, co-localised puncta number, and co-localised puncta area. Consistent with the quantification at the cell soma, there were no significant differences in the absolute number of synaptophysin puncta expressed at the processes (**Figure 6.6A**; WT-WT, 11.47; KO-KO, 11.3; WT-MIX, 9.9259; KO-MIX, 10.708; n=3; Culture condition, *F (2,8) =0.888, P=0.448;* Cell line*, F (1,8) =0.397, P=0.546*; two-way ANOVA). There was a trend towards more homer puncta being expressed in KO processes when compared to WT, independent of the culture condition; however, this was not deemed significant (**Figure 6.6B**; WT-WT, 15.268; KO-KO, 19.044; WT-MIX, 13.887; KO-MIX, 17.082; n=3; Culture condition, *F (2,8) =0.353, P=0.713,*; Cell line, *F (1,8) =1.253, P=0.295*; two-way ANOVA). Furthermore, there were no significant differences in the overall number of co-localised puncta (**Figure 6.6C;** WT, 4.3218; KO-KO, 4.5053; WT-MIX, 3.6667; KO-MIX, 3.5485; n=3; Culture condition, *F (2,8) =1.143, P=0.366*; Cell line, *F(1,8) =0.024, P=0.881*; two-way ANOVA) or synapse area (**Figure 6.6D**; WT-WT, 4.3218; KO-KO, 4.5053; WT-MIX, 3.6667; KO-MIX, 3.5485; n=3; Culture condition, *F (2,8) =0.548, P=0.598*; Cell line, *F (1,8) =0.451 P=0.521*; two-way ANOVA).

Taken together, these detailed quantitative analyses revealed that there were no significant differences in the number of these specific pre- and post-synaptic proteins being expressed (synaptophysin and homer, respectively), the number of synapses being formed, or the density of synapses in WT-WT, KO-KO, WT-MIX, and KO-MIX neurons, at the soma or at the processes. However, differences in the proportion of WT:WT, KO:KO, WT:KO, and KO:WT synapses being formed in separate and mixed cultures could be further assessed to determine whether PCDH19 is altering synaptogenesis in co-cultured mouse ESC-derived neurons. This analysis would require the tracing of KO neuronal processes as well as WT processes (see Discussion).

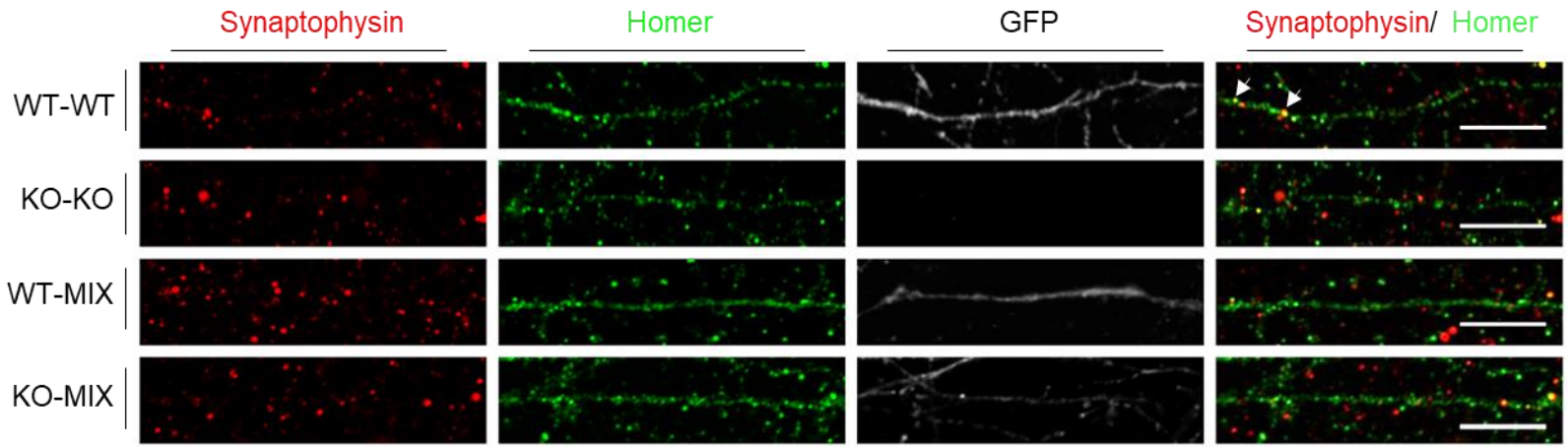

Figure 6.5: Detecting synapses at neuronal processes. Representative single plane images of day *in vitro* 14 *Pcdh19* WT, KO, WT-MIX and KO-MIX processes, immuno-stained with synaptophysin (red), homer (green), and GFP (grey) Arrows indicate examples of co-localised puncta. GFP, green fluorescent protein. WT, wild-type; KO, knock-out. Scale bars: 10 µM.

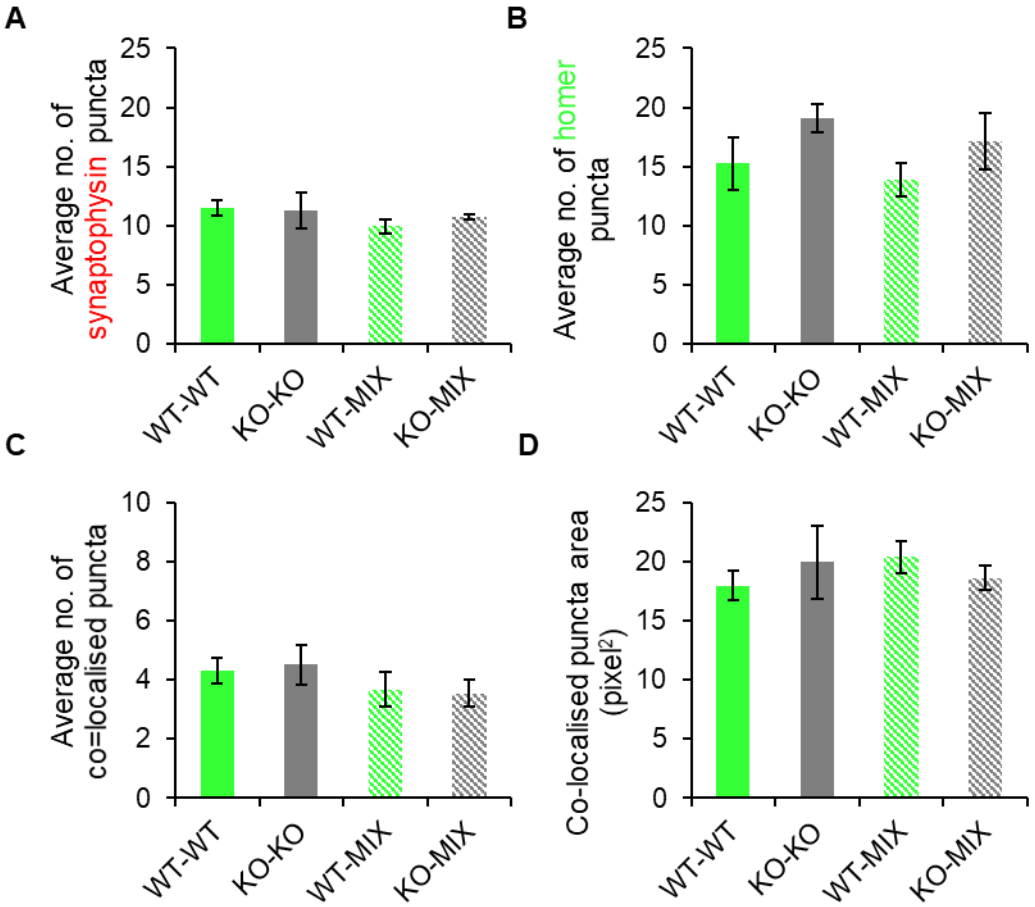

Figure 6.6: PCDH19 does not affect synapse formation at the processes in mouse ESC-derived neurons. Synapse analysis of DIV14 Tau-GFP and *Pcdh19* KO ESC- derived neurons in separate cultures (WT and KO, respectively) and co-cultures (WT-MIX and WT-MIX, respectively). Quantification of **(A)** the number of synaptophysin and **(B)** homer puncta expressed. **(C)** Quantification of the number of co-localised puncta (synaptophysin+ homer+). **(D)** Quantification of the co-localised puncta (synapse) area per region of interest. Data represented at the mean ± standard error of the mean. All quantifications were taken from three independent differentiations and ≥12 images per differentiation (WT-WT, n=62; KO-KO, n=45; WT-MIX; n=51; KO-MIX, n=58, when n= individual no. of processes analysed). Data are represented as the mean ± standard error of the mean. GFP, green fluorescent protein; WT, wild-type; KO, knock-out; MIX, co-culture.

6.2.3 PCDH19 affects spontaneous activity in multi-electrode array (MEA) experiments

Live imaging and histological staining have demonstrated that *Pcdh19* WT and KO cells in separate and mixed cultures form extensive neurite connections and that synapses are formed in both cell lines and cultures. However, this does not determine the electrophysiological functionality of the neurons and whether they are capable of spontaneous electrochemical activity. Therefore, it would be useful to optimise the culture system to be used to assess the mass electrochemical functionality of the neurons in each culture condition.

To conduct an initial assessment of spontaneous activity in WT, KO, and mixed cultures, and to highlight any differences therein, the dissociated aggregates were plated on multi-electrode array (MEA) plates at $5x10^5$ cells per well, and any spontaneous activity was recorded. This plating density was decided after an initial assessment of activity in cells that were plated at $1x10^5$, $2.5x10^5$, $5x10^5$, $7.5x10^5$ cells per well. Little to no activity was recorded at $1x10^5$ or $2.5x10^5$ by DIV10, but activity was detectable in neurons plated at $5x10^5$ and $7.5x10^5$ cells per well.

Electrical signals were generated in ESC-derived neurons from each cell culture, and localised field potential changes (i.e., spikes) were identified using an automated threshold-based spike detection method described in Chapter 2 **Section 2.15**. Spontaneous activity was recorded over a test phase duration of 2 minutes at 37°C, and the spikes were time stamped and imported into a custom-made MATLAB script to conduct a spike and burst property analysis.

Both single spikes and spontaneous bursting activity were observed as early as DIV10 in all cultures. As no recordings were conducted at earlier time points, it is conceivable that activity may be initiated earlier (Barth *et al.* 2014).

The density in these cultures is critical for long-term survival and stable network activity (Bibel *et al.* 2007). As mentioned above, plating at the density used for previous histological experiments ($2.5x10^5$ cells per well) gave little to no burst activity within the network. Hence, to be able to detect early firing in these neurons, cells were plated at a high density ($5x10^5$ per well). This meant that the quality of the neurons declined much faster. Furthermore, neurons at such high densities started to cluster together over time, as opposed to forming a monolayer of cells. This influenced the number of electrodes

detecting extracellular spontaneous firing and produced increased variability between wells. Optimisation of coating substrates and cell density would be needed to ensure cells grew as an evenly distributed monolayer. In future experiments, it would also be useful to assess activity at earlier time points as well, in case the quality deteriorated prior to the DIV10 recordings. Due to these issues with the current MEA plating, synchronicity could not be measured in this experiment and the results presented thus far would need to be further confirmed with an optimised cell plating.

To determine the appropriate DIV to be used for spike and burst analysis, burst count was measured over a 2-minute phase duration in WT neurons from DIV10 to DIV16. It was observed that burst number peaked at DIV10 and plateaued at DIV12 before rapidly declining at DIV14. At DIV16, little to no burst activity was observed. Therefore, to ensure the cells were of the highest quality for the assessment of spike and burst properties, DIV12 neurons were used to compare the different cultures. Six independent differentiations were plated on 6 24-well MEA plates altogether, with 8 wells used for each culture type (8 WT, 8 KO, 8 MIXED wells per plate). Finally, an average recording was taken from each independent differentiation.

6.2.3.1 Analysis of spike properties

To select for active neuronal networks, only electrodes that detected ≥50 spikes per 2-minute recording were assessed. This also ensured that any false-positive neuronal activity that came from background noise was eliminated. The spike frequency, inter-spike interval, and peak-to-peak amplitude of spikes were assessed as depicted in the schematic spike raster plot in **Figure 6.7A**. Firstly, the spike frequency was calculated as the number of spikes over time (total number of spikes/ 120 seconds). A trend towards a lower spike frequency in both KO and mixed cultures compared to WT neurons was observed at DIV12. However, due to the large variability between WT ESC differentiations, this difference was not deemed significant (**Figure 6.7B**; WT, 5.0 (n=6); KO, 2.0 (n=5); MIX, 2.8 (n=6); *F (2,14) =3.129, P=0.075;* one-way ANOVA). Next, the inter-spike interval was calculated as the average time difference between two spikes. No differences were observed in the inter-spike interval at DIV12 (**Figure 6.7C**; WT, 522188 (n=6); KO, 595306 (n=5); MIX, 497451 (n=6); *F (2,14) =0.317, P=0.734;* one-way ANOVA). Finally, the average peak-to-peak amplitude was calculated as the negative spike amplitude subtracted from the maximum spike amplitude. When assessing WT, KO and MIXED cultures it was observed that there were no differences in the peak-to-peak amplitude between cultures (**Figure 6.7D**; WT, 19493315 (n=6); KO, 15446306 (n=5); MIX, 19547152 (n=6); *df=2, test statistic=1.426, P=0.490*; Kruskal-Wallis test).

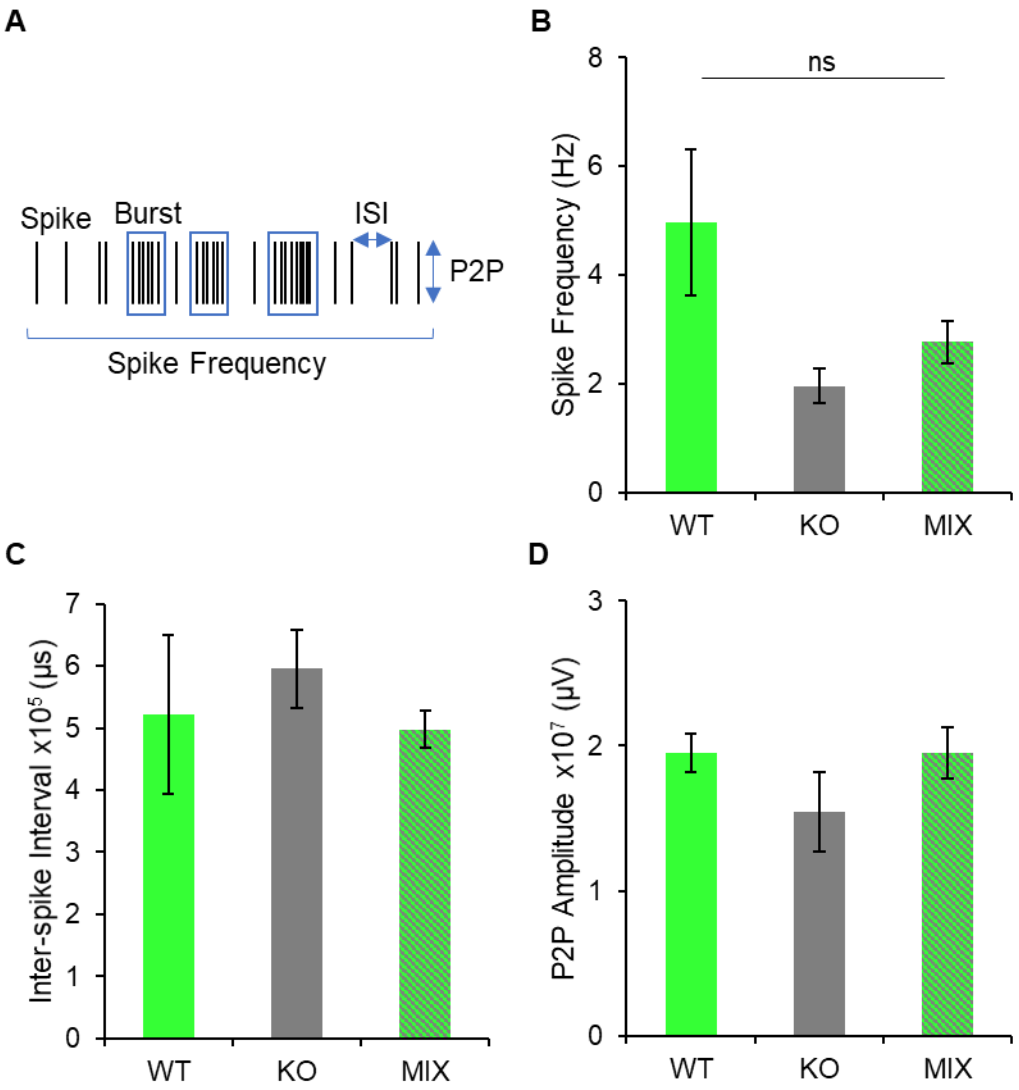

Figure 6.7: PCDH19 does not significantly affect spontaneous spike properties in mouse ESC-derived neurons. **(A)** Schematic representation of a spike raster plot, indicating the difference between a spike and a burst, and the parameters measured during the spike analysis. **(B-D)** Quantitive analysis of **(B)** spike frequency, **(C)** inter-spike interval and **(D)** peak to peak amplitude after 2-minute recordings of spontaneous activity in DIV12 WT, KO, and MIX neurons. Data represented as the mean ± standard error. ISI, inter-spike interval; WT, wild-type; KO, knock-out; Hz, hertz; µs, microseconds; µV, microvolts; P2P, peak to peak amplitude.

6.2.3.2 Analysis of burst properties

Of the electrodes that detected burst activity, the burst frequency, burst duration, and within burst spike frequency was measured as represented in **Figure 6.8A**. As not all independent differentiations gave rise to spontaneous burst activity at DIV12, the analysis was conducted using a minimum of 3 independent differentiations.

First, the burst frequency was calculated as the number of bursts over time (total number of burst / 120 seconds). It was determined that there was a trend towards both KO and mixed cultures having a lower burst frequency than WT neurons at DIV12. However, this again, was not deemed significant (**Figure 6.8B**; WT, 5.0 (n=5); KO, 2.0 (n=3); MIX, 2.8 (n=3); *df=2, test statistic=3.733, P=0.155;* Kruskal-Wallis test). Next, the average burst duration was calculated as the last time point of the burst subtracted from the first time point of that same burst. It was observed that there were no differences in the duration when comparing WT, KO, and mixed cultures (**Figure 6.8C**; WT, 29537 (n=5); KO, 43202 (n=3); MIX, 25833 (n=3); *F (2,8) = 2.213*, *P=0.172;* One-way ANOVA). Finally, the intra-burst spike frequency was calculated as the number of spikes within a burst divided by the duration of a burst. Interestingly, there was a significant difference in the intra-burst spike frequency between the three cultures (**Figure 6.8D**; WT, 167.3 (n=5); KO, 220.5 (n=3); MIX, 176.9 (n=3); *F (2,8) =6.586, P=0.020;* one-way ANOVA). Upon post hoc analysis, KO cultures had a significantly higher intra-burst spike frequency compared to WT cultures, whereas mixed did not (WT 167.3 (n=5) vs. KO, 220.5 (n=3); *P=0.018*; WT vs. MIX, *P=0.804*; Bonferroni post hoc). In addition, there was a trend towards a higher intra-burst spike frequency in KO cultures compared to the mixed culture (KO), 220.5 (n=3) vs. MIX, 176.9 (n=3); *P=0.072;* Bonferroni post-hoc).

Overall, the results indicate that MEA can be used to assess electrical activity in this *in vitro* system; however, optimisation is required for further assessment of network firing. This data suggests that *Pcdh19* KO and mixed neurons may be less excitable than WT (as discussed in **Section 6.3.4.1**). Interestingly, the KO cells had a significantly higher intra-burst spike frequency; an effect that wasn't seen in the mixed culture. As epilepsy causes hyper-excitability and hyper-synchronised firing of neurons, it would be of great interest to optimise the MEA to assess burst synchronicity. Furthermore, it would be of interest to assess if there is an imbalance of excitatory and inhibitory responses, which would be expected if these neurons had an "epileptic" phenotype. Therefore,

pharmacological intervention would be necessary to target excitatory and inhibitory neurons individually. For example, the competitive $GABA_A$ receptor antagonist, bicuculline would block all $GABA_A$ responses, allowing for the assessment of excitatory responses alone.

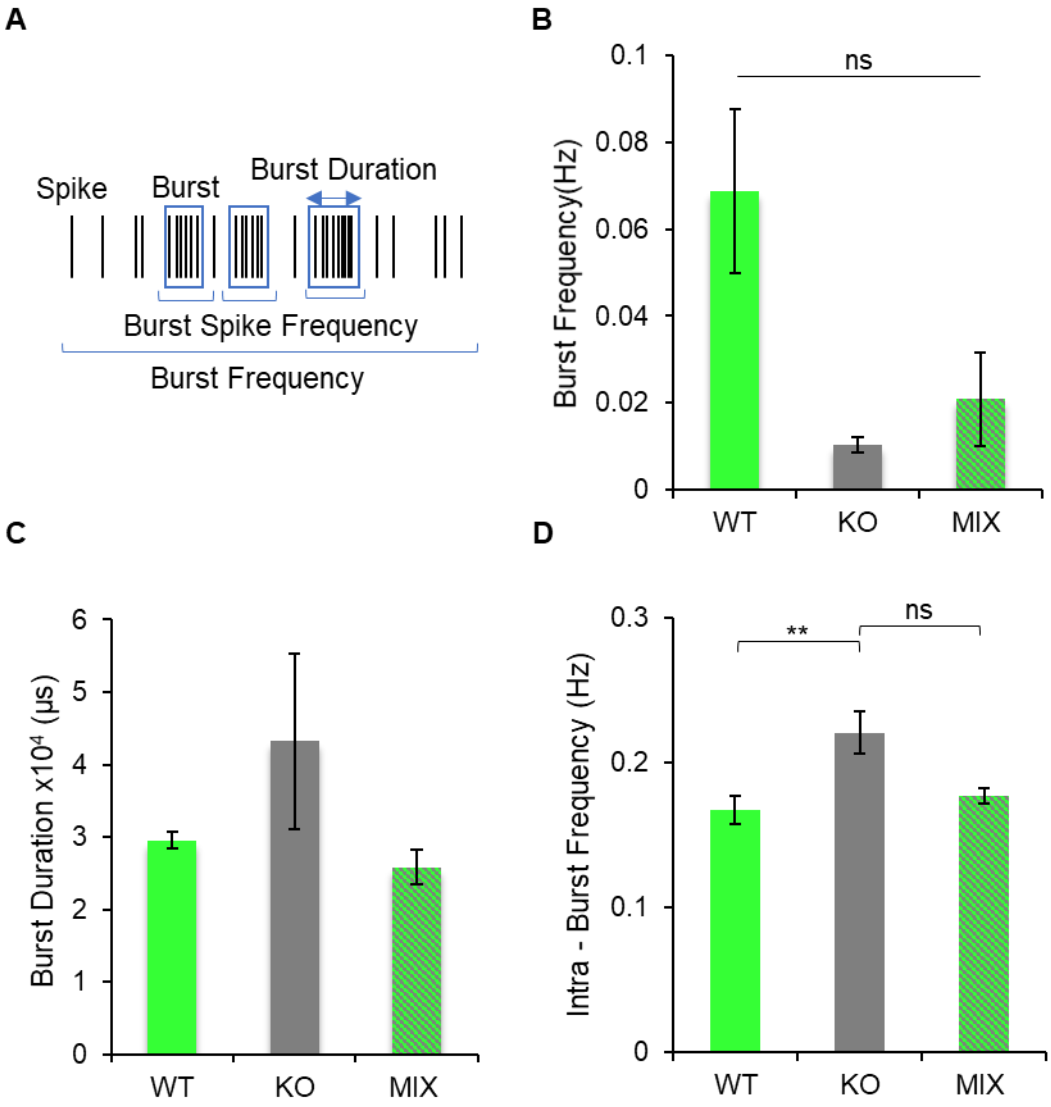

Figure 6.8: Lack of PCDH19 affects burst firing in mouse ESC-derived neurons. Schematic representation of a spike raster plot, indicating the difference between a spike and burst and the parameters measured during a burst analysis. Quantitive analysis of the **(B)** burst frequency, **(C)** burst duration, and **(D)** burst spike frequency after 2 minutes recording of spontaneous activity in DIV12 WT, KO, and MIX neurons. Data represented as the mean ± standard error. WT, wild-type; KO, knock-out; Hz, hertz; µs, microseconds**.**

6.2.4 Assessment of calcium responses in homogenous and mosaic cultures

6.2.4.1 Optimisation of calcium imaging experiments

To study intracellular calcium handling in WT and KO ESC-derived neurons in separate (WT-WT and KO-KO) and mixed cultures (WT-MIX and KO-MIX), potassium chloride (KCl)-evoked intracellular calcium influx was measured using fluorescent calcium indicators and live calcium imaging.

WT and KO NPs were plated on coverslips as separate or mixed cultures, and a total of $2.5x10^5$ cells were plated per coverslip. At DIV15 ± 1DIV, WT, KO, and mixed ESC-derived neurons were loaded with Fura-2 and coverslips were placed under a confocal microscope, connected to a monochromator-based fluorimeter system. Once coverslips were secured, they were continuously perfused with basic extracellular solution (ECS). Neurons were left to habituate under the microscope for a minimum of 30 minutes before recording. Fura-2 was alternately excited at 340 nm and 380 nm, and re-emission was captured at 510 nm in all the cell lines (**Figure 6.9A**). Additionally, GFP signal was effectively captured at 488 nm and used to detect Tau-GFP (WT) neurons that were discriminated from GFP- KO cells within the mixed culture (**Figure 6.9B**; white dotted borders indicate GFP- KO cells within the mixed culture). To record changes in calcium influx over time, regions of interest were selected around individual cell bodies and images were continuously taken every 3 seconds to measure the change in fluorescent signal.

To optimise neuronal calcium responses, neurons were first subjected to 30 seconds pulses of different concentrations of KCl (10 mM, 15 mM, 30 mM, and 60 mM) followed by 300 seconds wash-out with ECS. Results were automatically recorded and expressed as the ratio of fluorescence intensity (340 nm/380 nm) and normalized to the first 30 seconds at the baseline level ($\Delta F/F_0 = (F - F_0) / F_0$, where F represents the average background emission fluorescence intensity, and F_0 represents the baseline F). Individual traces were plotted over time (**Figure 6.9C**). Sharp peaks were seen upon stimulation as voltage-gated calcium channels (VGCCs) opened, allowing calcium to enter the cells, causing there to be an increase in $\Delta F/F_0$. Once KCl was washed out, cells recovered, returning to baseline. A small evoked peak was visible with 10 mM KCl, which increased as the concentration of KCl increased. Recovery to baseline was seen after

cells were subjected to 10, 15, and 30 mM KCl; however, cells failed to recover and reach baseline after being pulsed with 60 mM KCl. Due to the size of the response and recovery, it was concluded that KCl-evoked responses for subsequent experiments would be taken using 30 mM KCl.

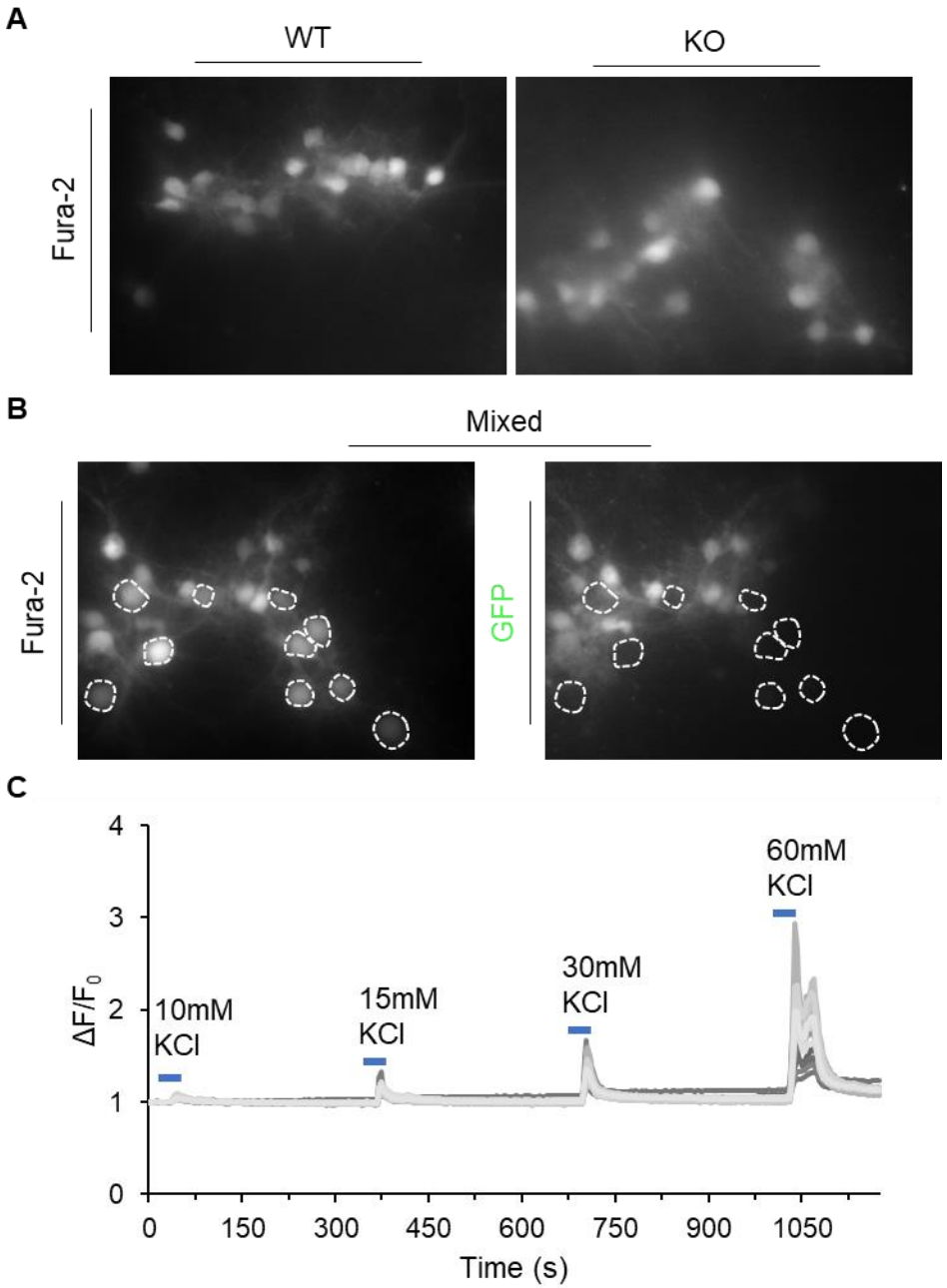

Figure 6.9: Optimisation of calcium imaging in mouse ESC-derived neurons. (A) Representative images of DIV14 WT and *Pcdh19* KO neurons loaded with Fura-2, captured at 510 nm. **(B)** Representative image of WT and KO cells in a mixed culture (WT-MIX and KO-MIX) loaded with Fura-2, alongside detection of GFP in the WT neurons, captured at 488nm. White dotted borders indicate GFP- KO cells in the MIX culture. **(C)** Normalised trace of the ratio of intensity from Fura-2 calcium imaging in DIV14 WT neurons where calcium influx was evoked using increasing concentrations of KCl. Each line indicates the measurements taken from a signal cell trace. WT, wild-type; KO, knock-out; GFP, green fluorescent protein; KCl, potassium chloride; $\Delta F/F_0$, normalised ratio of intensity; s, seconds.

6.2.4.2 PCDH19 affects KCl-evoked calcium responses in separate and mixed cultures

To determine whether there were differences in KCl-evoked calcium responses between WT and *Pcdh19* KO neurons in separate and mixed cultures, calcium influx was analysed using Fura-2, exposing neurons to 30 mM KCL for 30 seconds before wash-out with ECS, as conducted in **Section 6.2.4.1**. Average and individual cell traces were plotted as the normalised ratio of fluorescent intensity over time for each culture and cell type (**Figure 6.10**). It was observed that WT-WT, KO-KO, WT-MIX, and KO-MIX neurons all responded to KCl treatment with an increased calcium influx upon stimulation, with a rise in the ratio of fluorescent intensity and recovery phase back to a baseline level once washed with ECS.

There appeared to be some differences in the individual KCl-evoked calcium responses from each cell line. First, the average peak response was lower in KO-KO, WT-MIX, and KO-MIX cultures, compared to WT-WT. Also, WT responses appeared to be significantly more varied than in the other cell populations. Additionally, both WT-MIX and KO-MIX cell traces had smaller peak responses before and after the highest KCl-evoked peak response (**Figure 6.10**; black arrows). Although these small peak responses could be reflective of a disruptive external or internal influx of calcium (first peak) and a disrupted calcium clearance (last peak), it is likely to reflect an artefact of the perfusion system. In support of this notion, they only appeared in two out of nine recordings, and in all cells from those two recordings. These visual differences between cultures and cells highlighted the need to quantify certain calcium parameters, including the baseline and peak properties. Ratios from individual cells of interest per coverslip were averaged and represent one independent experiment for subsequent baseline and peak measurements. The two recordings which were believed to give a perfusion artefact in the mixed culture were discarded from the quantifications on peak measurements.

The baseline ratio of intensity was calculated as the average baseline over the first 30 seconds before stimulation (F_0). The KCl-evoked responses were next analysed quantitatively. The time to peak, peak amplitude, and recovery time were calculated as depicted in **Figure 6.11A**. A two-way ANOVA was conducted to assess the influence of culture condition (WT, KO, and MIX) and cell type (WT and KO) on baseline intensity and peak properties. No differences were observed in baseline intensity when comparing

groups (**Figure 6.11A**; WT-WT=0.54 (n=9); KO-KO=0.62 (n=7); WT-MIX=0.62 (n=9); KO-MIX =0.62 (n=9); Culture condition, *F (2,29) =2.155, P=0.133*; Cell line, *F (1,29) =0.058, P=0.812;* two-way ANOVA).

Interestingly, upon analysis of the average KCl-evoked peak amplitude, there was a significant difference between groups (**Figure 6.11B;** Culture condition*, F (2,25) =3.461, P=0.047*; Cell line, *F (1,25) =0.001, P=0.971*; two-way ANOVA). Although there were no differences between WT-MIX and KO-MIX neurons (WT-MIX, 1.60 (n=7) vs. KO-MIX, 1.60 (n=7), *P=0.971*; Bonferroni post-hoc) mixed neurons overall had a significantly lower peak amplitude compared to WT neurons (WT, 2.32 (n=7) vs. MIX (WT-MIX, 1.60 (n=7) and KO-MIX, 1.60 (n=7)); *P=0.031*; Bonferroni post-hoc). Although KO neurons also appeared to have a lower peak amplitude compared to WT, this was not deemed significant (WT, 2.32 (n=7) vs. KO, 1.70 (n=8); *P=0.180*; Bonferroni post-hoc). Next, the average time it took for the cells to reach their peak KCl-evoked response from 10% above baseline intensity was quantified. There appeared to be a trend towards a reduced time to peak response in the mixed culture when compared to WT and KO cultures, but it did not reach significance (**Figure 6.11C**; WT=16.36 (n=9); KO=13.79 (n=8); MIX-WT=6.12 (n=7); MIX-KO= 5.87 (n=7); Culture condition, *F (2,25) =2.681, P=0.088*; Cell line, *F (1,25) =0.004 ,P=0.951*; two-way ANOVA). Lastly, the average recovery time was calculated as the time taken to reach 10% above baseline from the peak and it was observed that there were no significant differences between groups (**Figure 6.11D;** WT=60.94 (n=9); KO=72.33 (n=8); MIX-WT=62.77 (n=7); MIX-KO=59.86 (n=7); Culture condition, *F (2,25) =0.460, P=0.636*; Cell line, *F (1,25) = 0.089, P=0.768*; two-way ANOVA).

Taken together, the results indicate that calcium imaging can be used to study PCDH19 co-cultures. It was shown that both KO and mixed cultures had a lower KCl-induced calcium response compared to WT cultures. Although there were no significant differences in the time to peak response, there was a trend towards a reduced time in the mixed culture compared to the separate cultures. This may be an indication of a delayed opening of VGCCs or a different proportion of certain VGCCs. However, with some unusual smaller peak responses in the mixed cultures further recordings and pharmacological blockade of the different VGCC would be required to confirm this response.

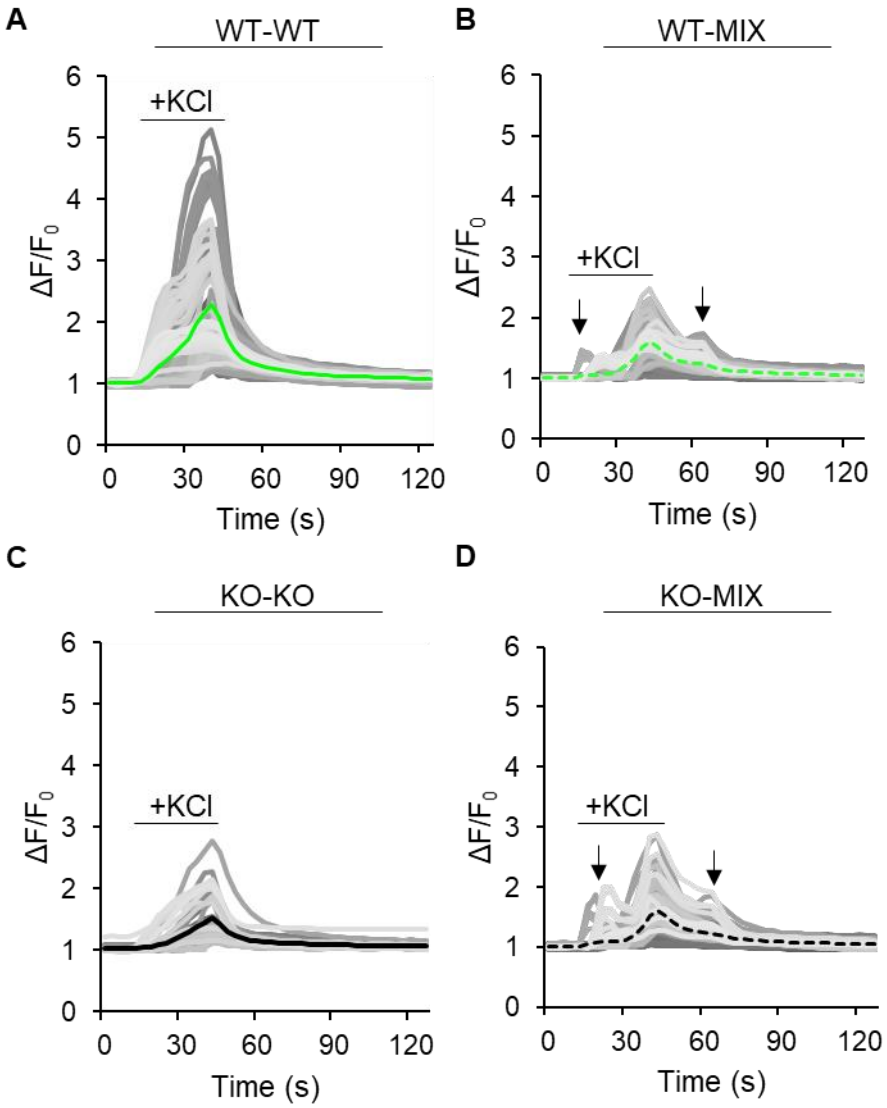

Figure 6.10: KCl-evoked calcium responses vary in WT and *Pcdh19* KO cells from separate and mixed cultures. KCl-evoked calcium influx in WT (**A and B**; green lines) and *Pcdh19* KO (**C and D**; black lines) at DIV15 ± 1DIV neurons in separate (**A and C**; bold line) and mixed (**B and D**; dotted line) cultures recorded using *in vitro* calcium imaging. Data represented as normalised traces of the Fura-2 ratio of intensity ($\Delta F/F_0$). All greyscale lines represent single-cell traces and highlighted lines (green and black) show the average trace per cell type. Black arrowheads indicate small peak responses before and after the KCl-evoked peak response in mixed cultures. KCl, potassium chloride; WT, wild-type; KO, knock-out; s, seconds.

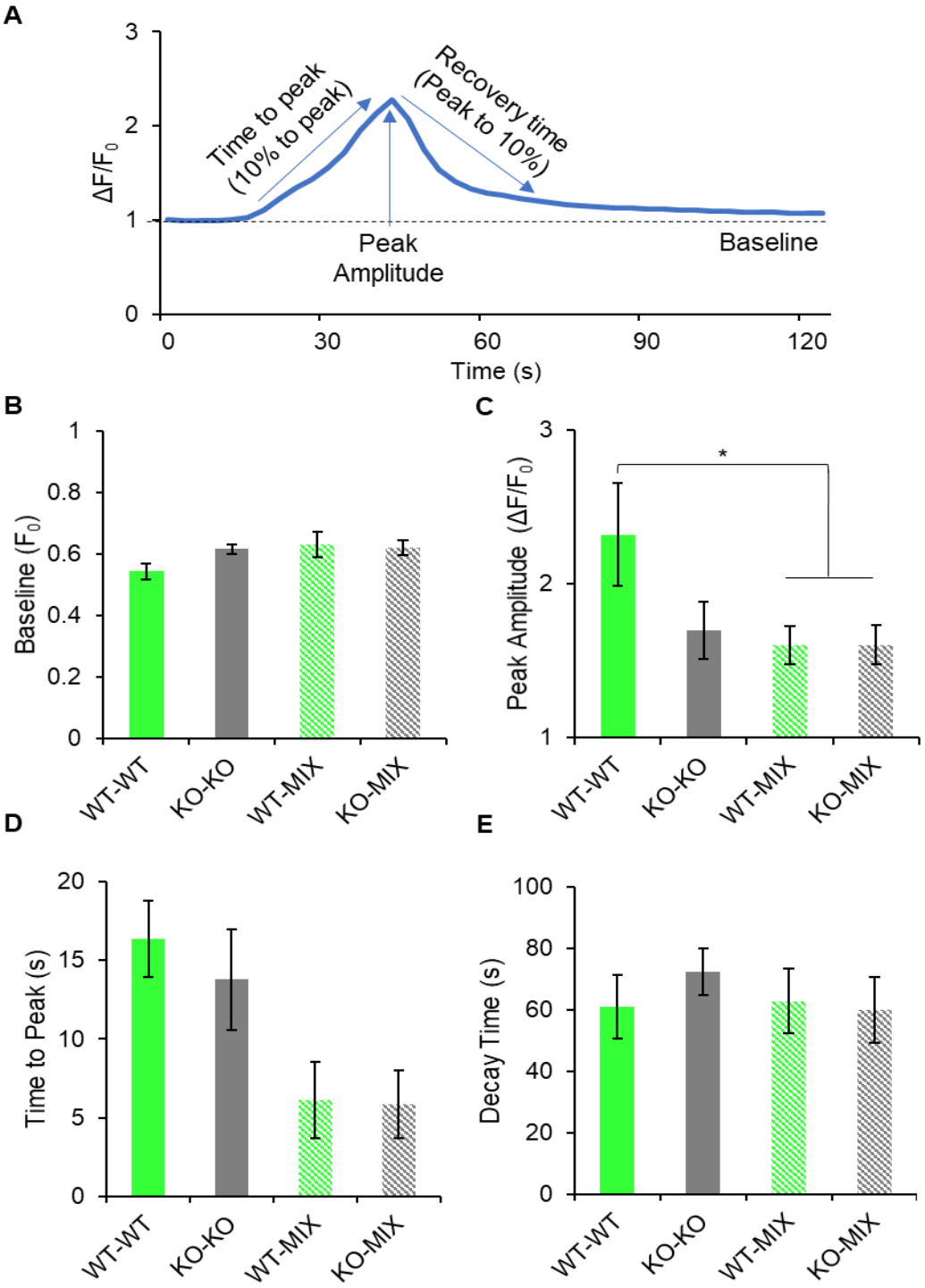

Figure 6.11: PCDH19 affects KCl-evoked calcium influx in separate and mixed cultures. (A) Graphical representation of the parameters measured during KCl-evoked calcium influx. DIV15 ± 1DIV WT, KO, WT-MIX and KO-MIX neurons quantifications of **(B)** baseline values, **(C)** peak amplitude, **(D)** time to peak, and **(E)** recovery time. Data represented as the mean ± standard error. WT, wild-type; KO, knock-out, s, seconds.

6.3. Discussion

This chapter focused on a novel co-culture system developed as a disease model relevant to EIEE9 and mimicking the PCDH19 mosaicism found in heterozygous females and somatically mutated males. To achieve this, Tau-GFP (WT) and *Pcdh19* KO NPs were mixed to generate a 1:1 co-culture that formed maturing neuronal networks over time; similar to those seen in separate WT and KO neuronal cultures in Chapter 5. Importantly, within the co-culture, it was possible to detect a GFP signal in the Tau-GFP WT neurons, to discriminate WT cells from KO in live and fixed cultures. Using this system, preliminary studies were conducted to assess synapse number and neuronal activity. From these initial studies, it was found that there were no overall differences in synapse number or density when assessing the post-synaptic cell in separate and mixed cultures. However, this synapse analysis did not take into consideration the type or proportion of synapses formed within the co-culture; therefore, further experiments are required to study these specific synaptic connections. Furthermore, MEA and calcium imaging techniques were tested using these neurons, to determine whether electrophysiological properties could be measured with this co-culture system. Interestingly, preliminary results revealed differences in neuronal activity in KO and co-cultured neurons that may open new avenues for further research into PCDH19 mosaicism and synaptic function.

6.3.2 An in vitro co-culture system was generated to study PCDH19 mosaicism

There were two possible time points during the differentiation procedure in which the WT and KO cells could be mixed: before and after cellular aggregation. However, neural induction and neurogenesis during cellular aggregation is complex and variable. In addition, in the previous Chapter it was found that the *Pcdh19* KO line generated a lower absolute number of cells than WT during the aggregation process; therefore, a pre-aggregation mixing of the two progenitors may have favoured WT cells differentiating over KO cells and so the ratio of WT to KO neurons could have been skewed. Consequently, to reduce the complexities and ensure a 1:1 ratio, WT and KO progenitors were mixed just before NPs were plated. Once plated, the progenitors homogenously mixed and differentiated into interconnected neuronal networks, that were able to form synapses and exhibited neuronal firing activity.

There has been one recently published study that used mouse progenitor cells and human induced pluripotent stem cell (iPSC)-derived neurons to generate a co-culture system to study PCDH19 during neurogenesis (Homan *et al.* 2018). However, a disadvantage of this system was that WT and KO neurons were not differentially labelled and could not be discriminated from one another. By contrast, the co-culture system described in this Chapter illustrates an efficient way of discerning between WT and KO cells as a result of GFP expression in the WT cells. This distinction is relevant because, as seen when studying progenitor behaviour in the developing heterozygous cortices in Chapter 4, PCDH19 expressing and non-expressing neurons in the mixed cultures could show different electrophysiological properties, behaviours or connections. However, it is important to note that in the WT culture a sparse number of cells did not express GFP, therefore emphasising the need to trace the KO neurons as well as the WT in future experiments. It is also possible that the WT cells that are GFP negative are non-neuronal, but this would need to be clarified using neuronal-specific markers and quantitative analysis.

One disadvantage of this *in vitro* culture system is the inability to mimic the cortical architecture. This is particularly important to consider when comparing *in vivo* and *in vitro* results as it has been previously published and found in Chapter 3 that PCDH19 expressing and non-expressing cells segregated from one another during early cortical development, which leads to an asynchronous proliferation of KO and WT cells (Pederick *et al.* 2018). Furthermore, work conducted in the Martinez-Garay laboratory has shown that the progeny of these progenitor cells continues to develop in segregated "columnar-like" regions during postnatal stages. In this *in vitro* system, WT and KO cells were mixed homogeneously and shown to be extensively interconnected without any apparent segregation. Furthermore, due to the networks being highly intermixed it was not possible to trace single neurons processes and connections. Therefore, the possibility that the *in vitro* results represent an artefact cannot be completely ruled out, which emphasises the need for *in vivo* experiments to be conducted to clarify any phenotypic features found in these co-cultures.

6.3.3. Lack or mosaic expression of PCDH19 did not alter overall synapse number

A primary aim of this Chapter was to understand the pathogenic mechanism of EIEE9 and to determine whether the cellular interference theory was correct. Therefore, the hypothesis that states that there is a disruption in synaptic contacts between PCDH19 expressing neurons and PCDH19 non-expressing neurons was challenged. In previous work, PCDH19 has been localised to synapses and synaptosome fractions *in vivo* and synapses *in vitro* (Pederick *et al.* 2016). In contrast, PCDH19 was found not to be a constitutive component of formed synapses in hippocampal neurons showing minimal co-registration with pre and post-synaptic proteins and only 30% co-registration with synapses (Hayashi *et al.* 2017). Using the co-culture system established, synapse number and density were assessed in the “cortical-like” neurons around the cell soma and in the processes.

When assessing the number of synapses formed in *Pcdh19* WT, KO, and mixed cultures, it was determined that there were no differences in synapse number or density. It is important to note that *Pcdh19* KO cultures were able to form synapses similar to WT neurons. Hence, complete lack of PCDH19 did not alter the formation of synapses. This correlates with there being no aberrant changes in electrocorticogram network activity when assessing cortical neurons in KO mice (Pederick *et al.* 2018) and no epileptiform features of the disorder in *PCDH19* hemizygous males (Dibbens *et al.* 2008; Depienne *et al.* 2009). It could be hypothesised that within the KO culture, PCDH19 is being compensated for with a closely related δ2-protocadherin such as PCDH10 or PCDH17. Bisogni *et al*. found that the loss of one δ-protocadherin can alter the combination and relative surface expression of the co-expressed δ-protocadherins, supporting the notion that there could be a compensation in KO cultures (Bisogni *et al.* 2018). An alternative hypothesis could be that PCDH19 on its own is not essential during synapse formation or neuronal activity.

The question remains whether the notion of cellular interference is correct, i.e. whether cell communication is altered in a mixture of neurons expressing and not expressing PCDH19, leading to an epileptic phenotype. As KO neurons were not fluorescently labelled during this experiment, it was not possible to conduct an analysis that further looked at the proportion of the different types of synapses formed within the co-culture

(i.e., WT:WT, KO:KO, WT:KO, and KO:WT pre- and post-synaptic connections). Although there were no substantial differences in overall synapse number, synapse formation and function within the co-culture system could still be affected. For example, WT:WT and KO:KO synaptic connections may be favoured over WT:KO and KO:WT. An alternative hypothesis may be that WT:KO and KO:WT synaptic connections alter synaptic function. To test these hypotheses, a KO cell line expressing another fluorescent protein, such as blue fluorescent protein (BFP) from the *Mapt (tau)* locus would be useful to trace the synaptic connections made by KO neurons. Interestingly, Garcia *et al*. have shown how it is possible to use a genetically modified rabies virus for retrograde trans-synaptic circuit tracing, engineering an ESC line incorporating a fluorescent reporter, the Rabies-G glycoprotein, and the avian TVA receptor into the ROSA26 locus (Garcia *et al.* 2012). Once these cells are infected with the rabies virus functionally connected neurons can then be visualised. This would be particular interesting to use in a PCDH19 mosaic culture to study whether *Pcdh19* KO and "WT" neurons present with defects in circuit formation.

If a disruption in connectivity is found in these co-cultures, this could be due to mosaic expression of PCDH19 altering specific cadherin combinational codes required for correct synapse formation and function. As mentioned in **Section 6.3.1**, cadherin specificity is vastly studied as a mode of molecular diversity that is required to initiate and regulate normal synaptogenesis and circuit formation (Krishna-K *et al.* 2011; Friedman *et al.* 2015; Mountoufaris *et al.* 2017; Bisogni *et al.* 2018). Cellular adhesive outcomes have been found to be dependent on which δ-protocadherins are co-expressed in cis; therefore, altered expression of PCDH19 could prevent certain synapses being formed or change synapse functionality (Pederick *et al.* 2018).

Although not studied in this chapter, it would be interesting to assess dendritic morphology. Interestingly, clustered protocadherins play a role in regulating dendritic morphology in cortical neurons (Garrett *et al.* 2012; Suo *et al.* 2012; Molumby *et al.* 2016). Furthermore, clustered protocadherins are expressed in ESC-derived neurons (Wada *et al.* 2018). δ-protocadherins can alter the adhesive affinities of clustered protocadherins (Bisogni *et al.* 2018); therefore, it could be hypothesised that PCDH19 mosaicism could lead to disruptive dendritic branching through the alteration of clustered protocadherin's adhesiveness. Dendritic morphology has been studied previously and Hayashi *et al.* observed that there were no differences in apical and basal dendritic

morphology in either *Pcdh19* KO or HET layer Va mouse cortical neurons (Hayashi *et al.* 2017). However, using this method, it was not possible to trace whether the dendrites studied within the HET cortex were PCDH19 expressing or PCDH19 non-expressing cells, which could affect the results. Contradictory to the Hayashi *et al.* paper stating that there were no differences in dendritic morphology, Bassani *et al*. found that PCDH19 knockdown reduced and increased the lengths of rat hippocampal apical and basal dendrites, respectively (Bassani *et al.* 2018). In this experiment, a mosaic environment was created, therefore, it is possible that PCDH19 mosaicism was the driver of this phenotype, complementing the hypothesis described above. Alternatively, effects may be different in cortical and hippocampal neuronal subtypes. In summary, alongside the analysis of synapse number and proportions, it would be interesting to use dendritic markers to assess morphological properties of individual cells in a separate and co-cultured environment, studying length and outgrowth in individual cells in separate and mixed cultures.

In addition, PCDH19 function in intracellular signalling could be vital in the assembly of synapses. PCDH19 is known to interact with the WAVE regulating complex via its WIRS binding domain and is able to enhance Rac1-mediated WRC activation to regulate actin cytoskeleton dynamics (Tai *et al.* 2010; Hayashi *et al.* 2017). Correct maintenance of actin cytoskeleton is vital for dendritic spine function and neuronal connectivity (Spence and Soderling 2015), therefore, the *Pcdh19* knockdown experiment described above that showed an alteration in dendritic morphology in GABAergic neurons, also points towards a role of PCDH19 in cytoskeleton organization and possibly microtubule dynamics (Bassani *et al.* 2018). Supporting this theory, several other protocadherins have been shown the regulate microtubule dynamics (Keeler *et al.* 2015). PCDH19 also binds to non-POU domain-containing octamer binding protein p54nrb/NONO (NONO), an RNA- and DNA binding protein that plays multiple roles in gene expression regulation (Pham *et al.* 2017). Loss of NONO is associated with human intellectual disability and NONO-deficient mice have defects in GABAergic synapse formation (Mircsof *et al.* 2015). Therefore, PCDH19 may play a role in gene expression required for synapse function.

In summary, using a mouse ESC-derived neuronal culture system, PCDH19 was found not to be a constitutive component required for synapse formation on its own. However, further experiments are required to determine whether there are differences in the proportion or distribution of synaptic connections in the co-culture. Furthermore, if

differences are observed it is possible that a mixture of PCDH19 expressing and non-expressing could alter specific combinational codes that are required during various stages of synapse formation, including dendrite elongation.

6.3.4. PCDH19's effect on neuronal activity indicates there may be alterations in connectivity and cellular composition

6.3.4.1. Alterations in neuronal activity found using MEA

MEA allows for the long-term, non-invasive visualisation of neuronal activity in multiple neuronal populations. MEA can be used to model the epileptic phenotype present in many disorders. Normal activity is asynchronous, however when a seizure occurs deficits in neuronal activity and communication can be visualised as hyper-excitability and hyper-synchronised spontaneous burst firing of multiple neurons. For example, using MEA, higher-frequency firing, and synchronous activity has been observed in mouse hippocampal neurons with mutations in *SCN1A,* the most commonly mutated gene in epilepsy (Hedrich *et al*. 2014). To determine whether the co-culture had an "epileptic" phenotype, it was of particular interest to study firing activity and burst synchronicity within the neuronal network. Moreover, this assessment could determine if the co-culture was an appropriate *in vitro* disease model to study PCDH19 mosaicism and to elaborate on the physiological functions of PCDH19.

Unfortunately, there were multiple issues with the plating of the cultures that may have affected the results found thus far. Firstly, the culture quality declined much faster on the MEA plates than on regular plates, which in part could have been due to the high density required to detect activity in these cultures. Furthermore, neurons tended to cluster over time, which increased the variability and the likelihood that some electrodes were not coming into contact with any neurons; preventing a reliable analysis of burst synchronisation across electrodes. It is therefore necessary to optimise the MEA procedure to tailor it for this *in vitro* system for further functional studies to be conducted. Using a different coating substrate may enhance the survival, attachment and distribution of neurons; coating substrates optimised previously for recordings of activity in iPSC, and human ESC-derived neurons included Matrigel and polyethylenimine (PEI) (Heikkilä *et al.* 2009; Telezhkin *et al.* 2015). In addition, using glass-bottom MEA plates would allow for the study of cell morphology and culture over time as the cells were not visible

using the MEA plates available. Moreover, cell viability assays would be useful during the optimisation of the protocol.

Despite these plating issues, all cultures were able to fire spontaneous bursts. WT firing activity appeared to be considerably more variable than in *Pcdh19* KO or mixed neurons. As different cortical cell-types have distinctive physiological and morphological properties (Feldmeyer and van Aerde 2013), it is possible that the variability stems from the electrodes recording certain neuronal subtypes in the WT networks, and the lack of variability in the *Pcdh19* KO and mixed neurons may be due to an altered proportion of certain neuronal cell types. However, this is not the most likely explanation, as KO and WT cultures expressed the same cortical cell markers and in similar proportions (Chapter 5), even if it was not always possible to determine statistically whether there were differences in the proportion of certain cell types. Alterations in physiological properties are therefore a more plausible explanation.

Although the frequency of spike and burst activity was not significantly different between cultures, there was a trend towards KO and mixed cultures being less excitable overall, suggesting that the connectivity within these networks is less effective. Although these preliminary results would need to be confirmed, it was interesting to note that KO cells had a considerably higher intra-burst spike frequency when compared to both WT and co-cultured neurons. Given the link between PCDH19 and EIEE9, it will be important to extend these observations in future experiments. Burst firing reflects the orchestrated interaction of neurons and is governed by the level of presynaptic firing, connective responses, and the balance of excitation and recovery and is directly related to threshold potentials, current densities, and input resistance. Therefore, it would be of interest to study whether there are alterations in these primary cell-intrinsic properties using whole-cell patch clamping. Moreover, bursting plays a role in synaptic plasticity and information processing, signifying the development of new synapses and networks (Maeda *et al.* 1995; Lisman 1997). Taken together, certain intrinsic cellular parameters or network connections could be altered in cultures lacking of mosaically expressing PCDH19.

Using iPSC-derived neurons from patients with EIEE9 (i.e., mixed PCDH19 expressing and non-expressing neurons), it was observed that the patient-derived neurons were more excitable, exhibiting an increased mean firing rate and burst frequency compared to WT neurons (PCDH19 Alliance Biennial Professional and Family Conference, 2018).

This discrepancy between results may be due to the issues that arose during the plating of “cortical-like” neurons on the MEA plates or may be due to differences between mouse and human neuronal development as discussed in more depth in the general discussion.

In Chapter 5 and previously published, a percentage of the neurons generated from this differentiation protocol are GABAergic: 5-10% of cells expressed glutamic acid decarboxylase 65/67. Epileptic seizures are the most relevant phenotype in EIEE9 and are a consequence of excitatory and inhibitory imbalances in neurotransmission, which leads to the hyper-excitability and hyper-synchronised burst firing of multiple neurons. The measurement of spontaneous activity conducted in these cultures did not discriminate between excitatory or inhibitory neurons. Therefore, the spike and burst activity analysed could have come from either excitatory or inhibitory neurons. Moreover, the cytoplasmic region of PCDH19 was found to bind to the $GABA_A$ receptor alpha subunit and can regulate receptor surface availability, while downregulation of PCDH19 reduced the excitability of inhibitory hippocampal neurons (Bassani *et al.* 2018). Therefore, for future experiments it would be useful to use a $GABA_A$ receptor antagonist, such as bicuculine, to block fast inhibitory neurotransmission in each culture. This would allow the isolation of excitatory neuron transmissions to determine whether unusual activity in either KO or mutant cultures is due to an effect of PCDH19 on inhibitory or excitatory transmission, or both.

Overall, preliminary MEA data revealed that PCDH19 may be altering neuronal activity in mouse ESC-derived “cortical-like” neurons. With further optimisation of this MEA system, further studies could be conducted to measure burst synchronised activity, and excitatory and inhibitory transmission in WT, KO, and co-cultures, to determine whether this *in vitro* system is an appropriate disease model of EIEE9 and to determine the function of PCDH19 in neuronal transmission.

6.3.4.2. Alterations in KCl-evoked calcium responses found using calcium imaging

In an excitatory neuron, transient calcium influx is reflective of the availability and efficiency of the opening of calcium channels at the cell surface (including VGCC’s, α-amino-3-hydroxy-5-methyl-4-isoxazolepropionic acid (AMPA), N-methyl-D-aspartate (NMDA) glutamate-type receptors, nicotinic acetylcholine receptors, and transient receptor type C (TPRC) channels) and the calcium-induced calcium release from the

internal stores (that is mainly from the endoplasmic reticulum (ER) through inositol triphosphate receptors and ryanodine receptors). Following KCl-evoked depolarisation, it was observed that mixed neurons had a significantly lower peak calcium response compared to WT neurons. Although not significant, KO neurons also behaved similarly to the co-cultures. This result indicates that the amount of calcium entering the cell after stimulation is reduced in cultures with altered expression of PCDH19. A possible explanation could be that alteration of PCDH19 causes a disruption in the availability or distribution of certain calcium channels at the cell surface. Interestingly, mass spectrometry data from the Martinez-Garay laboratory after immunoprecipitation of PCDH19 from the adult mouse cortex have revealed interactions with the voltage-dependent L-type calcium channel subunit beta 3 and beta 4 (Cacnb3 and Cacnb4, respectively), and calcium voltage-gated channel auxiliary subunit gamma 8 (Cacng8), which is a type I transmembrane AMPA receptor regulatory protein. Hence, PCDH19 may by modulating these receptors. Thus, it would be interesting to use calcium channel blocker experiments, for example, blocking L-type calcium channels using Nifedipine or nimodipine, and AMPA channels using the competitive AMPA/ kainate receptor antagonist, cyanquixaline (6-cyano-7-nitroquinoxaline-2,3-dione) (CNQX), to measure the percentage inhibition in KCl-evoked calcium responses, comparing WT, KO and mixed neuronal cultures (WT-MIX and KO-MIX). Moreover, it would be interesting to determine whether PCDH19 was affecting calcium-induced calcium release from the internal stores. Using the same method, the percentage inhibition of the KCl-evoked responses could be measured in combination with ryanodine receptors antagonist, Dantrolene, for example.

Although not the most likely explanation, it remains a possibility that there are differences in the expression of cell types in each culture as described in **Section 6.3.4.1**. It is known that different cortical cell-types in the mammalian cortex show different distributions and densities of calcium channel types (Giffin *et al.* 1991). Therefore, it is possible that the change in KCl-evoked response is due to differences in the proportion of specific cells between cultures. This explanation highlights the need to optimise the staining procedure to clarify the preliminary characterisation conducted of the cultures so far.

Interestingly, WT cells within the mixed culture respond differently to those in a WT culture (reduced peak amplitude response in compared to WT cultures). How PCDH19 could be involved in this differential behaviour is not known, but, it is possible that the

altered behaviour is due to a trans-synaptic regulatory effect. Excitatory synapses formed between individual cortical neurons can have differential signalling effects, depending on the target neuron (Markram *et al.* 1998). When co-cultures of N-cadherin KO and WT neurons were generated, pre-synaptic absence of N-cadherin led to a reduction in synaptic responses to a single action potential in excitatory neurons, whereas post-synaptic absence had no effect (Jüngling *et al.* 2006). Similarly, presynaptic absence of *Pcdh19* could be causing a post-synaptic WT neuron in the co-cultured environment to reduce its stimulus-evoked response.

Although the calcium imaging data collected so far is very preliminary, there are some interesting avenues of research that could be considered for future experiments to understand the physiological properties of *Pcdh19* WT, KO, and mosaic neuronal cultures. As the time course and amplitude of the calcium response is mostly dependent on the distribution and efficiency of calcium entry mechanisms and calcium binding proteins, a starting point would be to study PCDH19's effect on certain calcium channels, particularly those that have been shown to interact with PCDH19.

6.3.5 Concluding remarks

In summary, a novel mouse ESC-derived neuronal co-culture system has been generated to study PCDH19's role in synaptogenesis and to study the theory of cellular interference. *Pcdh19* KO and WT neurons were distinguishable in the co-culture system due to the Tau-GFP reporter in the WT ESC-derived neurons, making this system highly advantageous when studying differential behaviour between neurons expressing and not expressing PCDH19. During a preliminary assessment of synapse formation, no differences were observed in the number or density of synapses formed in WT and KO cells in separate and mixed cultures. However, as the KO neurons were not labelled with a fluorescent marker it was not possible to study the proportion of certain synaptic connections (WT:WT, KO:KO, WT:KO, KO:WT) within the co-culture system. It was also determined that this co-culture system could be used to measure neuronal activity via MEA and calcium imaging experiments. Although very preliminary, KO and mixed neurons have an altered excitability and a reduced KCl-evoked calcium response when compared to WT neurons, opening up new avenues of research, assessing aberrant network activity and specific calcium entry mechanisms and calcium-binding proteins in association with PCDH19.

Chapter 7: General Discussion

The results obtained in this thesis show that PCDH19 plays a role in mouse cortical neurogenesis *in vivo.* Also, a new ESC-derived neuronal co-culture system has been generated to determine a putative role of PCDH19 in synapse formation and connectivity. It has been revealed that PCDH19 does not affect the overall number of synapses formed in this system, but that physiological properties appear to be altered in both PCDH19 KO and co-cultures.

7.1 Summary of the role of PCDH19 in neurogenesis

By using *in situ* hybridisation combined with immunohistochemistry, *Pcdh19* mRNA was found to be expressed in the proliferative region of the mouse developing cortex, in a spatial and temporal pattern that was complementary to the neurogenic gradient. With high expression juxtaposed to proliferating radial glial cells (RGC) and downregulated expression in regions populated by intermediate progenitor cells (IPC), it was proposed that PCDH19 could be playing a role in RGC maintenance. Moreover, *Pcdh19* was found to be expressed transiently in early future subplate cells and potentially in Cajal-Retzuis cells or interneurons at the preplate. Interestingly, when using the *Pcdh19* KO mouse model, it was found that complete lack of PCDH19 did not have an impact on neurogenesis. However, in the early developing *Pcdh19* heterozygous (HET) mouse cortices, an unusual cell sorting arrangement of PCDH19 expressing and non-expressing progenitors existed, which correlated with an altered progenitor behaviour that was dependent on PCDH19 expression. By combining β-galactosidase as a reporter to detect *Pcdh19* KO cells with EdU labelling, it was found that within the HET cortex PCDH19 non-expressing (PCDH19-) regions had an increased fraction of mitotic cells, cells in S-phase, and cells leaving the cell cycle at E11.5, relative to the PCDH19 expressing (PCDH19+) regions. Matching this observation, PCDH19- regions contained more IPCs and early-born neurons and less RGCs compared to PCDH19+ regions. Hence, it appeared that cells that lacked PCDH19 within the HET brain underwent premature neurogenesis, whilst PCDH19+ cells also altered their neurogenic behaviour, leading to an overall compensation of this change. Although the mechanism by which this occurs is still unknown, it appears that this shift in progenitor behaviour was not due to an increase in direct neurogenesis, as demonstrated by the lack of differences in Tis21

positive RGC progenitors. Importantly, when comparing the cell cycle parameters and cell-types in the WT, KO, and HET cortices overall, there were usually no differences, meaning that the aberrant changes seen between the two cell populations were cancelled out at the whole cortex level. Interestingly, it appeared that PCDH19+ cells within the HET cortex compensated for the premature neurogenic behaviour of the PCDH19- cells. Whether this compensation is intrinsic to the molecular mechanisms at play or is due to a wider regulatory process remains to be investigated.

As explained in more detail in Chapter 4 **Section 4.3.2**, incompatible binding affinities between PCDH19+ and PCDH19- RGCs may, in part, be causing the segregation of PCDH19+ and PCDH19- progenitor cells in the developing cortex. This segregation could lead to the changes in neurogenic behaviour as it could affect direct communication between RGC cell populations or cause differential responses to external signals due to deviations in cellular composition. Changes in cellular and molecular characteristics such as spindle orientation, the inheritance of cell fate determinants, or differential signalling through certain molecular pathways (e.g. Notch, Slit/Robo, FGF) may cause these variances in progenitor behaviour. Moreover, these factors may not be mutually exclusive. This unusual progenitor cell behaviour also indicates that the proportion of cells that are PCDH19+ or PCDH19- in each PCDH19-expressing layer of the HET cortex may be altered, potentially contributing to any alterations in connectivity.

7.2 Summary of the role of PCDH19 in synapse formation and function

To study the role of PCDH19 in synaptogenesis and connectivity, an *in vitro* system of ESC-derived “cortical-like” neurons was chosen. Pure cultures of *Pcdh19* KO neurons, and mixed cultures of PCDH19 expressing (Tau-GFP; WT) and non-expressing (*Pcdh19* KO) cells plated at a 1:1 ratio were established. This system proved to be highly advantageous as WT and *Pcdh19* KO neurons could be discriminated from one another within the mixed culture, both during immunohistochemical synapse analysis, and during live electrophysiological studies. Both KO and mixed cultures were able to generate maturing neurons that formed synapses and were electrophysiologically active. A preliminary analysis of synapse number and density revealed that PCDH19 did not affect overall numbers in KO or mixed cultures relative to WT cultures (even when assessing the WT and *Pcdh19* KO neurons individually in the mixed culture); however, it is essential

to expand on this analysis to further consider the proportion of certain synaptic connections within the mixed culture by tracing the KO neuronal contact sites as discussed in **Section 6.3.3**. These results could then shed light on whether there is a skewing of connections that would support the theory of cellular interference.

MEA experiments revealed that KO cultures had an increased intra-burst excitability, and although not significant, both KO and mixed cultures had reduced excitability, indicating that there may be alterations in intrinsic cell properties (i.e., threshold potential, input resistance, and current densities) or network connections. With an improved MEA system it would be important to study burst synchronicity and inhibitory and excitatory responses to determine whether there is any epileptiform activity which could correlate with that seen in patients with Early Infantile Epileptic Encephalopathy 9 (EIEE9).

Finally, using *in vitro* calcium imaging experiments, basic potassium chloride (KCl)-evoked calcium responses were measured in these cultures to get an idea of calcium handling within each culture system. Interestingly, it was revealed that the peak KCl-induced response was lower in both KO and mixed cultures. There are several ways in which these differences could be explained as described in more detail in **Section 6.3.4.2**. They could be due to altered distribution or amount of certain voltage-gated calcium channels. As previous mass spectrometry analysis conducted in the Martinez-Garay laboratory has revealed that PCDH19 interacts with voltage-dependent L-type calcium channel subunits, L-type calcium channel blockers, such as nifedipine or nimodipine, could be used to test whether the calcium responses are affected by this interaction. Additionally, different number and types of calcium channels are expressed in specific cortical neurons (Giffin *et al.* 1991), and as the percentage of cortical cell-types expressed in KO and WT neurons was not statistically analysed, it remains a possibility that there are different proportions of certain cell types in each culture. Moreover, there could be differences in the percentage of inhibitory neurons that could reduce activity-induced excitatory responses. Finally, it is also important to highlight that WT cells changed their behaviour in the mixed culture, reducing their KCl-evoked calcium response compared to WT cells in a WT culture. Although the reason for this phenomenon is unknown, it is hypothesised that PCDH19 may be involved in trans-synaptic regulation, and lack of PCDH19 at a pre-synaptic site could alter the synaptic response in a WT cell. Tracing the synaptic connections within the mixed culture would

be vital for subsequent studies to look at specific connection and the functional impact these cells have at an individual cell level.

7.3 Craniofrontonasal syndrome: cell sorting behaviour and its role during cortical neurogenesis and synapse formation

During this thesis, an unusual cell sorting behaviour was observed between PCDH19+ and PCDH19- cells within the HET mouse cortex. This sorting arrangement was also recently published, and data in this thesis and in other papers has confirmed that the cell sorting is not due to random X-inactivation (Pederick *et al.* 2018). The impact this segregation may have on early and late cortical development, including during the establishment of brain circuitry, is not yet determined. However, this is an important factor that may contribute to the pathogenic mechanism of EIEE9.

Although unusual, the cell segregation pattern underlying the X-linked inheritance of EIEE9 is not entirely novel. Craniofrontonasal syndrome (CFNS) is a disorder that commonly leads to craniosyntosis of the coronal sutures, orbital hypertelorism and bifid nasal tip (van den Elzen *et al.* 2014). CFNS is an X-linked disorder that holds a similar inheritance pattern as EIEE9, as heterozygous females and males harbouring somatic mutations are affected, while hemizygous males are usually spared or show less severe symptoms (Wieland *et al.* 2004; Twigg *et al.* 2013). CFNS heterozygous females display mosaic expression of the ephrinB1 gene *(EFNB1).* This gene codes for the ephrin-B1 ligand, which binds to Eph receptors and is a signalling molecule that mediates boundary formation in a number of tissue structures. The theory of cellular interference was also considered in this disorder and studies have been conducted using heterozygous female mice with the mutated *Efnb1*(Compagni *et al.* 2003; Twigg *et al.* 2013). Studying this disorder and its cell sorting behaviour could provide valuable information on the effects of cell sorting behaviour in EIEE9.

Ephrin B1 HET cortices display a similar cell segregation pattern as *Pcdh19* HETs and the cellular mechanism behind this segregation has been further studied (Arvanitis *et al.* 2013). The three main hypotheses are: (1) the differential adhesion hypothesis, where the number and distribution of cell adhesion molecules drives the segregation due to varying adhesive strengths; (2) the cell-cell repulsion theory, where segregating cells are repelled from one another; and (3) the differential interfacial tension hypothesis, where

the differences in cortical tension between cells can lead to a change in forces (or interfacial tension) at the contact site (Brodland 2002). Eph-ephrin signalling has been found to modulate adhesion through regulation of the clustering of cadherins, supporting the differential adhesion theory (Fagotto *et al.* 2013). Additionally, at the dorsal ectoderm-mesoderm boundary in early Xenopus embryos, complementary expression of ephrin/Eph pairs was able to generate a repulsive signal at the boundary, complementing the cell-cell repulsion theory (Rohani *et al.* 2014). Alternatively, when ephrin-B1 exhibited mosaic expression in HEK293 cells, ephrin B kinase unidirectional signalling led to Rho kinase activity and the generation of cortical actin-myosin contractility differences between cells expressing and not expressing ephrin B1, which have been speculated to cause altered interfacial tensions, fitting with the differential interfacial tension hypothesis (O'Neill *et al.* 2016). Together these studies highlight that although it has been hypothesised that incompatible binding affinities of protocadherins lead to the unusual cell-sorting arrangements found in the *Pcdh19* HET cortices (Pederick *et al.* 2018) it is important to take into consideration other possible cell sorting theories, as described above for ephrin-Eph cell segregation, that could provide alternative although not mutually exclusive explanations.

Cell sorting occurred at E10.5 in *ephrin B1* HET cortices, similar to *Pcdh19* HET cortices (Arvanitis *et al.* 2013; Pederick *et al.* 2018). Interestingly, ephrin B was found to promote integrin-based cell-adhesion of apical progenitors to the ventricular zone of the cortex and is critical for the integrity of the neuroepithelium during neurogenesis (Arvanitis *et al.* 2013). As PCDH19 has a conserved integrin binding RGD sequence motif within the EC2 sequence (Cooper *et al.* 2016), it is possible that PCDH19 is similarly regulating RGC maintenance at the apical membrane via an integrin-based cell-cell and cell-extracellular matrix adhesion mechanism. Also, PCDH19 progenitor behaviour has not been studied as early as E10.5, therefore, it would be of interest to determine whether PCDH19 promotes a similar phenotype at this early developmental age. *Ephrin B1* knockdown experiments have also shown that ephrin B1 regulates neural progenitor cell maintenance, preventing neuronal differentiation (Qiu *et al.* 2008), correlating with that seen with *Pcdh19* knockdown experiments (Fujitani *et al.* 2017).

Ephrin B ligands have also been shown to be involved in synapse development, regulating the assembly of pre-synaptic specializations (McClelland *et al.* 2009), the

development of filopodia-like protrusions and spine maturation (Segura *et al.* 2007), and synaptic transmission (Hruska and Dalva 2012). Also, the ephrin B3 ligand from the same family has been shown to function as a competitive signal, regulating synapse number in individual cortical neurons by competing for the limited EphB2 presynaptic protein binding sites (McClelland *et al.* 2010). It has been observed that WT and ephrin B3$^{-/-}$ separate neuronal cultures develop a similar and "normal" number of synapses. However, in cortical co-cultures, where WT neurons were mixed with ephrin B3$^{-/-}$ neurons at a 1:10 ratio, respectively, the WT neurons had a significantly higher number of synapses than WT neurons cultured separately. In contrast, when mixing ephrin B3$^{-/-}$ neurons with WT neurons at a 1:10 ratio, respectively, ephrin B3$^{-/-}$ neurons formed significantly fewer synapses than ephrin B3$^{-/-}$ in separate cultures (McClelland *et al.* 2010). With regards to PCDH19, it would be particularly interesting to carry out a similar experiment, using ESC-derived neurons to determine whether there are competitive signals that could lead to alterations in synapse number and density. This competitive signalling could underlie a mechanism where the number of synapses a neuron receives is dependent on the neurons that co-exist, complementing the theory of cellular interference.

Although the phenotypic features of the two disorders are different, similarities in the inheritance and potential functional roles of the genes during corticogenesis reveals how cell segregation and tissue mosaicism could underly alterations in progenitor behaviour and synapse formation. Therefore, the study of CFNS may help gain insight into possible physiological and pathological mechanisms that underly EIEE9.

7.4 Advantage and disadvantages of the mouse as a model for EIEE9

During this thesis, the focus has been on the use of the *Pcdh19* KO mouse model. Although there have been considerable advancements in the study of PCDH19 using a *Pcdh19* KO mouse model, there are a number of similarities and differences in development and evolution of mice and human that need to be considered when translating mouse models to human studies. Being aware of these factors will help create more translatable hypotheses of the pathogenic mechanism that underly EIEE9.

Unlike zebrafish, where copies of *Pcdh19* are located on chromosome 14, the mouse model is particularly advantageous as *Pcdh19* is located on the X-chromosome and is

subjected to random X-inactivation (Dibbens *et al.* 2008). Furthermore, the *Pcdh19* heterozygous mice present with a mosaic expression of PCDH19 which offers a similarity with *PCDH19* heterozygous females and somatically mutated males with EIEE9 (Dibbens *et al.* 2008; Depienne and LeGuern 2012). Additionally, both mouse and human cortices develop in a similar pattern, forming a six-layered neocortical structure. And although there are differences in the composition of progenitors in the human and mouse cortex, it is clear that the mouse cortex present with a variety of comparable progenitor cell types. A progenitor that is extensively studied in the developing human cortex is the basal RGCs (bRGCs): a type of progenitor cell that is abundant in the primate neocortex and is essential in the expansion of the human SVZ to generate the outer SVZ and cortical folding (Hansen *et al.* 2010). Several types of these bRGCs exist, including apical bRGC, basal bRGC, bipolar bRGC, and transient bRGC (Betizeau *et al.* 2013). Interestingly, there is a sparse population of these bRGCs in the mouse lateral neocortex (Wang *et al.* 2011) and greater numbers in the medial neocortex that are highly related to the bRGCs found in the gyrencephalic neocortex (Vaid *et al.* 2018). In addition, bRGCs in subapical positions have been identified in the mouse cerebral cortex (Pilz *et al.* 2013). Although not directly studied in this thesis, due to these similarities in mouse and human, it would be interesting to study whether these basal RGCs also segregate in the heterozygous brain, as in humans this could lead to abnormal folding which is seen in patients with EIEE9 (Pederick *et al.* 2018).

It is important to note that when studying *Pcdh19* HET mice no apparent spontaneous seizure phenotype is seen in postnatal and adult mice (Pederick *et al.* 2016; Hayashi *et al.* 2017). However, electrocorticogram (ECoG) recordings have shown abnormal network brain activity in the *Pcdh19* heterozygous mice and behaviourally, a decreased fear response that was not seen in hemizygous males (Hayashi *et al.* 2017; Pederick *et al.* 2018). These results highlight that PCDH19 is altering neuronal interactions somehow and the differential phenotype in KO and HET mice does correlate with that seen in hemizygous males and heterozygous females.

There are, however, disadvantages to the use of the mouse model. The human cortex is much larger and more complex than the mouse cortex, so there are, of course, some differences in their development. Firstly, human cortices are gyrencephalic (folded), while mouse cortices are lissencephalic (smooth) which is linked to the differences in

neuronal and glial amplification, production, and diversity (Borrell and Calegari 2014; Sun and Hevner 2014). In addition, it has been shown that the first mitotic neurons in the preplate of the human cortex are not found in mouse, and are different from Cajal-Retzuis cells (Bystron *et al.* 2006). Furthermore, although both mouse and human progenitor cells generate neurons throughout cortical development, most neuronal and glial cells are generated prenatally in humans, whereas most glial cells are generated postnatally in mouse (Kriegstein and Alvarez-Buylla 2009). Also, when considering IPCs, human IPCs undergo multiple rounds of transit amplification before neuronal differentiation, whereas mouse IPC's have limited rounds of proliferation (LaMonica *et al.* 2013).

Together, these comparisons address some of the major advantages and disadvantages of the PCDH19 mouse model. Although there are differences between human and mouse cortical development, there are obvious similarities and evidence of evolutionarily conserved cell types and mechanisms that should be investigated in mouse models to provide a platform for future human studies.

7.5 Advancements of *in vitro* stem cell systems to study PCDH19

In vitro cultures have only recently been published to study PCDH19, using mouse neural stem progenitor cell (NSPC)-derived neurons (Homan *et al.* 2018), and human induced pluripotent stem cell (iPSC)-derived neurons (Compagnucci *et al.* 2015; Homan *et al.* 2018). During this thesis, *Pcdh19* KO embryonic stem cells (ESCs) have been derived from the *Pcdh19* KO mouse model to generate "cortical-like" neurons to study synapse formation and function.

It is favourable to use *in vitro* studies to assess EIEE9's disease mechanism, due to the scalability and the purity of the cultures, making them useful for drug screening, imaging assays, and genome-wide analysis. However, there are drawbacks with these culture systems that are being addressed more recently with the development of 3D cultures. One major limitation is the physical interactions these cultures have with the plastic dish. Interactions with the dish can prevail over other cell-cell interactions, causing alterations in apical-basal polarity or changes in the cells' physiological properties as the cells become flat on the dish (Kawaguchi *et al.* 2017). In addition, the cytoarchitecture of the cortex is lost using 2D cultures, which is particularly important in this instance due to the PCDH19 mosaicism and aberrant cell sorting behaviour found in the *Pcdh19* HET mouse

cortices. Therefore, approaches have been taken to create 3D cultures referred to as organoids or organ spheroids, with more complex cell-cell interactions, the freedom for proliferative expansion and a higher cell diversity and maturity (Lancaster and Knoblich 2014a, b). Specifically, a method has been generated that produces a laminated "cerebral cortex-like" structure from human pluripotent stem cells; generating electrophysiologically mature deep and superficial layered neurons and astrocytes that can form functional synapses (Pasca *et al.* 2015). This organoid differentiation procedure would be particularly useful as *Pcdh19* heterozygous organoids could be generated to determine whether the unusual cell sorting arrangements are present in these cultures, and to subsequently determine whether PCDH19 expressing and non-expressing progenitor cells deviate in proliferative behaviour as seen in the mouse model. These studies could then lead to the assessment of the distribution of neurons and connectivity in the maturing *Pcdh19* HET organoids.

As many neuropsychiatric disorders including epilepsy and autism spectrum disorder (ASD) are associated with dysfunctional communication between excitatory glutamatergic neurons and GABAergic interneurons (Rubenstein and Merzenich 2003; Marin 2012), subpallium and pallium organoids have recently been fused together to generate interacting human "assembloids" to study the communication between excitatory and inhibitory systems (Birey *et al.* 2017). Although not yet published, there have been new advancements in the study of EIEE9 using assembloids. Interestingly, when studying the differential gene expression in control and EIEE9 patient derived assembliods using RNA sequencing, several genes were downregulated or upregulated. Gene ontology analysis showed an enrichment of genes involved in homophilic cell adhesion, synapse assembly and positive regulation of motility in these assembliods highlighting a possible synaptic function of PCDH19 (PCDH19 Alliance Conference 2018). Future work using these assembliods would allow for the study of inhibitory neuronal migration, inter-regional interactions, and circuit assembly to shed light on connectivity and the theory of cellular interference in EIEE9.

Despite the considerable amount of progress made establishing the human organoid system, there are some drawbacks with their use. For example, some of the cell types that influence early cortical development and progenitor behaviour, such as endothelial cells and microglia are missing in these organoids (Di Lullo and Kriegstein 2017). These

organoids also lack additional structural features of the primary developing cortex, such as a RGC scaffold and correct cortical layering and circuitry (Di Lullo and Kriegstein 2017), which would need to be considered when comparing to the human developing cortex.

7.6 Studying other protocadherins to understand PCDH19's role in brain morphogenesis

Different cadherins have unique spatial and temporal expression patterns during CNS development that differ from each other in terms of region, circuit, and cell-type. There is however a degree of overlapping expression, where cells express multiple cadherins that interact in cis and trans to form combinational codes that regulate brain morphogenesis and contribute to the complexity of the neocortex (Gaitan and Bouchard 2006; Kim *et al.* 2007; Etzrodt *et al.* 2009; Hertel and Redies 2011; Krishna-K *et al.* 2011). At the individual cell level, cell sorting behaviours and cell adhesion have been shown to be dependent on the expression of multiple protocadherins (Bisogni *et al.* 2018; Pederick *et al.* 2018). Loss of a single protocadherin alters the combination of protocadherins expressed and can change cell-cell interactions, leading to altered functionality through both adhesion and signalling processes (Thu *et al.* 2014; Bisogni *et al.* 2018). It is therefore important to study other cadherins that show overlapping expression with PCDH19 or are evolutionarily similar to PCDH19 to obtain further information about the physiological and pathophysiological role of PCDH19.

As explained previously, N-cadherin associates with PCDH19 in cis to form a strongly adhesive complex (Biswas *et al.* 2010; Emond *et al.* 2011). This robust adhesiveness is governed by PCDH19 (Emond *et al.* 2011); hence, it is likely that N-cadherin's functional role during brain development could partially be regulated by PCDH19. N-cadherin is expressed highly throughout early cortical development and is required for the organization of neuroepithelial cells and RGCs in the mouse cortex (Kadowaki et al. 2007). N-cadherin maintains adherens junction integrity during the transition of NEs to RGCs and regulates neuronal progenitor cell proliferation and the switch from proliferating to neurogenic divisions. The down-regulation of N-cadherin leads to the loss of apical-basal polarity in RGCs and an increase in neuronal differentiation (Miyamoto *et al.* 2015). PCDH19 may be involved in the maintenance of proliferative RGCs and apical-

basal polarity is altered in HET iPSCs (Homan *et al.* 2018). It could be hypothesised that PCDH19 might play a role in the adhesiveness of N-cadherin at the adherens junctions of RGCs as discussed in Chapter 4 **Section 4.3.2**. N-cadherin has also been shown to be localised perisynaptically during early development (Uchida *et al.* 1996), and in close proximity to the synapse later on. N-cadherin affects synaptic function by regulating axonal outgrowth and presynaptic bouton stabilization, by binding to β-catenin and activating downstream intracellular signalling pathways (Bekirov *et al.* 2008). It would, therefore, be important to study these stages of synaptic assembly with regards to PCDH19.

PCDH19's two most closely related δ2-protocadherins are PCDH10 and PCDH17. Interestingly, all three protocadherins have a peak expression during early corticogenesis in human (Ip *et al.* 2010). Their evolutionary conservation indicates that they may share functional roles. PCDH10 is required for thalamocortical and corticothalamic projections during embryonic development, and axonal guidance and extension in striatal neurons (Uemura *et al.* 2007). Moreover, PCDH10 plays a crucial role in cortical synapse elimination via the degradation of PSD-95 (Tsai *et al.* 2012). This elimination is associated with Fragile X-syndrome but is also a common mechanism underlying ASD, and as ASD is a phenotypic feature of EIEE9, this could highlight a conserved function between PCDH10 and PCDH19. PCDH17 is important in the assembly of presynaptic specializations of the corticobasal ganglia circuits (Hoshina *et al.* 2013). PCDH17 also regulates axonal extension of amygdala neurons through the recruitment of WAVE complex components to cell-cell interaction sites, converting axons into motile structures (Hayashi *et al.* 2014). In addition, PCDH17 mediates axon growth and soma topography in the ocular motor systems of zebrafish through protocadherin-mediated repulsion (Asakawa and Kawakami 2018). As PCDH19 also contains a WIRS binding domain and has been shown to bind to components of the WAVE complex (Hayashi *et al.* 2017) it might play a similar role in axonal development. Overall, as PCDH10 and PCDH17 are evolutionarily similar to PCDH19 and are involved in synapse formation and circuit assembly, it is highly likely that PCDH19 may function similarly in other distinctive regions of the developing brain.

Finally, aside from the cadherins discussed in detail, a recent mass spectrometry analysis in the Martinez-Garay laboratory has revealed that PCDH19 interacts with a

number of other cadherins in the adult cortex. These include classical cadherins, 10, 11, 18, 20, δ1 protocadherins 1, 7, 9, and multiple subtypes of α, β, and γ -protocadherins. Therefore, an in-depth characterisation of these protocadherins in neurogenesis and synapse formation, as well as an assessment on whether these cadherins together form a combinatorial code with PCDH19, may provide information regarding protocadherin-mediated function in cortical development, cell-segregation, adhesion and circuit formation.

7.7 Future directions

The results presented so far have provided a platform for understanding the role of PCDH19 in both neurogenesis and synapse formation, and future experiments could stem from this current work.

With regards to PCDH19 in neurogenesis, it is important to determine whether the differences seen in the neurogenic behaviours of PCDH19 WT and KO progenitors within the HET are sustained over time. Therefore, the analysis conducted thus far using birth dating strategies and cell-type markers should be repeated at earlier and later embryonic ages. Additionally, within the HET cortices, PCDH19 KO RGCs could be contributing more neurons to layers VI and V, and less to the upper layers IV and III/II of the developing cortex. The X-GFP mouse model could provide an excellent tool to trace PCDH19 WT, and KO progenitor progeny to study any differences in layer contribution. Furthermore, alterations in neuronal cell distribution due to differential progenitor behaviour within the matured HET cortices may lead to alterations in brain circuitry and could be studied electrophysiologically using brain slices and whole cell patch clamp experiments.

Future studies are also required to determine the cellular and molecular mechanisms that govern the differential neurogenic behaviour of the two progenitor cell populations within the HET cortex. This mechanism would not only be essential in understanding the pathogenesis underlying EIEE9, but also will be crucial in determining the general mechanism controlling the switch from proliferative to neurogenic divisions in neural progenitors. Cellular and molecular features that could be studied in future experiments include apicobasal polarity, spindle orientation, cell cycle length and molecular signalling pathways such as Notch and FGF signalling. Interestingly, it has already been shown

that lack of PCDH19 causes loss of apical-basal polarity in iPSC's *in vitro* (Homan *et al.* 2018) and it has been discussed that there is an interaction between PCDH19 and FGFR2, raising the possibility of differential signalling in the presence/absence of PCDH19 (Cortical Development Conference 2017). Therefore, it is important to expand on these findings using the *Pcdh19* HET mouse for further assessment.

In this study, co-cultured PCDH19 WT and KO mouse "cortical-like" neurons were generated to model cellular mosaicism which is associated with EIEE9 in humans. As the main aim was to use this co-culture to assess the theory of cellular interference, it is important to continue on from the preliminary analysis conducted so far. With the addition of a traceable *Pcdh19* KO cell line, the number of synapses formed between WT:WT, KO:KO, WT:KO and KO:WT synaptic partners within the HET cortex could be determined. Additionally, it would be of interest to generate co-cultures with different ratios of WT and KO neurons, to study competitive signalling effects. As the key phenotypic feature of EIEE9 is epilepsy, it is also important to study the electrophysiological properties of these neurons, to understand whether there is hyper-synchronised, hyper-excitable neuronal firing within the co-cultures that is reminiscent of that seen in EIEE9. If this is indeed found in this culture system, it would be essential to correlate this phenotype with any changes that may be present in synapse assembly during the differentiation and maturation of these "cortical-like" neurons.

7.8 Concluding remarks

EIEE9 is a debilitating disorder that causes early onset epilepsy and a multitude of cognitive disabilities. Although an increasing number of studies are trying to decipher the pathogenic mechanism that underpins EIEE9, this mechanism is yet to be determined. As cadherins are known to have multiple roles during brain morphogenesis, it is difficult to pinpoint the exact function that is associated with the disorder. In fact, the disease mechanism will most probably incorporate both the cell-cell adhesive functions and intracellular signalling functions of PCDH19.

The unusual inheritance pattern of EIEE9 implicates mosaicism as the critical factor in the disease. The results presented in this thesis prove how important the mosaicism is during the early stages of cortical development and reveals how individual behaviours of PCDH19 expressing and PCDH19 non-expressing progenitor cells may have an impact

on neuronal distribution rather than overall neuronal number. It is possible that the aberrant changes in neurogenic behaviour between these two cell populations could later affect circuit formation by altering synapse assembly and function. Therefore, it is important to study progenitor fate and use the *in vitro* system generated in this thesis to study whether the mosaic expression of PCDH19 alters synapse number between specific synaptic partners, to prove and understand the impact cellular interference may have on EIEE9. Combining the *in vivo* and *in vitro* mouse models used in this thesis, significant advances in the understanding of the molecular and cellular mechanisms underlying the pathophysiology of EIEE9 could be achieved in the future.

Bibliography

Aaku-Saraste, E., Hellwig, A. and Huttner, W. B. (1996). Loss of Occludin and Functional Tight Junctions, but Not ZO-1, during Neural Tube Closure—Remodeling of the Neuroepithelium Prior to Neurogenesis. *Developmental Biology* **180**(2):664-679.

Ahmari, S. E., Buchanan, J. and Smith, S. J. (2000). Assembly of presynaptic active zones from cytoplasmic transport packets. *Nat Neurosci* **3**(5):445-451.

Alcántara, S., Ruiz, M., D'Arcangelo, G., Ezan, F., De Lecea, L., Curran, T., . . . Soriano, E. (1998). Regional and cellular patterns of reelin mRNA expression in the forebrain of the developing and adult mouse. *Journal of Neuroscience* **18**(19):7779-7799.

Alsanie, W. F., Niclis, J. C., Hunt, C. P., De Luzy, I. R., Penna, V., Bye, C. R., . . . Parish, C. L. (2017). Specification of murine ground state pluripotent stem cells to regional neuronal populations. *Sci Rep* **7**(1):16001.

Alsina, B., Vu, T. and Cohen-Cory, S. (2001). Visualizing synapse formation in arborizing optic axons in vivo: dynamics and modulation by BDNF. *Nat Neurosci* **4**(11):1093-1101.

Anggono, V. and Huganir, R. L. (2012). Regulation of AMPA receptor trafficking and synaptic plasticity. *Curr Opin Neurobiol* **22**(3):461-469.

Arai, Y., Pulvers, J. N., Haffner, C., Schilling, B., Nusslein, I., Calegari, F. and Huttner, W. B. (2011). Neural stem and progenitor cells shorten S-phase on commitment to neuron production. *Nat Commun* **2**:154.

Arvanitis, D. N., Béhar, A., Tryoen-Tóth, P., Bush, J. O., Jungas, T., Vitale, N. and Davy, A. (2013). Ephrin B1 maintains apical adhesion of neural progenitors. *Development* **140**(10):2082.

Asakawa, K. and Kawakami, K. (2018). Protocadherin-Mediated Cell Repulsion Controls the Central Topography and Efferent Projections of the Abducens Nucleus. *Cell Rep* **24**(6):1562-1572.

Asami, M., Pilz, G. A., Ninkovic, J., Godinho, L., Schroeder, T., Huttner, W. B. and Gotz, M. (2011). The role of Pax6 in regulating the orientation and mode of cell division of progenitors in the mouse cerebral cortex. *Development* **138**(23):5067-5078.

Attardo, A., Calegari, F., Haubensak, W., Wilsch-Brauninger, M. and Huttner, W. B. (2008). Live imaging at the onset of cortical neurogenesis reveals differential appearance

of the neuronal phenotype in apical versus basal progenitor progeny. *PLoS One* **3**(6):e2388.

Barakat, T. S. and Gribnau, J. (2010). X chromosome inactivation and embryonic stem cells. *Adv Exp Med Biol* **695**:132-154.

Barth, L., Sütterlin, R., Nenniger, M. and Vogt, K. E. (2014). Functional differentiation of stem cell-derived neurons from different murine backgrounds. *Frontiers in cellular neuroscience* **8**:49-49.

Bassani, S., Cwetsch, A. W., Gerosa, L., Serratto, G. M., Folci, A., Hall, I. F., . . . Passafaro, M. (2018). The female epilepsy protein PCDH19 is a new GABAAR-binding partner that regulates GABAergic transmission as well as migration and morphological maturation of hippocampal neurons. *Hum Mol Genet* **27**(6):1027-1038.

Bekirov, I. H., Nagy, V., Svoronos, A., Huntley, G. W. and Benson, D. L. (2008). Cadherin-8 and N-cadherin differentially regulate pre- and postsynaptic development of the hippocampal mossy fiber pathway. *Hippocampus* **18**(4):349-363.

Berry, C. T., Sceniak, M. P., Zhou, L. and Sabo, S. L. (2012). Developmental up-regulation of vesicular glutamate transporter-1 promotes neocortical presynaptic terminal development. *PLoS One* **7**(11):e50911.

Bertram, E. H. (2013). Neuronal circuits in epilepsy: do they matter? *Exp Neurol* **244**:67-74.

Betizeau, M., Cortay, V., Patti, D., Pfister, S., Gautier, E., Bellemin-Ménard, A., . . . Dehay, C. (2013). Precursor Diversity and Complexity of Lineage Relationships in the Outer Subventricular Zone of the Primate. *Neuron* **80**(2):442-457.

Bibel, M., Richter, J., Lacroix, E. and Barde, Y.-A. (2007). Generation of a defined and uniform population of CNS progenitors and neurons from mouse embryonic stem cells. *Nature Protocols* **2**:1034.

Bibel, M., Richter, J., Schrenk, K., Tucker, K. L., Staiger, V., Korte, M., . . . Barde, Y.-A. (2004). Differentiation of mouse embryonic stem cells into a defined neuronal lineage. *Nature Neuroscience* **7**(9):1003-1009.

Bielle, F., Griveau, A., Narboux-Neme, N., Vigneau, S., Sigrist, M., Arber, S., . . . Pierani, A. (2005). Multiple origins of Cajal-Retzius cells at the borders of the developing pallium. *Nat Neurosci* **8**(8):1002-1012.

Birey, F., Andersen, J., Makinson, C. D., Islam, S., Wei, W., Huber, N., . . . Paşca, S. P. (2017). Assembly of functionally integrated human forebrain spheroids. *Nature* **545**(7652):54-59.

Bisogni, A. J., Ghazanfar, S., Williams, E. O., Marsh, H. M., Yang, J. Y. H. and Lin, D. M. (2018). Tuning of delta-protocadherin adhesion through combinatorial diversity. *eLife* **7**:e41050.

Biswas, S., Emond, M. R., Duy, P. Q., Hao le, T., Beattie, C. E. and Jontes, J. D. (2014). Protocadherin-18b interacts with Nap1 to control motor axon growth and arborization in zebrafish. *Mol Biol Cell* **25**(5):633-642.

Biswas, S., Emond, M. R. and Jontes, J. D. (2010). Protocadherin-19 and N-cadherin interact to control cell movements during anterior neurulation. *J Cell Biol* **191**(5):1029-1041.

Borrell, V. and Calegari, F. (2014). Mechanisms of brain evolution: Regulation of neural progenitor cell diversity and cell cycle length. *Neuroscience Research* **86**:14-24.

Bresler, T., Shapira, M., Boeckers, T., Dresbach, T., Futter, M., Garner, C. C., . . . Ziv, N. E. (2004). Postsynaptic Density Assembly Is Fundamentally Different from Presynaptic Active Zone Assembly. *The Journal of Neuroscience* **24**(6):1507.

Brodland, G. W. (2002). The Differential Interfacial Tension Hypothesis (DITH): a comprehensive theory for the self-rearrangement of embryonic cells and tissues. *J Biomech Eng* **124**(2):188-197.

Bruses, J. L. (2006). N-cadherin signaling in synapse formation and neuronal physiology. *Mol Neurobiol* **33**(3):237-252.

Bultje, R. S., Castaneda-Castellanos, D. R., Jan, L. Y., Jan, Y. N., Kriegstein, A. R. and Shi, S. H. (2009). Mammalian Par3 regulates progenitor cell asymmetric division via notch signaling in the developing neocortex. *Neuron* **63**(2):189-202.

Bystron, I., Rakic, P., Molnar, Z. and Blakemore, C. (2006). The first neurons of the human cerebral cortex. *Nat Neurosci* **9**(7):880-886.

Calegari, F., Haubensak, W., Haffner, C. and Huttner, W. B. (2005). Selective lengthening of the cell cycle in the neurogenic subpopulation of neural progenitor cells during mouse brain development. *J Neurosci* **25**(28):6533-6538.

Calegari, F. and Huttner, W. B. (2003). An inhibition of cyclin-dependent kinases that lengthens, but does not arrest, neuroepithelial cell cycle induces premature neurogenesis. *J Cell Sci* **116**(Pt 24):4947-4955.

Caviness, V. S., Jr. (1982). Neocortical histogenesis in normal and reeler mice: a developmental study based upon [3H]thymidine autoradiography. *Brain Res* **256**(3):293-302.

Chang, H., Hoshina, N., Zhang, C., Ma, Y., Cao, H., Wang, Y., . . . Li, M. (2017). The protocadherin 17 gene affects cognition, personality, amygdala structure and function, synapse development and risk of major mood disorders. *Mol Psychiatry*.

Charalampopoulos, I., Remboutsika, E., Margioris, A. N. and Gravanis, A. (2008). Neurosteroids as modulators of neurogenesis and neuronal survival. *Trends Endocrinol Metab* **19**(8):300-307.

Chen, B., Brinkmann, K., Chen, Z., Pak, C. W., Liao, Y., Shi, S., . . . Rosen, M. K. (2014a). The WAVE regulatory complex links diverse receptors to the actin cytoskeleton. *Cell* **156**(1-2):195-207.

Chen, C.-C., Lu, J. and Zuo, Y. (2014b). Spatiotemporal dynamics of dendritic spines in the living brain. *Frontiers in neuroanatomy* **8**:28-28.

Chen, X. and Gumbiner, B. M. (2006). Paraxial protocadherin mediates cell sorting and tissue morphogenesis by regulating C-cadherin adhesion activity. *J Cell Biol* **174**(2):301-313.

Cholfin, J. A. and Rubenstein, J. L. (2008). Frontal cortex subdivision patterning is coordinately regulated by Fgf8, Fgf17, and Emx2. *J Comp Neurol* **509**(2):144-155.

Clapcote, S. J. and Roder, J. C. (2005). Simplex PCR assay for sex determination in mice. *Biotechniques* **38**(5):702, 704, 706.

Compagni, A., Logan, M., Klein, R. and Adams, R. H. (2003). Control of skeletal patterning by ephrinB1-EphB interactions. *Dev Cell* **5**(2):217-230.

Compagnucci, C., Petrini, S., Higuraschi, N., Trivisano, M., Specchio, N., Hirose, S., . . . Terracciano, A. (2015). Characterizing PCDH19 in human induced pluripotent stem cells (iPSCs) and iPSC-derived developing neurons: emerging role of a protein involved in controlling polarity during neurogenesis. *Oncotarget* **6**(29):26804-26813.

Compagnucci, C., Piemonte, F., Sferra, A., Piermarini, E. and Bertini, E. (2016). The cytoskeletal arrangements necessary to neurogenesis. *Oncotarget*.

Cooper, S. R., Jontes, J. D. and Sotomayor, M. (2016). Structural determinants of adhesion by Protocadherin-19 and implications for its role in epilepsy. *Elife* **5**.

Costa, M. R., Wen, G., Lepier, A., Schroeder, T. and Gotz, M. (2008). Par-complex proteins promote proliferative progenitor divisions in the developing mouse cerebral cortex. *Development* **135**(1):11-22.

Cárdenas, A., Villalba, A., de Juan Romero, C., Picó, E., Kyrousi, C., Tzika, A. C., . . . Borrell, V. (2018). Evolution of Cortical Neurogenesis in Amniotes Controlled by Robo Signaling Levels. *Cell* **174**(3):590-606.e521.

Dalva, M. B., McClelland, A. C. and Kayser, M. S. (2007). Cell adhesion molecules: signalling functions at the synapse. *Nature reviews. Neuroscience* **8**(3):206-220.

de Lange, I. M., Rump, P., Neuteboom, R. F., Augustijn, P. B., Hodges, K., Kistemaker, A. I., . . . Brilstra, E. H. (2017). Male patients affected by mosaic PCDH19 mutations: five new cases. *Neurogenetics* **18**(3):147-153.

Dean, B., Keriakous, D., Scarr, E. and Thomas, E. A. (2007). Gene expression profiling in Brodmann's area 46 from subjects with schizophrenia. *Aust N Z J Psychiatry* **41**(4):308-320.

Dehay, C. and Kennedy, H. (2007). Cell-cycle control and cortical development. *Nat Rev Neurosci* **8**(6):438-450.

Dehay, C., Kennedy, H. and Kosik, Kenneth S. (2015). The Outer Subventricular Zone and Primate-Specific Cortical Complexification. *Neuron* **85**(4):683-694.

Deidda, G., Bozarth, I. F. and Cancedda, L. (2014). Modulation of GABAergic transmission in development and neurodevelopmental disorders: investigating physiology and pathology to gain therapeutic perspectives. *Frontiers in cellular neuroscience* **8**:119-119.

del Río, J. A., Martinez, A., Fonseca, M., Auladell, C. and Soriano, E. (1995). Glutamate-like Immunoreactivity and Fate of Cajal-Retzius Cells in the Murine Cortex as Identified with Calretinin Antibody. *Cerebral Cortex* **5**(1):13-21.

Delaunay, D., Cortay, V., Patti, D., Knoblauch, K. and Dehay, C. (2014). Mitotic Spindle Asymmetry: A Wnt/PCP-Regulated Mechanism Generating Asymmetrical Division in Cortical Precursors. *Cell Reports* **6**(2):400-414.

Depienne, C., Bouteiller, D., Keren, B., Cheuret, E., Poirier, K., Trouillard, O., . . . Leguern, E. (2009). Sporadic infantile epileptic encephalopathy caused by mutations in PCDH19 resembles Dravet syndrome but mainly affects females. *PLoS Genet* **5**(2):e1000381.

Depienne, C. and LeGuern, E. (2012). PCDH19-related infantile epileptic encephalopathy: an unusual X-linked inheritance disorder. *Hum Mutat* **33**(4):627-634.

Di Lullo, E. and Kriegstein, A. R. (2017). The use of brain organoids to investigate neural development and disease. *Nature reviews. Neuroscience* **18**(10):573-584.

Dibbens, L. M., Tarpey, P. S., Hynes, K., Bayly, M. A., Scheffer, I. E., Smith, R., . . . Gécz, J. (2008). X-linked protocadherin 19 mutations cause female-limited epilepsy and cognitive impairment. *Nat Genet* **40**(6):776-781.

Dong, Z., Yang, N., Yeo, S. Y., Chitnis, A. and Guo, S. (2012). Intralineage directional Notch signaling regulates self-renewal and differentiation of asymmetrically dividing radial glia. *Neuron* **74**(1):65-78.

Duan, X., Krishnaswamy, A., De la Huerta, I. and Sanes, Joshua R. (2014). Type II Cadherins Guide Assembly of a Direction-Selective Retinal Circuit. *Cell* **158**(4):793-807.

Duan, X., Krishnaswamy, A., Laboulaye, M. A., Liu, J., Peng, Y. R., Yamagata, M., . . . Sanes, J. R. (2018). Cadherin Combinations Recruit Dendrites of Distinct Retinal Neurons to a Shared Interneuronal Scaffold. *Neuron* **99**(6):1145-1154.e1146.

Dumont, E. C. (2009). What is the bed nucleus of the stria terminalis? *Progress in neuro-psychopharmacology & biological psychiatry* **33**(8):1289-1290.

Duszyc, K., Terczynska, I. and Hoffman-Zacharska, D. (2015). Epilepsy and mental retardation restricted to females: X-linked epileptic infantile encephalopathy of unusual inheritance. *J Appl Genet* **56**(1):49-56.

Eckler, M. J., Nguyen, T. D., McKenna, W. L., Fastow, B. L., Guo, C., Rubenstein, J. L. R. and Chen, B. (2015). Cux2-positive radial glial cells generate diverse subtypes of neocortical projection neurons and macroglia. *Neuron* **86**(4):1100-1108.

Emond, M. R., Biswas, S., Blevins, C. J. and Jontes, J. D. (2011). A complex of Protocadherin-19 and N-cadherin mediates a novel mechanism of cell adhesion. *J Cell Biol* **195**(7):1115-1121.

Emond, M. R., Biswas, S. and Jontes, J. D. (2009). Protocadherin-19 is essential for early steps in brain morphogenesis. *Dev Biol* **334**(1):72-83.

Englund, C., Fink, A., Lau, C., Pham, D., Daza, R. A., Bulfone, A., . . . Hevner, R. F. (2005). Pax6, Tbr2, and Tbr1 are expressed sequentially by radial glia, intermediate progenitor cells, and postmitotic neurons in developing neocortex. *J Neurosci* **25**(1):247-251.

Etzrodt, J., Krishna-K, K. and Redies, C. (2009). Expression of classic cadherins and delta-protocadherins in the developing ferret retina. *BMC neuroscience* **10**:153-153.

Fagotto, F., Rohani, N., Touret, A.-S. and Li, R. (2013). A Molecular Base for Cell Sorting at Embryonic Boundaries: Contact Inhibition of Cadherin Adhesion by Ephrin/Eph-Dependent Contractility. *Developmental Cell* **27**(1):72-87.

Farhy-Tselnicker, I. and Allen, N. J. (2018). Astrocytes, neurons, synapses: a tripartite view on cortical circuit development. *Neural Development* **13**(1):7.

Feldmeyer, D. and van Aerde, K. I. (2013). Morphological and Physiological Characterization of Pyramidal Neuron Subtypes in Rat Medial Prefrontal Cortex. *Cerebral Cortex* **25**(3):788-805.

Feng, Y. and Walsh, C. A. (2004). Mitotic Spindle Regulation by Nde1 Controls Cerebral Cortical Size. *Neuron* **44**(2):279-293.

Franco, S. J., Gil-Sanz, C., Martinez-Garay, I., Espinosa, A., Harkins-Perry, S. R., Ramos, C. and Muller, U. (2012). Fate-restricted neural progenitors in the mammalian cerebral cortex. *Science* **337**(6095):746-749.

Franco, S. J., Martinez-Garay, I., Gil-Sanz, C., Harkins-Perry, S. R. and Müller, U. (2011). Reelin regulates cadherin function via Dab1/Rap1 to control neuronal migration and lamination in the neocortex. *Neuron* **69**(3):482-497.

Friedman, H. V., Bresler, T., Garner, C. C. and Ziv, N. E. (2000). Assembly of new individual excitatory synapses: time course and temporal order of synaptic molecule recruitment. *Neuron* **27**(1):57-69.

Friedman, L. G., Benson, D. L. and Huntley, G. W. (2015). Cadherin-based transsynaptic networks in establishing and modifying neural connectivity. *Curr Top Dev Biol* **112**:415-465.

Fujitani, M., Zhang, S., Fujiki, R., Fujihara, Y. and Yamashita, T. (2017). A chromosome 16p13.11 microduplication causes hyperactivity through dysregulation of miR-484/protocadherin-19 signaling. *Mol Psychiatry* **22**(3):364-374.

Gaiano, N., Nye, J. S. and Fishell, G. (2000). Radial glial identity is promoted by Notch1 signaling in the murine forebrain. *Neuron* **26**(2):395-404.

Gaitan, Y. and Bouchard, M. (2006). Expression of the delta-protocadherin gene Pcdh19 in the developing mouse embryo. *Gene Expr Patterns* **6**(8):893-899.

Gao, P., Postiglione, M. P., Krieger, T. G., Hernandez, L., Wang, C., Han, Z., . . . Shi, S. H. (2014). Deterministic progenitor behavior and unitary production of neurons in the neocortex. *Cell* **159**(4):775-788.

Garcia, I., Huang, L., Ung, K. and Arenkiel, B. R. (2012). Tracing synaptic connectivity onto embryonic stem cell-derived neurons. *Stem Cells* **30**(10):2140-2151.

Garner, C. C., Zhai, R. G., Gundelfinger, E. D. and Ziv, N. E. (2002). Molecular mechanisms of CNS synaptogenesis. *Trends in Neurosciences* **25**(5):243-250.

Garrett, Andrew M., Schreiner, D., Lobas, Mark A. and Weiner, Joshua A. (2012). γ-Protocadherins Control Cortical Dendrite Arborization by Regulating the Activity of a FAK/PKC/MARCKS Signaling Pathway. *Neuron* **74**(2):269-276.

Gaspard, N., Bouschet, T., Herpoel, A., Naeije, G., van den Ameele, J. and Vanderhaeghen, P. (2009). Generation of cortical neurons from mouse embryonic stem cells. *Nature Protocols* **4**:1454.

Gazina, E. V., Morrisroe, E., Mendis, G. D. C., Michalska, A. E., Chen, J., Nefzger, C. M., . . . Petrou, S. (2018). Method of derivation and differentiation of mouse embryonic stem cells generating synchronous neuronal networks. *Journal of Neuroscience Methods* **293**:53-58.

Gerosa, L., Francolini, M., Bassani, S. and Passafaro, M. (2018). The role of Protocadherin 19 (PCDH19) in neurodevelopment and in the pathophysiology of early infantile epileptic encephalopathy-9 (EIEE9). *Dev Neurobiol*.

Gerrow, K., Romorini, S., Nabi, S. M., Colicos, M. A., Sala, C. and El-Husseini, A. (2006). A preformed complex of postsynaptic proteins is involved in excitatory synapse development. *Neuron* **49**(4):547-562.

Giffin, K., Solomon, J. S., Burkhalter, A. and Nerbonne, J. M. (1991). Differential expression of voltage-gated calcium channels in identified visual cortical neurons. *Neuron* **6**(3):321-332.

Gil-Sanz, C., Espinosa, A., Fregoso, S. P., Bluske, K. K., Cunningham, C. L., Martinez-Garay, I., . . . Muller, U. (2015). Lineage Tracing Using Cux2-Cre and Cux2-CreERT2 Mice. *Neuron* **86**(4):1091-1099.

Gil-Sanz, C., Franco, S. J., Martinez-Garay, I., Espinosa, A., Harkins-Perry, S. and Müller, U. (2013). Cajal-Retzius cells instruct neuronal migration by coincidence signaling between secreted and contact-dependent guidance cues. *Neuron* **79**(3):461-477.

Goodman, K. M., Rubinstein, R., Thu, C. A., Bahna, F., Mannepalli, S., Ahlsen, G., . . . Shapiro, L. (2016). Structural Basis of Diverse Homophilic Recognition by Clustered alpha- and beta-Protocadherins. *Neuron* **90**(4):709-723.

Gotz, M. and Barde, Y. A. (2005). Radial glial cells defined and major intermediates between embryonic stem cells and CNS neurons. *Neuron* **46**(3):369-372.

Gribnau, J. and Barakat, T. S. (2017). X-chromosome inactivation and its implications for human disease. *bioRxiv*:076950.

Gu, X., Liu, B., Wu, X., Yan, Y., Zhang, Y., Wei, Y., . . . Zhao, C. (2011). Inducible genetic lineage tracing of cortical hem derived Cajal-Retzius cells reveals novel properties. *PLoS One* **6**(12):e28653.

Gärtner, A., Fornasiero, E. F. and Dotti, C. G. (2014). Cadherins as regulators of neuronal polarity. *Cell adhesion & migration* **9**(3):175-182.

Götz, M. and Huttner, W. B. (2005). The cell biology of neurogenesis. *Nat Rev Mol Cell Biol* **6**(10):777-788.

Hadjantonakis, A.-K., Gertsenstein, M., Ikawa, M., Okabe, M. and Nagy, A. (1998). Non-invasive sexing of preimplantation stage mammalian embryos. *Nature Genetics* **19**:220.

Hansen, D. V., Lui, J. H., Parker, P. R. and Kriegstein, A. R. (2010). Neurogenic radial glia in the outer subventricular zone of human neocortex. *Nature* **464**(7288):554-561.

Hanzlik, E. and Gigante, J. (2017). Microcephaly. *Children (Basel)* **4**(6).

Hasegawa, S., Kobayashi, H., Kumagai, M., Nishimaru, H., Tarusawa, E., Kanda, H., . . . Yagi, T. (2017). Clustered Protocadherins Are Required for Building Functional Neural Circuits. *Frontiers in molecular neuroscience* **10**:114-114.

Hatakeyama, J., Wakamatsu, Y., Nagafuchi, A., Kageyama, R., Shigemoto, R. and Shimamura, K. (2014). Cadherin-based adhesions in the apical endfoot are required for active Notch signaling to control neurogenesis in vertebrates. *Development* **141**(8):1671-1682.

Haubensak, W., Attardo, A., Denk, W. and Huttner, W. B. (2004). Neurons arise in the basal neuroepithelium of the early mammalian telencephalon: a major site of neurogenesis. *Proc Natl Acad Sci U S A* **101**(9):3196-3201.

Hayashi, S., Inoue, Y., Hattori, S., Kaneko, M., Shioi, G., Miyakawa, T. and Takeichi, M. (2017). Loss of X-linked Protocadherin-19 differentially affects the behavior of heterozygous female and hemizygous male mice. *Sci Rep* **7**(1):5801.

Hayashi, S., Inoue, Y., Kiyonari, H., Abe, T., Misaki, K., Moriguchi, H., . . . Takeichi, M. (2014). Protocadherin-17 mediates collective axon extension by recruiting actin regulator complexes to interaxonal contacts. *Dev Cell* **30**(6):673-687.

Hayashi, S. and Takeichi, M. (2015). Emerging roles of protocadherins: from self-avoidance to enhancement of motility. *J Cell Sci* **128**(8):1455-1464.

Hedrich, U. B., Liautard, C., Kirschenbaum, D., Pofahl, M., Lavigne, J., Liu, Y., . . . Lerche, H. (2014). Impaired action potential initiation in GABAergic interneurons causes hyperexcitable networks in an epileptic mouse model carrying a human Na(V)1.1 mutation. *J Neurosci* **34**(45):14874-14889.

Heikkilä, T. J., Ylä-Outinen, L., Tanskanen, J. M. A., Lappalainen, R. S., Skottman, H., Suuronen, R., . . . Narkilahti, S. (2009). Human embryonic stem cell-derived neuronal cells form spontaneously active neuronal networks in vitro. *Experimental Neurology* **218**(1):109-116.

Hendzel, M. J., Wei, Y., Mancini, M. A., Van Hooser, A., Ranalli, T., Brinkley, B. R., . . . Allis, C. D. (1997). Mitosis-specific phosphorylation of histone H3 initiates primarily within pericentromeric heterochromatin during G2 and spreads in an ordered fashion coincident with mitotic chromosome condensation. *Chromosoma* **106**(6):348-360.

Hertel, N. and Redies, C. (2011). Absence of layer-specific cadherin expression profiles in the neocortex of the reeler mutant mouse. *Cereb Cortex* **21**(5):1105-1117.

Hertel, N., Redies, C. and Medina, L. (2012). Cadherin expression delineates the divisions of the postnatal and adult mouse amygdala. *J Comp Neurol* **520**(17):3982-4012.

Hevner, R. F., Neogi, T., Englund, C., Daza, R. A. and Fink, A. (2003). Cajal-Retzius cells in the mouse: transcription factors, neurotransmitters, and birthdays suggest a pallial origin. *Brain Res Dev Brain Res* **141**(1-2):39-53.

Hirano, S. and Takeichi, M. (2012). Cadherins in brain morphogenesis and wiring. *Physiol Rev* **92**(2):597-634.

Hirokawa, N., Noda, Y., Tanaka, Y. and Niwa, S. (2009). Kinesin superfamily motor proteins and intracellular transport. *Nature Reviews Molecular Cell Biology* **10**:682.

Homan, C. C., Pederson, S., To, T. H., Tan, C., Piltz, S., Corbett, M. A., . . . Gecz, J. (2018). PCDH19 regulation of neural progenitor cell differentiation suggests asynchrony of neurogenesis as a mechanism contributing to PCDH19 Girls Clustering Epilepsy. *Neurobiol Dis* **116**:106-119.

Hoshina, N., Tanimura, A., Yamasaki, M., Inoue, T., Fukabori, R., Kuroda, T., . . . Yamamoto, T. (2013). Protocadherin 17 Regulates Presynaptic Assembly in Topographic Corticobasal Ganglia Circuits. *Neuron* **78**(5):839-854.

Hruska, M. and Dalva, M. B. (2012). Ephrin regulation of synapse formation, function and plasticity. *Molecular and cellular neurosciences* **50**(1):35-44.

Hulpiau, P. and van Roy, F. (2009). Molecular evolution of the cadherin superfamily. *Int J Biochem Cell Biol* **41**(2):349-369.

Huntley, G. W. and Jones, E. G. (1990). Cajal-Retzius neurons in developing monkey neocortex show immunoreactivity for calcium binding proteins. *J Neurocytol* **19**(2):200-212.

Iacopetti, P., Michelini, M., Stuckmann, I., Oback, B., Aaku-Saraste, E. and Huttner, W. B. (1999). Expression of the antiproliferative gene TIS21 at the onset of neurogenesis identifies single neuroepithelial cells that switch from proliferative to neuron-generating division. *Proc Natl Acad Sci U S A* **96**(8):4639-4644.

Ing-Esteves, S., Kostadinov, D., Marocha, J., Sing, A. D., Joseph, K. S., Laboulaye, M. A., . . . Lefebvre, J. L. (2018). Combinatorial Effects of Alpha- and Gamma-Protocadherins on Neuronal Survival and Dendritic Self-Avoidance. *J Neurosci* **38**(11):2713-2729.

Ip, B. K., Wappler, I., Peters, H., Lindsay, S., Clowry, G. J. and Bayatti, N. (2010). Investigating gradients of gene expression involved in early human cortical development. *Journal of anatomy* **217**(4):300-311.

Ippolito, D. M. and Eroglu, C. (2010). Quantifying synapses: an immunocytochemistry-based assay to quantify synapse number. *J Vis Exp* (45).

Jacobs, E. C., Campagnoni, C., Kampf, K., Reyes, S. D., Kalra, V., Handley, V., . . . Campagnoni, A. T. (2007). Visualization of corticofugal projections during early cortical development in a tau-GFP-transgenic mouse. *Eur J Neurosci* **25**(1):17-30.

Johnson, W. G. (1980). Metabolic interference and the + - heterozygote. a hypothetical form of simple inheritance which is neither dominant nor recessive. *American journal of human genetics* **32**(3):374-386.

Juberg, R. C. and Hellman, C. D. (1971). A new familial form of convulsive disorder and mental retardation limited to females. *J Pediatr* **79**(5):726-732.

Jüngling, K., Eulenburg, V., Moore, R., Kemler, R., Lessmann, V. and Gottmann, K. (2006). N-Cadherin Transsynaptically Regulates Short-Term Plasticity at Glutamatergic Synapses in Embryonic Stem Cell-Derived Neurons. *The Journal of Neuroscience* **26**(26):6968.

Kang, W., Wong, L. C., Shi, S.-H. and Hébert, J. M. (2009). The Transition from Radial Glial to Intermediate Progenitor Cell Is Inhibited by FGF Signaling during Corticogenesis. *The Journal of Neuroscience* **29**(46):14571.

Kawaguchi, D., Yoshimatsu, T., Hozumi, K. and Gotoh, Y. (2008). Selection of differentiating cells by different levels of delta-like 1 among neural precursor cells in the developing mouse telencephalon. *Development* **135**(23):3849-3858.

Kawaguchi, K., Kageyama, R. and Sano, M. (2017). Topological defects control collective dynamics in neural progenitor cell cultures. *Nature* **545**:327.

Kawauchi, T., Sekine, K., Shikanai, M., Chihama, K., Tomita, K., Kubo, K., . . . Hoshino, M. (2010). Rab GTPases-dependent endocytic pathways regulate neuronal migration and maturation through N-cadherin trafficking. *Neuron* **67**(4):588-602.

Keeler, A. B., Molumby, M. J. and Weiner, J. A. (2015). Protocadherins branch out: Multiple roles in dendrite development. *Cell Adhesion & Migration* **9**(3):214-226.

Kim, S. Y., Chung, H. S., Sun, W. and Kim, H. (2007). Spatiotemporal expression pattern of non-clustered protocadherin family members in the developing rat brain. *Neuroscience* **147**(4):996-1021.

Kim, S. Y., Mo, J. W., Han, S., Choi, S. Y., Han, S. B., Moon, B. H., . . . Kim, H. (2010). The expression of non-clustered protocadherins in adult rat hippocampal formation and the connecting brain regions. *Neuroscience* **170**(1):189-199.

Kim, S. Y., Yasuda, S., Tanaka, H., Yamagata, K. and Kim, H. (2011). Non-clustered protocadherin. *Cell Adh Migr* **5**(2):97-105.

Kolc, K. L., Sadleir, L. G., Scheffer, I. E., Ivancevic, A., Roberts, R., Pham, D. H. and Gecz, J. (2018). A systematic review and meta-analysis of 271 PCDH19-variant individuals identifies psychiatric comorbidities, and association of seizure onset and disease severity. *Mol Psychiatry*.

Konno, D., Shioi, G., Shitamukai, A., Mori, A., Kiyonari, H., Miyata, T. and Matsuzaki, F. (2008). Neuroepithelial progenitors undergo LGN-dependent planar divisions to maintain self-renewability during mammalian neurogenesis. *Nat Cell Biol* **10**(1):93-101.

Kosodo, Y., Roper, K., Haubensak, W., Marzesco, A. M., Corbeil, D. and Huttner, W. B. (2004). Asymmetric distribution of the apical plasma membrane during neurogenic divisions of mammalian neuroepithelial cells. *Embo j* **23**(11):2314-2324.

Kowalczyk, T., Pontious, A., Englund, C., Daza, R. A., Bedogni, F., Hodge, R., . . . Hevner, R. F. (2009). Intermediate neuronal progenitors (basal progenitors) produce pyramidal-projection neurons for all layers of cerebral cortex. *Cereb Cortex* **19**(10):2439-2450.

Kriegstein, A. and Alvarez-Buylla, A. (2009). The glial nature of embryonic and adult neural stem cells. *Annu Rev Neurosci* **32**:149-184.

Kriegstein, A., Noctor, S. and Martinez-Cerdeno, V. (2006). Patterns of neural stem and progenitor cell division may underlie evolutionary cortical expansion. *Nat Rev Neurosci* **7**(11):883-890.

Krishna-K, K., Hertel, N. and Redies, C. (2011). Cadherin expression in the somatosensory cortex: evidence for a combinatorial molecular code at the single-cell level. *Neuroscience* **175**:37-48.

LaMonica, B. E., Lui, J. H., Hansen, D. V. and Kriegstein, A. R. (2013). Mitotic spindle orientation predicts outer radial glial cell generation in human neocortex. *Nat Commun* **4**:1665.

Lancaster, M. A. and Knoblich, J. A. (2012). Spindle orientation in mammalian cerebral cortical development. *Current Opinion in Neurobiology* **22**(5):737-746.

Lancaster, M. A. and Knoblich, J. A. (2014a). Generation of cerebral organoids from human pluripotent stem cells. *Nat Protoc* **9**(10):2329-2340.

Lancaster, M. A. and Knoblich, J. A. (2014b). Organogenesis in a dish: modeling development and disease using organoid technologies. *Science* **345**(6194):1247125.

Lefebvre, J. L., Kostadinov, D., Chen, W. V., Maniatis, T. and Sanes, J. R. (2012). Protocadherins mediate dendritic self-avoidance in the mammalian nervous system. *Nature* **488**(7412):517-521.

Li, H., Chang, Y.-W., Mohan, K., Su, H.-W., Ricupero, C. L., Baridi, A., . . . Grumet, M. (2008). Activated Notch1 maintains the phenotype of radial glial cells and promotes their adhesion to laminin by upregulating nidogen. *Glia* **56**(6):646-658.

Lisman, J. E. (1997). Bursts as a unit of neural information: making unreliable synapses reliable. *Trends Neurosci* **20**(1):38-43.

Llorca, A., Ciceri, G., Beattie, R., Wong, F. K., Diana, G., Serafeimidou, E., . . . Marin, O. (2018). Heterogeneous progenitor cell behaviors underlie the assembly of neocortical cytoarchitecture. *bioRxiv*:494088.

Lukaszewicz, A., Savatier, P., Cortay, V., Kennedy, H. and Dehay, C. (2002). Contrasting Effects of Basic Fibroblast Growth Factor and Neurotrophin 3 on Cell Cycle Kinetics of Mouse Cortical Stem Cells. *The Journal of Neuroscience* **22**(15):6610.

Lyon, M. F. (1961). Gene Action in the X-chromosome of the Mouse (Mus musculus L.). *Nature* **190**:372.

Machon, O., Backman, M., Machonova, O., Kozmik, Z., Vacik, T., Andersen, L. and Krauss, S. (2007). A dynamic gradient of Wnt signaling controls initiation of neurogenesis

in the mammalian cortex and cellular specification in the hippocampus. *Dev Biol* **311**(1):223-237.

Maeda, E., Robinson, H. P. and Kawana, A. (1995). The mechanisms of generation and propagation of synchronized bursting in developing networks of cortical neurons. *J Neurosci* **15**(10):6834-6845.

Magrinelli, E., Wagener, R. J. and Jabaudon, D. (2018). Simultaneous production of diverse neuronal subtypes during early corticogenesis. *bioRxiv*:369678.

Malatesta, P., Hartfuss, E. and Gotz, M. (2000). Isolation of radial glial cells by fluorescent-activated cell sorting reveals a neuronal lineage. *Development* **127**(24):5253-5263.

Manabe, N., Hirai, S.-I., Imai, F., Nakanishi, H., Takai, Y. and Ohno, S. (2002). Association of ASIP/mPAR-3 with adherens junctions of mouse neuroepithelial cells. *Developmental Dynamics* **225**(1):61-69.

Marin, O. (2012). Interneuron dysfunction in psychiatric disorders. *Nat Rev Neurosci* **13**(2):107-120.

Marin, O. and Rubenstein, J. L. (2001). A long, remarkable journey: tangential migration in the telencephalon. *Nat Rev Neurosci* **2**(11):780-790.

Marini, C., Darra, F., Specchio, N., Mei, D., Terracciano, A., Parmeggiani, L., . . . Guerrini, R. (2012). Focal seizures with affective symptoms are a major feature of PCDH19 gene-related epilepsy. *Epilepsia* **53**(12):2111-2119.

Markram, H., Wang, Y. and Tsodyks, M. (1998). Differential signaling via the same axon of neocortical pyramidal neurons. *Proceedings of the National Academy of Sciences* **95**(9):5323.

Martinez-Garay, I., Gil-Sanz, C., Franco, S. J., Espinosa, A., Molnar, Z. and Mueller, U. (2016). Cadherin 2/4 signaling via PTP1B and catenins is crucial for nucleokinesis during radial neuronal migration in the neocortex. *Development* **143**(12):2121-2134.

Martynoga, B., Drechsel, D. and Guillemot, F. (2012). Molecular control of neurogenesis: a view from the mammalian cerebral cortex. *Cold Spring Harb Perspect Biol* **4**(10).

Martynoga, B., Morrison, H., Price, D. J. and Mason, J. O. (2005). Foxg1 is required for specification of ventral telencephalon and region-specific regulation of dorsal telencephalic precursor proliferation and apoptosis. *Dev Biol* **283**(1):113-127.

Matsuzaki, F. and Shitamukai, A. (2015). Cell Division Modes and Cleavage Planes of Neural Progenitors during Mammalian Cortical Development. *Cold Spring Harbor perspectives in biology* **7**(9):a015719-a015719.

McAllister, A. K. (2007). Dynamic aspects of CNS synapse formation. *Annual review of neuroscience* **30**:425-450.

McClelland, A. C., Hruska, M., Coenen, A. J., Henkemeyer, M. and Dalva, M. B. (2010). Trans-synaptic EphB2-ephrin-B3 interaction regulates excitatory synapse density by inhibition of postsynaptic MAPK signaling. *Proceedings of the National Academy of Sciences of the United States of America* **107**(19):8830-8835.

McClelland, A. C., Sheffler-Collins, S. I., Kayser, M. S. and Dalva, M. B. (2009). Ephrin-B1 and ephrin-B2 mediate EphB-dependent presynaptic development via syntenin-1. *Proc Natl Acad Sci U S A* **106**(48):20487-20492.

McConnell, S. K., Ghosh, A. and Shatz, C. J. (1994). Subplate pioneers and the formation of descending connections from cerebral cortex. *J Neurosci* **14**(4):1892-1907.

McConnell, S. K. and Kaznowski, C. E. (1991). Cell cycle dependence of laminar determination in developing neocortex. *Science* **254**(5029):282-285.

Mellitzer, G., Xu, Q. and Wilkinson, D. G. (1999). Eph receptors and ephrins restrict cell intermingling and communication. *Nature* **400**(6739):77-81.

Meyer, G. (2010). Building a human cortex: the evolutionary differentiation of Cajal-Retzius cells and the cortical hem. *J Anat* **217**(4):334-343.

Mircsof, D., Langouët, M., Rio, M., Moutton, S., Siquier-Pernet, K., Bole-Feysot, C., . . . Colleaux, L. (2015). Mutations in NONO lead to syndromic intellectual disability and inhibitory synaptic defects. *Nature neuroscience* **18**(12):1731-1736.

Miyamoto, Y., Sakane, F. and Hashimoto, K. (2015). N-cadherin-based adherens junction regulates the maintenance, proliferation, and differentiation of neural progenitor cells during development. *Cell adhesion & migration* **9**(3):183-192.

Mizutani, K., Yoon, K., Dang, L., Tokunaga, A. and Gaiano, N. (2007). Differential Notch signalling distinguishes neural stem cells from intermediate progenitors. *Nature* **449**(7160):351-355.

Molumby, M. J., Keeler, A. B. and Weiner, J. A. (2016). Homophilic Protocadherin Cell-Cell Interactions Promote Dendrite Complexity. *Cell Rep* **15**(5):1037-1050.

Morrow, E. M., Yoo, S. Y., Flavell, S. W., Kim, T. K., Lin, Y., Hill, R. S., . . . Walsh, C. A. (2008). Identifying autism loci and genes by tracing recent shared ancestry. *Science* **321**(5886):218-223.

Mountoufaris, G., Chen, W. V., Hirabayashi, Y., O'Keeffe, S., Chevee, M., Nwakeze, C. L., . . . Maniatis, T. (2017). Multicluster Pcdh diversity is required for mouse olfactory neural circuit assembly. *Science* **356**(6336):411-414.

MuhChyi, C., Juliandi, B., Matsuda, T. and Nakashima, K. (2013). Epigenetic regulation of neural stem cell fate during corticogenesis. *International Journal of Developmental Neuroscience* **31**(6):424-433.

Nadarajah, B., Brunstrom, J. E., Grutzendler, J., Wong, R. O. and Pearlman, A. L. (2001). Two modes of radial migration in early development of the cerebral cortex. *Nat Neurosci* **4**(2):143-150.

Narayanan, B., Soh, P., Calhoun, V. D., Ruano, G., Kocherla, M., Windemuth, A., . . . Pearlson, G. D. (2015). Multivariate genetic determinants of EEG oscillations in schizophrenia and psychotic bipolar disorder from the BSNIP study. *Transl Psychiatry* **5**:e588.

Nelson, B. R., Hodge, R. D., Bedogni, F. and Hevner, R. F. (2013). Dynamic interactions between intermediate neurogenic progenitors and radial glia in embryonic mouse neocortex: potential role in Dll1-Notch signaling. *J Neurosci* **33**(21):9122-9139.

Nguyen, L., Besson, A., Roberts, J. M. and Guillemot, F. (2006). Coupling cell cycle exit, neuronal differentiation and migration in cortical neurogenesis. *Cell Cycle* **5**(20):2314-2318.

Nieto, M., Monuki, E. S., Tang, H., Imitola, J., Haubst, N., Khoury, S. J., . . . Walsh, C. A. (2004). Expression of Cux-1 and Cux-2 in the subventricular zone and upper layers II-IV of the cerebral cortex. *J Comp Neurol* **479**(2):168-180.

Nieto, M., Schuurmans, C., Britz, O. and Guillemot, F. (2001). Neural bHLH Genes Control the Neuronal versus Glial Fate Decision in Cortical Progenitors. *Neuron* **29**(2):401-413.

Noctor, S. C., Flint, A. C., Weissman, T. A., Dammerman, R. S. and Kriegstein, A. R. (2001). Neurons derived from radial glial cells establish radial units in neocortex. *Nature* **409**(6821):714-720.

Noctor, S. C., Martinez-Cerdeno, V., Ivic, L. and Kriegstein, A. R. (2004). Cortical neurons arise in symmetric and asymmetric division zones and migrate through specific phases. *Nat Neurosci* **7**(2):136-144.

O'Neill, A. K., Kindberg, A. A., Niethamer, T. K., Larson, A. R., Ho, H. H., Greenberg, M. E. and Bush, J. O. (2016). Unidirectional Eph/ephrin signaling creates a cortical actomyosin differential to drive cell segregation. *J Cell Biol* **215**(2):217-229.

Ogawa, M., Miyata, T., Nakajima, K., Yagyu, K., Seike, M., Ikenaka, K., . . . Mikoshiba, K. (1995). The reeler gene-associated antigen on Cajal-Retzius neurons is a crucial molecule for laminar organization of cortical neurons. *Neuron* **14**(5):899-912.

Ohnuma, S., Philpott, A. and Harris, W. A. (2001). Cell cycle and cell fate in the nervous system. *Curr Opin Neurobiol* **11**(1):66-73.

Osheroff, H. and Hatten, M. E. (2009). Gene expression profiling of preplate neurons destined for the subplate: genes involved in transcription, axon extension, neurotransmitter regulation, steroid hormone signaling, and neuronal survival. *Cereb Cortex* **19 Suppl 1**:i126-134.

Park, S.-Y., Yoon, S. N., Kang, M.-J., Lee, Y., Jung, S. J. and Han, J.-S. (2016). Hippocalcin Promotes Neuronal Differentiation and Inhibits Astrocytic Differentiation in Neural Stem Cells. *Stem cell reports* **8**(1):95-111.

Pasca, A. M., Sloan, S. A., Clarke, L. E., Tian, Y., Makinson, C. D., Huber, N., . . . Pasca, S. P. (2015). Functional cortical neurons and astrocytes from human pluripotent stem cells in 3D culture. *Nat Methods* **12**(7):671-678.

Pederick, D. T., Homan, C. C., Jaehne, E. J., Piltz, S. G., Haines, B. P., Baune, B. T., . . . Thomas, P. Q. (2016). Pcdh19 Loss-of-Function Increases Neuronal Migration In Vitro but is Dispensable for Brain Development in Mice. *Sci Rep* **6**:26765.

Pederick, D. T., Richards, K. L., Piltz, S. G., Kumar, R., Mincheva-Tasheva, S., Mandelstam, S. A., . . . Thomas, P. Q. (2018). Abnormal Cell Sorting Underlies the Unique X-Linked Inheritance of PCDH19 Epilepsy. *Neuron* **97**(1):59-66.e55.

Pedraza, M., Hoerder-Suabedissen, A., Albert-Maestro, M. A., Molnar, Z. and De Carlos, J. A. (2014). Extracortical origin of some murine subplate cell populations. *Proc Natl Acad Sci U S A* **111**(23):8613-8618.

Perez, D., Hsieh, D. T. and Rohena, L. (2017). Somatic Mosaicism of PCDH19 in a male with early infantile epileptic encephalopathy and review of the literature. *Am J Med Genet A* **173**(6):1625-1630.

Pham, D. H., Tan, C. C., Homan, C. C., Kolc, K. L., Corbett, M. A., McAninch, D., . . . Gecz, J. (2017). Protocadherin 19 (PCDH19) interacts with paraspeckle protein NONO to co-regulate gene expression with estrogen receptor alpha (ERalpha). *Hum Mol Genet* **26**(11):2042-2052.

Pilaz, L. J., Patti, D., Marcy, G., Ollier, E., Pfister, S., Douglas, R. J., . . . Dehay, C. (2009). Forced G1-phase reduction alters mode of division, neuron number, and laminar phenotype in the cerebral cortex. *Proc Natl Acad Sci U S A* **106**(51):21924-21929.

Pilz, G.-A., Shitamukai, A., Reillo, I., Pacary, E., Schwausch, J., Stahl, R., . . . Götz, M. (2013). Amplification of progenitors in the mammalian telencephalon includes a new radial glial cell type. *Nature communications* **4**:2125-2125.

Price, D. J., Aslam, S., Tasker, L. and Gillies, K. (1997). Fates of the earliest generated cells in the developing murine neocortex. *J Comp Neurol* **377**(3):414-422.

Qiu, R., Wang, X., Davy, A., Wu, C., Murai, K., Zhang, H., . . . Lu, Q. (2008). Regulation of neural progenitor cell state by ephrin-B. *The Journal of Cell Biology* **181**(6):973.

Rakic, P. (1971). Guidance of neurons migrating to the fetal monkey neocortex. *Brain Research* **33**(2):471-476.

Rakic, P. (1995). A small step for the cell, a giant leap for mankind: a hypothesis of neocortical expansion during evolution. *Trends in Neurosciences* **18**(9):383-388.

Ramon Y Cajal, S. (1952). Structure and connections of neurons. *Bull Los Angel Neuro Soc* **17**(1-2):5-46.

Reddy, D. S. (2010). Neurosteroids: endogenous role in the human brain and therapeutic potentials. *Progress in brain research* **186**:113-137.

Reynolds, A. B. (2007). p120-catenin: Past and present. *Biochimica et biophysica acta* **1773**(1):2-7.

Rohani, N., Parmeggiani, A., Winklbauer, R. and Fagotto, F. (2014). Variable Combinations of Specific Ephrin Ligand/Eph Receptor Pairs Control Embryonic Tissue Separation. *PLOS Biology* **12**(9):e1001955.

Romasko, E. J., DeChene, E. T., Balciuniene, J., Akgumus, G. T., Helbig, I., Tarpinian, J. M., . . . Tayoun, A. N. A. (2018). PCDH19-related epilepsy in a male with Klinefelter syndrome: Additional evidence supporting PCDH19 cellular interference disease mechanism. *Epilepsy Research* **145**:89-92.

Rousso, D. L., Pearson, C. A., Gaber, Z. B., Miquelajauregui, A., Li, S., Portera-Cailliau, C., . . . Novitch, B. G. (2012). Foxp-mediated suppression of N-cadherin regulates neuroepithelial character and progenitor maintenance in the CNS. *Neuron* **74**(2):314-330.

Rubenstein, J. L. and Merzenich, M. M. (2003). Model of autism: increased ratio of excitation/inhibition in key neural systems. *Genes Brain Behav* **2**(5):255-267.

Rubinstein, R., Goodman, K. M., Maniatis, T., Shapiro, L. and Honig, B. (2017). Structural origins of clustered protocadherin-mediated neuronal barcoding. *Seminars in Cell & Developmental Biology* **69**:140-150.

Rubinstein, R., Thu, C. A., Goodman, K. M., Wolcott, H. N., Bahna, F., Mannepalli, S., . . . Honig, B. (2015). Molecular logic of neuronal self-recognition through protocadherin domain interactions. *Cell* **163**(3):629-642.

Ryan, S. G., Chance, P. F., Zou, C. H., Spinner, N. B., Golden, J. A. and Smietana, S. (1997). Epilepsy and mental retardation limited to females: an X-linked dominant disorder with male sparing. *Nat Genet* **17**(1):92-95.

Sabo, S. L., Gomes, R. A. and McAllister, A. K. (2006). Formation of presynaptic terminals at predefined sites along axons. *J Neurosci* **26**(42):10813-10825.

Sano, K., Tanihara, H., Heimark, R. L., Obata, S., Davidson, M., St John, T., . . . Suzuki, S. (1993). Protocadherins: a large family of cadherin-related molecules in central nervous system. *Embo j* **12**(6):2249-2256.

Sansom, S. N., Griffiths, D. S., Faedo, A., Kleinjan, D. J., Ruan, Y., Smith, J., . . . Livesey, F. J. (2009). The level of the transcription factor Pax6 is essential for controlling the balance between neural stem cell self-renewal and neurogenesis. *PLoS Genet* **5**(6):e1000511.

Sauer, F. C. (1935). Mitosis in the neural tube. *Journal of Comparative Neurology* **62**(2):377-405.

Schaarschuch, A. and Hertel, N. (2018). Expression profile of N-cadherin and protocadherin-19 in postnatal mouse limbic structures. *J Comp Neurol* **526**(4):663-680.

Scheffer, I. E., Turner, S. J., Dibbens, L. M., Bayly, M. A., Friend, K., Hodgson, B., . . . Berkovic, S. F. (2008). Epilepsy and mental retardation limited to females: an under-recognized disorder. *Brain* **131**(Pt 4):918-927.

Schmid, R. S., McGrath, B., Berechid, B. E., Boyles, B., Marchionni, M., Sestan, N. and Anton, E. S. (2003). Neuregulin 1-erbB2 signaling is required for the establishment of radial glia and their transformation into astrocytes in cerebral cortex. *Proc Natl Acad Sci U S A* **100**(7):4251-4256.

Scholz, K. P. and Miller, R. J. (1995). Developmental changes in presynaptic calcium channels coupled to glutamate release in cultured rat hippocampal neurons. *J Neurosci* **15**(6):4612-4617.

Scholzen, T. and Gerdes, J. (2000). The Ki-67 protein: from the known and the unknown. *J Cell Physiol* **182**(3):311-322.

Schrenk-Siemens, K., Perez-Alcala, S., Richter, J., Lacroix, E., Rahuel, J., Korte, M., . . . Bibel, M. (2008). Embryonic stem cell-derived neurons as a cellular system to study gene function: lack of amyloid precursor proteins APP and APLP2 leads to defective synaptic transmission. *Stem Cells* **26**(8):2153-2163.

Segura, I., Essmann, C. L., Weinges, S. and Acker-Palmer, A. (2007). Grb4 and GIT1 transduce ephrinB reverse signals modulating spine morphogenesis and synapse formation. *Nat Neurosci* **10**(3):301-310.

Sekine, K., Honda, T., Kawauchi, T., Kubo, K. and Nakajima, K. (2011). The outermost region of the developing cortical plate is crucial for both the switch of the radial migration mode and the Dab1-dependent "inside-out" lamination in the neocortex. *J Neurosci* **31**(25):9426-9439.

Sekine, K., Kubo, K. and Nakajima, K. (2014). How does Reelin control neuronal migration and layer formation in the developing mammalian neocortex? *Neurosci Res* **86**:50-58.

Shapira, M., Zhai, R. G., Dresbach, T., Bresler, T., Torres, V. I., Gundelfinger, E. D., . . . Garner, C. C. (2003). Unitary assembly of presynaptic active zones from Piccolo-Bassoon transport vesicles. *Neuron* **38**(2):237-252.

Shapiro, L. and Weis, W. I. (2009). Structure and biochemistry of cadherins and catenins. *Cold Spring Harbor perspectives in biology* **1**(3):a003053-a003053.

Shepherd, N. A., Richman, P. I. and England, J. (1988). Ki-67 derived proliferative activity in colorectal adenocarcinoma with prognostic correlations. *The Journal of Pathology* **155**(3):213-219.

Shikanai, M., Nakajima, K. and Kawauchi, T. (2011). N-cadherin regulates radial glial fiber-dependent migration of cortical locomoting neurons. *Communicative & integrative biology* **4**(3):326-330.

Solter, D. and Knowles, B. B. (1975). Immunosurgery of mouse blastocyst. *Proc Natl Acad Sci U S A* **72**(12):5099-5102.

Spence, E. F. and Soderling, S. H. (2015). Actin Out: Regulation of the Synaptic Cytoskeleton. *The Journal of biological chemistry* **290**(48):28613-28622.

Spruston, N. (2008). Pyramidal neurons: dendritic structure and synaptic integration. *Nature Reviews Neuroscience* **9**:206.

Sun, T. and Hevner, R. F. (2014). Growth and folding of the mammalian cerebral cortex: from molecules to malformations. *Nat Rev Neurosci* **15**(4):217-232.

Suo, L., Lu, H., Ying, G., Capecchi, M. R. and Wu, Q. (2012). Protocadherin clusters and cell adhesion kinase regulate dendrite complexity through Rho GTPase. *J Mol Cell Biol* **4**(6):362-376.

Südhof, T. C. (2018). Towards an Understanding of Synapse Formation. *Neuron* **100**(2):276-293.

Tai, K., Kubota, M., Shiono, K., Tokutsu, H. and Suzuki, S. T. (2010). Adhesion properties and retinofugal expression of chicken protocadherin-19. *Brain Res* **1344**:13-24.

Takahashi, T., Nowakowski, R. S. and Caviness, V. S., Jr. (1993). Cell cycle parameters and patterns of nuclear movement in the neocortical proliferative zone of the fetal mouse. *J Neurosci* **13**(2):820-833.

Takahashi, T., Nowakowski, R. S. and Caviness, V. S., Jr. (1996). The leaving or Q fraction of the murine cerebral proliferative epithelium: a general model of neocortical neuronogenesis. *J Neurosci* **16**(19):6183-6196.

Takano, T., Xu, C., Funahashi, Y., Namba, T. and Kaibuchi, K. (2015). Neuronal polarization. *Development* **142**(12):2088-2093.

Takeichi, M. (2007). The cadherin superfamily in neuronal connections and interactions. *Nat Rev Neurosci* **8**(1):11-20.

Takeichi, M. and Abe, K. (2005). Synaptic contact dynamics controlled by cadherin and catenins. *Trends Cell Biol* **15**(4):216-221.

Takiguchi-Hayashi, K., Sekiguchi, M., Ashigaki, S., Takamatsu, M., Hasegawa, H., Suzuki-Migishima, R., . . . Tanabe, Y. (2004). Generation of reelin-positive marginal zone cells from the caudomedial wall of telencephalic vesicles. *J Neurosci* **24**(9):2286-2295.

Tamamaki, N., Nakamura, K., Okamoto, K. and Kaneko, T. (2001). Radial glia is a progenitor of neocortical neurons in the developing cerebral cortex. *Neurosci Res* **41**(1):51-60.

Tan, C., Shard, C., Ranieri, E., Hynes, K., Pham, D. H., Leach, D., . . . Gecz, J. (2015). Mutations of protocadherin 19 in female epilepsy (PCDH19-FE) lead to allopregnanolone deficiency. *Hum Mol Genet* **24**(18):5250-5259.

Tan, S. S., Faulkner-Jones, B., Breen, S. J., Walsh, M., Bertram, J. F. and Reese, B. E. (1995). Cell dispersion patterns in different cortical regions studied with an X-inactivated transgenic marker. *Development* **121**(4):1029-1039.

Taverna, E., Gotz, M. and Huttner, W. B. (2014). The cell biology of neurogenesis: toward an understanding of the development and evolution of the neocortex. *Annu Rev Cell Dev Biol* **30**:465-502.

Taylor, H. B., Khuong, A., Wu, Z., Xu, Q., Morley, R., Gregory, L., . . . Wilkinson, D. G. (2017). Cell segregation and border sharpening by Eph receptor-ephrin-mediated heterotypic repulsion. *Journal of the Royal Society, Interface* **14**(132):20170338.

Telezhkin, V., Schnell, C., Yarova, P., Yung, S., Cope, E., Hughes, A., . . . Kemp, P. J. (2015). Forced cell cycle exit and modulation of GABAA, CREB, and GSK3β signaling promote functional maturation of induced pluripotent stem cell-derived neurons. *American Journal of Physiology-Cell Physiology* **310**(7):C520-C541.

Terracciano, A., Specchio, N., Darra, F., Sferra, A., Bernardina, B. D., Vigevano, F. and Bertini, E. (2012). Somatic mosaicism of PCDH19 mutation in a family with low-penetrance EFMR. *Neurogenetics* **13**(4):341-345.

Terracciano, A., Trivisano, M., Cusmai, R., De Palma, L., Fusco, L., Compagnucci, C., . . . Specchio, N. (2016). PCDH19-related epilepsy in two mosaic male patients. *Epilepsia* **57**(3):e51-55.

Thiffault, I., Farrow, E., Smith, L., Lowry, J., Zellmer, L., Black, B., . . . Saunders, C. (2016). PCDH19-related epileptic encephalopathy in a male mosaic for a truncating variant. *Am J Med Genet A* **170**(6):1585-1589.

Thu, C. A., Chen, W. V., Rubinstein, R., Chevee, M., Wolcott, H. N., Felsovalyi, K. O., . . . Maniatis, T. (2014). Single-cell identity generated by combinatorial homophilic interactions between alpha, beta, and gamma protocadherins. *Cell* **158**(5):1045-1059.

Togashi, H., Abe, K., Mizoguchi, A., Takaoka, K., Chisaka, O. and Takeichi, M. (2002). Cadherin regulates dendritic spine morphogenesis. *Neuron* **35**(1):77-89.

Toma, K. and Hanashima, C. (2015). Switching modes in corticogenesis: mechanisms of neuronal subtype transitions and integration in the cerebral cortex. *Frontiers in neuroscience* **9**:274-274.

Trachtenberg, J. T., Chen, B. E., Knott, G. W., Feng, G., Sanes, J. R., Welker, E. and Svoboda, K. (2002). Long-term in vivo imaging of experience-dependent synaptic plasticity in adult cortex. *Nature* **420**(6917):788-794.

Trivisano, M., Lucchi, C., Rustichelli, C., Terracciano, A., Cusmai, R., Ubertini, G. M., . . . Specchio, N. (2017). Reduced steroidogenesis in patients with PCDH19-female limited epilepsy. *Epilepsia*.

Tsai, N.-P., Wilkerson, J. R., Guo, W., Maksimova, M. A., DeMartino, G. N., Cowan, C. W. and Huber, K. M. (2012). Multiple autism-linked genes mediate synapse elimination via proteasomal degradation of a synaptic scaffold PSD-95. *Cell* **151**(7):1581-1594.

Tucker, K. L., Meyer, M. and Barde, Y. A. (2001). Neurotrophins are required for nerve growth during development. *Nat Neurosci* **4**(1):29-37.

Tuoc, T. C., Boretius, S., Sansom, S. N., Pitulescu, M. E., Frahm, J., Livesey, F. J. and Stoykova, A. (2013). Chromatin regulation by BAF170 controls cerebral cortical size and thickness. *Dev Cell* **25**(3):256-269.

Twigg, S. R. F., Babbs, C., van den Elzen, M. E. P., Goriely, A., Taylor, S., McGowan, S. J., . . . Wilkie, A. O. M. (2013). Cellular interference in craniofrontonasal syndrome: males mosaic for mutations in the X-linked EFNB1 gene are more severely affected than true hemizygotes. *Human molecular genetics* **22**(8):1654-1662.

Uchida, N., Honjo, Y., Johnson, K. R., Wheelock, M. J. and Takeichi, M. (1996). The catenin/cadherin adhesion system is localized in synaptic junctions bordering transmitter release zones. *J Cell Biol* **135**(3):767-779.

Uemura, M., Nakao, S., Suzuki, S. T., Takeichi, M. and Hirano, S. (2007). OL-Protocadherin is essential for growth of striatal axons and thalamocortical projections. *Nat Neurosci* **10**(9):1151-1159.

Vaid, S., Camp, J. G., Hersemann, L., Oegema, C. E., Heninger, A.-K., Winkler, S., . . . Namba, T. (2018). A novel population of Hopx-dependent basal radial glial cells in the developing mouse neocortex. *Development*.

van den Elzen, M. E. P., Twigg, S. R. F., Goos, J. A. C., Hoogeboom, A. J. M., van den Ouweland, A. M. W., Wilkie, A. O. M. and Mathijssen, I. M. J. (2014). Phenotypes of craniofrontonasal syndrome in patients with a pathogenic mutation in EFNB1. *European journal of human genetics : EJHG* **22**(8):995-1001.

van Harssel, J. J., Weckhuysen, S., van Kempen, M. J., Hardies, K., Verbeek, N. E., de Kovel, C. G., . . . Brilstra, E. H. (2013). Clinical and genetic aspects of PCDH19-related epilepsy syndromes and the possible role of PCDH19 mutations in males with autism spectrum disorders. *Neurogenetics* **14**(1):23-34.

Vanhalst, K., Kools, P., Staes, K., van Roy, F. and Redies, C. (2005). delta-Protocadherins: a gene family expressed differentially in the mouse brain. *Cell Mol Life Sci* **62**(11):1247-1259.

Vasistha, N. A., Garcia-Moreno, F., Arora, S., Cheung, A. F., Arnold, S. J., Robertson, E. J. and Molnar, Z. (2015). Cortical and Clonal Contribution of Tbr2 Expressing Progenitors in the Developing Mouse Brain. *Cereb Cortex* **25**(10):3290-3302.

Veliskova, J. (2007). Estrogens and epilepsy: why are we so excited? *Neuroscientist* **13**(1):77-88.

Vernon, A. E., Devine, C. and Philpott, A. (2003). The cdk inhibitor p27Xic1 is required for differentiation of primary neurones in Xenopus. *Development* **130**(1):85-92.

Vicente-Manzanares, M., Hodges, J. and Horwitz, A. R. (2009). Dendritic Spines: Similarities with Protrusions and Adhesions in Migrating Cells. *The open neuroscience journal* **3**:87-96.

Vigers, A. J. and Pfenninger, K. H. (1991). N-type and L-type calcium channels are present in nerve growth cones. Numbers increase on synaptogenesis. *Developmental Brain Research* **60**(2):197-203.

Wada, T., Wallerich, S. and Becskei, A. (2018). Stochastic Gene Choice during Cellular Differentiation. *Cell Rep* **24**(13):3503-3512.

Waites, C. L., Craig, A. M. and Garner, C. C. (2005). Mechanisms of vertebrate synaptogenesis. *Annu Rev Neurosci* **28**:251-274.

Wang, M. (2011). Neurosteroids and GABA-A Receptor Function. *Frontiers in endocrinology* **2**:44-44.

Wang, X., Tsai, J. W., LaMonica, B. and Kriegstein, A. R. (2011). A new subtype of progenitor cell in the mouse embryonic neocortex. *Nat Neurosci* **14**(5):555-561.

Washbourne, P., Bennett, J. E. and McAllister, A. K. (2002). Rapid recruitment of NMDA receptor transport packets to nascent synapses. *Nat Neurosci* **5**(8):751-759.

Washbourne, P., Liu, X. B., Jones, E. G. and McAllister, A. K. (2004). Cycling of NMDA receptors during trafficking in neurons before synapse formation. *J Neurosci* **24**(38):8253-8264.

Wernig, M., Tucker, K. L., Gornik, V., Schneiders, A., Buschwald, R., Wiestler, O. D., . . . Brustle, O. (2002). Tau EGFP embryonic stem cells: an efficient tool for neuronal lineage selection and transplantation. *J Neurosci Res* **69**(6):918-924.

Wieland, I., Jakubiczka, S., Muschke, P., Cohen, M., Thiele, H., Gerlach, K. L., . . . Wieacker, P. (2004). Mutations of the ephrin-B1 gene cause craniofrontonasal syndrome. *American journal of human genetics* **74**(6):1209-1215.

Winden, K. D., Yuskaitis, C. J. and Poduri, A. (2015). Megalencephaly and Macrocephaly. *Semin Neurol* **35**(3):277-287.

Winkler, C. C., Yabut, O. R., Fregoso, S. P., Gomez, H. G., Dwyer, B. E., Pleasure, S. J. and Franco, S. J. (2018). The Dorsal Wave of Neocortical Oligodendrogenesis Begins Embryonically and Requires Multiple Sources of Sonic Hedgehog. *J Neurosci* **38**(23):5237-5250.

Wojcik, S. M., Rhee, J. S., Herzog, E., Sigler, A., Jahn, R., Takamori, S., . . . Rosenmund, C. (2004). An essential role for vesicular glutamate transporter 1 (VGLUT1) in postnatal development and control of quantal size. *Proceedings of the National Academy of Sciences of the United States of America* **101**(18):7158-7163.

Wong, G. K., Baudet, M. L., Norden, C., Leung, L. and Harris, W. A. (2012). Slit1b-Robo3 signaling and N-cadherin regulate apical process retraction in developing retinal ganglion cells. *J Neurosci* **32**(1):223-228.

Wu, C., Niu, L., Yan, Z., Wang, C., Liu, N., Dai, Y., . . . Xu, R. (2015). Pcdh11x Negatively Regulates Dendritic Branching. *J Mol Neurosci* **56**(4):822-828.

Wu, H., Luo, J., Yu, H., Rattner, A., Mo, A., Wang, Y., . . . Nathans, J. (2014). Cellular resolution maps of X chromosome inactivation: implications for neural development, function, and disease. *Neuron* **81**(1):103-119.

Wu, Q., Zhang, T., Cheng, J. F., Kim, Y., Grimwood, J., Schmutz, J., . . . Maniatis, T. (2001). Comparative DNA sequence analysis of mouse and human protocadherin gene clusters. *Genome Res* **11**(3):389-404.

Yamagata, M., Duan, X. and Sanes, J. R. (2018). Cadherins Interact With Synaptic Organizers to Promote Synaptic Differentiation. *Frontiers in molecular neuroscience* **11**:142-142.

Yasuda, S., Tanaka, H., Sugiura, H., Okamura, K., Sakaguchi, T., Tran, U., . . . Yamagata, K. (2007). Activity-induced protocadherin arcadlin regulates dendritic spine number by triggering N-cadherin endocytosis via TAO2beta and p38 MAP kinases. *Neuron* **56**(3):456-471.

Ying, Q. L., Stavridis, M., Griffiths, D., Li, M. and Smith, A. (2003). Conversion of embryonic stem cells into neuroectodermal precursors in adherent monoculture. In: *Nat Biotechnol*. Vol. 21. United States, pp. 183-186.

Yoon, K., Nery, S., Rutlin, M. L., Radtke, F., Fishell, G. and Gaiano, N. (2004). Fibroblast growth factor receptor signaling promotes radial glial identity and interacts with Notch1 signaling in telencephalic progenitors. *J Neurosci* **24**(43):9497-9506.

Yu, J. S., Koujak, S., Nagase, S., Li, C. M., Su, T., Wang, X., . . . Parsons, R. (2008). PCDH8, the human homolog of PAPC, is a candidate tumor suppressor of breast cancer. *Oncogene* **27**(34):4657-4665.

Zacchetti, A., van Garderen, E., Teske, E., Nederbragt, H., Dierendonck, J. H. and Rutteman, G. R. (2003). Validation of the use of proliferation markers in canine neoplastic and non-neoplastic tissues: comparison of KI-67 and proliferating cell nuclear antigen (PCNA) expression versus in vivo bromodeoxyuridine labelling by immunohistochemistry. *Apmis* **111**(3):430-438.

Zhang, J., Woodhead, G. J., Swaminathan, S. K., Noles, S. R., McQuinn, E. R., Pisarek, A. J., . . . Chenn, A. (2010). Cortical neural precursors inhibit their own differentiation via N-cadherin maintenance of beta-catenin signaling. *Dev Cell* **18**(3):472-479.

Zimmer, C., Tiveron, M. C., Bodmer, R. and Cremer, H. (2004). Dynamics of Cux2 expression suggests that an early pool of SVZ precursors is fated to become upper cortical layer neurons. *Cereb Cortex* **14**(12):1408-1420.

Zou, C., Huang, W., Ying, G. and Wu, Q. (2007). Sequence analysis and expression mapping of the rat clustered protocadherin gene repertoires. *Neuroscience* **144**(2):579-603.